Winter 2013

Investigation of NbNx Thin Films and Nanoparticles Grown by Pulsed Laser Deposition and Thermal Diffusion

Ashraf Hassan Farha
Old Dominion University

INVESTIGATION OF NbN$_x$ THIN FILMS AND NANOPARTICLES GROWN BY

PULSED LASER DEPOSITION AND THERMAL DIFFUSION

by

Ashraf Hassan Farha
B.Sc. June 1999, Ain Shams University, Egypt
M.Sc. February 2004, Ain Shams University, Egypt

A Dissertation Submitted to the Faculty of
Old Dominion University in Partial Fulfillment of the
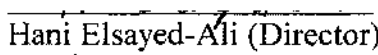Requirements for the Degree of
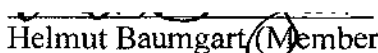
DOCTOR OF PHILOSOPHY

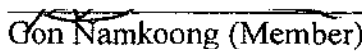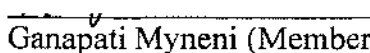ELECTRICAL AND COMPUTER ENGINEERING

OLD DOMINION UNIVERSITY
December 2013

Approved by:

Hani Elsayed-Ali (Director)

Helmut Baumgart (Member)

Gon Namkoong (Member)

Ganapati Myneni (Member)

ABSTRACT

INVESTIGATION OF NbN$_x$ THIN FILMS AND NANOPARTICLES GROWN BY PULSED LASER DEPOSITION AND THERMAL DIFFUSION

Ashraf Hassan Farha
Old Dominion University, 2013
Director: Dr. Hani Elsayed-Ali

Niobium nitride films (NbN$_x$) were grown on Nb and Si (100) substrates using pulsed laser deposition (PLD), laser heating, and thermal diffusion methods. Niobium nitride films were deposited on Nb substrates using PLD with a Q-switched Nd: YAG laser (λ = 1064 nm, 40 ns pulse width, and 10 Hz repetition rate) at different laser fluences, different nitrogen background pressures and deposition temperatures. The effect of changing PLD parameters for films done by PLD was studied. The seen observations establish guidelines for adjusting the laser parameters to achieve the desired morphology and phase of the grown NbN$_x$ films.

When the fabrication parameters are fixed, except for laser fluence, surface roughness, deposition rate, nitrogen content, and grain size increases with increasing laser fluence. Increasing nitrogen background pressure leads to change in the phase structure of the NbN$_x$ films from mixed -Nb$_2$N and cubic δ-NbN phases to single hexagonal β-Nb$_2$N. A change in substrate temperature led to a pronounced change in the preferred orientation of the crystal structure, the phase transformation, surface roughness, and composition of the films.

The structural, electronic, and nanomechanical properties of niobium nitride PLD deposited at different nitrogen pressures (26.7-66.7 Pa) on Si(100) were investigated. The NbN$_x$ films exhibited a cubic δ-NbN with a strong (111) orientation. A correlation between surface morphology, electronic, and superconducting properties was found. The

highly-textured δ-NbN films have a T_c up to 15.07 K. The film was deposited at a nitrogen background pressure of 66.7 Pa exhibited improved superconducting properties and showed higher hardness values as compared to films deposited at lower nitrogen pressures. NbN nanoclusters that were deposited on carbon coated Cu-grids using PLD at laser fluence of 8 J/cm^2 were observed.

Niobium nitride is prepared by heating of Nb sample in a reactive nitrogen atmosphere (133 Pa) at a temperature of 900 °C. The results suggest that the niobium nitride was crystalline in the single phase of hexagonal β-Nb$_2$N. As heating time increased, film growth continued with improvement in hardness and modulus.

The XRD of samples prepared by a thermal diffusion method at low nitrogen pressure and high temperatures were reported. The samples were prepared at temperatures ranging from 1250–1500 °C. 2D-XRD images of samples, processed at temperature range from 1250 –1500 °C at pressure of 1.3×10^{-3} Pa, showed the formation of an α phase. As pressure increased to 0.13 Pa, an α-NbN phase mixed with β-Nb$_2$N phase appeared.

Niobium nitride samples were prepared by laser nitridation using a Q-switched Nd: YAG nanosecond laser and Ti: sapphire femtosecond lasers. The effects of laser fluence on the formed phase, surface morphology, and electronic properties of the NbN$_x$ were investigated. Samples were prepared using Nd: YAG laser are of NbN$_x$ in the cubic δ-NbN phase. The femtosecond laser-nitrided samples were prepared by different laser fluences of 0.1–1.3 mJ/cm^2 at 4.0×10^4 Pa nitrogen pressure. NbN$_x$ samples with mixedα, β and δ phases were observed. The cubic δ-NbN structure is dominated over the other two phases.

This dissertation is dedicated to my parents, my wife Samira, and my children: Mohamed, Rawda and Rana.

ACKNOWLEDGEMENTS

I would like to express my profound gratitude and appreciation to my advisor Prof. Dr Hani Elsayed-Ali. I appreciate all his contributions, ideas, funding and invaluable support that make my PhD studies fruitful. He was my biggest chance during my academic working out at ODU. His expertise on the subject and critical feedback strengthen the thesis and see it through to completion. It has been an honor to work with such a kind of successful scientist and professor. Also I need to express my many thanks to my country Egypt for granted me this PhD scholarship and financial support I got to study in US.

I particularly thank to Prof. Yuksel Ufuktepe who increased our productivity and his positive encouragement help, and for all his contributions that I couldn't be very successful without his supervision and experience. I'd like to thank my entire committee Dr Helmut Baumgart, Dr Gon Namkoong and Dr Ganapati Myneni for taking the time to review my dissertation and providing valuable insight and suggestions.

My thanks and gratitude goes to my family, back home in Egypt, for all their love, inspiration and prayers for me, especially my mother Fathia Mahgoub and my father Saeed Farha who raised; loved and supported me in all my life. Words cannot express my love and thanks for them. Lastly, I want to express my grateful, love and acknowledgments to my wife Samira Abdel Aziz whom I love. Thanks for her continuous love and supports she did during my studying for PhD. And I am thankful for my children, Mohamed Farha, Rawda Farha and Rana Farha, whom I love. I can't imagine a life without them. I wish them all my best in their life.

TABLE OF CONTENTS

LIST OF TABLES

LIST OF FIGURES

CHAPTER I

INTRODUCTION

I.1. BACKGROUND AND MOTIVATION

Niobium nitride (NbN) is one of the nitrides of transition metals. NbN_x films show many interesting properties, such as high hardness, chemical inertness, and relatively high superconductivity transition temperature (17.3 K). These properties make NbN_x films valuable for many superconductor-related applications, such as infrared imaging photo-detectors, superconducting magnets, and other microelectronic devices [1, 2] and superconducting RF cavities [3-7]. Not only can NbN_x be used in superconductivity applications, but it is a good candidate for applications requiring corrosive resistant coatings and hard material. For example, NbN coatings enhance wear resistance of steel surfaces [8]. These good superconductive and mechanical properties of NbN_x thin films are influenced by their crystallographic structure and chemical composition [9, 10].

An NbN system has a complex phase diagram with a wide range of compositions [8]. Different phases of NbN form as the nitrogen-to-metal ratio changes. Several stable phases with different structures have been reported [11]. A list of NbN phases includes α-Nb(N), which is a cubic solid solution formed by dissolving nitrogen in Nb metal, cubic δ-NbN(cubic), hexagonal phases β-Nb_2N, ϵ-NbN and δ'-NbN phases, and the γ-Nb_4N_3 tetragonal phase [12, 13]. Both γ and δ phases have been widely used in many superconducting applications because of their relatively high T_c compared to other phases. Superconductive properties of NbN are affected by the stoichiometric compositions and the crystal structures [14].

A laser provides a monochromatic and coherent high power beam of photons. This results in high power densities at focus and allows the use of pulsed laser for ablating materials. The properties of plasma formation from laser ablation are dependent on the laser's parameters, such as energy density (fluence) laser pulse duration, wavelength, polarization, and laser repetition rate as well as the material being treated [15]. These parameters need to be optimized for each particular material to receive the benefits of laser processing at their surfaces and improving the surface properties. There is much interest in using a surface treatment that leads to creating and improving material properties. A variety of surface treatments results as the laser power density changes from lower to higher values, depending on the temperature achieved by the absorption process. The applied time of laser irradiation is an important variable parameter to determine the effect of the thermal heating [16]. Processes which rely on surface heating without melting, such as surface heating for hardening or annealing, occur at relatively low energy densities [16]. Others require surface melting and/or evaporations. Forming new materials can result in such as surface alloying, deeper surface hardening, and pulsed laser deposition [16, 17]. The wavelength of the laser affects the reflectivity and absorption of the material. Reflectivity can be defined as the ratio of reflected intensity from the surface of the material to the incident intensity, while absorption determines how the amplitude of the incident radiation is deposited over the distance in the sample. One of the key parameters in controlling a laser-material interaction process is the amount of energy being used, which predicts the type of material modification that will occur [16].

Pulsed laser deposition (PLD) became a widely used technique after the success of producing films with a stoichiometry close to that of bulk target. In 1987, Dijkkamp *et al.* showed that Yttrium barium copper oxide (YBCO) superconductor films, with composition close to that of the bulk material, were produced by PLD [18]. Since that work, PLD has been used extensively to grow thin films from many materials [19]. The principle of PLD is that a high-powered pulsed laser is focused onto a target that causes material removal (ablation) and forms a plasma plume. Then, the martials from the plume are allowed to condensate to form a thin film [15]. In contrast to its simplicity, the mechanism of PLD is rather complex. PLD is a non-thermal growth technique in which interactions and material modifications are described by physical and chemical processes. this includes breaking or creating chemical bonds for ensembles of species that cannot be described by a single temperature distribution [20].

PLD can work in an ultrahigh vacuum or in a reactive gas atmosphere. One or more targets can be also used. This makes it easy to prepare samples that are difficult to prepare through thermal evaporations [19]. The kinetic energy of particles during PLD can be varied by changing the laser fluence or increasing the pressure of the background gas [19, 21]. Varying the laser fluence shows slight changes in the properties of the film, while changing the kinetic energy of the deposited particles by increasing inert gas pressure has stronger influence on texture and microstructure properties of the film [19]. Deposition of metallic films (e.g., Ag, Fe and Fe/Ag) under an inert gas atmosphere (Ar) showed a reduction in both particle energy, and re-sputtering of the surface atoms compared to films deposited in ultra-high vacuum (UHV) was reported [21]. The reduction in particle energy was explained by scattering of ablated material in a diluted

gas (4.0 Pa) [21]. Changes in background pressure can cause changes in stress conditions of the film or even result in growth of a stress-free film [19].

Thermal diffusion is a technique used for materials processing, either as a bulk or a thin film [3, 22, 23]. The first work done on thermal diffusion of NbN was reported in 1941 [5]. In this method, niobium is heated at high temperatures in a nitrogen gas background. Niobium has high reactivity to nitrogen gas at high temperatures that causes the diffusion of gas in Nb to form NbN. The diffusion occurs by movement of lattice defects. The type of defects determines the mechanism of diffusion. Nitrogen diffused in Nb by vacancy diffusion mechanism occurs in both γ and δ niobium nitrides [24, 25]. This means that large concentrations of nitrogen vacancies exist in these two phases. The amount of nitrogen that can be interstitially absorbed by niobium is a function of the temperature and the nitrogen pressure [26]. The results of the solubility of nitrogen in Nb differ to some extent between different studies. This may be due to the methods of preparation, see, for example, [26] and the references within. Since, upon cooling of samples, the amount of nitrogen that can be retained in solution changes, this may cause conflicts in the atomic percentages of alpha phase in Nb lattice, even when the Sieverts apparatus is free from the problem of nitrogen loss during cooling down [27]. Also, the extremely rapid rate of formation of other nitrides prevents α-NbN from retaining more than about 1.0 at. %. These make it difficult to determine alpha phase by XRD, as reported by Cost and Wert [27].

Much work has been done on high-temperature reactive diffusion to form different phases of NbN$_x$. Interest in using thermal diffusion technique comes from its advantages, such as simplicity and low cost. Thermal diffusion can be applied to samples

with complicated geometries and gives homogenous thickness and thick nitride layers which can be prepared in a few seconds. The advantages of using a thermal diffusion method make it much more favorable than other methods. Theoretical works are predicting good performances of NbN_x if it replaces Nb in superconducting applications of rf cavities [6].

Several experimental works were done using the thermal diffusion method to find equilibrium phases and structural properties of the formed NbN phases. Most of these were done on powder samples, with only a few on bulk samples. Some of these studies were done to study the formation of niobium nitrides for possible usages in superconducting rf cavities [3-7]. Most were done using heating. Also, these were done at higher nitrogen gas pressures to obtain phases that show high superconducting transition temperature T_c, such as δ-NbN, γ-NbN and β-Nb$_2$N phases. α-Nb(N) solid solution phase could be obtained as Nb is heated at temperatures as low as 800 °C or heated for short reaction time as low as 60 sec [5, 26]. Other phases of niobium nitrides are formed at higher temperatures or longer reaction times [28]. Few works deal with mechanical and structural properties of the formed NbN. In the present study, the formation of different NbN phases at various nitrogen pressures and their influence on the morphology and crystal structure were explored.

In this dissertation, lasers were used in several applications for fabricating NbN. These include heating of the niobium surface, producing cubic and hexagonal phases of niobium nitride, depositing thin films of niobium nitride on silicon wafers and niobium substrates at different conditions. The treated materials were examined using X-ray diffraction (XRD), electron probe microanalysis (EPMA), energy-dispersive X-ray

spectroscopy (EDS), scanning electron microscopy (SEM), transmission electron microscopy (TEM), atomic force microscopy (AFM), X-Ray photoelectron spectroscopy (XPS) and nanoindentation for nanomechanical measurements.

This dissertation is based on references [29-35] and is organized as follows: Chapter II presents an overview on properties of niobium and niobium nitride materials that are used for film fabrication. The structural and other properties of these materials as well as a survey on previous work done on NbN_x by PLD and thermal diffusion are given. Chapter III describes the experimental techniques used to fabricate samples and characterization techniques. The chapter also addresses the laser ablation of matter, plume characteristics, and thin film formation. In Chapter IV, NbN_x thin films on Nb substrates are obtained by changing PLD experimental parameters: temperature, pressure, and laser fluence. The effects of changes in the substrate temperature, nitrogen background pressure and laser on the grown phases and the morphology of NbN_x films are studied. Chapter V presents the fabrication of NbN_x thin films on Si substrate. The effect of nitrogen background pressure of pulsed laser deposited NbN_x films on Si (100) is discussed and characterization of that using XRD, SEM, AFM, XPS, superconductivity and nanoindentation. Chapter VI discusses the formation of NbN_x samples by thermal diffusion at high and low mitogen pressure. In this chapter, samples are studied for the phase formation, electronic structure and nanomechanical characterizations.

CHAPTER II

OVERVIEW ON NIOBIUM AND NIOBIUM NITRIDE

SUPERCONDUCTOR MATERIALS

II.1. INTRODUCTION

Superconductivity was first discovered in mercury by Dutch physicist Heike Onnes at Leiden University in 1911. Later, he won the Nobel Prize in physics in 1913 for his work on liquidation of gases and discovery of superconductivity [36]. When the temperature of mercury was decreased to liquid helium temperature (4.2 K), the resistance of mercury suddenly disappeared. A year later, superconductivity of tin and lead confirmed that superconductivity is not a unique property for mercury. More superconducting elements were discovered later [36].

Transition metal nitrides have attracted attention for use in different technical applications due to their unusual mechanical, thermal, and electrical properties, such as chemical and thermal stabilities and high electrical conductivity [37]. The bonding in the transition metal nitrides is a mixture of three types of bonding: metallic, covalent and ionic components [38]. NbN is one of interstitial transition metal nitrides in which nitrogen atoms occupy interstitial sites between metal atoms [39]. These interstitial nitrides are early transition metals of groups IV and VI, formed by dissolution of nitrogen atoms into the metal lattices in which the metal atoms form lattices of (fcc), simple hexagonal or hexagonal closed-packed (hcp) structures, while the nitrogen atoms set in the interstitial sites between the metal atoms [39].

Since most applications of niobium nitride NbN are related to its superconductive properties, there is much interest in studying superconductivity of NbN_x. The

superconductivity of NbN was first reported in 1941 [40]. Presently, the highest T_c value reported for cubic NbN_x thin films is about 17.3 K [14, 41]. NbN_x has recently received much attention for its superconductive microelectronic applications [42]. The fabrication of tunnel junctions for superconductor-insulator-superconductor (SIS) receivers, high resolution X-ray detectors and high-field magnets are some of the examples of the applications of NbN_x films [12]. The NbN_x with a cubic rock salt structure (δ-NbN) is the commonly studied phase in the NbN system. High quality single crystals or polycrystalline NbN_x films are needed for high T_c values. The superconductive properties of NbN_x films are affected by the stoichiometric compositions and by the crystal structures of the NbN_x films [14].

Other useful properties of NbN_x, such as thermal stability, chemical inertness, and good mechanical properties make it very useful as a corrosion protective coating for surfaces. The high melting point of NbN allows it to withstand different thermal effects without degradation [12]. Applications of superconducting materials that have higher critical current with high magnetic fields include high-field magnets for accelerators, such as the Large Hadron Collider (LHC), power transmission applications and higher resolutions Nuclear Magnetic Resonance (NMR) scanners. Efforts were concentrated on increasing the critical magnetic field (H_c) of superconductors by doping [43, 44]. Doping of NbN_x sputtered thin films with Gd increases the films' resistivity and, as a result, the critical magnetic field increases [45]. Another way to increase the critical magnetic field and the critical current is by having nanocrystalline superconductors [43]. The properties of the nanocrystalline materials are different when compared to their bulk materials [39, 43]. The size of the superconductor influences the superconductivity parameters of that

material. For example, it has been reported that there are more than two order of magnitude enhancements of the critical fields of Sn nanoparticles (15 nm particle size) than bulk material [39].
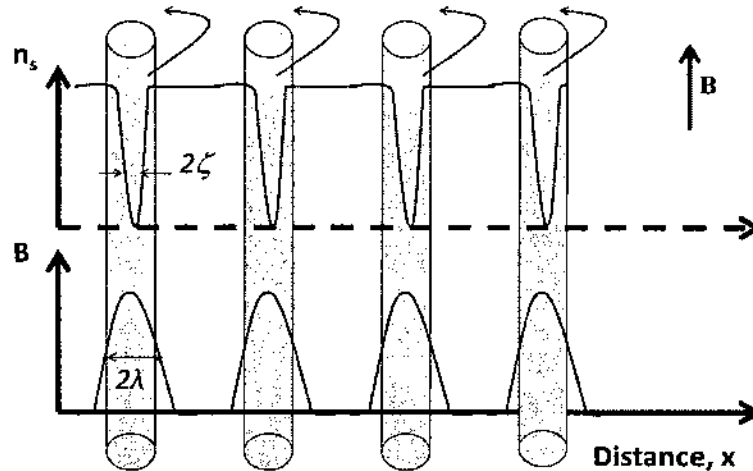
Fig. II.1. Variation of magnetic field strength B and the number of density of superconducting electrons (ns) in type-II superconductor. Redrawn from [46].

Nanocrystalline materials have very small grain sizes which mean an increase in the critical current. The defects act as pinning centers for the magnetic flux in the vortices, and this results in high resistivity and a high of H_c field [47]. Also, the grain boundaries in nanocrystalline are different from those of conventional grains. The superconductors can carry very high current without any resistance. In large magnetic fields, the vortices moving in type-II superconductor causes energy dissipation and limit current flow through the material and hence electrical resistance suppresses the

superconductivity of the materials [48]. Defects can be introduced to the materials that cause pinning of these vortices.

Using nanometer scale particles is the key feature to give essential pinning to the vortexes, otherwise if large defects are made then the vortices will still move within them. NbN nanoparticles work as artificial pinning centers for the magnetic field flux. The introduction of NbN nanoparticles into polycrystalline high temperature superconductors leads to an increase in the critical current and also an increase in the magnetization of the samples [43]. These increases are related to the decrease in the size of the nanoparticles comparable to the coherence length of material, see Refs. [48, 49]. In Type II superconductors, the penetration depth is much larger than the coherence length ($\lambda > \zeta$) so it exists in a mixed state of normal and superconducting areas, called a vortex state, as shown in Fig. II.1 [46]. Normal states are in form of cores. The core has a size of coherence length (ζ). The supercurrent flows in circles around these tubes and this why they are called vortices. Magnetic field penetration occurs through the normal states. A perpendicular force to the vortices results as current flows around. The resistance increases in vortices as current flow and that limits the superconductor applications of Type II superconductors. Impurities could be added to Type II superconductors to avoid this energy dissipation effect. The defects cause pinning of the vortices to their places that maintaining zero electric resistivity and hence sustain the superconducting state [46]. Fig. II.1 shows how the number of density of superelectrons n_s and the magnetic field strength B vary over with the distance for Type II superconductors. Nanowires superconductor single-photon detectors (SSPDs) are one of the applications on

nanomaterial superconductors [50, 51]. SSPDs have high efficiency to detect single photon with high speed [51].

II.2. Nb AND NbN SUPERCONDUCTOR MATERIALS

Properties and applications of Nb are introduced in this section. This is followed by more details on different structures of NbN_x and most common applications of NbN_x superconductors. In the next sections, NbN_x thin films preparation methods are covered. Reviews from pervious publications on NbN_x thin films deposited by pulsed laser deposition (PLD) are presented. Characteristics and effects of changing laser and other experimental conditions, such as deposition pressure and substrate temperature, are given. A discussion on the importance of superconductor nanoparticles and their application is given. Applications of NbN_x and initial results obtained from this work are also introduced.

II.2.1. PROPERTIES AND SUPERCONDUCTIVITY OF Nb

Niobium is a transition metal of group V within the Periodic Table with a soft grey color and body-centered cubic crystal structure. It is usually found in minerals with tantalum [52]. Nb has atomic number of 41 with electronic configuration $[Kr].4d^4.5s^1$. This makes Nb like other transition metals, with an inner shell that is not completely filled (4d in Nb case) [52]. Nb is Type II superconductor and has the highest critical transition temperature of all elements (9.3 K) [53, 54]. A paramagnetic effect was observed in Nb samples [55]. This effect is much more pronounced in Type II superconductors than in Type I superconductors [56]. In paramagnetic materials, there are free magnetic dipole moments with random orientations. Under a magnetic field, the dipoles in paramagnetic materials will point in direction of the field and results in a net

positive magnetization in the direction of the field. Paramagnetic was observed at the surface of niobium resulting from the defected native oxides on the surface [55]. Also, they resist organic and inorganic compounds and acids such as HCl, H_2SO_4, HNO_3 and nitro-hydrochloric acids (Aqua Regis) [52]. All these properties and, especially the superconductivity, make Nb very attractive in industrial applications. A common application of Nb is in steel industry. Hard metal alloys of niobium carbides, nitrides, borides and silicides are very stable compounds. They are characterized by high bond energy that results in a high modulus of elasticity and a high melting point [57]. Oxygen, also, can easily dissolve in interstitial sites of the Nb body-centered lattice; numerous oxides could be formed; and this could significantly affect the Nb properties [58]. As an example, the addition of oxygen to Nb changes its electrical properties from conductor Nb to insulator Nb_2O_5 [52]. An addition of a very small amount (~ 0.1%) of Nb to steel forms compounds such as NbC and NbN_x. These compounds help increase the strength, ductility, and hardening of steel [59]. Also, Nb is used in nonlinear optical materials, such as $KNbO_3$ and $KNbO_2B_5$, which are used in harmonic generators, frequency mixers, and other electro-optical applications [60]. Nb is used for superconducting rf cavity applications for particle accelerators [61-64].

The solubility of oxygen in Nb increases as temperature increases [58]. Handling of Nb in air causes a formation of an unavoidable native oxide layer on its surface. Many studies assumed that this layer principally consisted of Nb_2O_5 [65]. Others observed NbO with different thicknesses [66]. Thickness and compositions of this native oxide layer is complex. It depends on ambient conditions, oxygen partial pressure, temperature, and duration of exposure. The presence of the oxide layer on an Nb surface affects

superconductivity properties of Nb. Also heating of Nb will enhance the diffusion of oxygen to the inside of bulk Nb. A decrease in superconductivity critical temperature was observed as the amount of oxygen increased in Nb films [63]. Most of the studies done on the effect of oxide layers on Nb are related to superconducting applications such as superconductivity of rf cavity [62, 64].

Also, Nb is widely used in the fabrication of Josephson Tunnel Junctions for superconductor applications, such as superconducting quantum interference devices (SQUIDs) and single-photon detectors [67-69]. SQUIDs can be used in medical devices, such as studying activity in the brain, and other measurements on magnetic properties of materials. Also, superalloys of Nb, such as Ni-based alloys, are widely used for high temperature aerospace applications [70]. The term super alloy refers to alloys that have excellent mechanical performance and good stability against corrosion and oxidation at elevated temperatures [70]. Nb can form an alloy with many different elements such as NbTi, Nb_3Sn and Nb_3Ge, which are superconductors with transition temperatures of 10, 18 and 23 K with an upper critical field at 4.2 K of 15, 30 and 37 Tesla, respectively. These high critical fields makes Nb superconductor alloys very good choices to be used as wires in high power superconducting magnets [52]. These alloys are difficult to use in the commercial market because they are brittle [54].

II.2.2. PROPERTIES, STRUCTURE AND APPLICATIONS OF NbN

NbN_x has complex phase diagrams with a wide range of compositions. Different phases of NbN can be formed as the nitrogen-to-metal ratio is changed. Fig. II.2 shows the phase diagram of NbN system [71]. As the percent of nitrogen changes, different phases or mixtures of NbN compositions result. α-NbN phase has a bcc structure with

lattice constant of 3.303 at 2 % of N in Nb [72]. As the percent of nitrogen increases, it shows mixture of both α-NbN and hexagonal β-Nb$_2$N phase. Then the β-Nb$_2$N phase in the range NbN$_{0.4}$–NbN$_{0.5}$. With a nitrogen percentage increase, β-Nb$_2$N is mixed with γ-Nb$_4$N$_3$ tetragonal. Near stoichiometry, three phases with different structures, namely, δ-NbN, δ'-NbN and ε-NbN, were reported [72, 73]. The δ'-NbN has hexagonal (B8$_1$) structure (NiAs) that appears as a metastable phase during the phase transformation from δ-NbN to ε-NbN phase [73].
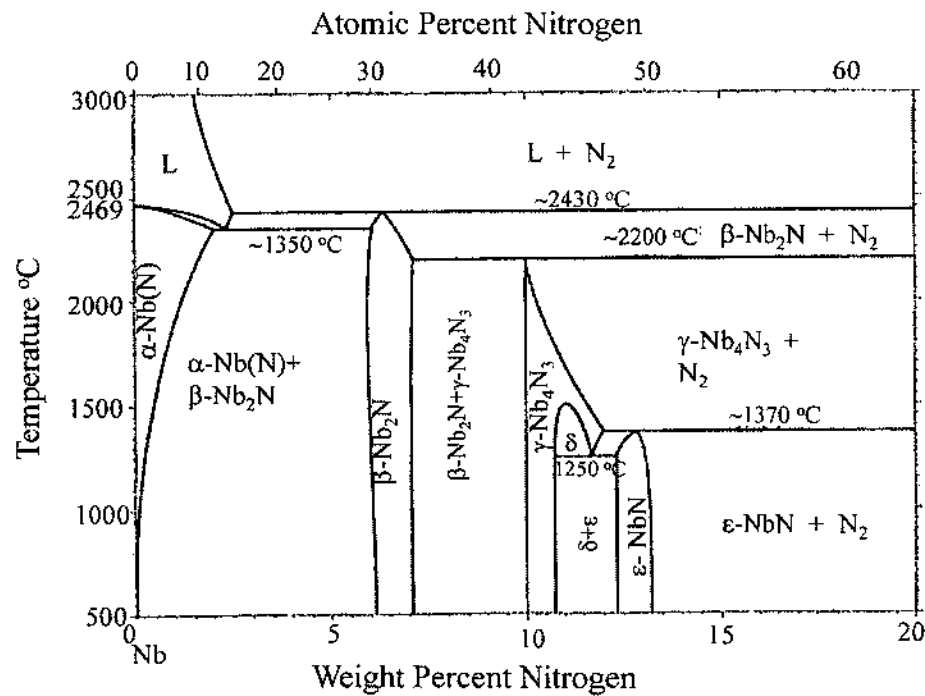
Fig. II.2. Phase diagram of NbN (Adapted from ASM Handbook, 1990) [71].

δ-NbN ε-NbN γ-Nb₄N₃ β-Nb₂N

δ-NbN ε-NbN γ-Nb$_4$N$_3$ β-Nb$_2$N

(a) Cubic B1, NaCl-type structure

(b) Hexagonal (Bi), TiP-type structure

(c)Tetragonal, deformed NaCl-type structure

(d) Hexagonal, Fe₂N-type structure
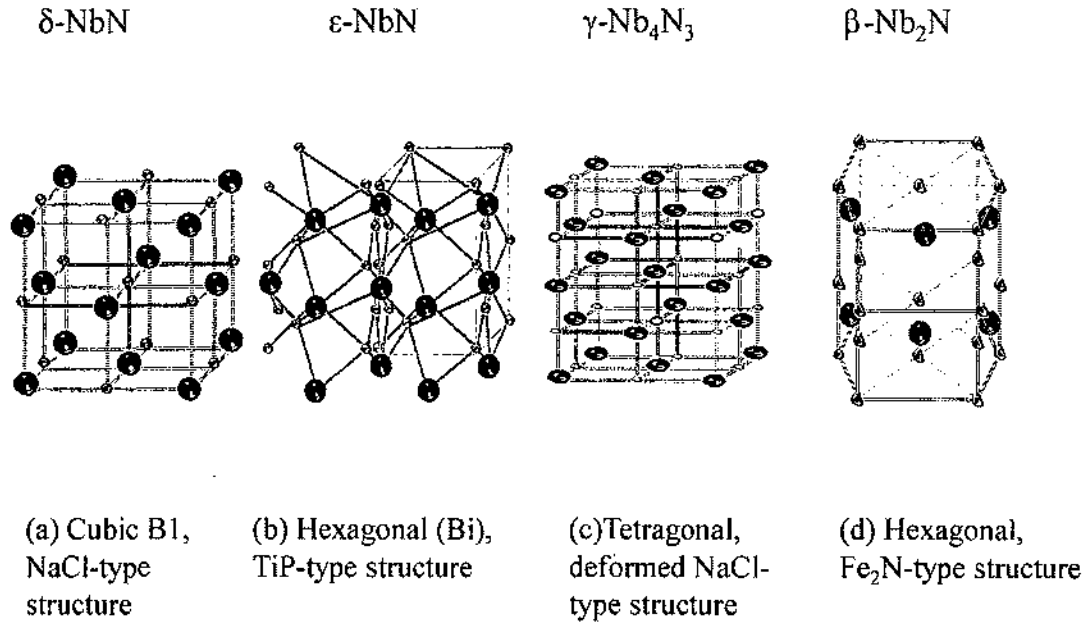
Fig. II.3. Crystallographic structures of NbN: (a) cubic B1, (b) hexagonal Bi, (c) Tetragonal, and (d) hexagonal of Nb$_2$N. The bigger spheres correspond to the metallic Nb sites; the smaller spheres represent N atoms, while small spheres with bold edges correspond to vacancy. The notation of ◉ means the site is occupied by only half of nitrogen atom. From [74].
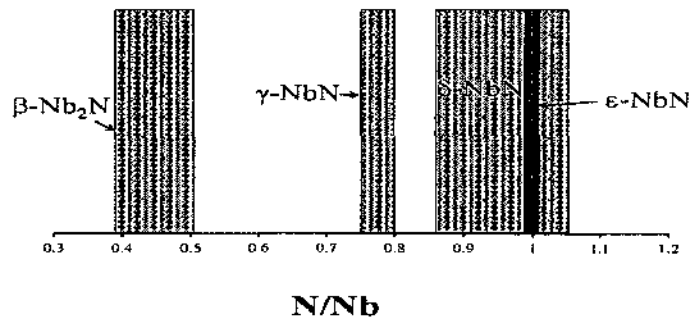
Fig. II.4. Composition ranges of NbN for four different phases. Redrawn from [26].

Nitrogen atoms have lattice arrangements in the hexagonal structure in both δ' and ε phases. They are distinguished by different sequences of niobium atoms in the c direction. The δ' phase has an ABAB . . . sequence, whereas ε has an AABBAA BB... sequence [13]. γ- Nb_4N_3 phase has a tetragonal structure with a = 4.382 and c = 4.316 Å lattice constants [73]. Fig. II.3 shows examples of theses NbN phases. The δ-NbN phase has cubic B1 (NaCl) structure with 4.3927 Å lattice constant. The hexagonal (B_i) structure (TiP) is for ε-NbN with a = 2.96 and c = 5.535 Å lattice constants. The tetragonal phase is a distorted NaCl structure due to nitrogen deficiency, as shown in Fig. II.3(c). Another structure far from stoichiometry is β-Nb_2N phase with hexagonal structure (Fe_2N) with a = 3.055 and c = 4.948 Å lattice constants shown Fig. II.3 (d). Fig. II.4 shows the composition ranges for four phases (β-Nb_2N, γ-NbN, ε-NbN and δ-NbN) of NbN system [13].

II.3. NbN_x THIN FILM PREPARATION METHODS

There are many methods to prepare nitride thin films. In physical vapor deposition (PVD), the transition metal is evaporated by electron beam or plasma as in plasma-enhanced physical vapor deposition (PEPVD) [75], or sputtering and then reacted with nitrogen at low pressure. There are some limitations on PVD, such as formation of defects in the film, and this is because of poor coverage of these methods. Another method is chemical vapor deposition (CVD), and its alternatives, such as metal-organics chemical vapor deposition (MOCVD) and atomic layer deposition (ALD) [14]. In these techniques, the nitrides metal films are deposited from the reaction of their chlorides in the gas phase with ammonia/nitrogen or ammonia/hydrogen/nitrogen mixtures. Then, after reaction, the products nucleate on the substrates to form uniform nitride films. The

conformity of thin films results by CVD methods is higher than those obtained by PVD methods [76].

There are several reports on the growth and characterization of metastable nitride compounds such as CN_x and c-BN [77]. Different phases of transition metals can be formed as the nitrogen-to-metal ratio is changed. NbN_x thin films have been prepared for many applications by different techniques, such as reactive ion sputtering [41, 78], ion beam deposition [52] and chemical vapor deposition (CVD) [14]. In all of these methods, to obtain single-crystal NbN_x thin films, the substrate was heated to temperatures between 350 to 1200 °C. Such a high-substrate temperature may induce impurity diffusion and that prevents the potential application of single-crystal NbN_x films in fabricating superconducting devices and circuits.

II.3.1. NbN_X FILM FABRICATION

II.3.1.1. PULSED LASER DEPOSITION OF NbN_X

Pulsed laser deposition (PLD) has been used to grow various compounds. Epitaxial NbN_x films were grown by PLD on MgO (100) substrates [37]. Both MgO and NbN have a B1 (NaCl) structure and a lattice mismatch of less than 4%, therefor MgO is a natural candidate for an epitaxial substrate [37]. PLD is a well-developed method for preparation of metastable compounds that form as transient phases because of high quenching rate that occurs to the films prepared by PLD [79]. One of the advantages of PLD is that the target stoichiometry can be transferred easily to the film. In PLD very short high-energy laser pulses are focused onto a solid martial target. This causes rapid heating, vaporization and ionization of the target material, resulting in a dense plasma plume above the target. This vapor is collected on the substrate.

Bhat *et al.* [80] grew NbN_x on MgO (100) and SiN_x/Si substrates using PLD at substrate temperature of 600 °C. SiN_x instead of SiO_x substrates was used because SiN_x is more stable at high temperatures. Using SiO_x causes oxygen diffusion into the grown films at high temperature and that may corrupt the superconducting properties of nitride films. The maximum observed T_c here was 16 K for films deposited on MgO at 8 Pa N_2 pressure. The NbN_x film deposited on SiN_x/Si substrate shows maximum T_c ~12 K at slightly higher N_2 pressure than those on MgO. In addition, the films on SiN_x/Si were amorphous, while those grown on MgO were (100) textured. T_c values of films prepared by PLD show sensitivity to N_2 background pressure.

Boffa *et al.* [81] studied the effect of changing the substrate temperature, nitrogen pressure and gas flow on NbN_x films grown by PLD. MgO (100) substrate and Nd: YAG laser ($\lambda = 532$ nm) in pure N_2 background were used in this work. The deposition was done at nitrogen operating pressures either at static or constant flow of N_2. The films were deposited at substrate temperatures ranging from 400 to 650 °C. An NbN cubic structure was obtained at different conditions, substrate temperatures and nitrogen pressures. The best superconducting characteristics were obtained for samples deposited at 600 °C in static N_2 atmosphere at a pressure of 8 Pa.

Growth of NbN_x films by PLD was also reported in [82].The laser source used was a KrF Excimer laser ($\lambda = 248$ nm), 10 Hz focused into Nb target at laser fluence of 6 J/cm^2 in reactive gas atmosphere of N_2 (10% H_2). The structural and electrical properties of the deposited films grown on MgO (100) and fused silica substrates were studied as a function of substrate temperature at gas pressure of 8 Pa. Highly textured (100) NbN_x film was obtained on MgO (100) with $T_c = 16.6$ K and ρ (20 K) = 60 $\mu\Omega$ cm at 600 °C,

while films grown on fused silica under the same conditions were polycrystalline with T_c = 11.3 K and higher resistively at ρ (20 K) = 120 $\mu\Omega$ cm than films deposited on MgO substrate. The improvements in the electrical properties of the films are due to the reduction of the grain boundaries and increasing of the mean free path within the individual grain as film goes from polycrystalline films (on fused silica) to highly oriented films on MgO (100). The growth of crystalline NbN_x films of different phases by PLD, ($0 \leq x \leq 1.3$) is described in [83]. This was achieved by changing the pressure of the reactive gas during growth under the same conditions as that described previously [37]. Also Treece *et al.* used same conditions to study the structural and electrical properties of new phase of NbN_x films ($0 \leq x \leq 1.2$), grown by PLD on MgO (100) [84, 85]. As they concluded, the growths of this new phase are due to aspects of PLD, such as high energies of ablated species and the very large instantaneous growth rates.

PLD was used to grow NbN/MgO/NbN multilayer hetero-structures [86]. Nd: YAG laser operating at λ = 532 nm, pulse width 10 ns, and energy density in the range 1 – 2.5 J/cm^2 was used. The layers were grown on SrTiO (100) substrates. A rotating multiple-target holder system allowed depositions of the multilayers without air exposure. The ablations were done from pure Nb and Mg targets under different pressures of N_2 and O_2, respectively. The static operating pressures were achieved by maintaining the chamber with a certain amount of gas. The N_2 pressure was 8 Pa and the O_2 pressure, was 100 Pa. The substrate temperature was 550 °C for Nb and 250 °C for Mg during the ablation. The NbN_x layers consist of δ- NbN cubic phase since the layers show T_c = 14 K. The NbN_x layers grown on the MgO show different morphologies with a

higher density of microholes and greater granularity compared to the single NbN_x layer grown on the substrate [86].

II.3.1.2. THERMAL DIFFUSION OF NbN_x

Niobium has high reactivity with nitrogen especially if it is heated at high temperatures. Several studies have been done on thermal diffusion in bulk Nb, powder and thin films [3-7, 13, 23, 26, 27, 87-90]. Treatment of Nb samples at different heating temperatures or environment pressures results in samples with different properties.

Fabbricatore *et al.* [4] reported on using nitrogen diffusion at high nitrogen and temperatures in the range of 9.9 − 29.9 x 10^3 Pa and 1000 − 2000 °C, respectively. Films with mixed phases were obtained. Temperatures below 1300 °C gave only β and α phases of NbN_x. As the temperature was increased to 1300 °C and above, γ, δ and ε phases were identified. Tu *et al.* [5], reported on thermal diffusion of nitrogen into bulk niobium at 800 °C, results in samples with surface resistance lower than that of Nb by 2–3 times. Nothing was reported there on the diffusion mechanism of nitrogen in NbN_x samples. The mechanisms of nitrogen diffusion in niobium were reported for different phases of NbN_x [3]. The diffusion occurs by movement of lattice defects. The types of defects determine the mechanism of diffusion. Nitrogen diffused in Nb was by vacancy diffusion mechanism in both γ and δ niobium nitrides [24, 25]. This means a large concentration of nitrogen vacancies existed in these two phases.

Benvenuti *et al.* [6] studied formation of niobium nitride by reactive diffusion at 1270 − 1500 °C and nitrogen pressure in the range 10^3 − 10^5 Pa. They studied the influence of annealing time, nitriding pressure and nitriding temperature on critical temperatures of β, γ and δ phases. As they reported, applying higher temperatures or

longer process times results in poor quality films. Also, nitriding should be carried out at 10^5 Pa and 1380 °C or higher for more than 6 min to get higher T_c value.

Niobium nitrides with both δ and β phases grown by thermal nitriding in the range 1100 – 1900 °C at 150 kPa were indicated [3]. As samples cooled down to less than 1350 °C, thin layer of δ phase transformed into γ, ε and δ' phases. Lengauer *et al.* [11] studied high-temperature nitridation of niobium annealed in high-purity nitrogen of various pressures, times and temperatures below 1400 °C [11]. Phase transformations of γ-Nb$_4$N$_3$ to δ-NbN and η-NbN to δ-NbN were observed between 1070 and 1300 °C, respectively. In their previous work, an investigation was done in nitrogen pressure range $10^3 – 3 \times 10^6$ Pa and temperature range 1400 – 1800 °C [91]. As they reported, choice of nitrogen pressure considerably affected the growth rate and homogeneity ranges of NbN phases [91].

Most of these works were done using the thermal annealing method to find the equilibrium phases and structural properties of these phases. Also, these works were done at higher nitrogen gas pressures to obtain phases that show high superconducting transition temperature T_c, such as the δ-NbN, γ-NbN and β-Nb$_2$N phases. Here, the interest is obtaining alpha NbN solid solution phase by doing experiments at lower nitrogen pressures than previously reported. A series of experiments were performed to investigate the formation of NbN$_x$ on Nb at different annealing temperatures and nitrogen pressures using the thermal annealing method. The formation of different phases at various nitrogen pressures and their influence on the morphology and crystal structure were explored.

CHAPTER III

THIN FILM GROWTH BY PULSED LASER DEPOSITION

III.1. INTRODUCTION

Pulsed laser deposition (PLD) is an attractive deposition technique because of its simplicity and success of depositing thin films of complex compounds. The first experiment on PLD was reported in 1965 using a ruby laser [92]. The discovery of electronic Q-switches allowed for laser designs with highly energetic short pulses in the nanosecond range [93]. There were extensive efforts to develop the lasers and PLD systems. Many materials were difficult to deposit at before, such as high-transition temperature superconducting films, oxides films, and other different materials, but they became relatively easy to be grown by PLD. PLD allows for overcoming problems that may arise in the preparation of these kinds of materials. This includes requirements to control the composition and use of reactive gas background during the growth of the film [93, 94].

In PLD, high-energy laser pulses are focused to evaporate material from the surface of the target. As a result, ablated species (called a plasma plume) are ejected normal to the target. The plume expands in a forward direction with velocity distribution depending on the background condition. The film growth on the substrate that is placed at the opposite direction to a target occurs after the condensing of the ablated species. As a result of absorption of the laser photons, the material melts and vaporizes. Depending on the properties of the laser and those of the substrate, the qualities, stoichiometric and uniformity of thin films can be achieved. Fig. III.1 shows a schematic which describes how the PLD mechanism is done inside a vacuum chamber.

Laser beam

Focusing lens

Target carrousel

Window port

Target

Substrate

Laser plume

Sample stage

Vacuum chamber
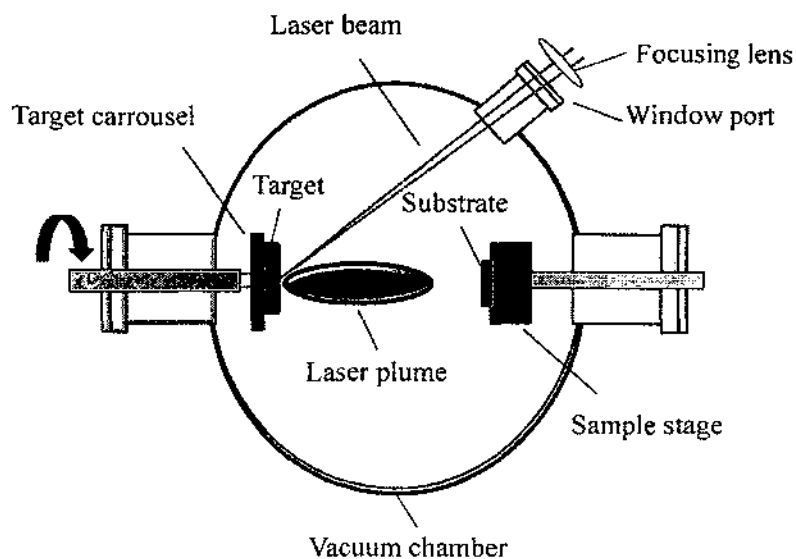
Fig. III.1. A schematic of typical PLD mechanism.

PLD has many advantages that include a relatively simple experimental apparatus, the capability to create particles with high-energy, and the growth of high quality film at low temperatures with stoichiometric preservation. The reason for this can be understood from the generation and transport of the ablation species at a very high kinetic energy, resulting in enhanced surface diffusion reducing the growth temperature for epitaxial growth. In addition, multitargets with a smaller size than that required for sputtering can be used to grow multilayer films of different materials without breaking the vacuum or interrupting the deposition process [79]. Also, PLD can take place in a vacuum chamber either under high/ultrahigh vacuum or in the presence of some background gas. In reactive PLD, a solid target that consists of the material of interest is

ablated under a reactive gas atmosphere. As a result, a new compound is collected on the substrate.

Films formed by PLD using ns lasers can have some macroscopic particles in them. These particulates are as large as a few microns, which may affect the properties of the films [20]. The origin of these particulates on the surface may be related to thermal effects during the laser-matter interaction. Their formation mechanism is linked to the ejection of droplets from the molten target. The use of femtosecond lasers shows some advantages. Different studies were done to compare quality and properties of films using ns and fs lasers for PLD [95-98].

The advantage of using a fs laser is that ablation occurs without thermal diffusion. In other words, the ablation results from multiphoton ionization, hence, no thermal melting occurs. This also overcomes low optical absorption in wide band gap materials [94, 95]. Once shorter laser pulses of picosecond or femtosecond scales were used, the thermal processes, which occur in laser ablation, are greatly modified [99]. The effect of pulse length on the ablation process is governed by the heat diffusivity of the material, velocity of sound, and the time for electron-electron thermalization and electron-phonon coupling [100]. For short laser pulses as in a femtosecond laser, the ablation is considered a direct solid-vapor transition. In this case, the thermal conduction into the target is neglected since the lattice is heated on a picosecond time scale and results in the creation of vapor and plasma [101]. The threshold laser fluence for evaporation of femtosecond pulses and picosecond lasers is independent of pulse durations, while in the nanosecond case it grows as $(\tau_i)^{1/2}$. This is why, with long laser pulses, there will be enough time for the thermal wave to propagate into the target and to create a relatively large layer of

melted material. In this case, the evaporation occurs from the liquid metal [101]. Also, femtosecond ablation lowers the fluence required for ablation by a factor of $10 - 10^2$ compared to ns ablation. This is due to better spatial concentration of fs pulses compare to ns pulses [102, 103]. PLD was previously used to study the growth of nitride compounds, e.g., [97, 102] and oxides, e.g., [95, 104].

The advantages of PLD can be summarized as follows [79, 93]:

(i)   A high preservation of stoichiometry;

(ii)   The ability to produce films out of any material (solid or liquid) targets and in the form of multicomponent or multilayered films;

(iii)   Epitaxial growth at low temperature;

(iv)   High deposition rate leads to producing smoother films particularly for meta films;

(v)   Flexible and easy to implement;

(vi)   Growth in any environment, under vacuum or ambient gas;

(vii)   Greater control of growth and thickness of films;

(viii) The energy source is outside the deposition chamber. This minimizes the possibility of impurities and increases flexibility to grow different materials [20]; and

(ix)   growth mode that separates the nucleation and growth phases, which can alert growth and morphologies.

Like any deposition technique, although there are advantages, there are some disadvantages in PLD:

(i)   The production of macroscopic particulates during the ablation process; leads to higher roughness.

(ii)   It covers small area (several square centimeters). This is because of the highly forward-directed plume expansion property.

(iii) There are defects in the film caused by bombardment of the film by high kinetic energy condensing atoms and ions.

(iv)   There are inhomogeneous fluxes and angular energy distributions within the ablation plume. The flux falls off rapidly with a distance from target.

The unique pulsed feature of PLD makes it different from other techniques. PLD offers an instantaneous high deposition rate ($\sim10^6$ ML/min) which is by 5–6 orders of magnitude relative to that of thermal deposition [105]. Low deposition rates could lead to long deposition times. The deposition rate can be increased by decreasing the target to substrate distance or by increasing the laser energy/fluence. Rapid deposition of energetic species helps to enhance adatom surface diffusion. Therefore, lower temperature epitaxial growth could be achieved by PLD.

III.2. MECHANISM OF PLD

PLD involves complicated interactions between a plume species and laser interactions with material species. Also, it includes the formation of the plume with a high energetic species and their transfer through the plasma to the substrate. That makes the theory behind PLD complicated. Furthermore, the laser ablation process and the plume expansion under background gas pressure are more complicated than that of a vacuum. The mechanism of PLD for thin film formation is achieved by four stages which will be discussed in more detail in the following sections [79, 93].

(i) Laser-target interaction and ablation of the target material.

(ii) Dynamics of the ablated species (surface melting and species ejection).

(iii) Deposition of the ablated species and growth of thin film.

(iv) Growth mode of thin film.

Fig. III.2 shows schematic diagrams of the processes of laser interactions with target and plasma, plasma expansion, and film growth.

Substrate

Laser beam   Pulse duration

(a)   (b)   (c)   (d)
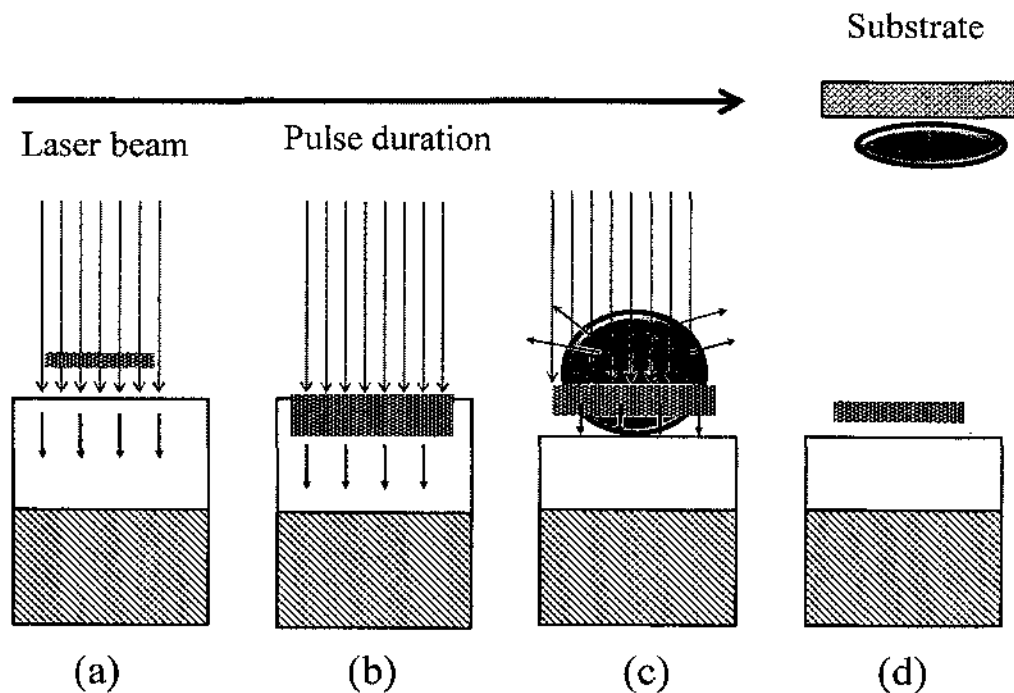
Fig. III.2. Schematic diagram showing mechanism of PLD. (a) Absorption of laser radiation as indicated by long arrows; shaded areas indicate melted material and short arrows indicate motion of solid–liquid interface. (b) Surface melt propagates into the solid. (c) Absorption of incident laser radiation by the plume and plasma formation. (d) Condensation on substrate and film growth [106].

III.2.1. LASER-TARGET INTERACTION AND ABLATION OF THE TARGET MATERIAL

When the focused laser beam hits the surface of the target, all elements in the target are rapidly heated to their evaporation temperature. Then, species are ablated from the target surface with the same stoichiometry as that in the target. The rate of ablation is dependent on the fluence of the laser irradiating the surface. This ejection of materials from targets takes about tens of picoseconds of the laser pulse [107]. The plasma plume results as the ejected species continuously absorb energy from the laser pulse, as shown in Fig. III.2. The rate of the energy transfer from the laser to the target is a function of temperature gradient for the target surface, thermal conductivity of the target material and the optical properties, including absorption coefficient and reflectivity of the target material [108]. Therefore, the coupling of the laser energy to the target surface increases as the optical penetration depth, the surface reflectivity and the thermal diffusivity of the target all decrease. There is a minimum value of laser energy density that causes vaporization of the target species that is called threshold value. This threshold laser fluence energy varies from material to material. Other factors that influence the coupling of the laser energy to the target surface are duration and energy of the laser pulse and also the surface roughness and density of the target materials [79]. The main parameters of interest in such laser absorption mechanisms are the peak surface temperature and the volume of the heated region, both of which are governed by the optical, the thermal properties of the target and the laser peak intensity I. The energy transport from laser pulses into the metal can be described as a two-temperature heat diffusion model in one dimension [101]:

$$C_e \frac{\partial T_e}{\partial t} = K \frac{\partial^2 T}{\partial z^2} + (1 - R)\alpha I_\circ \exp(-\alpha z) - \gamma(T_e - T_i) \qquad \text{(III.1)}$$

$$C_i \frac{\partial T_i}{\partial t} = \gamma(T_e - T_i), \qquad \text{(III.2)}$$

where z is the direction perpendicular to the target surface. The first term in Equation (III.1) is the rate of heat flux and the second term is the laser heating source term. R is reflectivity, α, absorption coefficient; and K thermal conductivity of the target. T_e, T_i, C_e and C_i are temperatures and heat capacities of electron and lattice subsystems (phonon component). I is the laser peak intensity. γ is the parameter that characterizes the electron-lattice coupling [101]. The coupling factor γ is related to the heat capacity of the electron and lattice by $\tau_e = C_e/\gamma$ and $\tau_i = C_i/\gamma$, where τ_e is the electron cooling time, and τ_i is the lattice heating time ($\tau_e \ll \tau_i$). The relation between these two time scales and laser pulse duration time τ_L defines the femtosecond, picosecond and nanosecond regimes of the laser-metal interaction [101].

The ejection of the materials from the target is a complex process. Contributions for the target excitation and sputtering mainly come from electronic excitations. Other thermal contributions are dominated if longer laser pulses are used. The formation of wavelike structures on the target surface after laser irradiation is evidence for thermal contribution [106]. An unwanted effect is phase explosion, which occurs as a result of explosive boiling of the target material at higher laser fluence and this causes ejection of particulates. These particulates may also result if the target surface has some pores on it and is not perfectly flat. Also, another thing which affects the uniformity and stoichiometry of the films is formation of secondary sputtering as a result of the back-scattering of some of the ablated material [106].

III.2.2. DYNAMICS OF THE ABLATED SPECIES

The plume tends to move toward the substrate in a cone shape [109]. The expansion of a plasma plume in ambient gas is different from that in a vacuum. The plume expansion in a vacuum is characterized by certain characteristics: First, the plasma expansion is isothermal during the time of the laser pulse. After termination of the laser pulse, it expands adiabatically [100]. During the adiabatic expansion, there is no heat exchange occurring at any instant between the system and its surrounding. So, in this process, the internal energy of the plume is converted to work that is represented by a decrease in the pressure of the gas as the volume is expanded. As plasma expands, thermal energy is converted into kinetic energy and that causes rapid cooling of the plasma [100]. The temperature of the plume drops as evidence of the decrease in internal energy. The recombination of the ionized species makes the temperature decrease much more slowly than predicted. The plasma temperature typical value for the temperature during the initial expansion is as high as 10^4 K [100]. Second, Knudsen layer (KL) is formed. A Knudsen layer is a thin layer of thermally activated vapor that forms at some distance from the surface where Maxwell-Boltzmann velocity distribution is not at equilibrium (Fig. III.3) [110]. In KL, the ablated particles absorb laser energy and this causes transformation of anisotropic velocity distribution into an isotropic one. Then, collisions with the plasma in a few mean-free paths from the target surface establishes thermodynamic equilibrium [93]. Third, the collisions between the particles lead to an anisotropic forward expansion of the plume in a normal direction to the target [100]. Fig. III.3 shows the formation of melted surface and vapors, and flows by a Knudsen layer under ambient gas [111].

The shorter dimension of plasma in one direction is the highest velocity. The dimensions of the plasma in transverse directions to the target are much larger than the parallel direction. As a result, plasma will be accelerated more rapidly in a forward direction than in other directions. This strong forward direction is caused by pressure gradients in axial and radial directions of the plume [112]. The plasma will retain its elliptical shape during expansion and this controls the density distribution of particles in it which will affect the deposition profile. The plasma is assumed to have exponential density gradient with linear increase in the velocity of species with distance from target surface [100].
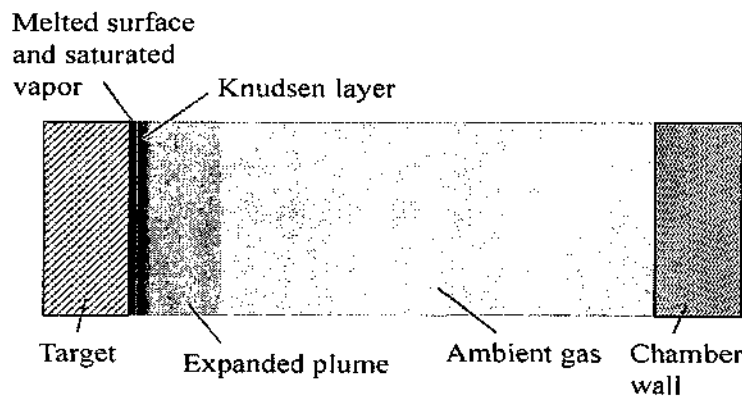
Fig. III.3. Laser ablated plume flow under ambient gas. From [111].

The plume angular dependence have the form [112]

$$\frac{dN}{d\Omega} = a\cos\theta + b\cos^n\theta, \qquad\qquad (\text{III.3})$$

where a, b, and n are material dependents, with n values reported in the range of 4–14 [113]. According to this equation, the distribution of the plume is described with two components, $\cos\theta$ distribution, which has considerable thermal energy as in conventional thermal evaporation [114], and the other component has $\cos^n\theta$ distribution, which is dominated distribution of the plume. This component is close to stoichiometric and has high expansion velocities ($\sim 10^6$ cm/s) [114]. Fig. III.4 shows the schematic of the plume shape as a function of n. The relation of the vapor pressure with the temperature is given though the Clausius-Clapeyron equation [115]:

$$P = P_0 \exp\left[\left(\frac{LM}{\rho RT_b}\right)\left(1 - \frac{T_b}{T}\right)\right], \tag{III.4}$$

where L, M and ρ are specific heat, molecular weight and density of the target material, respectively; R is gas constant (= 8.3145 J mol^{-1} K^{-1}), and T_b is boiling temperature at pressure P_0. Generally, the typical velocities of the particles during the isothermal expansion in vacuum are in the range of 10^5–10^6 cm/s [115].
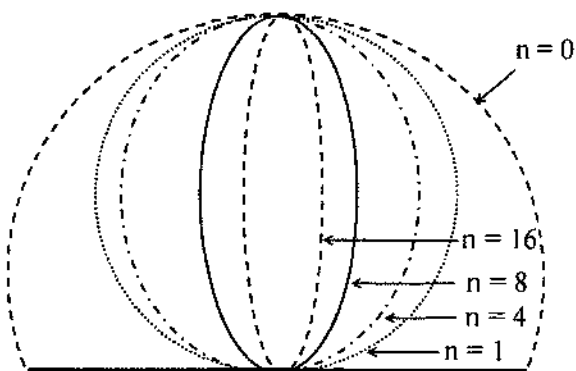
Fig. III.4. The shape of PLD plasma plume as a function of n. From [114].

The expansion velocities of species are different depending on their masses. Ion velocities are higher than those of neutral species. In absorption spectroscopy, ground-state atoms and ions have been observed in the plume after the initial expansion [108]. The existence of fast neutrals in the plume can be explained by recombination of fast ions with electrons or resonant charge exchange between fast ions and neutrals [100].

Under background gas, there will be some force on the plume from the plasma-gas interaction. Under reactive background gases, the chemical reactivity of ablation species is enhanced by the addition of a separate ion source. This may cause a lowering in the activation energy needed for dissociation of the gas molecule and formation of films with nearly stoichiometric composition at lower temperatures or even at room temperature [116]. Carrying out PLD in background gas induces reactions with ablated elements to form compound with used gases or compensate for any loss of an elemental component of the target [15].

The beginning of the expansion of the plume under a background gas is similar to expansion in a vacuum. Then, the plume expansion is controlled by the interaction of the plume with the background gas. This is depends on the type and pressure of background gas in use [117]. In other words, more collisions will occur as the gas pressure increases and that means the number of ablated particles that are reaching the substrate without any collision will decrease. The shape of the plasma plume is directly related to particle density. The shape of the plume is sharpened in the forward direction since the acceleration is much stronger in the forward direction. The sharpening of the plume indicates the formation of shock waves at the front [118]. The spot size of the laser and the plasma temperature have significant effects on the uniformity of deposited films

[119]. The target-to-substrate distance is another parameter that governs distribution of the ablated materials [120].

III.2.3. DEPOSITION OF THE ABLATED SPECIES AND GROWTH OF THIN-FILM

Many factors, such as density, energy, and the type of the condensing material, as well as the temperature and the physical-chemical properties of the substrate, affect the growth of the films. The two main thermodynamic parameters for the growth mechanism are the substrate temperature T_s and the supersaturation [121]. Supersaturation in vapor is defined as a vapor of a compound that has higher partial pressure that exceeds normal saturation vapor pressure. So, in supersaturation, the density of vapor is high and that makes atomic separation short and condensation occurs. The way particles nucleate determines the structure and morphology of the film. The nucleation process depends on the interfacial energies between phases present at the substrate, condensing material, and vapor. Nucleus size depends on the deposition rate and the substrate temperature. Small supersaturation leads to large nuclei, which subsequently unite together. As the supersaturation increases, the nucleus size shrinks to minimum critical height like of the atomic diameter and two-dimensional layer formed. For very large supersaturation, layer-by-layer nucleation will occur [122].

The ejected species impinges onto the substrate surface and may induce various types of damage to the substrate due to their high energies. The neutrals have kinetic energies in the range of a few eV to tens of eV [96]; at the same time, the kinetic energy of ions is significantly larger. These energetic species may cause sputtering of some surface atoms. That creates compressive stress pulses normal to the surface of the liquid. The estimated value of this pressure is about 10^3 to 10^4 Pa [123].

Film growth mainly depends on both the substrate temperature T and supersaturation, which are related by a thermodynamic driving force (ΔM) equation $\Delta M = k_B T ln(\frac{R}{R_e})$, where R is the actual deposition rate, and R_e is the equilibrium value of deposition rate at the temperature T, and k_B is Bolztman's Constant [121]. At equilibrium, ΔM is zero, and at condensation it is positive and negative during sublimation or evaporation. For PLD, the deposition rate is order of magnitudes higher than the conventional method, (10^{16}–10^{22} cm^2/s) which leads to a very high degree of supersaturation in plasma [115].

The structure of deposited films is determined by diffusion of particles on the substrate surface. The certain amount of energy that is provided to the adatoms determines diffusion processes [113]. This energy is initiated from kinetic or potential energy, of the adsorbate or can be supplied thermally by substrate heating. The rate of surface diffusion depends on a variety of factors, including the energy of the incoming adsorbate, the strength of the surface-adatom bond, orientation of the surface lattice, densities of atomic steps, surface reconstruction, attraction and repulsion between surface species, and externally–supplied energy [121]. The diffusion coefficient, D, of adatom migrates on surface with diffusion energy E_{diff} given by: $D = D_o \, exp\left(-E_{diff}/k_B T\right)$, where D_o is diffusion coefficient constant corresponding to the pre-exponential. The time that atoms coming from the vapor stay on surface before desorption is called residence time τ_{ad} and it is given by: $\tau_{ads} = (1/\nu) exp(E_{ads}/k_B T)$, where E_{ads} is by adsorption energy. For diffusion to occur, it is expected that $E_{diff} < E_{ads}$. This energy can originate from kinetic or potential energy of the adsorbate or can be supplied thermally by substrate heating [115].

III.2.4. GROWTH MODES OF THIN FILM

The growth mode of epitaxial film depends on surface energies of both substrate and adsorbents and on the interface energy of film and substrate. During film growth, different processes occur for the incoming atoms on the substrate surface, such as diffusion, nucleation on islands (clusters), diffusion on clusters, detachment from the island, diffusion along a step edge, detachment from an island, diffusion of cluster surface or detached from and remain on the substrate surface. There are three growth modes for nucleation and growth of the films [124]:

i. Three-dimensional island (Volmer-Weber) growth,

ii. Two-dimensional layer by layer (Frank-van der Merwe) growth, and

iii. Two-dimensional growth of monolayers followed by nucleation and growth of three-dimensional islands (Stranski-Krastinov) growth.

These growth mechanisms are shown in Fig. III.5(a) and show Volmer–Weber growth as small clusters nucleate on the substrate and grow to form three-dimensional islands [125]. Frank–Van der Merwe or layer-by-layer growth is shown in Fig. III.5(b). In layer-by-layer growth the depositing atoms are more strongly bonded to the substrate than to each other. The Stranski–Krastanov mode is shown in Fig. III.5(c) is a combination of the layer-by-layer and island growth [124]. In the following section, brief descriptions of these modes are given.

III.2.4.1. VOLMER-WEBER GROWTH

Volmer-Weber growth of three-dimensional (3D) islands results if there is an energy loss due to formation of the film as shown in Fig. III.5(a). Therefore the Volmer-Weber growth is considered a non-wetting growth [125]. The growth or dissolution of the

cluster is governed by the difference between the total free energy of the cluster and energy needed to assemble the individual atoms. The clusters will be stable if this difference in energy is above the critical cluster size [124]. Island growth occurs when the surface energy of the film exceeds that of the substrate ($\gamma_{Film} + \gamma_{Interface} \geq \gamma_{Substrate}$) γ_{Film}, $\gamma_{Substrate}$, and $\gamma_{Interface}$ are surface-free energies of film, substrate- and interfacial-free energy between film and substrate, respectively. The possibility of getting Volmer-Weber growth increases as the cluster nucleation rate increases. This increase can be achieved by either increasing the deposition rate or decreasing the substrate temperature. The growth is by the formation of large numbers of nuclei on the surface, then, their nucleation occurs. This mode of growth was presented for many metals grown on insulators [124].

III.2.4.2. FRANK-VAN DER MERWE GROWTH

In the two-dimensional, layered structures Frank-van der Merwe growth mode or layer-by-layer growth mode, a new layer is nucleated only after completion of the first layer. In other words; nucleation and growth of islands that are only one monolayer thick is completed and coalesced before significant clusters of the next film layer is developed. Fig. III.5(b) shows the layer-by-layer growth mode. In this case, there is no free energy barrier to nucleation [121]. The adatoms of deposit material are more strongly attracted to the substrate than they are to each other [124]. This is opposite to the Volmer-Weber mode case, where the deposit atoms are more strongly bound to each other than to the substrate. Layer-by-layer growth will result, assuming the substrate temperature is high enough to achieve thermodynamic equilibrium [126]. This mode was observed in epitaxial growth of metal and semiconductor with close lattice match.

III.2.4.3. STRANSKI-KRASTINOV GROWTH

The Stranski-Krastinov growth mode is considered an intermediate between the two previous modes and is much more common [121]. It characterized by both 2D layer and 3D islands growth, as shown in Fig. III.5(c). This happens when there is a significant lattice mismatch between the film and substrate. The first deposited few monolayers follow the Frank-van der Merwe growth mode. The key parameter that determines the growth mode is the interface energy. The strain results from the lattice mismatch. That increases the interfacial energy because the strain energy increases with the thickness. At some critical thickness, the interfacial free energy will exceed the surface energy of the substrate and the growth mode transformation from the 2D wetting layers growth to 3D islands occurs. This mode observed in metal-metal and metal-semiconductor [124].
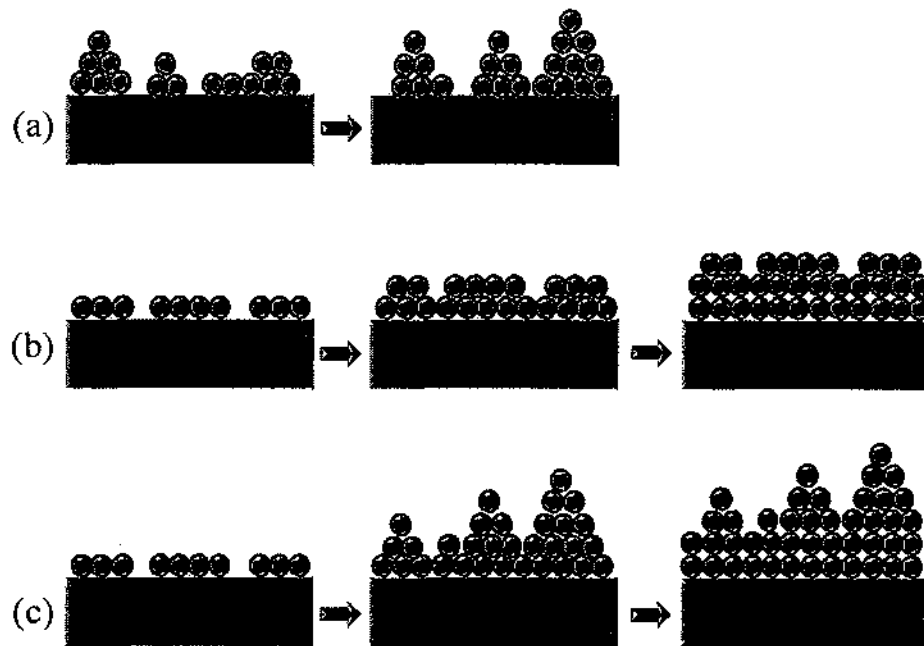
Fig. III.5. Schematics of thin film growth modes. (a) Volmer–Weber (b) Frank–Van der Merwe and (c) Stranski–Krastanov growth. From [114].

CHAPTER IV

EXPERIMENTAL TECHNIQUES

IV.1. INTRODUCTION

Niobium nitride (NbN) has recently received interesting attention in the fabrication of tunnel junctions for superconducting applications of SIS receivers, resolution X-ray detectors, and high-field magnets. NbN_x exhibited supercomputing transitions above 10 K, which is one of the important considerations for using the superconductor in electrical applications. NbN_x films commonly have known cubic FCC or rock salt structure. NbN has bulk T_c of about 16 K; the cubic phase shows high values of T_c; besides that, it is mechanically and chemical stable and of large superconducting energy gap. Also, it can easily be created in thin film form.

Several reports have been done on the growth and characterization of metastable nitride compounds, such as CN_x and c-BN [77]. Different phases of transition metals can be formed as nitrogen-to-metal ratio is changed. Transition metal nitrides have important superconducting properties because they are metal, have high melting points, and are very hard. NbN_x thin films have been prepared for many applications by using different techniques, such as reactive ion sputtering, ion beam deposition and chemical vapor deposition (CVD). In all these methods to obtain single crystal NbN_x thin films, the substrate was heated to temperatures between 350 to 1200 °C. Such a high-substrate temperature may induce impurity diffusion and that prevents the potential application of single-crystal NbN_x films in fabricating superconducting devices and circuits. PLD has been used to grow various compounds.

IV.2. PULSED LASER DEPOSITION SYSTEM

Fig. IV.1 shows schematic diagram of a PLD system in which films were grown by PLD in the current research. As shown in the diagram, a six-way 8-inch stainless steel chamber is used for deposition. The chamber is pumped down to UHV via a roughing pump (Edwards), a turbo pump (Varian, 70 l/s), and an ion pump (Varian, 300 l/s). A vacuum can be reached of ~ 6.66×10^{-6} Pa without backing. If the system is backed, a base pressure of $<1.3 \times 10^{-7}$ Pa can be reached. A convectron gauge is used for pressure readings from 101, 325 Pa down to 0.13 Pa. An ion gauge is used to monitor the pressure from 0.13 Pa down to 1.3×10^{-9} Pa. A "homemade" sample holder, which is used to mount the substrate, was designed to heat the sample. The substrate holder is mounted on a manipulator (a 4.5 inch conflate flange), which enables the azimuthial rotation of the sample by 360° and the adjustment of the sample-to-target distance. The target is mounted on an electrically rotated sample holder with a variable rotation speed. The rotation of the target minimizes the formation of particulates by exposing a fresh area to the laser pulses all the time. A nanosecond Nd: YAG laser (Lumonics, 45 ns, 1064 nm and 10 Hz) is used to ablate the Nb targets. More technical details of such a system are found in Appendix A. The laser hits the target at ~ 45° through a 2.5 inch glass window.
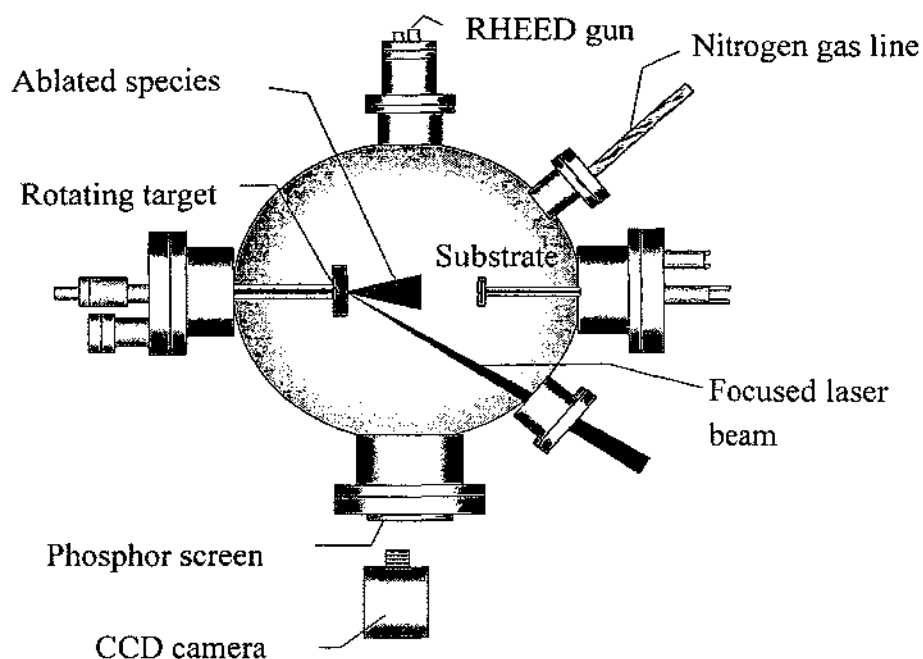
Fig. IV.1. UHV chamber used for the PLD.

IV.3. CHARACTERIZATION TECHNIQUES

IV.3.1. X-RAY DIFFRACTION

In this study, a theta: 2-theta goniometer was used. The goniometer refers to the assembly of the sample holder, detector, and associated gear mechanism. For this kind of scan the X-ray tube is stationary, and both the sample and detector move simultaneously by the angles theta and 2-theta, respectively. In this setup, the distance from the X-ray focal spot to the sample is the same as from the sample to the detector, with the detector moving on a circle.

XRD measurements were done at X-ray Crystallography Center at the College of William & Mary using a Bruker-AXS three-circle diffractometer. A Bruker SMART APEX II instrument is equipped with graphite-monochromated CuK_α radiation and a SMART Apex II CCD detector. The X-ray source of the wavelength of 1.5406 Å (Cu-$K\alpha$ line) is fixed, and both the charge coupled device (CCD) detector (2θ) and sample (ω) are movable. The detector (2θ) covers about 30° per image position. Three image positions were used for the experiment. In each case, the angle 2θ is the center position of the 30° CCD image, so that the angles of incidence and diffraction are equal.

The crystallite size of deposited films was examined using X-ray diffraction. The investigation of a crystallite size is performed by measuring the broadening of a particular peak in a diffraction pattern associated with a particular set of planes from the crystal unit cell. The average crystallite size in this work is obtained from the Scherrer relation [127].

$$D = \frac{K\lambda}{\beta \cos\theta},$$ (IV.1)

where λ and β are the X-ray wavelength and Full Width at Half-Maximum (FWHM) of the XRD peak, respectively. The constant K is the Scherrer constant, sometimes called the shape factor, and is taken as 0.94. The shape factor depends on the way it is used to determine the width and crystallite shape [128]. K can be 0.62 − 2.08 and the most common value of K is 0.94 − 0.89. For spherical crystals the value 0.94 is used for K if FWHM is used, while 0.89 is used if integral breadth is considered [128]. FWHM is the width of the diffraction peak in radians at half-way of the height between the background and the peak maximum. The integral breadth is defined as the total area under the peak divided by the peak height. A careful evaluation for the peaks and the background is

required. Scherrer's equation can be used for small particles determination (100 nm or crystallite smaller). In this case, this dominates the peak-broadening compared to strain. Scherrer equation does not include instrumental and strain broadening effects; it just considers line broadening that is entirely caused by size effect [129]. According to Equation (IV.1), the narrower the diffraction peak is, the larger the crystallite size. For the correct result on the crystallite size, the broadening from strain effect and the instrumental profile width must be separated. Multiple peaks need to be analyzed to separate these effects from integrated width calculations [130]. Also, the variation in the c/a ratio for hexagonal phases (so-called hexagonality) can be calculated from XRD as a function of investigating parameters of the laser. The lattice constants "a" and "c" were calculated from one or more of the peaks of the XRD pattern. The following equation is used for lattice constant calculations for the hexagonal phase [131]:

$$\frac{1}{d_{hkl}^2} = \frac{4}{3}\left(\frac{h^2+hk+k^2}{a^2}\right) + \frac{l^2}{c^2} \tag{IV.2}$$

IV.3.1.1. TEXTURE COEFFICIENT

The degree of texture in the films was measured using an integrated peak intensity analysis of XRD. A texture coefficient can give the dominant reflection and therefore, shows the preferred orientation of the deposited films. This may be useful for the fabrication of films of the desired orientation in the applications, as it is reported on the effect of the grain size and the texture degree of NbN_x films on the electrical, optical, and catalytic properties [132]. The integrated intensity of diffraction peaks decreased while FWHM increased. The texture coefficient (TC) or an average texture coefficient from XRD data, was calculated using the following equation [133]:

$$TC(hkl) = \frac{I(hkl)}{I_0(hkl)} \left\{ \frac{1}{n} \sum \frac{I(hkl)}{I_0(hkl)} \right\}^{-1},$$ (IV.3)

where I(hkl) are measured peak intensities of (hkl) reflection; I_0(hkl) are powder diffraction intensities of the standard data; and n is the number of reflections used in the calculations. For example, if the following (hkl) reflections from XRD spectra: (100), (002), (102), (110), (103), (112) and (202) for β-Nb_2N, were used in texture coefficient calculations, then n = 7 and I_0(hkl) are intensities of the standard data for these reflections. For a preferentially oriented sample, the texture coefficient TC(hkl) should be greater than one. In order to select the dominant reflections which show the strong texture in the films, TC (hkl) was calculated.
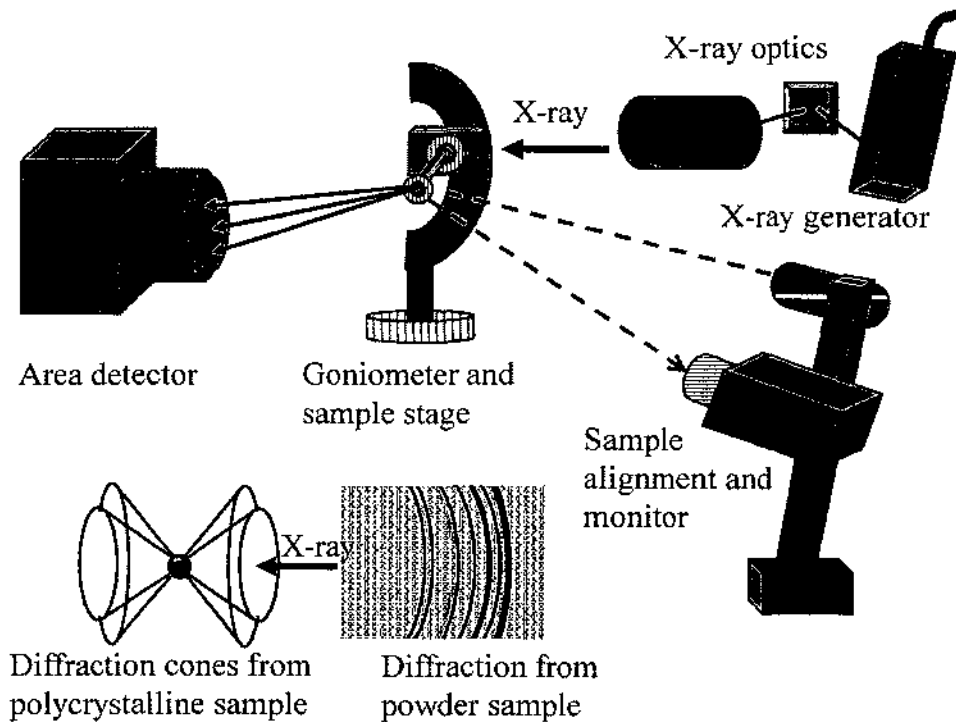
Fig. IV.2. Components of two-dimensional XRD (XRD2) system: X -ray source X-ray optics; goniometer and sample stage; sample alignment and monitor; and area detector. Diffraction cones from a polycrystalline sample and diffraction from powder.

Two-dimensional X-ray diffraction (2D) XRD, sometimes written as (XRD^2), images resulted from thecollection of the diffraction pattern with the area detector. Two-dimensional X-ray diffraction system consists of five basic components [134]. Fig. IV.2 shows basic components in an XRD^2 system, namely, X-Ray Source, X-Ray optics, goniometer and sample stage, sample alignment, monitor, and area detector, is shown in Fig. IV.2. The diffraction cones from a polycrystalline sample in 3D and diffraction rings from powder samples are shown.

The two-dimensional diffractometer is based on the four-circle diffractometer [131]. One circle is for the detector position and the other three for sample positions on the three-circle goniometer [134]. In the case of conventional XRD, the measurements are limited to the diffractometer plane and any variation of the diffraction pattern in Z direction is not considered. On the other hand, with the two-dimensional detector, the diffraction measured, whole or part of diffraction rings, is measured depending on the detector to sample distances and detector size [131]. Fig. IV.3 shows the geometric of the diffraction cones in the laboratory coordinates system (XYZ). The X-ray incident in X-direction and the apex angles of the cones are determined by the 2θ values given by the Bragg equation. The γ angle is used to describe the variation of the diffraction pattern along the diffraction ring. The γ angle takes a value from 0 to 360° and 2θ takes a value from 0 to 180°. The intersection of the 2D detector plane with the diffraction cone forms so-called conic section or diffraction ring. The conic section takes circle shape when the detector is in axis. The 2D diffraction image collected in a single exposure is referred to as a frame, which is stored as intensity values on 2D pixels [134].
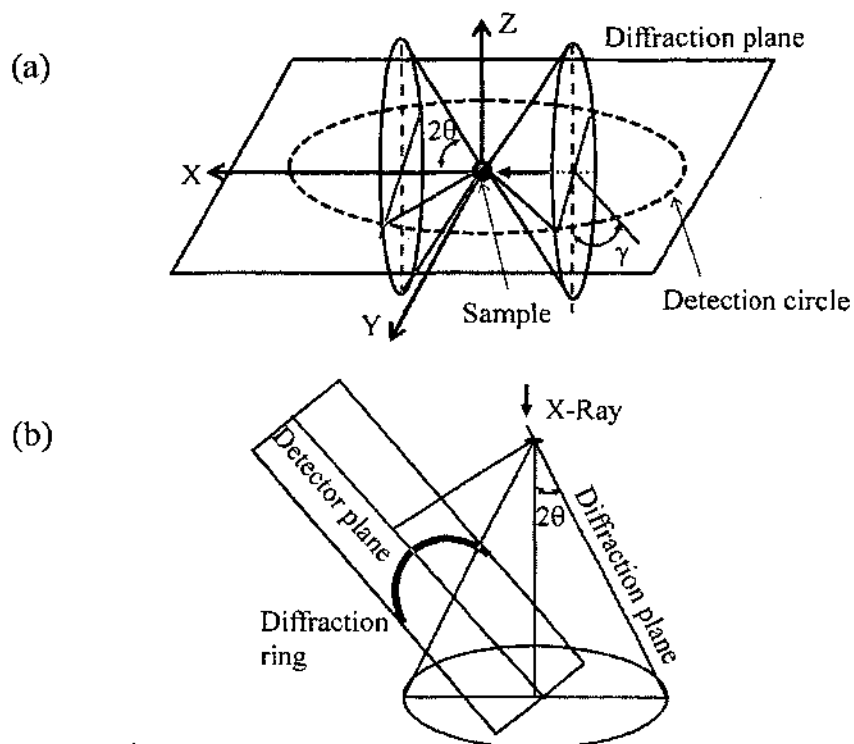
Fig. IV.3. (a) The geometry of a diffraction cone. (b) Diffraction cone and the conic section by a 2D detector plane.

IV.3.2. ELECTRON PROBE MICRO ANALYSIS

Electron probe micro analysis (EPMA) is based on bombarding the samples with accelerated electrons and then measuring the intensity ratio of characteristic X-rays emitted (usually at K and L-edges) from the sample. The signal of the sample is compared to that of a standard sample of known chemical composition. Thus, the atomic ratios are calculated. EPMA measurements were made at Electron Probe Microanalysis Labs at Old Dominion University. The CAMECA SX 100 equipment was used for EPMA measurements. This machine is equipped with five spectrometers and large

crystals for analyzing spots on materials down to about five microns and with an accuracy in the tens of parts per million. The samples were bombarded with electrons accelerated at 10 kV and 100 nA. The chemical composition value of each film is an average of at least 5 measurements performed on different sample places.

IV.3.3. SCANNING ELECTRON MICROSCOPY

Scanning electron microscopy (SEM) is based on collecting information from secondary electrons emitted from the surface as the result of scanning the sample surface using an electron beam with energies between 5 to 30 kV. The intensity of the collected electrons depends on the angle between the emitting surface and the detector. Regions in the specimen emitting an intense signal appear brighter than regions emitting a weaker signal. This contrast allows the formation of a surface image. The lateral resolution in SEM, in the range of 100 nm, limits the observations of nanostructures. The surface topography and morphology can be examined for the purpose of this research. Also, conformity of film in case of film deposition in trench microstructures is also evaluated. Conformity is defined as the ratio between the film thickness of a point taken at center bottom of the trench and the reference thickness that is measured at the top of the microstructure [135]. Thickness can be evaluated by SEM. The fracture cross-section of NbN_x films on Si was examined.

IV.3.4. ENERGY DISPERSIVE X-RAYS SPECTROSCOPY

Energy dispersive X-ray spectroscopy is an analytical capability used for elemental characterization and quantification of the chemical compositions near the surface of the samples. This technique depends on measuring the energy of the X-rays that are emitted from the sample. The X-rays resulted as the electron beam excited the

electrons in the sample; these excited electrons changed their orbitals. Counts and energy emitted X–rays are measured energy-dispersive spectrometer. Accuracy in EDX depends on the energy of the X-ray and density and thickness of material. This can result in reduced accuracy in inhomogeneous and rough samples. The chemical composition of (N/Nb = x) of the NbN$_x$ films was determined by EDX. The EDX measurements were done using an Hitachi S-4700 field emission scanning electron microscope (FESEM) operated at 15 kV accelerating voltage, working distance 8 to 12 mm, and counting time of 200 s. The FESEM microscope is equipped with a Röntec EDX detector to determine the chemical composition.

IV.3.5. ATOMIC FORCE MICROSCOPY

The atomic force microscope (AFM) belongs to the scanning probe microscopy (SPM) branch. AFM was invented by three scientists, Binnig, Quate and Gerber in 1986 [136]. From its name, it refers to the interactions between the probe and sample on the atomic level. The AFM is like all other scanning probe microscopes, uses a sharp tip that moves over the surface of the sample. The tip is attached at the end of a cantilever, which bends in response to the force between the tip and the sample. The cantilever itself bends in consistency with the surface. The AFM images are obtained by measuring this force on a sharp tip. The AFM images result as the tip scans the surface with line by line scans and assembles topographical images. A laser beam is reflected from the cantilever and collected by a position sensitive photodiode. Any deflection of the cantilever results in one photodiode collecting more light than the other photodiode, producing an output signal which is proportional to the deflection of the cantilever. The information of the deflection is used to assemble an image. AFM images can illustrate the topography and

morphology of the surface. All of the images in this work were obtained in air using the tapping mode on Digital Instruments Dimension 3100 atomic force microscope (Veeco Instruments Inc.). The AFM is equipped with a NanoScope IIIa controller to control the microscope head and scanning and operated using NanoScope VI software. Silicon tips with 10 nm tip radius and resonant frequency ± 100 kHz were used. In the tapping mode the tip taps the surface for a very short time of this oscillation period. AFM is capable of scanning to sub-Angstrom (Å) resolution in all directions with extremely precise positioning. Both the horizontal and vertical resolutions depend on the distance between tip and sample; the lower the tip, the higher the resolution.

IV.3.6. HIGH-RESOLUTION TRANSMISSION ELECTRON MICROSCOPY

In high-resolution transmission electron microscopy (HRTEM) high-energy electrons (100 keV–1 MeV) are transmitted through the sample to generate an image of the internal structure of the sample. Usually, a very thin film sample is deposited on a thin carbon coated Cu grid or prepared by a series of grinding, polishing and ion-milling steps to be thin enough for the transmission of electrons. The resulting image displays structural details at very high spatial resolution. JEOL JEM-2100F high-resolution transmission electron microscope was used for TEM images recording. HRTEM operates with ZrO/W field emission gun. The transmitted electron beam is affected by the structures and objects in the sample. This transmitted beam is then projected onto a phosphor screen, forming the image. The dark areas in the image mean fewer electrons were transmitted through and that represents areas of the sample with thicker or denser materials and vice versa. Different type images can be obtained by TEM. Bright field images, dark field images, and high-resolution lattice images.

CHAPTER V

PULSED LASER DEPOSITION OF NbN_x THIN FILMS ON Nb
SUBSTRATE

V.1. INTRODUCTION

Niobium nitride NbN_x thin films potentially have been used in many applications. Most of the applications are related to superconducting properties NbN_x thin films [137-141]. The good superconductivity of NbN_x films allows them to be used in low-temperature superconducting electronics, such as tunnel junctions [12, 75]. Optoelectronic applications of NbN_x films are such as the single-photon infrared photo detector [50] and the nano-structured X-ray detectors [142, 143]. In addition to the superconductivity, NbN_x films showed excellent mechanical properties, such as high hardness and toughness compared to Nb, and this makes it a suitable material for protective-wear coatings [144-146]. Because of these attractive properties of NbN_x thin films, considerable efforts have been devoted to study their growth and characterization.

Pulsed laser deposition (PLD) is a relatively simple and promising technique for preparation of highly textured thin films. PLD allows the stoichiometric transfer of a material from a solid target to a substrate. One of the advantages of PLD is that it can be used to deposit thin films in reactive gases. This reactive PLD is widely used for fabrication of many thin films, such as high-temperature superconductor oxides, semiconductors, and nitrides [93]. PLD is used to deposit thin films in reactive gases. The influence changing of PLD fabrication parameters, such as laser fluence, substrate temperature, and ambient gas pressure on the microstructure of NbN_x films, has been

previously studied [80-86, 147-151]. NbN$_x$ thin films prepared by PLD have non-stoichiometry and phase change as nitrogen content in the film is changing [86, 147]. Most studies on NbN$_x$ films are related to superconducting properties using Si or MgO substrates [137, 138, 152]. Growth of NbN$_x$ films on Nb substrates is studied for the possibility for improving the performance of superconducting radio frequency (SRF) cavities that are used for linear particle accelerator [153, 154]. Coating Nb cavities with superconductors with higher T$_c$ and lower critical field than Nb, such as NbN$_x$, could reduce surface resistance and, hence, increase the field for vortex penetration greater than that of Nb and that increases the quality factor [155]. Another importance of coating Nb substrates with NbN$_x$ layer is to increase surface hardness and provide a barrier for hydrogen diffusing into Nb [40].

A series of experiments were performed to understand the processing parameters and optimize them to obtain high quality NbN$_x$ films by PLD. NbN$_x$ films were deposited onto Nb substrates with varying laser fluences, nitrogen background pressure and substrate temperature. The films were examined by using various characterization techniques such as XRD, SEM, and AFM. The changes in laser fluence, nitrogen background pressure and substrate temperature have significant influence on properties of formed NbN$_x$ film, such as phase formation, size of the crystallites, and surface roughness. Highly textured NbN$_x$ layers can be prepared on a single Nb crystal using PLD. Study variations of structure, texture and morphology of NbN$_x$ thin films grown on Nb substrate by PLD are presented. The control of surface microstructure plays a key role in determining the surface properties and film quality for various applications.

V.2. EXPERIMENTAL DETAILS

NbN_x films were grown on Nb single-crystal substrate by ablating Nb target in nitrogen background. The chamber was equipped with a turbo-molecular and ion pump operated at a base pressure of $\sim 1.3 \times 10^{-7}$ Pa. A pulsed Nd: YAG laser beam (wavelength 1064 nm, repetition rate 10 Hz, pulse duration 40 ns) was focused with a 50 cm focal length lens at 45° onto a rotating (25 rpm) Nb metal target (99.995% pure). The background pressure of the ambient nitrogen gas was measured with a convectron gauge. The nitrogen operating pressure was achieved by filling the vacuum chamber with the amount of gas required to reach operating pressure. The samples were $8.6 \times 6.6 \times 0.7$ mm^3 cut by wire electro-discharge machining from an Nb slice of Ingot "H" from the Companhia Brasileira de Metalurgia e Mineração (CBMM) Company, Brazil. The samples were etched by the buffered chemical polishing (BCP) method [156]. The etched samples were rinsed in deionized water, dried under nitrogen flow, and then finally degassed for a few hours at 900 °C in UHV chamber under a base pressure of 1.3×10^{-7} Pa. X-ray diffraction (XRD) of cleaned Nb substrate indicates that most crystalline grains of Nb substrate exhibit crystallographic Nb (110), (200), (211), and (310) orientations [157]. The substrate to target distance is approximately 5 cm. The substrate temperature was measured using a chromel-alumel (K-type) thermocouple that was mechanically attached to the substrate surface. The temperature can be measured reproducibly and with an accuracy of ± 20 °C, which is mainly limited by the sample to the heater surface contact. The thickness of the deposited films is 20 ± 3 nm. Film thickness was obtained by following the same deposition conditions on silicon substrate then performing cross-section SEM measurements. The X-ray diffraction studies were carried out in a Bruker-

AXS three-circle diffractometer with graphite-monochromated CuK_{α} radiation and a SMART Apex II CCD detector. The crystallite size D is obtained from the Scherrer formula [127].

$$D = \frac{0.94\lambda}{B\cos\theta},$$ (V.1)

where λ (0.154056 nm) and B are the X-ray wavelength and full width at half-maximum (FWHM) of the XRD peak, respectively. The texture coefficient (TC) was calculated from XRD data, using the following equation [133]:

$$TC(hkl) = \frac{I(hkl)}{I_0(hkl)}\left\{\frac{1}{n}\sum\frac{I(hkl)}{I_0(hkl)}\right\}^{-1},$$ (V.2)

where I(hkl) are measured peak intensities of (hkl) reflection; I_0(hkl) are powder diffraction intensities of β-Nb_2N according to the standard data [23]; and n is the number of reflections used in the calculations. The morphology of the films was studied using JEOL JSM-6060 LV SEM and a Digital Instruments Dimension 3100 atomic force microscope (AFM). SEM images were taken at an accelerating voltage of 30 kV. All AFM images were taken in air using tapping mode. An energy dispersive X-ray spectroscopy (EDX) and an electron probe micro analyzer (EPMA) were used to determine the chemical composition of the samples. EPMA were done by point scan using a Cameca SX100. For the EDX measurements, an Hitachi S-4700 field emission scanning electron microscope (FESEM) equipped with a Röntec EDX detector was used to determine the chemical composition (N/Nb = x) of the NbN_x films. The FESEM was operated at 15 kV accelerating voltage, working distance 8 to 12 mm, and counting time 200 s. The concentrations of the A phase in an A+B mixed phase film was calculated by the following formula [158]:

$$A[\%] = \frac{\Sigma I_A}{\Sigma I_A + \Sigma I_B} \qquad\qquad (V.3)$$

where ΣI_A and ΣI_B are the sum of the integral intensities of A phase and B phase peaks in the measured XRD patterns. The deposition parameters of PLD include substrate temperature, target-to-substrate distance, background gas pressure, and laser wavelength, pulse width, repetition rate, and fluence. By adjusting the laser fluence, the microstructure and surface properties of the NbN_x films can be controlled. For effect of the laser fluence on the pulsed laser deposited NbN_x different laser fluences from 8 J/cm^2 to 40 J/cm^2 were used. Both substrate temperature and nitrogen background pressure were maintained at constant values 600 °C and 20.0 Pa, respectively, during all film growth processes. Nitrogen background pressure from 10.7 to 66.7 Pa was used with constant laser fluence of 15 J/cm^2 and substrate temperature of 600 °C to study the influence of nitrogen pressure. For effect of substrate temperatures NbN_x, films were deposited at different substrate deposition temperatures from RT to 950 °C under constant values of nitrogen pressure and laser energy density of 13.3 Pa and 15 J/cm^2, respectively.

V.3. RESULTS AND DISCUSSION

V.3.1. LASER FLUENCE EFFECT

V.3.1.1. STRUCTURE AND PHASE COMPOSITION

In order to study the effect of laser fluence on the structure NbN_x films, XRD patterns were obtained as shown in Fig. V.1. For a laser fluence range of 8–40 J/cm^2, highly textured films were obtained with mainly a hexagonal β-Nb$_2$N phase [159]. It is well known that the Nb-N system crystallizes in several phases and in most cases in a mixed-phase composition as presented by XRD patterns [37, 160]. In addition to the β-

Nb_2N phase, the XRD shows peaks that correspond to δ-NbN cubic [161] and δ'-NbN hexagonal [162] phases. The films prepared at low laser fluence (8 J/cm^2) showed mostly β-Nb_2N phase and weak reflection of δ'-NbN hexagonal phase. The crystal structure of the film obtained at 15 J/cm^2 showed mixed (cubic + hexagonal) phase of NbN_x and it became pure hexagonal phase with increasing laser fluence.
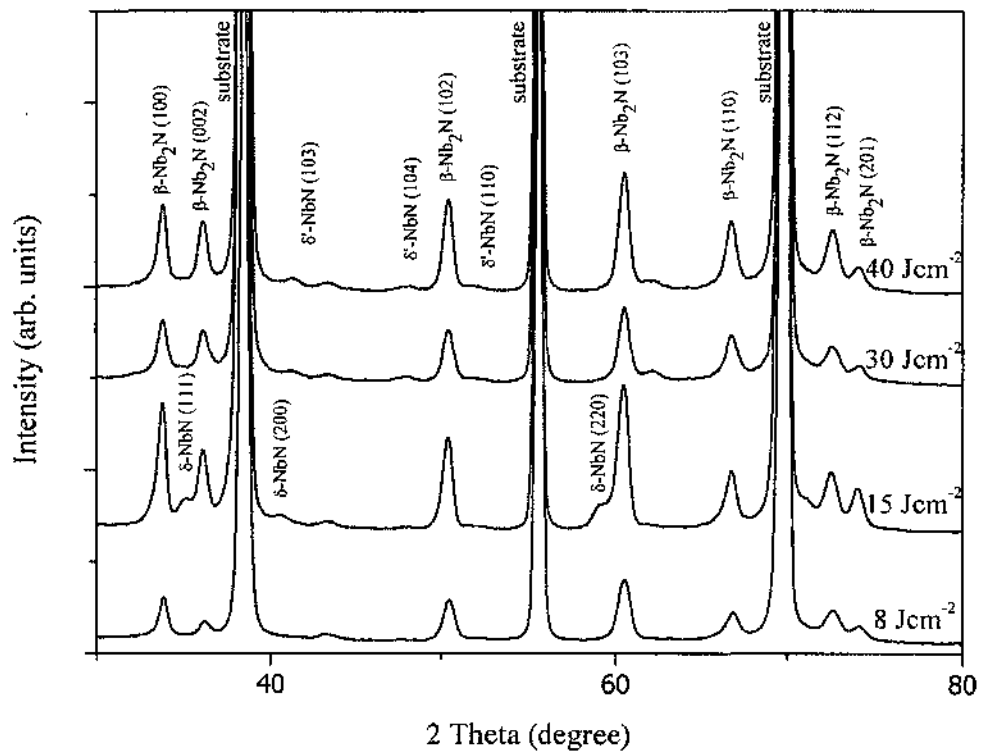
Fig. V.1. X-ray diffraction patterns of NbN_x films deposited at various laser fluences, constant nitrogen background pressure of 20.0 Pa, and substrate temperature of 600 °C.

The nitrogen content in the NbN_x films was obtained by EDX analyses. Fig. V.2 shows the chemical composition of the surface layer. The N/Nb ratio in the hexagonal β-Nb_2N phase was determined to be between 0.36±0.03 to 0.52±0.03, which is in

agreement with previously reported for NbN_x films [4, 13]. The N/Nb ratio in the film increased from 0.36 to 0.52 as the laser fluence was increased from 8 to 40 J/cm^2. The laser fluence not only controls the flux of niobium atoms and ions, but also it determines the energy of the ablated material and the extent of nitrogen dissociation and ionization. The higher the laser fluence, the more nitrogen dissociation and ionization will be created and this increases nitrogen content in the NbN_x film.

The crystallite size of the NbN_x films deposited at different laser fluences was examined using X-ray diffraction and the results are shown in Fig. V.3. The investigation of the hexagonal β-Nb_2N phase crystallite size is performed by measuring the broadening of the peak in a diffraction pattern. The mean crystallite size of the hexagonal phase from the different XRD peaks was calculated from the Scherrer formula, as shown in Fig. V.3. The crystallite size decreases with increasing the laser fluence, and then decreases for laser fluence at 40 J/cm^2. Increasing the laser fluence enhances the grain size of the NbN_x films. The Scherrer formula only addresses line broadening that is entirely caused by size effect with no contribution from lattice strain [129]. So it gives the minimum possible value of the average crystallite dimension. The peak broadening results from different contributions, such as an instrumental component, e.g., slit size, and usually includes instrument-related geometrical factors diffraction optics and sample contributions from sample transparency and sample geometry [163]. When no mechanical activation, such as ball milling and mechanical alloying, is used, the crystallite size is due to a nucleation and growth at high temperatures; only corrections for instrumental profile width should be considered in the Scherrer equation to obtain crystallite size [130].
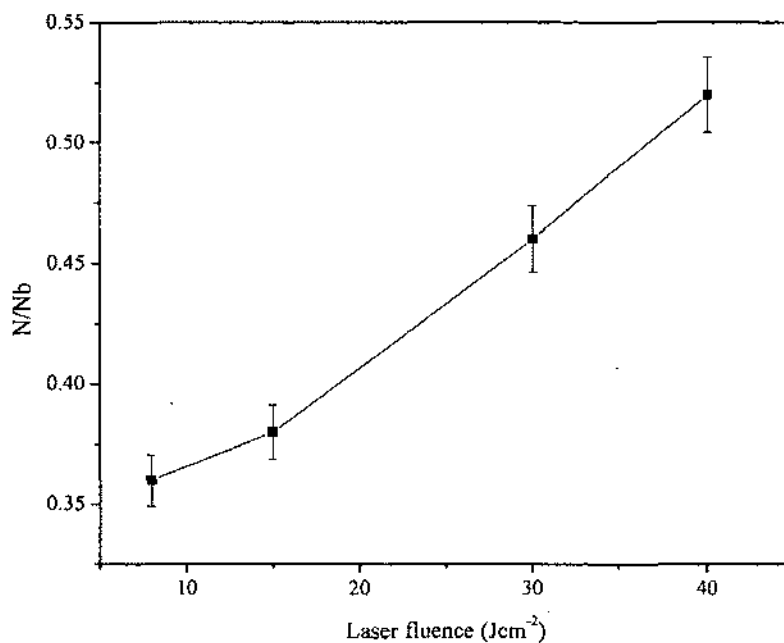
Fig. V.2. EDX measurement of N/Nb ratio in the NbN_x films for different laser fluences. The data points, along with error bars, represent an average of at least 3 spectra obtained across each sample area. The line is included as a guide.
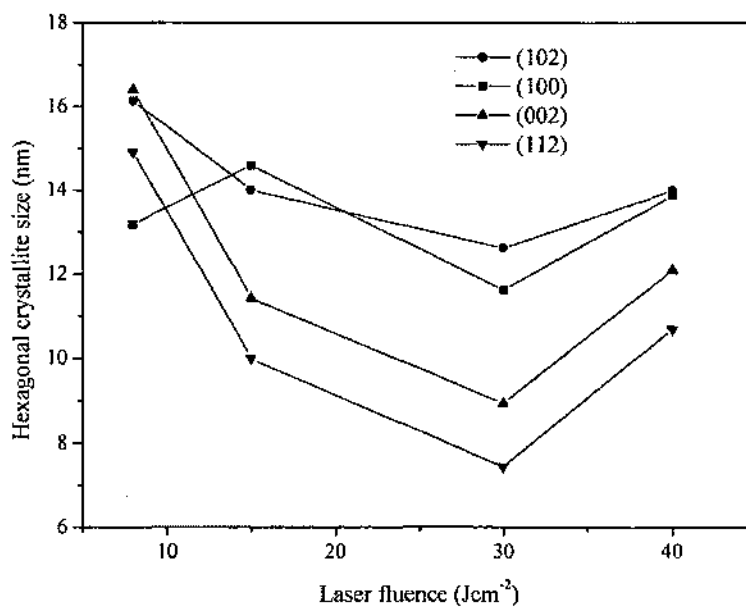
Fig. V.3. The mean hexagonal crystallite size as a function of laser fluence.

In PLD, increasing the laser fluence increases the kinetic energy of the particles being ejected from the target [120]. For higher laser fluence, the laser-produced plasma contains more energetic Nb particles. These particles have higher flux and kinetic energy. Therefore, once they arrive on the surface of the substrate, they will accumulate to form a larger grain on the substrate in order to minimize their surface energy [93]. The laser fluence significantly influences the film density and change in crystal structure. As the fluence was increased from 8 to 30 J/cm^2, a decrease in crystallite size was observed for the grown NbN$_x$ films because of the phase change from mixed (cubic + hexagonal) to pure hexagonal structure. The results in Fig. V.3 indicate that in the case of the film deposited with different laser fluences, the crystallite size of (102) and (100) orientated domains were observed to be changed from 12 to 16 nm, while the changes in crystallite size of (002) and (112) orientated domains are in the range of 8 to 16 nm.

V.3.1.2. TEXTURE COEFFICIENT

The degree of texture in the films was calculated using integrated peak intensity analyses of XRD. The (102) peak analyses are shown in Table V.1 for NbN$_x$ films deposited at laser fluence between 8 and 40 J/cm^2. The (102) peak has an FWHM of 0.58° to 0.75° and the peak positions are slightly shifted to higher 2-theta values. The peak shift indicates that the growth orientations of the grains in some of the films were tilted with respect to the substrate due to different internal strain. It is observed from Table V.1 that the lattice constant of β-Nb$_2$N films can be tuned by changing the laser fluence at a fixed nitrogen pressure and substrate temperature. The broadening of the (102) peaks of β-Nb$_2$N phase was observed for the film deposited at 30 J/cm^2 due to

lower crystalline quality which can be confirmed in XRD measurements, where the integrated intensity of the diffraction peak decreased while FWHM increased.

Table V.1. The degree of texture in the (102) plane of β-Nb$_2$N.

Laser fluence (J/cm^2)	FWHM (°)	Integrated peak intensity (arb. units)	Ratio of lattice constants c/a	Peak position (degree)
8	0.58	488	1.614	50.37
15	0.68	842	1.613	50.39
30	0.75	567	1.619	50.40
40	0.68	838	1.618	50.42

Table V.1 also shows the variation in the c/a ratio (hexagonality) as a function of the laser fluence. The lattice constants "a" and "c" were calculated from (102) and (100) peaks of the XRD pattern. The c/a ratio for laser fluence of 30 J/cm^2 is about 1.619, while the a-lattice parameter is 0.3059 nm and the c-lattice parameter is 0.4953 nm, which are almost the same as bulk values of β-Nb$_2$N [159]. This result indicates that the deposition condition gives us β-Nb$_2$N, whose atomic size is the same as the bulk. As shown in Table V.1, only the film deposited at highest laser fluence has (102) peak position at 50.42° and it came close to the standard powder diffraction value (50.46°) as the laser fluence was increased to 40 J/cm^2 [159].

In order to select the dominant reflections which show the strong texture in the NbN$_x$ films, an average texture coefficient was calculated. The following (hkl) diffraction peaks from XRD patterns corresponding to β-Nb$_2$N were used in texture coefficient

calculations: (100), (002), (102), (110), (103), (112) and (202). For a preferentially-oriented sample, the texture coefficient TC(hkl) is greater than one. Table V.2 summarizes the results of texture coefficient calculations for the observed (hkl) diffraction peaks at various laser fluences. Note that the values of the texture coefficient of the (100) (102) and (110) planes are greater than unity, while (002), (103), (112) and (202) planes are less than one. The intensities of (100) and (110) diffraction peaks reached maximum at the laser fluence of 15 J/cm^2, resulting in corresponding maximum texture coefficient. The texture coefficient for the (110) plane increases from 1.35 to 1.88 and then decreases to 1.68 with increase of laser fluence. On the other hand, the texture coefficient for (110) is dominant for most laser fluences, indicating that the (110) is the preferred orientation of most deposited films. This may be useful for the fabrication of oriented NbN_x films. The texture degree affects electrical, optical, and catalytic properties significantly [132].

Table V.2. The texture coefficient of different planes for NbN_x films on Nb grown at different laser fluences.

hkl	8 J/cm^2	15 J/cm^2	30 J/cm^2	40 J/cm^2	$TC_{av}(hkl)$
100	0.93	1.29	1.15	0.97	1.08
002	0.40	0.67	1.09	0.62	0.69
102	1.21	0.88	1.06	0.99	1.03
110	1.35	1.72	1.03	1.50	1.40
103	1.24	0.64	0.92	0.94	0.93
112	0.87	0.79	0.75	0.97	0.845
202	0.36	0.61	0.43	0.54	0.48
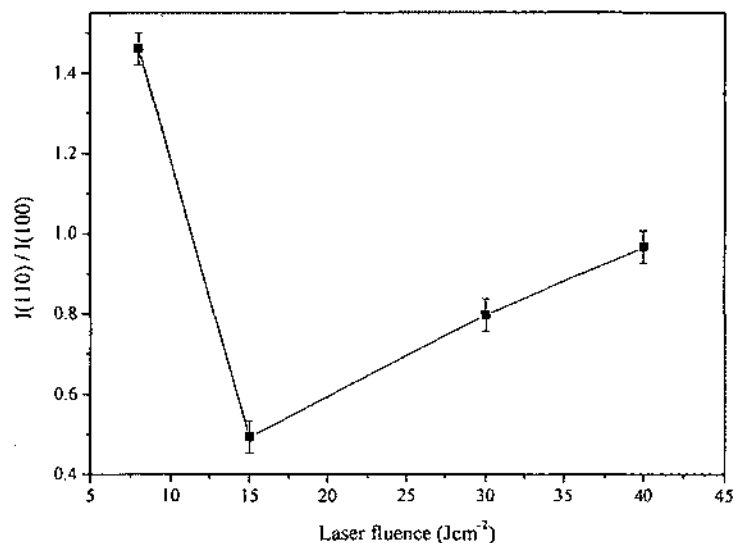
Fig. V.4. Texture coefficient ratio of the (110) diffraction peak to the (100) peak as function laser fluence. The error bars represent 2 % of data calculations.

The texture coefficient ratio of the (110) peak to the (100) peak, $I_{(110)}$ / $I_{(100)}$, as a function of the laser fluence is plotted in Fig. V.4. It can be seen that the intensity ratio first decreases with increasing laser fluence up to 15 J/cm^2 and then increases significantly. Accordingly, the decrease of $I_{(110)}$ / $I_{(100)}$ ratio indicates a decreasing amount of (110) texture. It can be concluded that the crystals formed at the beginning of film growth are dominantly (110) textured, but the (100) texture develops especially in the film deposited at 15 J/cm^2.

V.3.1.3. SURFACE MORPHOLOGY

The surface morphology of NbN$_x$ films was characterized by AFM and SEM. Fig. V.5 shows topographic AFM images of NbN$_x$ films deposited at different laser fluences. All AFM images were taken in air using tapping mode. For the films deposited at laser fluence of 8 AND 15 J/cm^2, micron-sized large particles with some small fraction of

smaller size islands were observed. As the laser fluence was increased to 30 J/cm^2, those large clusters disappeared, while the films became smoother. At this condition, some islands are also visible, as shown in Fig. V.5(c). Further increase in laser fluence resulted in more reduction in the fraction of the large clusters and increase in the smoothness of the deposited film. Controlling thin-film growth by changing the laser parameters, namely, fluence and repetition rate is a unique feature of PLD. Increasing the laser fluence is expected to result in higher flux and kinetic energy of ions and electrons in plume. The higher kinetic energy can promote formation of smooth NbN$_x$ films, which may contribute to the low surface roughness, as observed in Fig. VI.5. It was reported that lowering the deposition rate resulted in larger island size and rougher surface [164]. Previous PLD studies have discussed the growth rate and shown that the larger the laser fluence, the smaller the island's size, while the film became smoother [165]. Accordingly, lower laser fluences produce a smaller density of islands when compared to higher laser fluences.

SEM images of films grown at different laser fluences, shown in Fig. V.6, also confirm the same behavior observed in AFM images. As shown in Fig. V.6(a) the films grown at a laser fluence of 8 J/cm^2 show smoother surface. As the laser fluence was increased to 15 J/cm^2, clusters that were well distributed over the surface became visible, as seen in Fig. V.6 (b). Further increase in the laser fluences results in smoother surface, as shown in Fig. V.6(c) and (d).

(a)

(b)

(c)

(d)
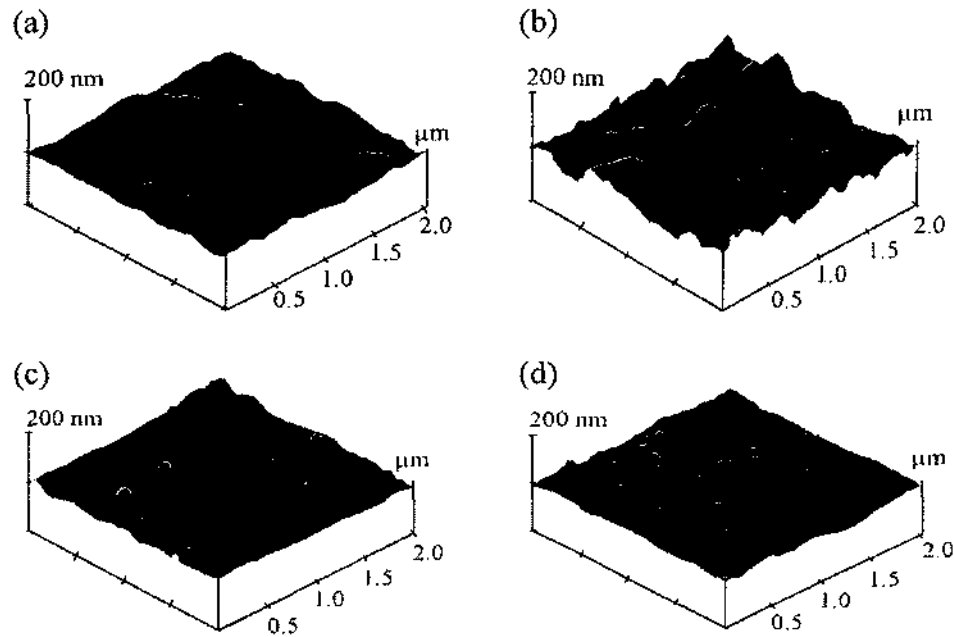
Fig. V.5. AFM images of NbN_x on Nb deposited with a laser fluence of (a) 8, (b) 15, (c) 30, and (d) 40 J/cm^2.

The root mean square (RMS) surface roughness was obtained from the AFM images. The dependence of the RMS value on the laser fluence over an area of 2000×2000 nm^2 and line scans at different fluences are shown in Fig. V.7 and its inset. The error bars in Fig. V.7 represent the variations in RMS roughness values in the line scans on three different AFM images with same area. The roughness of the film grown at 8 J/cm^2 is $\sim 14.0 \pm 2.5$ nm. For the films deposited with 15 J/cm^2, the surface is quite rough, with mixed (cubic + hexagonal) to pure hexagonal. The increase of the laser fluence to 30 J/cm^2 resulted in a rapid decrease of RMS to 12.4 ± 2.7 nm. A further increase of the laser fluence to 40 J/cm^2 leads to a decrease of RMS to 5.4 ± 2.3 nm.
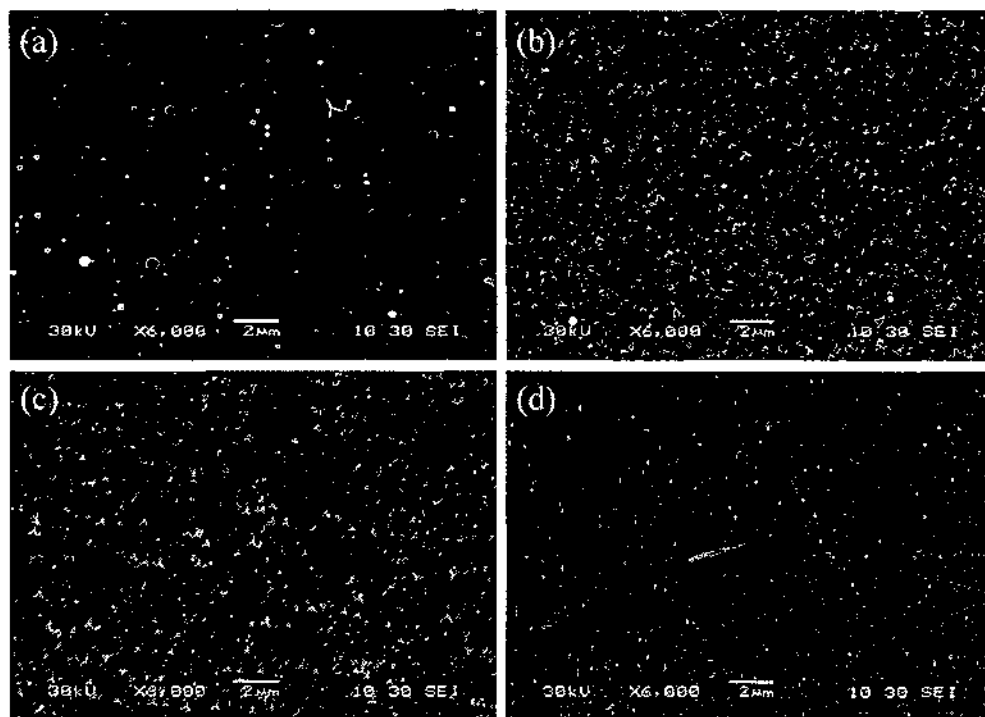
Fig. V.6. SEM images of the NbN$_x$ films deposited at different laser fluences (a) 8, (b) 15, (c) 30, and (d) 40 J/cm^2.
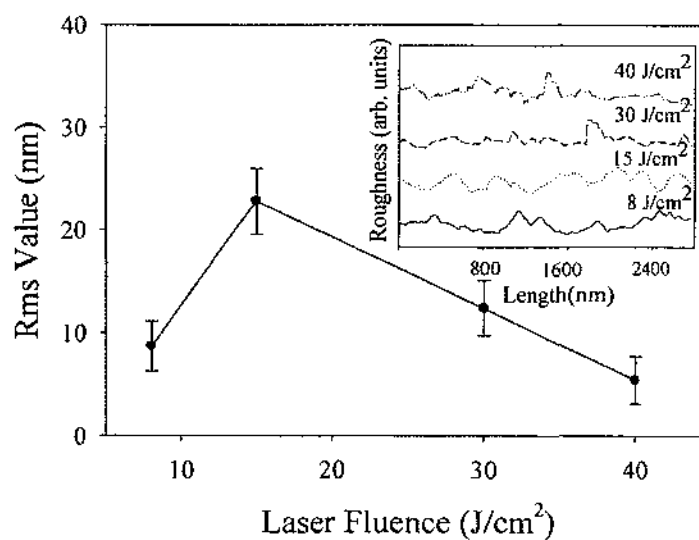
Fig. V.7. Dependence of RMS values on laser fluence. The inset shows individual line scans at different laser fluences.

V.3.2. BACKGROUND PRESSURE INFLUENCE

V.3.2.1. STRUCTURE AND PHASE COMPOSITION

The crystal structure of the NbN_x films was analyzed by X-ray diffraction measurements. Fig. V.8 shows XRD patterns of the NbN_x films prepared in various nitrogen background pressures between 10.7 and 66.7 Pa. The XRD patterns can be identified as these of cubic and hexagonal phases. In general, the patterns recorded from the films grown at different pressures have similar diffraction peaks corresponding to the β-Nb_2N and δ-NbN phases but show important differences on the relative intensities. In particular, the δ-NbN cubic phase appears at 13.4 and 20.0 Pa with corresponding planes of (111), (200), and (220), as well as reflections from β-Nb_2N [159, 161]. It can be seen that the phase composition of the NbN_x films changes with increasing nitrogen pressure P_{N_2}. The NbN_x films deposited using various nitrogen pressures had the following phase compositions: at 10.7 Pa mainly β-Nb_2N was observed but three weak reflections of hexagonal δ'-NbN appeared at 33.22° (001), 47.94° (101) and 62.25° (110) [166]; for 13.4-26.7 Pa range, the films consisted of a cubic δ-NbN mixture with hexagonal β-Nb_2N; and for 40.0-66.7 Pa range, a single-phase of hexagonal β-Nb_2N is identified. A single β-Nb_2N phase was observed at highest P_{N_2} used; however, δ-NbN mixed with the β-Nb_2N phase was obtained only in the pressure range of 13.4-26.7 Pa. The integrated intensity of peaks at the (111) and (200) of δ-NbN phase showed changes as P_{N_2} increased from 13.4 to 20.0 Pa. The diffraction intensity ratio (I $_{(111)}$/ I $_{(200)}$) increased from 0.52 to 1.18, indicating that the cubic texture of the film changes from

(200) to (111) as P_{N_2} is increased. The full-width at half-maximum (FWHM) of the (200) and (111) peaks increased with increases of P_{N_2} from 13.4 to 20.0 Pa. This indicates that the size of the (200) and (111) oriented crystallites in the NbN_x film decreased with increasing P_{N_2}, although the crystallite size of the hexagonal β-Nb_2N phase increased from 8.17 to 14.00 nm. At 66.7 Pa, the β-Nb_2N phase exists in NbN_x films with a predominant (100) texture.
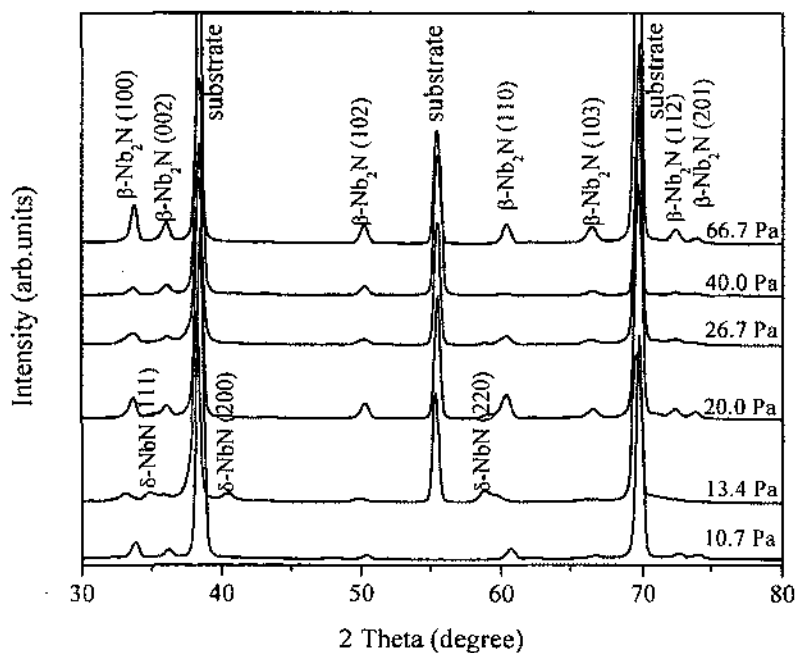
Fig. V.8. XRD patterns of NbN_x films deposited at various nitrogen pressures

Niobium forms several different nitride phases as the nitrogen-to-niobium ratios are changed in NbN_x [167]. Phase assignment of NbN_x is complicated by the nonstoichiometric nature of the transition metal nitrides. The nonstoichiometries can be

present as defects or vacancies of either the metal or nonmetal sublattices, or both, within a given phase [167]. Phase change may occur when the nitrogen background pressure changes. At pressures between 20.0 and 26.7 Pa, cubic and hexagonal phases were observed, and at pressure greater than 26.7 Pa, phase change occurred. High nitrogen pressure did not result in an increase in the amount of nitrogen in NbN_x but, on the contrary, the fraction of nitrogen atoms in NbN_x thin films was reduced as the nitrogen pressure was increased.

In Fig. V.8, the δ-NbN phase only appears at 13.4 and 20.0 Pa nitrogen pressure, hence, it can be expected that the texture of δ-NbN should be mainly governed by the atomic percentage of nitrogen in the film. It has been reported that in the case of the cubic and hexagonal NbN_x films, the atomic percentages of nitrogen is about 50% and 30%, respectively [168]. After ejection of Nb atoms and ions from the Nb target, collisions and scattering between ablated particles and gas molecules can be significant. The mean free path of the ablated particles is reduced in the presence of background nitrogen gas. Higher background nitrogen pressure lowers the kinetic energies of the ablated species in PLD and increases the recombination rate. Also, interaction with the ambient gas slows the ablation plume expansion. Time-resolved spectroscopy studies of the ablation plume expansion have shown that kinetic energies on the order of several 100 eV can be observed. These energies are sufficiently high to create defects in the growing film [169]. Therefore, higher nitrogen pressure causes lower deposition rate and resulting in less nitrogen ratio in the deposited film. Use of lower nitrogen pressure results not only in increasing particle fluxes from the target to the substrate but also in increasing the mean kinetic energies of the ablated species. It should be noted that some fraction of the species

in the ablated particle flux is ionized. The portion of these ions in the ablated particle flux is higher when the lower nitrogen pressure is used. As a consequence, the ratio of ions in the ablated particle flux decreases by increasing nitrogen pressure, and that affects the phase formation of NbN_x [170].
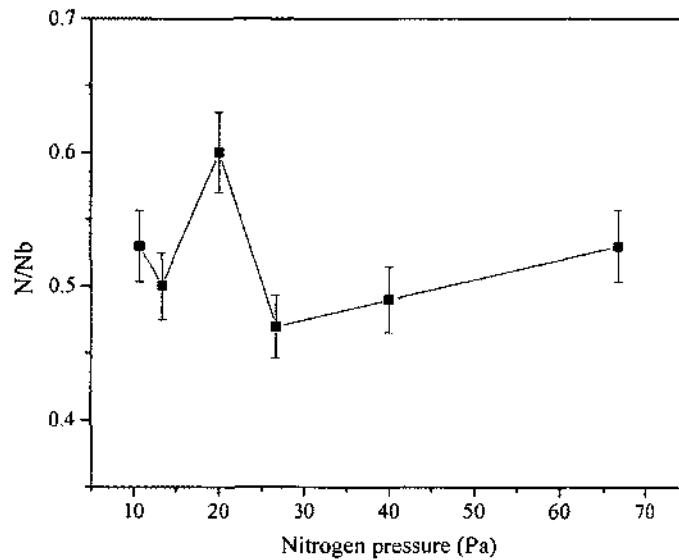
Fig. V.9. EDX measurement of N/Nb ratio in the NbN_x films as a function of nitrogen background pressure.

In order to determine the nitrogen content in the NbN_x films, EDX analyses have been performed. Fig. V.9 shows the chemical composition of the surface layer based on the EDX analyses. Through EDX analyses, the N/Nb ratio was between 0.47 ± 0.02 to 0.6 ± 0.02, which is in agreement with previously reported phase results of Nb-N systems [4, 13]. According to the phase diagram of the Nb-N system, a few single phases exist with increasing atomic ratio of nitrogen in the 500 and 1000 °C temperature range [168].

If the nitrogen content is between 30–35%, the β-Nb$_2$N hexagonal phase exists but the δ-NbN phase requires a higher nitrogen ratio (>50%). As the pressure increases, nitrogen ratio in the film increases and that affects the phase structure.

Treece *et al.* reported that on NbN$_x$ films deposited using PLD the nitrogen content in the NbN$_x$ films increases with nitrogen gas pressure [83]. They noted that the film compositions of Nb$_2$N, NbN, or Nb$_3$N$_4$ can easily by controlled by the background gas pressure in a dynamic equilibrium. In this case, the NbN$_x$ films with these phases were not deposited at static background gas pressure. The experimental conditions were optimized by changing laser power and nitrogen gas pressure. Nitrogen ion content is limited and did not increase with P_{N_2} due to saturation effect. However, results showed that an increase in P_{N_2} promotes the growth of hexagonal phase with the increase of very little amount of nitrogen content in the films, as shown in Fig. V.9.

The phase purity in NbN$_x$ films can also be concluded from the intensity of the hexagonal peaks in the XRD pattern in Fig. V.8. The amount of hexagonal β-Nb$_2$N has been calculated for the hexagonal phase concentration as the ratio of the sum of the intensities of the hexagonal peaks divided by the total sum of the intensities of all peaks of hexagonal and cubic phases [158]. The variation of hexagonal phase with background nitrogen pressure is shown in Fig. V.10. When P_{N_2} increases to 26.7 Pa, the main reflections of δ-NbN phase in the XRD disappear. The ratio of the cubic and hexagonal phase concentration is strongly affected by nitrogen pressure, e.g., at constant laser fluence and deposition temperature, the δ/β concentration ratio is 1.48 at 13.4 Pa and decreases to 0.19 at 20.0 Pa. The lowest P_{N_2} (10.7 Pa) results in minimum interaction between the ablated species and the gas ambient, while at the highest pressure (66.7 Pa)

the mean free path of ablated material decreases and that affects the phase of the film.

Phase composition of the film changes from mixed to pure hexagonal β-Nb$_2$N due to the

decrease of nitrogen content of the NbN$_x$ films. Nitrogen concentration in NbN$_x$ thin

films is reduced, which results in niobium-rich β-Nb$_2$N single phase. The number of

nearest-neighbor of N atoms for each Nb atom decreases from six to three when going

from the cubic to the hexagonal phase and the volume increases by about 2% [171].

The peak position of the (102) plane as a function of P_{N_2} is shown in Fig. V.10.

The peak position shows systematical changes with increasing nitrogen pressure; it first

goes through a maximum, then decreases, and finally increases. After 20.0 Pa, it slightly

shifts to lower diffraction angles as P_{N_2} is varied, which is indicative of a change in the

size of lattice of β-Nb$_2$N. There is a shift of the peaks to a lower diffraction angle of the

(102) plane in going from 13.4 to 26.7 Pa, indicating an increase in lattice constant.
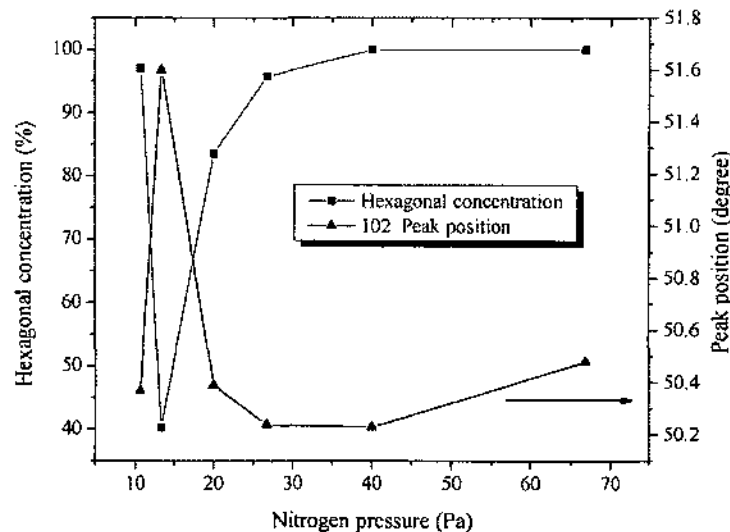
Fig. V.10. Hexagonal phase concentration (left y-axis) and variation of peak position of (102) plane (right y-axis) vs. nitrogen pressure. The solid line is drawn to guide the eye.

The FWHM of the (100) and (102) peaks changes with the variation of P_{N_2} as shown in Fig. V.11(a). The FWHM decreases with the increase in nitrogen pressure from 26.7 to 66.7 Pa. This indicates that the size of the (102) oriented grains in the film first decreases, with increasing P_{N_2}, and after changing to single hexagonal phase, size of the grains increases again. This was later confirmed by AFM observations. A similar effect was observed from all oriented planes in the hexagonal phase. An increase of the nitrogen pressure also caused a reduction in the defect structure of the remaining hexagonal lattice, a sharpening of the hexagonal peaks, and an increase in the Bragg diffraction angles. Here, the crystallinity of the hexagonal phase improved considerably, as indicated by the decrease of the FWHM of the Bragg peaks shown in Fig. V.11(a). The broadening of diffraction peaks observed for deposition at 13.4 and 26.7 Pa is usually attributed to either reduction in crystallite size, distribution of micro-strains within the crystallites, or a combination of both [172].

The crystallite size of the hexagonal β-Nb$_2$N phase was calculated using the Scherrer formula [127], as shown in Fig. V.11(b). The average crystallite size was found to vary in a narrow range from 8 to 14 nm with change in background pressure. Generally, the mean crystallite size increased with P_{N_2} but significantly reduced at 13.4 and 26.7 Pa, which is due to phase change with nitrogen background pressure from hexagonal to mixed, then from mixed to hexagonal phase. After phase change, the crystallite sizes increase in the pure hexagonal phase as the deposition pressure increases. A similar effect is reported in NbN$_x$ films prepared by reactive magnetron sputtering at various nitrogen partial pressures and attributed to different compressive stresses affecting the crystallite size [158].
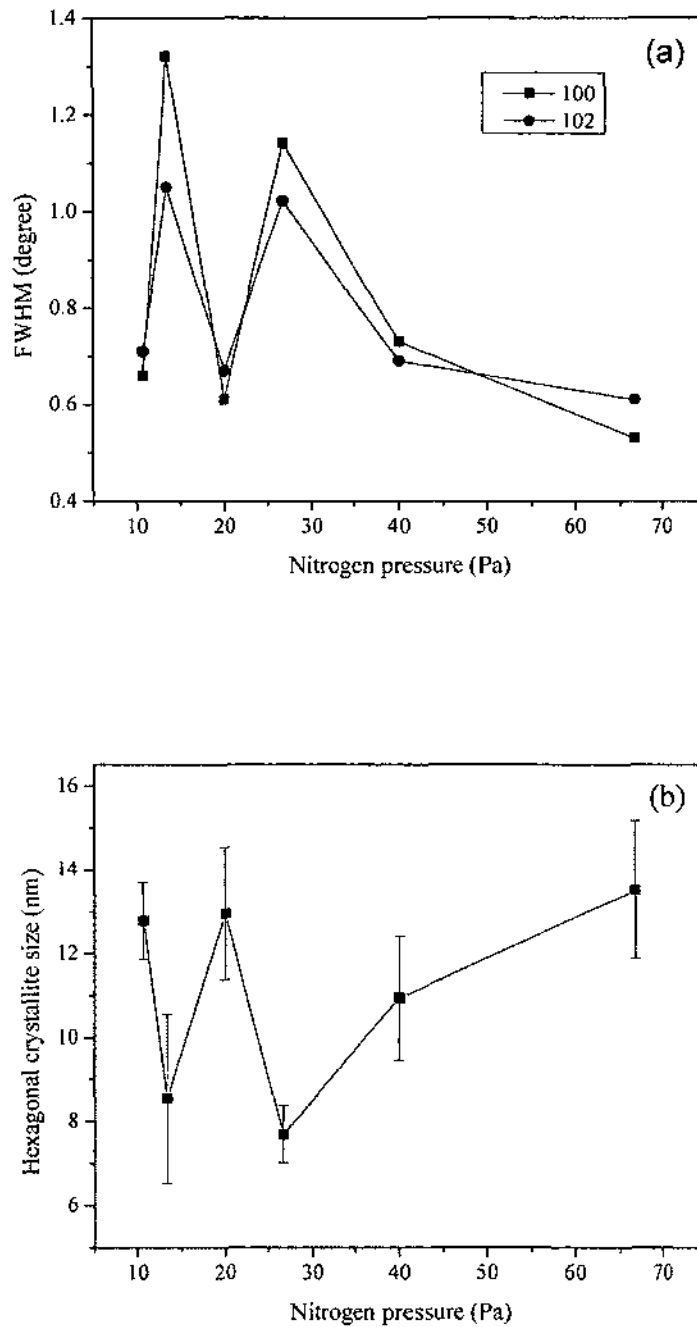
Fig. V.11. (a) Variation of FWHM of (102) and (100) planes with nitrogen pressure. (b) Average crystallite size of hexagonal phase β-Nb_2N as a function of background nitrogen pressure. The lines are drawn to guide the eye. The error bars are standard deviations calculated from four different orientations of phase β-Nb_2N in each sample.
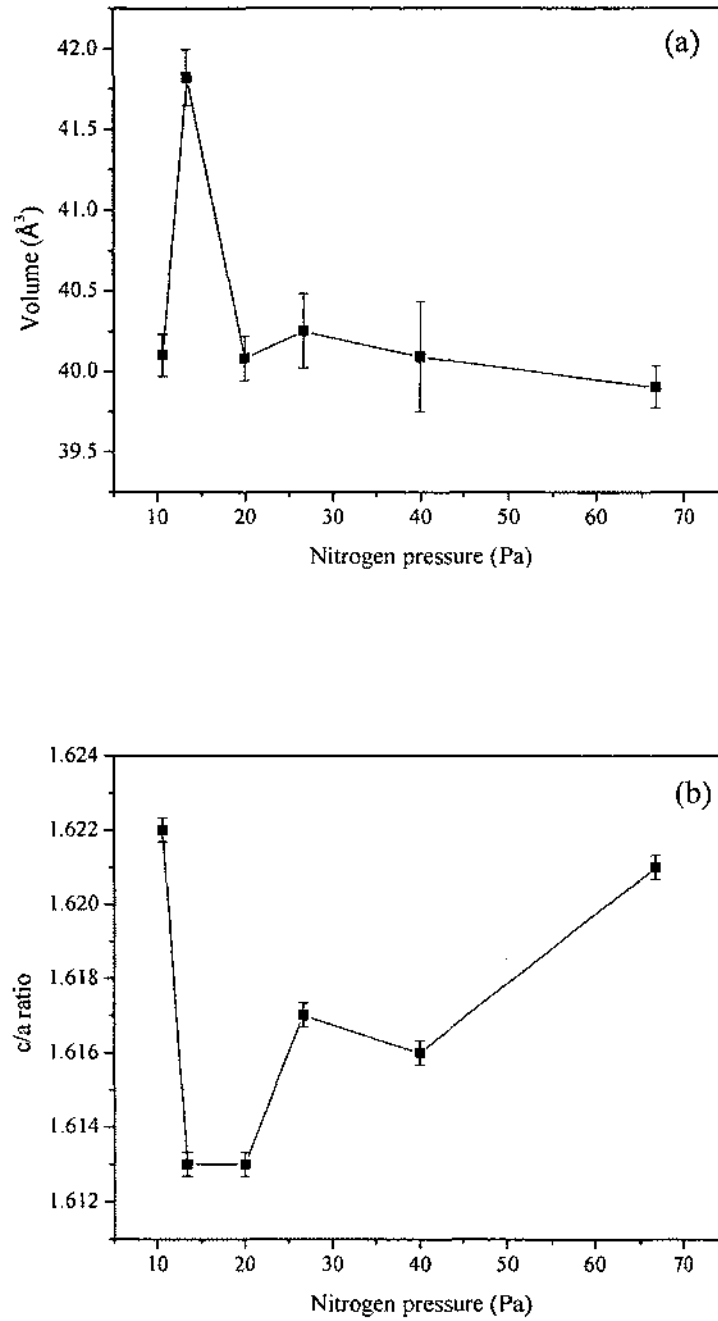
Fig. V.12. Variation of (a) unit cell volume and (b) c/a ratio of β-Nb$_2$N phase as a function of background nitrogen pressure. The solid lines are drawn as a guide to the eye. The error bars in the c/a ratios represent standard deviations calculated from different orientations for each sample.

A large variation in the lattice parameters was observed as nitrogen gas pressure was changed, as shown in Fig. V.12(a) and (b). The unit-cell parameter ratio (c/a) of the β-Nb$_2$N hexagonal phase was found to be changed from 1.613 to 1.621 with an increase of P_{N_2}, as shown in Fig. V.12(b). The film deposited at highest nitrogen pressure has a c/a ratio close to the bulk value of β-Nb$_2$N, which is 1.619 [157]. An increase of the c/a ratio with P_{N_2} was observed as a result of lattice expansion and growth of β-Nb$_2$N hexagonal phase. The hexagonal phase displays a qualitatively similar volume after the observed phase change at 26.7 Pa pressure. The c/a ratio increases slowly and reaches bulk value at 66.7 Pa. The hexagonal phase exhibits distorted structure at lower nitrogen pressures in the mixed other phase with a lower c/a ratio.

A deposition of NbN$_x$ thin films by magnetron sputtering under different nitrogen flow rates reveals that the compressive stress in the film increases gradually with an increasing nitrogen flow rate [173]. In the present work, as nitrogen background pressure was increased, the compressive stress in the NbN$_x$ films increased as well. Experimental observations have shown the presence of a maximum compressive stress developed when the energy of the incident ions is varied [174, 175]. The XRD results indicate that a significant amount of compressive stress in the NbN$_x$ films causes distortion of the unit cell due to nitrogen pressure during growth. As shown in Fig. V.12(a), the unit cell volume of the film has maximum value at 13.4 Pa nitrogen pressure due to a nitrogen deficiency in the film that causes an expansion of the unit cell. As the nitrogen background pressure increases, the compressive stress, created during the film growth, i.e., the intrinsic stress in the NbN$_x$ films, increases. On the other hand, the typical

particulate size created by PLD changes with background gas pressure and it increases as the gas pressure increases [93].

The influence of P_{N_2} on the film growth can also be seen for the lattice parameter values. Fig. V.12(b) gives the ratio of the lattice parameters of the hexagonal β-Nb_2N as a function of nitrogen background pressure. Determination of unit-cell parameters was based on XRD 2θ diffraction angle measurements. The occurrence of compressive stress would explain the increase of the lattice parameter. An increase in the lattice parameter with the P_{N_2} can be understood by a higher amount of lattice defects due to different nitrogen content on regular lattice sites [84].

The cubic lattice parameter in the NbN_x films is calculated as 0.4457 nm for films deposited at 13.4 Pa nitrogen and 0.4414 nm at 20.0 Pa. Note that the lattice parameter reported for stoichiometric δ-NbN is 0.4392 nm [166]. This shows that the lattice parameter of the cubic phase in the film is higher than the bulk value and also decreases with P_{N_2}. A decrease in the lattice constant of NbN_x with x >1 is expected, since for cubic materials with x~1, the lattice constant has been shown to increase with nitrogen content to a maximum when x = 1, decreasing with increased nitrogen incorporation. Bulk cubic NbN_x samples can maintain their structure over a broad range of x values 0.86<x<1 by incorporating N defects when x<1 and Nb vacancies when x>1. The lattice parameter increases as pressure increases, corresponding to a predominantly defective nitrogen sublattice where the nitrogen vacancies are progressively occupied. At higher pressures, the niobium sublattice becomes predominantly defective with formation of an increasing number of niobium vacancies and a decrease of the lattice parameter [167].

V.3.2.2. TEXTURE COEFFICIENT

The texture coefficients of (100), (002), (102), (110) and (103) planes, calculated from Equation (V.2), are shown in Table V.3. The hexagonal phase is strongly textured with (100) planes parallel to the substrate surface. This means that the deposited films are polycrystalline with a preferred orientation along the [100] direction. Similar results in preferred orientation of the [100] direction have been reported for Nb_2N films [83]. The preferred growth is generally favored by the deposition condition and specific interaction of the nucleus with the substrate surface. In the case of NbN_x films, the (100) plane has been observed to have minimum surface energy interaction.

Table V.3. The calculated values of texture coefficients of β-Nb_2N.

P_{N_2} (Pa)	(100)	(002)	(102)	(110)	(103)
10.7	1.49	0.89	0.37	1.01	0.68
13.4	1.55	0.93	0.62	1.37	0.45
20.0	1.37	0.63	0.92	1.35	0.59
26.7	1.76	0.76	0.65	1.00	0.80
40.0	1.42	1.18	1.18	0.49	0.71
66.7	1.37	0.62	1.24	0.57	1.16

V.3.2.3. SURFACE MORPHOLOGY

AFM and SEM were performed to examine the morphologies as well as finding a correlation between surface morphology and the phase change for the samples with increasing P_{N_2}. AFM images were taken in air using tapping mode. Fig. V.13 shows 3D-AFM images of NbN_x films deposited at different P_{N_2}. It is observed that AFM images of

films grown at 10.7 Pa consist of triangular submicron-sized islands, as shown in Fig. V.13(a). Once the ambient pressure was raised to 66.7 Pa, more regular shaped micron-sized particles are observed. SEM images for films grown at different nitrogen pressures, shown in Fig. V.14, also confirm the same behavior observed in AFM images. When the nitrogen pressure was increased to 13.4 Pa, the morphology of the islands became irregular. Irregular shape and size along with surface roughness, increased when the ambient nitrogen pressure was increased to 20.0 Pa. However, for a nitrogen pressure of 26.7 Pa, the surface became very smooth. Some regularly shaped islands started to appear at 40.0 Pa.
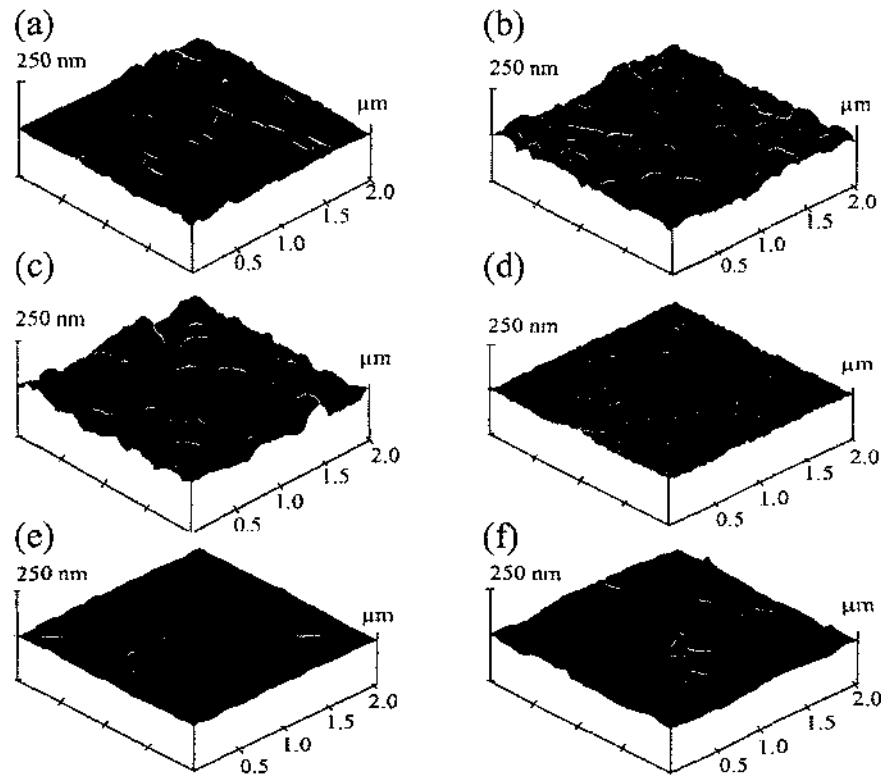
Fig. V.13. 3D-AFM images of the NbN$_x$ films deposited at different nitrogen background pressures (a) 10.7 Pa, (b) 13.4 Pa, (c) 20.0 Pa, (d) 26.7 Pa, (e) 40.0 Pa, and (f) 66.7 Pa.
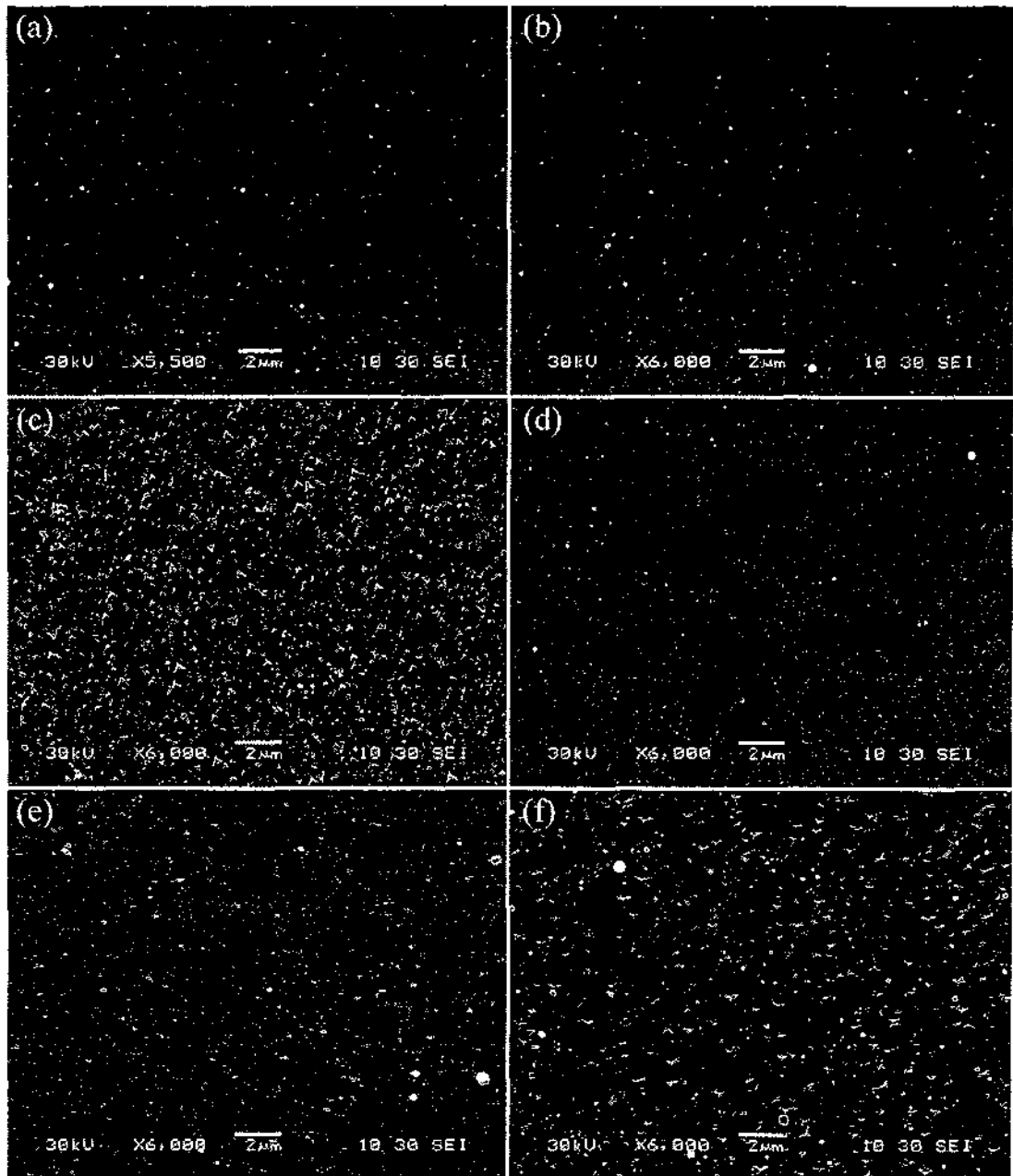
Fig. V.14. SEM images of the NbN$_x$ films deposited at different nitrogen background pressures (a) 10.7 Pa, (b) 13.4 Pa, (c) 20.0 Pa, (d) 26.7 Pa, (e) 40.0 Pa, and (f) 66.7 Pa.
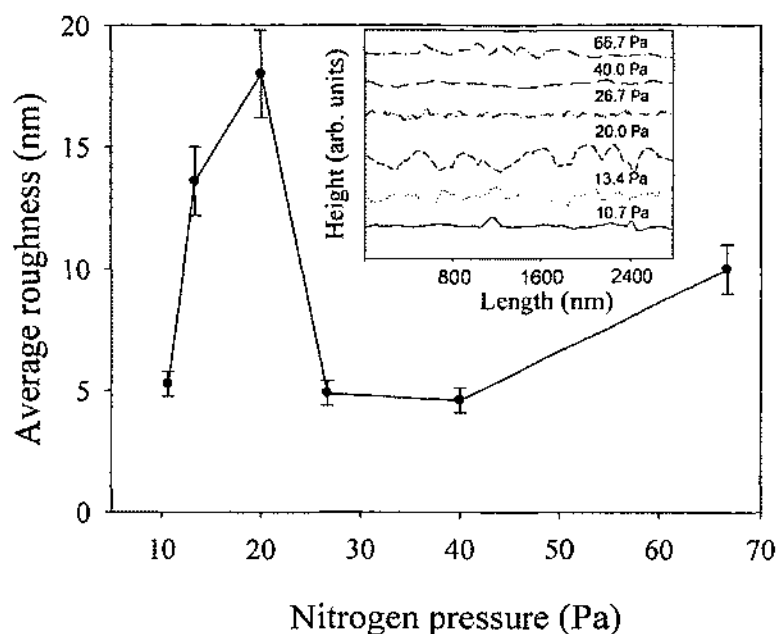
Fig. V.15. Average surface roughness of NbN$_x$ films at different pressures. The inset shows line scans across the samples prepared at different nitrogen pressures.

The root mean square surface roughness (R) was obtained from the AFM images. The average surface roughness versus ambient nitrogen pressure is plotted in Fig. V.15. The error bars in Fig. V.15 represent the standard deviation of RMS roughness calculated from three different line scans of AFM images with same area. The surface roughness increases with nitrogen pressure until 20.0 Pa, and then there is a sudden decrease in roughness. However, for the film grown at 66.7 Pa, the roughness increases compared to that grown at 26.7 Pa and 40.0 Pa. The decrease in surface roughness at 26.7 Pa is related to the phase change of NbN$_x$ film. Otherwise, an increase in the surface roughness is expected when the background pressure is also increased. In vapor phase deposition, the nucleation density and the clusters' sizes are determined through the competition between the atomic flux and the surface diffusion coefficient of adatoms.

The effect of background pressure is not trivial since change in N_2 pressure could cause change in flux of the atoms and their kinetic energy. Therefore, it is possible that pressure can also affect surface diffusion. The kinetic energy of adatoms decreases with the increase of the pressure. Higher adatom kinetic energy could promote formation of smooth NbN_x films, which is consistent with data shown in Fig. V.15. Line scans of the AFM images diagonally on the samples are shown in the inset of Fig. V.15. The surface roughness increased as the pressure was increased from 10.7 Pa to 20.0 Pa. Once the deposition pressure reached 26.7 Pa, the surface roughness decreased very sharply up to 40.0 Pa, then increased for the film grown at 66.7 Pa.

V.3.3. SUBSTRATE TEMPERATURE INFLUENCE

V.3.3.1. STRUCTURE AND PHASE COMPOSITION

Fig. V.16 shows the results of XRD NbN_x films prepared at different substrate deposition temperatures. The XRD pattern of the Nb substrate is also included in Fig. V.16 as a reference. The substrate temperature measurements are reproducible with an estimated accuracy of ±20 °C at 250 °C and ±50 °C at 950 °C. The accuracy is limited by the sample contact to the heater surface and the temperature gradient across the heater. The films grown at room temperature and 250 °C showed poor crystalline structures, while increasing the substrate temperature starts the better crystallization process. As the temperature increased from 450 to 650 °C, the films became highly textured and can be indexed with a mixture of cubic and hexagonal phases. NbN_x films deposited within the same temperature range were found to be with two or more phases [166, 176].
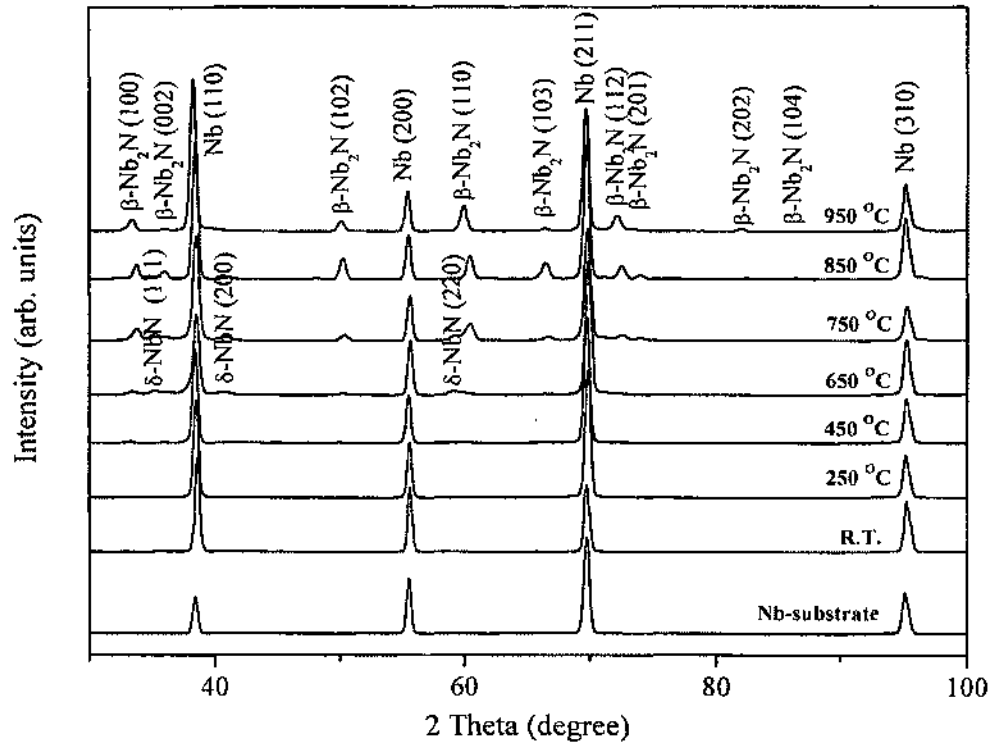
Fig. V.16. XRD patterns of NbN$_x$ thin films deposited on Nb substrate at different temperatures. The XRD pattern of the Nb substrate is also shown.

Further increase of the substrate temperature can lead to the formation of a sublayer of NbN$_x$ by reaction with the Nb substrate and higher nucleation density develops on the surface. At higher temperatures, adatoms on the substrate's surface gain thermal energy and surface diffusion is enhanced, thus promoting crystal growth. The transition from a textured microstructure to a densely packed crystal structure occurs over a range of temperatures. The substrate temperatures above 750 °C result in the formation of mainly films with β-Nb$_2$N phase.

In order to show the phase content for the NbN$_x$ films grown at different substrate temperatures, two of the XRD patterns of Fig. V.16 are redrawn in expanded scale, as shown in Fig. V.17. The two patterns show diffraction peaks of the β-Nb$_2$N, δ-NbN, and

δ'-NbN with differences in the relative intensities. In particular, the δ-NbN cubic phase appeared at 650, 750, and 850 °C with corresponding planes of (111), (200), and (220), as well as β-Nb₂N, δ'-NbN and Nb peaks from the substrate.
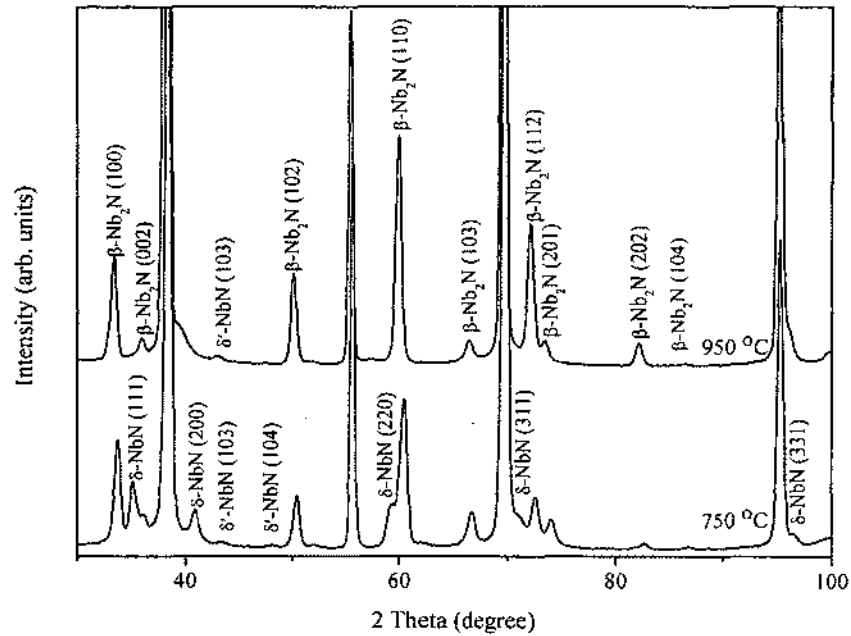
Fig. V.17. XRD patterns of NbN$_x$ thin films deposited at 750 and 950 °C. The patterns show diffraction peaks of the β-Nb₂N, δ-NbN, and δ'-NbN phases.

The possibility of nitride growth by heating the substrate in nitrogen pressure of 13.3 Pa for 60 min was checked and found not to affect the reported results. This is attributed to the low nitrogen background pressure used. The reactive PLD process involves the formation of highly reactive atomic nitrogen species in the plasma which interacts with the ablated Nb plume and the surface.

The chemical composition of the films was determined by EPMA. Fig. V.18(a) shows the stoichiometric coefficient x in NbN_x as a function of deposition temperature. The error bars on EPMA values represent the standard deviation for analyses of five points done on each sample. The atomic nitrogen ratio in the film increases with temperature up to 850 °C and then suddenly drops to 0.43 due to the phase change of NbN_x. It is noteworthy that δ cubic niobium nitride can be obtained within the range of x: $(0.57 < x < 0.99)$ [1]. The β-Nb_2N hexagonal phase, has a wide range of $x = 0.43 - 0.93$, which is in agreement with the phase diagram of the Nb-N system [3, 167]. Fig. V.18(b) shows a plot of the c/a ratio of β phase lattice parameters versus atomic percentage of nitrogen in the film. The c/a ratio is initially reduced as the composition changes from $NbN_{0.43}$ to $NbN_{0.57}$, which is consistent with the literature [91]. However, after the nitrogen content increases to $NbN_{0.57}$, the c/a ratio increases with increasing N/Nb ratio. The lattice parameter strongly depends on the crystal imperfection. The lattice constant, a, is independent of composition, but c increases with nitrogen content. Upon the deviation of x from 0.5, the c/a ratio increases.

Increasing the temperature not only changes the crystal orientation of the film but also changes the phases from mixed (cubic + hexagonal) to hexagonal (β-Nb_2N and δ'-NbN). When the substrate temperature reaches 650 °C, the cubic δ-NbN phase is detected with (111), (200), and (220) reflections at the initial growth NbN_x films. Treece et al [84, 85] pointed out that NbN_x films grown on MgO (100) by PLD acquire a metastable primitive cubic (PC) NbN_x. The metastable PC NbN_x phase is stabilized on MgO (100) and can be transformed to δ-NbN cubic phase by annealing of the sample. The δ-NbN cubic phase is observed in the range of 450 to 850 °C substrate temperature. In this case,

the cubic phase was formed in the higher than the suggested temperature range of PLD deposition conditions due to the different substrate material.
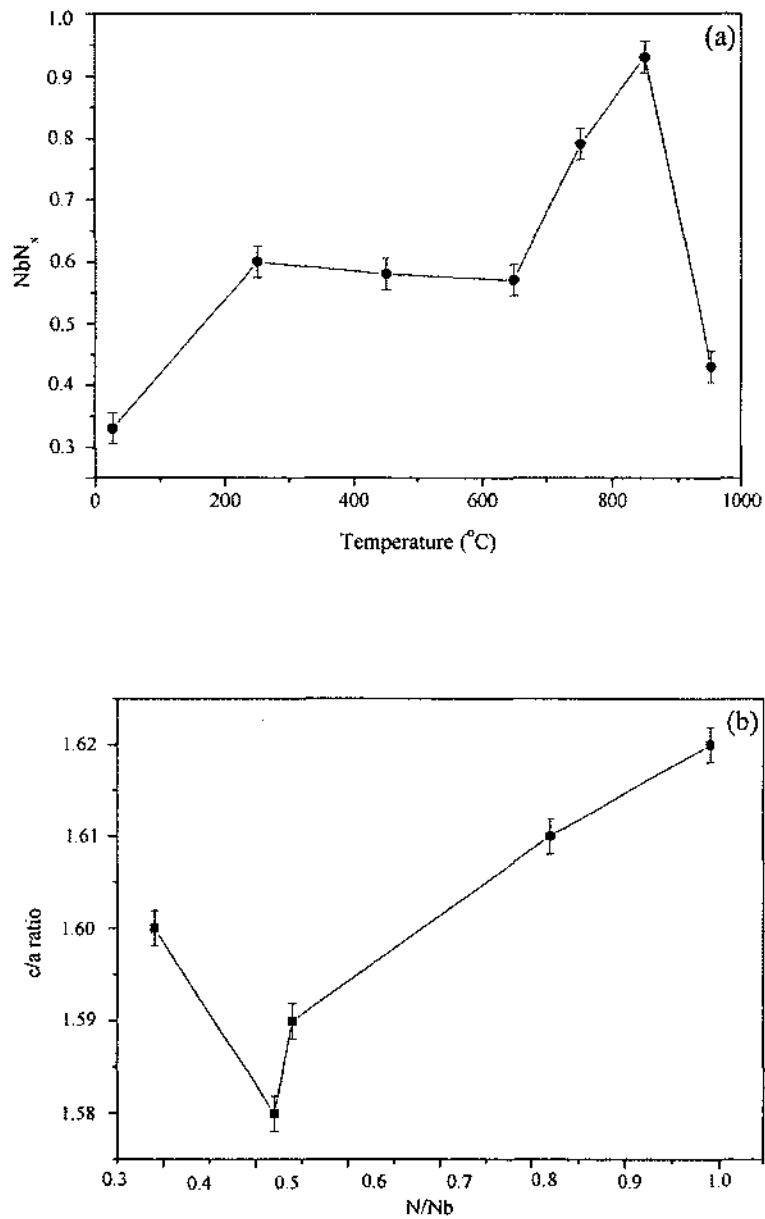
Fig. V.18. (a) Stoichiometric coefficient x in NbN_x films as a function of deposition temperature. (b) The lattice parameter c/a ratio of the hexagonal β-NbN_2. The drawn lines are to guide the eye.

V.3.3.2. TEXTURE COEFFICIENT

The texture factor of the δ-NbN phase is defined as the integrated intensity of an XRD peak relative to the integrated intensity of all peaks. Calculated texture factors were listed for the three peaks of the δ-NbN phase in Table V.4. It can be seen that the texture changes from a strong (200) orientation to a dominant (220) orientation, followed by an (111) orientation as the substrate temperature was increased from 450 to 750 °C. For δ-NbN cubic phase, the film deposited at 650 °C has a strong preferential (2 2 0) orientation, while the 750 °C sample shows (111) preferred crystallographic orientation.

The hexagonal phase concentration was calculated as the ratio of the sum of the intensities of the β hexagonal XRD peaks divided by the total intensities of all (β+δ+δ′) peaks. The effect of deposition temperature on the concentration of β hexagonal phase in the film is shown in Fig. V.19(a). When the deposition temperature is increased to 850 and 950 °C, the peaks from the δ-NbN phase in the XRD diffraction patterns disappear. The phase composition of the film was changed from a mixed phase to a hexagonal phase with mainly β-Nb$_2$N structure due to the decrease of nitrogen content of the NbN$_x$ films. A mainly hexagonal β-Nb$_2$N phase with a predominant (110) texture and some trace of δ′-NbN phase exists in the NbN$_x$ film deposited at 950 °C. For crystalline samples at high temperatures, the δ-NbN becomes unstable [177]. When NbN$_x$ films were subsequently annealed at about 1000 °C in UHV, a decrease of the nitrogen content in the NbN$_x$ films was observed (not shown here). This is in good agreement with results obtained by other studies on the effect of annealing temperature on nitrogen content in NbN$_x$ films [178].
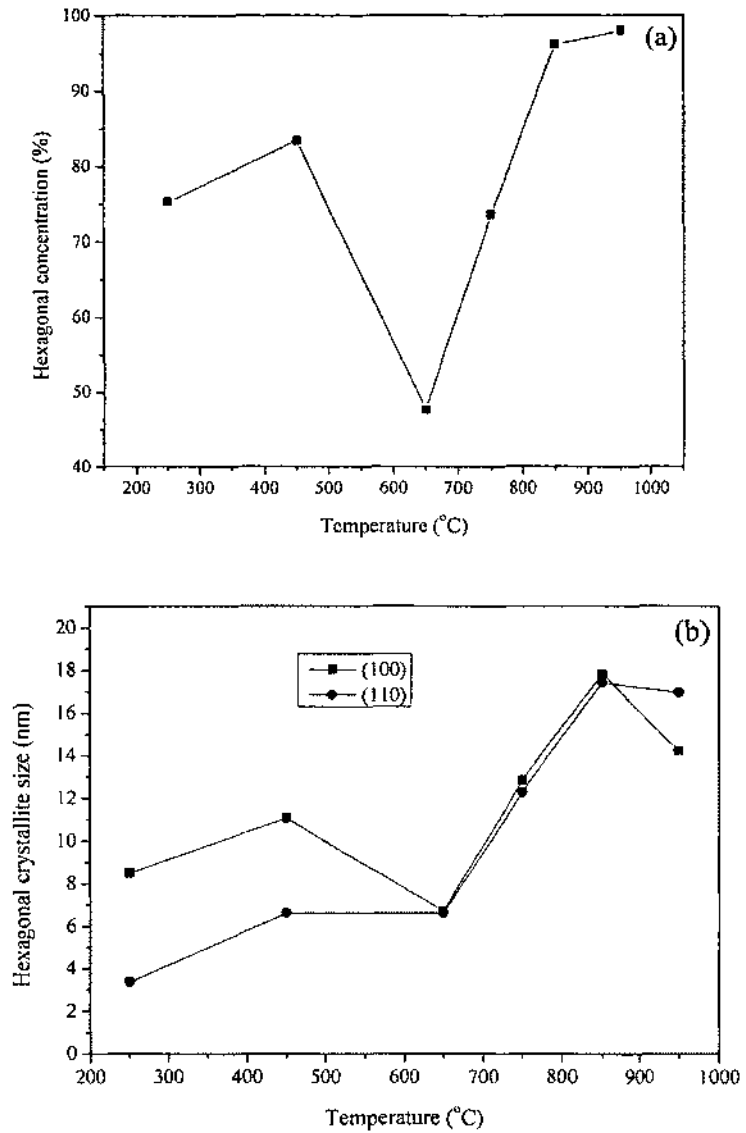
Fig. V.19. (a) Influence of the deposition temperature on (a) Concentration of the β-Nb₂N hexagonal phase. (b) The hexagonal crystallite size. The drawn lines guide the eye.

Table V.4. Texture factor of the cubic phase in NbN$_x$ films.

T$_{substrate}$ (°C)	I$_{111}$/I$_{total}$	I$_{200}$/I$_{total}$	I$_{220}$/I$_{total}$
450	NA	0.14	NA
650	0.20	0.21	0.28
750	0.24	0.19	0.14
850	NA	0.09	NA

The mean hexagonal crystallite sizes are determined from the XRD patterns for two crystallographic orientations of β-Nb_2N phase ((100) and (110)) as a function of substrate temperatures and plotted in Fig. V.19(b). The size of the crystallites ranges from 3 to 18 nm. It should be noted that the hexagonal crystallite sizes initially increase with temperature and then decrease at 650 °C as the cubic phase appears, then increase again with further increase in the deposition temperature. This increase of crystallite size is due to increased solid-state and surface diffusion coefficients with temperature [179]. A small decrease of crystallite size was observed in the film deposited at 950 °C due to phase change and loss of nitrogen in the film. The error bars in Fig. V.19(b) represent the standard deviation in calculating the hexagonal crystallite size from the XRD peaks of the same phase for different diffraction peaks.

V.3.3.3. SURFACE MORPHOLOGY

The influence of substrate temperature on the microstructures and surface properties of the films are investigated by AFM. Fig. V.20 shows topographic AFM images of NbN_x films deposited at different substrate temperatures. The AFM images consist of irregular submicron-sized features for the sample deposited at 450 °C, as shown in Fig. V.20(a).

When the substrate temperature is increased to 650 °C, very dense and almost uniform in height islands are visible in Fig. V.20(b). These islands show an increase in their average height and decrease in their density. A regular array of islands is observed as the temperature is increased to 750 °C, as shown in Fig. V.20(c). Once the temperature increased to 850 °C, low density micron-sized islands were observed. The AFM image for this condition reveals better crystalline structure and more uniform size distribution.

The root mean square values (RMS) of the surface roughness were obtained from AFM

images using Nanoscope V5.31r1 software.
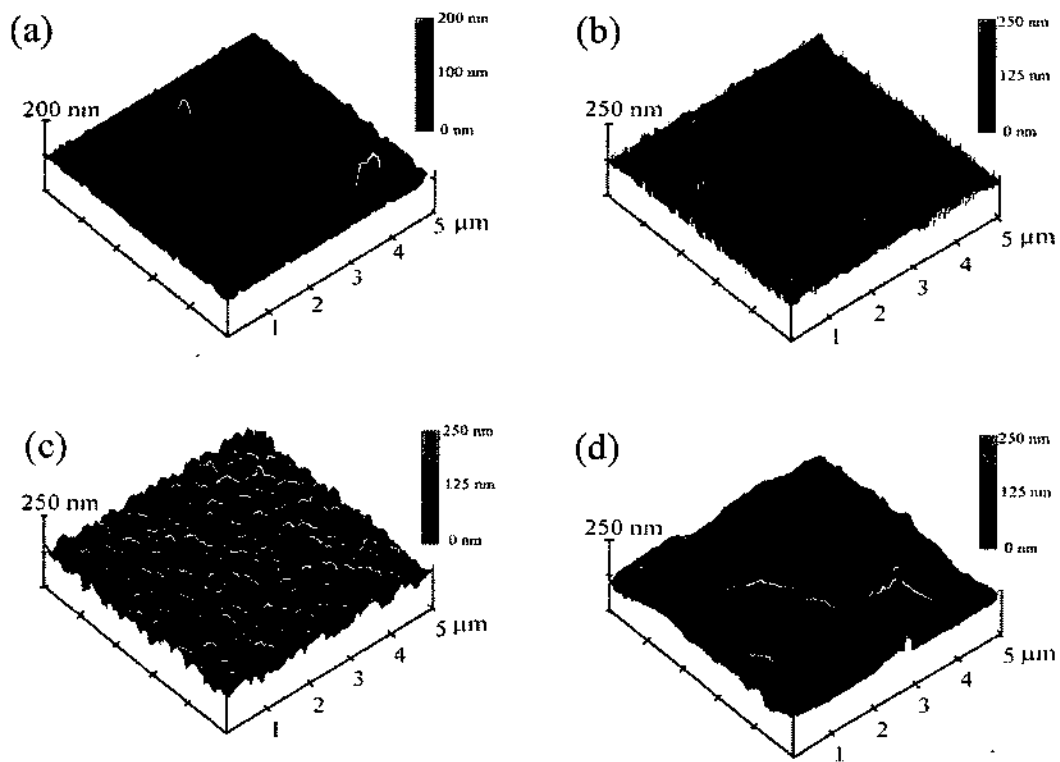
Fig. V.20. Topographic AFM images of films grown at (a) 450, (b) 650, (c) 750, and (d) 850 °C.
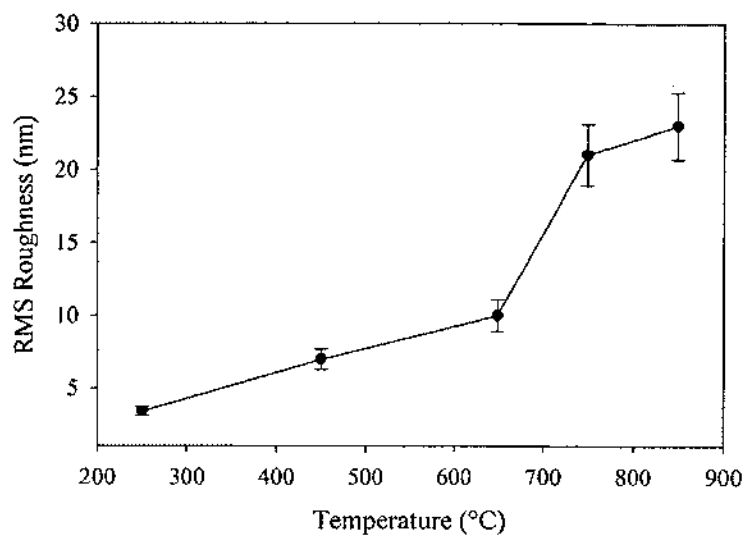
Fig. V.21. Surface roughness of NbN_x films.
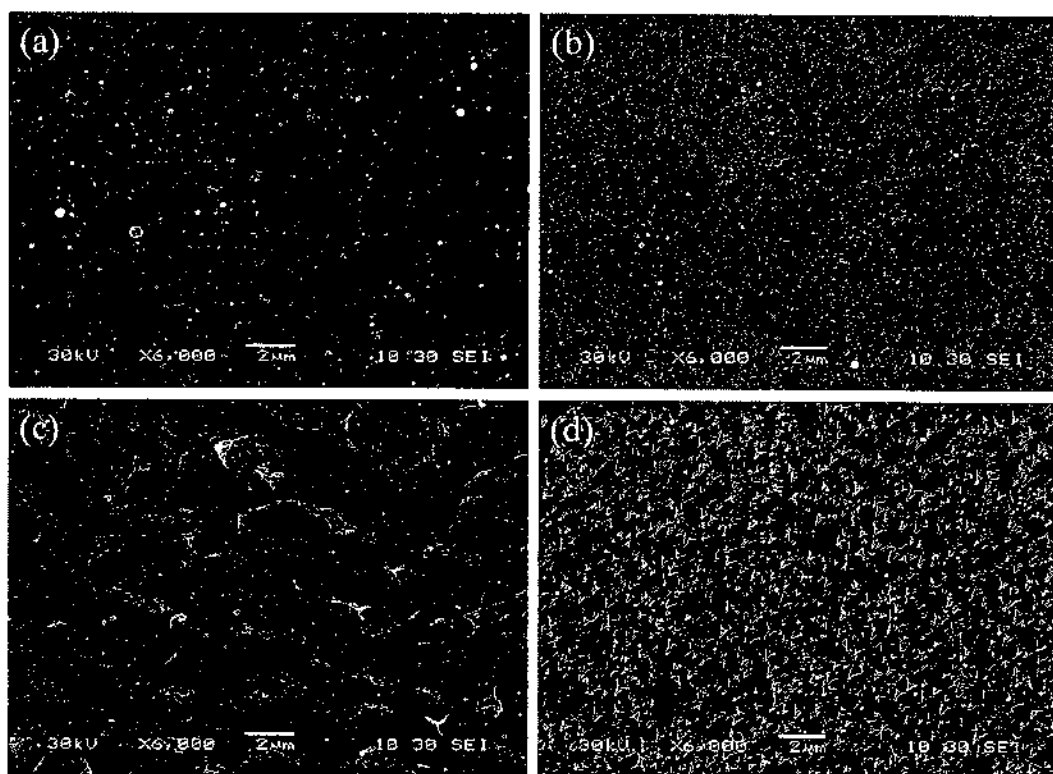
Fig. V.22. SEM images of the NbN_x films deposited at different substrate temperatures (a) 450, (b) 650, (c) 750, and (d) 850 °C.

Fig. V.21 shows the RMS roughness of NbN_x films as a function of substrate temperature. The error bars represent variations in RMS roughness in line scans from three different AFM images with same area. The RMS roughness of the film increased as the substrate temperature is increased. At substrate temperature of 450 °C, the RMS value is ~7 nm. When the temperature was increased to 650 °C, then to 750 °C, and finally to 850 °C, RMS values increased to 10, 21, and 23 nm, respectively. This is consistent with the results for the crystallite sizes that were obtained from XRD. The smaller the crystallite sizes the smother the surface. This is consistent with the results for the crystallite sizes that were obtained from the XRD that range from 3 to 18 nm. The smaller the crystallite sizes, the smoother the surface obtained in the film. Fig. V.22 shows SEM images for films grown at different substrate temperatures. As shown in Fig. V.22 (a)–(d), the same behaviors observed by AFM are confirmed by SEM images for films grown on substrates with temperatures that range from 450 to 850 °C.

V.4. CONCLUSIONS

V.4.1. LASER FLUENCE EFFECT

Pulsed laser deposition of NbN_x thin films on niobium substrate was carried out at different laser fluences. Detailed analyses of the texture and surface morphology of polycrystalline films were presented. The experimental results showed that the NbN_x film N/Nb ratio in NbN_x films increase with increasing laser fluence. The crystallite size of the deposited NbN_x films was calculated from the XRD spectra using Scherrer's formula. Increasing the laser fluence resulted in smoother films with larger grain size. The texture coefficient ratio calculations for β-Nb_2N phase showed that the preferred orientation of the deposited NbN_x films is (110).

V.4.2. BACKGROUND PRESSURE INFLUENCE

NbN_x thin films were prepared on Nb substrate by PLD at different gas pressure. The nitrogen pressure affects film composition and phase. A phase transition from hexagonal to mixed, then a single hexagonal phase occurred as the nitrogen gas pressure was increased from 10.7 to 66.7 Pa. The nitrogen pressure affected the ratio of the cubic-to-hexagonal phase. The present results indicate that the most favorable nitrogen background pressure for the formation of NbN_x with single β-Nb_2N phase by PLD is 66.7 Pa at 600 °C.

V.4.3. SUBSTRATE TEMPERATURE INFLUENCE

Niobium nitride thin films were grown by PLD on niobium substrate at different temperatures. The substrate temperature during deposition of NbN_x thin films on Nb significantly affects the phase, morphologies and crystallinity of the films. NbN_x film with highest concentration of β-Nb_2N hexagonal phase was obtained for substrate temperatures above 850 °C. A systematic increase in lattice parameters with substrate deposition temperature along with an increase in the size of the grains was observed. The cubic phase of NbN_x was formed for deposition at 650 °C and 750 °C, although it was mixed with the hexagonal phase. The atomic ratio of nitrogen in the film depends on the substrate temperature. The highest N/Nb = 0.93 ratio was obtained at deposition temperature of 850 °C, at which the highest lattice constant ratio of β phase (c/a) was obtained. XRD and AFM results showed that the crystallite sizes and surface roughness of the NbN_x films increased as the substrate temperature was increased.

CHAPTER VI

PROPERTIES OF NIOBIUM NITRIDES PREPARED BY REACTIVE THERMAL DIFFUSION

VI.1. INTRODUCTION

The phase diagram of the Nb–N system is very complex and several phases of NbN_x exist upon variation in the nitrogen-to-niobium atomic ratio x, which also affects the concentrations of nitrogen and niobium vacancies. From previous studies on the phase diagram of the NbN_x system [3, 91, 148, 180], the stable NbN_x phases are classified as: solid solution, basic Nb with nitrogen solid solution (bcc) α-Nb(N), (x<0.40); hexagonal (W_2C type) β-Nb_2N_x, (0.75<x<1.1); tetragonal (distorted NaCl type) γ-NbN_x (0.72< x < 0.84); cubic (NaCl type) δ-NbN, 0.72 < x < 1.06); hexagonal (anti-WC type) ϵ-NbN_x, 0.95 < x <1.0; hexagonal (TiP type) η-NbN_x, 0.92< x <1; and hexagonal (anti-NiAs type) δ'-NbN_x 0.95< x <0.98. Some of NbN_x phases show superconducting properties in the range of 9–17 K depending on their crystal structure. The cubic δ-NbN phase with highest T_c = 17.3 K makes it of great interest for many superconductor applications [181, 182].

Different methods are used to grow NbN_x films. One technique to obtain a thin NbN_x layer on Nb is by heating Nb at high temperature in nitrogen gas. Niobium is very reactive with nitrogen at high temperatures ($\geq$900 °C); therefore, NbN_x samples can be prepared in nitrogen atmosphere by heating the Nb substrate [3, 22, 89, 183]. This method of heating in a reactive gas atmosphere was used to study the phase diagram of

NbN_x [3, 4, 11, 91]. NbN_x showed non-stoichiometry and phase change with increasing nitrogen content [11, 91].

As mentioned before, nitriding the surface of Nb improves the mechanical properties of the surface by increasing hardness and wear resistance. New generation accelerators employ superconducting Nb radio frequency (RF) cavities to achieve the highest accelerating field. Hydrogen diffusion in Nb can adversely affect the performance of the superconducting RF cavity. A high-quality NbN_x coating on Nb increases hardness of the surface and also provides a barrier layer for hydrogen diffusion into Nb for potential application of RF cavities. Lengauer *et al.* [11] studied high-temperature nitridation of Nb heated in high-purity nitrogen of various pressures, times, and temperatures (below 1400 °C). Phase transformations of γ-Nb_4N_3 to δ-NbN and η-NbN to δ-NbN were observed at a temperature of 1070 and 1300 °C, respectively. These phase transformations were not observed in powder samples of NbN_x. The choice of nitrogen pressure considerably affects growth rate and homogeneity ranges of NbN_x phases [91]. Most of the work performed on thermal nitridation of Nb was focused on the study of the equilibrium phases and structural properties of the formed NbN_x layer but not much work dealt with electronic properties.

One motivation for this work was to grow a hard, conformal nitride coating on the sealing surface of niobium superconducting cavities. These cavities must be heated to over 1000 °C in vacuum, which results in softening of the seals made by tightening the Nb flanges with a gasket between them. Having these seal areas hardened by growing a thin layer of the hexagonal β-Nb_2N at mechanically weak areas would result in better mechanical stability of the superconducting niobium cavity and a more durable seal. In

the first part of this chapter, the goal was to obtain single hexagonal phase of NbN_x and investigate the structural, electronic, and mechanical properties of the surface layers prepared by thermal diffusion of nitrogen at different processing times. The formation of different NbN_x phases at various processing times and the effect of the processing time on the morphology, crystal structure, and electronic property were studied. For this part of the work, NbN_x was obtained at different processing times by heating Nb at 900 °C temperature under the same nitrogen background pressure (133 Pa). The nitrogen content in the NbN_x layers was found to increase with the processing time. These results are interpreted in view of crystal, surface, electronic, and chemical analyses.

The second part is an interest in obtaining an α-NbN solid solution phase by doing experiments at lower nitrogen pressure (as low as 1.0×10^{-3} Pa) and higher temperature (as high as 1500 °C) than previously reported. Not much work dealt with the mechanical and structural properties. In the present work, a series of experiments were performed to investigate formation of NbN_x layers on Nb at different heating temperatures and nitrogen pressures using the thermal diffusion method. The formation of different phases at various nitrogen pressures and their influence on the morphology and crystal structure were studied.

VI.2. EXPERIMENTAL SETUP

For the first part of the experiments, Nb substrates ($8.6 \times 6.6 \times 0.7$ mm^3) cut by wire electro-discharge machining from an Nb slice of ingot "H" from the company CBMM, Brazil, were used. The Nb slice from the ingot has large grains (several cm^2 areas); therefore, the samples were either single crystals or had a single grain boundary. For the second part, Nb ($8 \times 3 \times 0.2$ mm^3) and ($8.6 \times 6.6 \times 0.7$ mm^3) substrates were

used. The samples were etched by the buffered chemical polishing (BCP) method [156]. Approximately a 50 micron layer of material was removed by BCP that resulted in Nb substrates with 0.6 nm root-mean square (RMS) roughness for 2×2 μm^2 scan area, as determined by atomic force microscope (AFM). Before starting the nitridation of samples of the first part, the substrates were degassed for two hours at 900 ± 20 °C in the experimental chamber at a base pressure of 6.6×10^{-6} Pa. The background pressure of the nitrogen gas was controlled by a leak valve and measured with a convectron gauge. The nitrogen operating pressure was achieved by filling the vacuum chamber with N_2 gas and keeping constant during samples' heating time. For all samples, it takes about 20–30 sec to reach the desired nitrogen pressure. The temperature of the samples was measured using the optical pyrometer through a quartz window and controlled by current-voltage values applied to the heater wires. The first part is for thick samples done at different processing times, same nitrogen pressure of 133 Pa, and same substrate at a temperature of 900 ± 20 °C were heated using a ceramic heater, as shown in Appendix A.

For the second part, two types of heaters were used. Tungsten wire heater- baskets were used for sample heating of the thin samples and thick samples were used in the second part. A Type I heater with single tungsten wire baskets (ID 0.35 inches diameter = 0.03 inches, part # 74-1 from Ted Pella Inc.) was used. The second type is a 1" diameter heater manufactured by HeatWave Labs, Inc. The current was adjusted on the sample heaters to get the highest substrate temperature. The heat nitridation for the thin samples was done at different nitrogen pressures in the range 1.0×10^{-3} to 33.3 Pa and temperatures ranging from 1250–1500 °C. For thick samples, the maximum temperature that could be reached by Type I heater is 1150 °C. The samples were done at a processing time of 180

min. A Type II heater was used to heat Nb (0.7 mm thick) at 1000 °C , 0.66 Pa at

different heating times (10–60 min), and in a vacuum of 1.3 x10^{-5} Pa at 1000 °C. As

processing time is achieved, the UHV valve is opened to allow a pump down with turbo

plus mechanical pumps (it takes 10-15 sec). Then, sample must cool down for 1–1.5 hour

in a vacuum of 1.0x10^{-5} Pa.

XRD measurements were done using the Bruker-AXS three-circle diffractometer.

A Bruker SMART APEX II instrument is equipped with graphite-monochromated CuK_α

radiation and a SMART Apex II CCD detector. X-ray source of wavelength of 1.5406 Å

(Cu-Kα line) is fixed, and both the charge coupled device (CCD) detector (2θ) and

sample (ω) are movable. The detector (2θ) covers about 30° per image position. Three

image positions were used for the experiment. In each case, the angle 2θ is the center

position of the 30° CCD image, and each value is set so that the angles of incidence and

diffraction are equal. The chemical composition of the samples was determined by

electron probe micro analyzer (EPMA) point scan using a Cameca SX100.

A JEOL JSM-6060 LV SEM and a Digital Instruments Dimension 3100 AFM

were employed to study surface morphologies of the NbN_x. All AFM images were taken

in the air using a tapping mode. SEM images were taken at an accelerating voltage of 20

kV. X-ray photoelectron spectroscopy (XPS) and ultraviolet photoemission spectroscopy

(UPS) analyses were performed by Drs. Y. Ufuktepe and S. Kimura at the UVSOR

facility, Institute for Molecular Science, Japan, on the 100-mm radius hemispherical

photoelectron analyzer (VG Scienta SES-100) with Mg Kα X-ray radiation (hυ= 1253.6

eV) and an He discharge lamp as a source for UV radiation, which provides two narrow

lines at 21.2 eV (He I) and 40.8 eV (He II). All the results presented in this work were

obtained with He II. The base pressure of the photoemission chamber was better than 2.0×10^{-8} Pa. Surface cleaning of the samples was performed at room temperature by using Ar^+ ions sputtering in the preparation chamber. The energy scale of X-ray photoemission spectrum was calibrated by the binding energy of Au 4f level. The NbN_x were obtained by diffusion of nitrogen into the bulk niobium metal sheet.

The nanomechanical properties were measured by Md. Mamun and Dr A. Elmsutafa at ODU`s Applied Research Center, using the continuous stiffness measurement (CSM) technique of the Nanoindenter XP from Agilent. CSM technique enables the hardness and the elastic modulus to be continuously measured as a function of penetration depth as detailed elsewhere [184, 185]. Prior to measurement, the nanoindenter was calibrated using a three-sided diamond Berkovick tip on fused silica calibration standards. Each sample was tested at ten different locations using the same test parameters. The indenter penetrated the surface with a harmonic displacement oscillation target of 1nm at a frequency of 45 Hz to a depth of 1 μm with a strain rate of 0.05 per second. The effect of different heating times on the grown NbN_x by heating is reported. The nitrogen content in the NbN_x layers was found to increase with the processing time. These results are interpreted in view of crystal, surface, electronic and chemical structure analyses.

X-ray absorption near edge structure (XANES) measurements were performed on beamline 8.2 at Stanford Synchrotron Radiation Lightsource in the SLAC National Accelerator Laboratory. The total electron yield (TEY) mode was used for XANES measurements by measuring sample current. Current measurements were done using low noise preamplifier Stanford research system low noise preamplifier Model SR570. The

beam flux (I_0) signal from a gold grid was used to normalize the spectra. The chamber base pressure during the experiment was about 2.0×10^{-7} Pa.

VI.3. RESULTS AND DISCUSSION

VI.3.1. DIFFERENT PROCESSING TIMES

VI.3.1.1. STRUCTURE AND PHASE COMPOSITION

Results on Nb $8.6 \times 6.6 \times 0.7$ mm^3 samples are first discussed. Fig. VI.1 shows XRD patterns of NbN$_x$ samples in the same nitrogen background pressure (133 Pa) and substrate temperature of (900 °C) at different processing times (5–80 min). The formation of nitrides was observed, even though the sample was heated for a short time of five min. XRD of NbN$_x$ peaks in samples are attributed to β-Nb$_2$N hexagonal phase with (100), (002), (102), (110), (103), (112) and (201) orientations in 2-theta range 30-80 ° [159]. The intensity of the β-Nb$_2$N phase XRD peaks shows systematic increases as processing time increases. This improvement of the peaks is due to increasing the nitride thickness with the processing time. Also, it is observed from Fig. VI.1 that the XRD peak of β-Nb2N at (110) shows the highest intensity relative to other peaks for all samples. This is confirming that the β-Nb$_2$N phase in the samples is predominantly orientated in the (110) direction. The formation of these oriented β-Nb$_2$N crystals depends greatly on the crystallographic planes of the Nb substrate, as shown in Fig. VI.1. XRD peaks of Nb are predominantly orientated in the (110) direction. The change in the X-ray diffraction intensity, which is related to the integrated area under the peak, is shown as a function of time in Fig. VI.2. It is well known that the diffraction peak area is proportional to the mass of the material, which indicates an increase in thickness of the NbN$_x$ as a function

of time. The increased XRD intensity is due to thickness increase with the processing time and not an increase in density, as confirmed below by nitride thickness measurements using nanoindentation. Crystallite size calculations were done based on the Scherrer relation of the broadening of the XRD peak in a diffraction pattern. As seen in Fig. VI.1, there are systematic decreases in the width of the peak (FWHM) as time of heating increases. The narrower the diffraction peak, the larger the crystallite size. Fig. VI.3 shows that increasing the processing time enhances the crystallite size of the NbN_x layer from 17.5 to 19.2 nm. The error bars of the crystallite size are standard deviations calculated from data at different orientations.
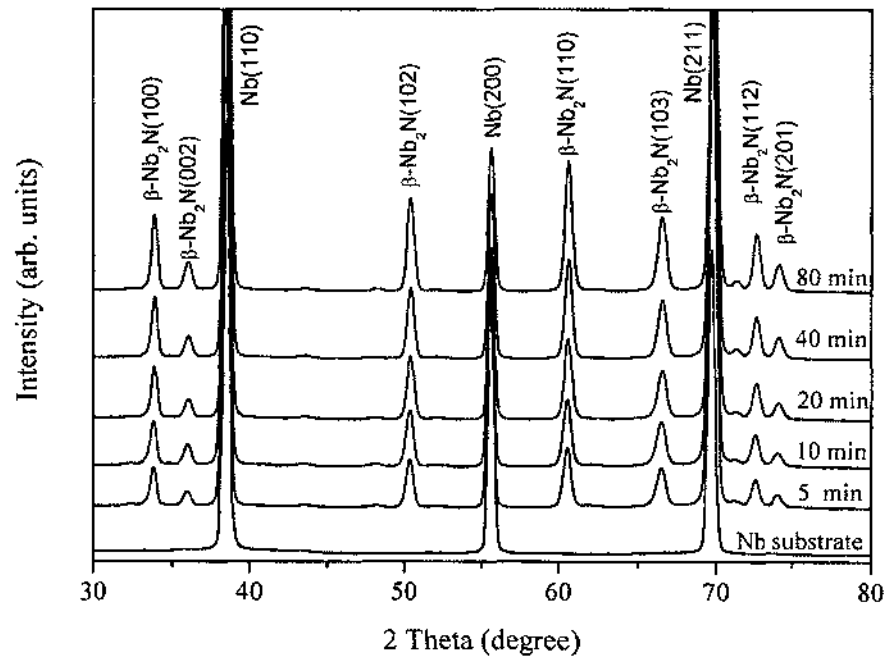
Fig. VI.1. X-ray diffraction patterns of NbN_x produced in different times by thermal processing at 900 °C.
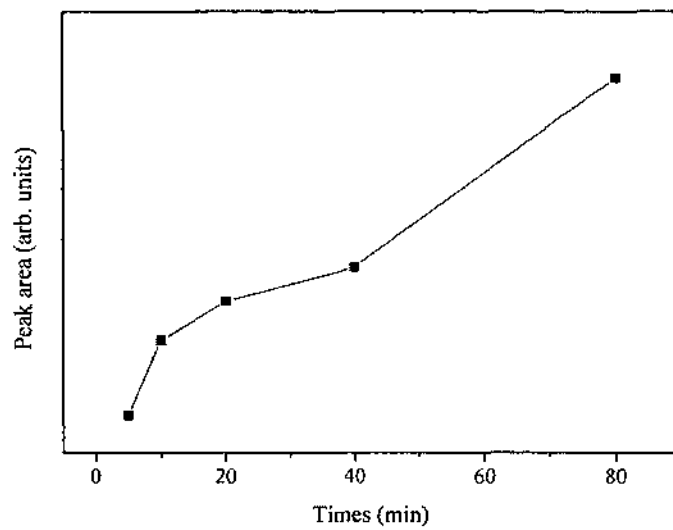
Fig. VI.2. XRD integrated intensity under the (110) peak as a function of time.
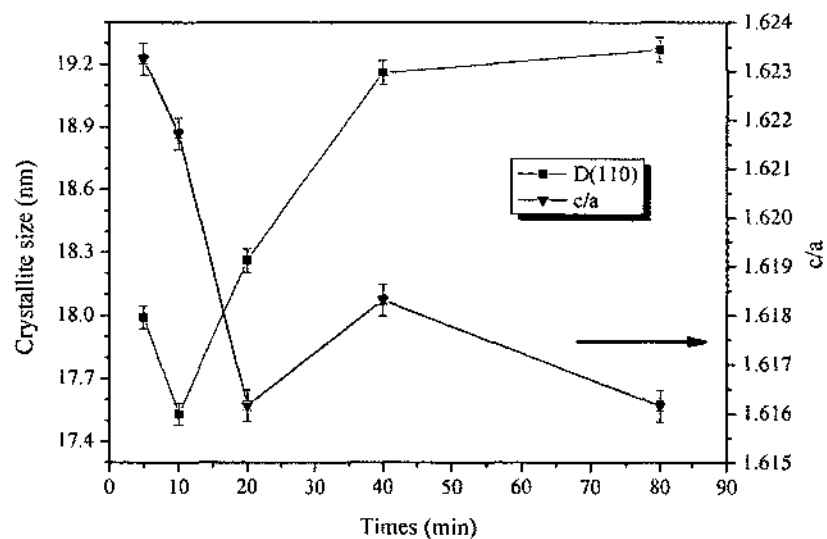
Fig. VI.3. The mean hexagonal crystallite size of (110) and lattice parameter (*c/a* ratio) of the hexagonal β-NbN₂ as a function of time. The drawn lines serve only to guide the eye.

The variation of the lattice parameter (c/a ratio) of the hexagonal β–Nb_2N is also shown in Fig. VI.3, and this is related to the N/Nb ratio in the NbN_x. The c/a ratio is initially increased as the processing time increased. However, after five min of processing, the c/a ratio decreases with increasing processing time. It is reported that decreases in lattice parameter of δ-NbN occurs as the results of a decrease in the number of metal vacancies in the samples, while maximal lattice parameter is achieved at smallest amount of nitrogen vacancies [186]. The decrease in c/a ratio here is due to the decrease in the amount of Nb vacancies as time increases and is in good agreement with nitrogen content observed in the samples by EPMA.
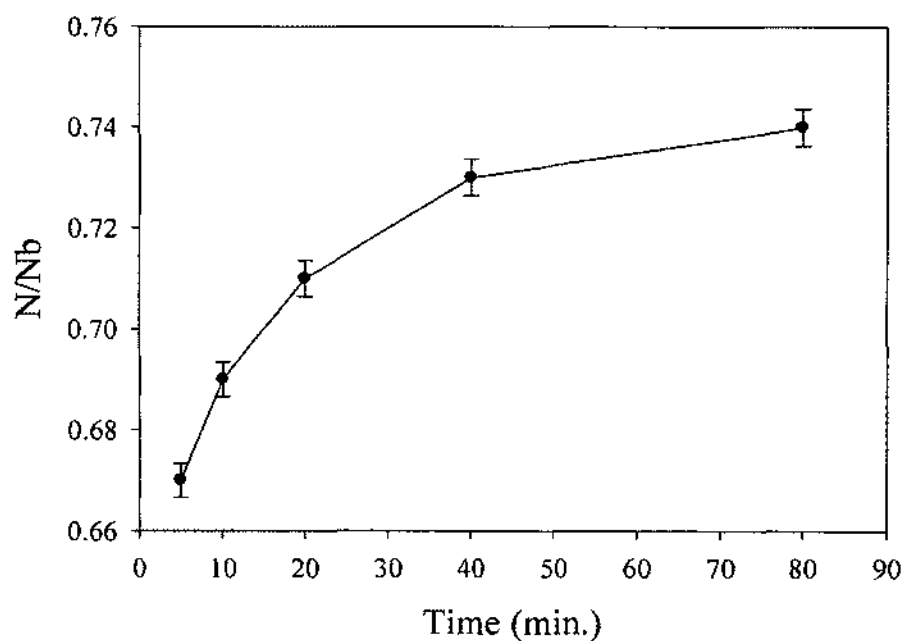
Fig. VI.4. EPMA measurement of N/Nb ratio in the NbN_x as a function of processing time.

The nitrogen content in the NbN_x layer was obtained by EPMA. Fig. VI.4 shows the variation of the N/Nb ratio with heating time. The N/Nb ratio in the hexagonal β-Nb_2N phase was determined to be between 0.67 ± 0.03 and 0.74 ± 0.03, which is in agreement with the phase diagram of the Nb-N system [3, 181]. The error bars in Fig. VI.4 represent the values of the standard deviation for analyses of five different points done on each sample. The N/Nb ratio in the NbN_x layer increases with the processing time.

Surface morphologies were studied using AFM and SEM measurements. Fig. VI.5 shows AFM images of NbN_x grown at different processing times. The surface morphology of NbN_x sample shows grains of random shapes. Fig. VI.6 shows SEM of NbN_x samples at different processing times. As shown from these images, triangular submicron-sized islands are present. The shapes and sizes of these islands did not show much change with the increasing times of processing. It should be noted here that AFM images show the grain size while XRD gives the crystallite size, and these can be different. A comparison of the root-mean square surface roughness (RMS) as a function of processing time is shown in Fig. VI.5(f). The RMS was obtained by performing line scans taken diagonally of the AFM images ($2\mu m \times 2\mu m$) using the Nanoscope V5.31r1 imaging software. The RMS value of surface roughness sharply increases with time from 35 nm at 5 min to 59 nm at 10 min and then stays around the same values of 52–56 nm with further increase in processing time.
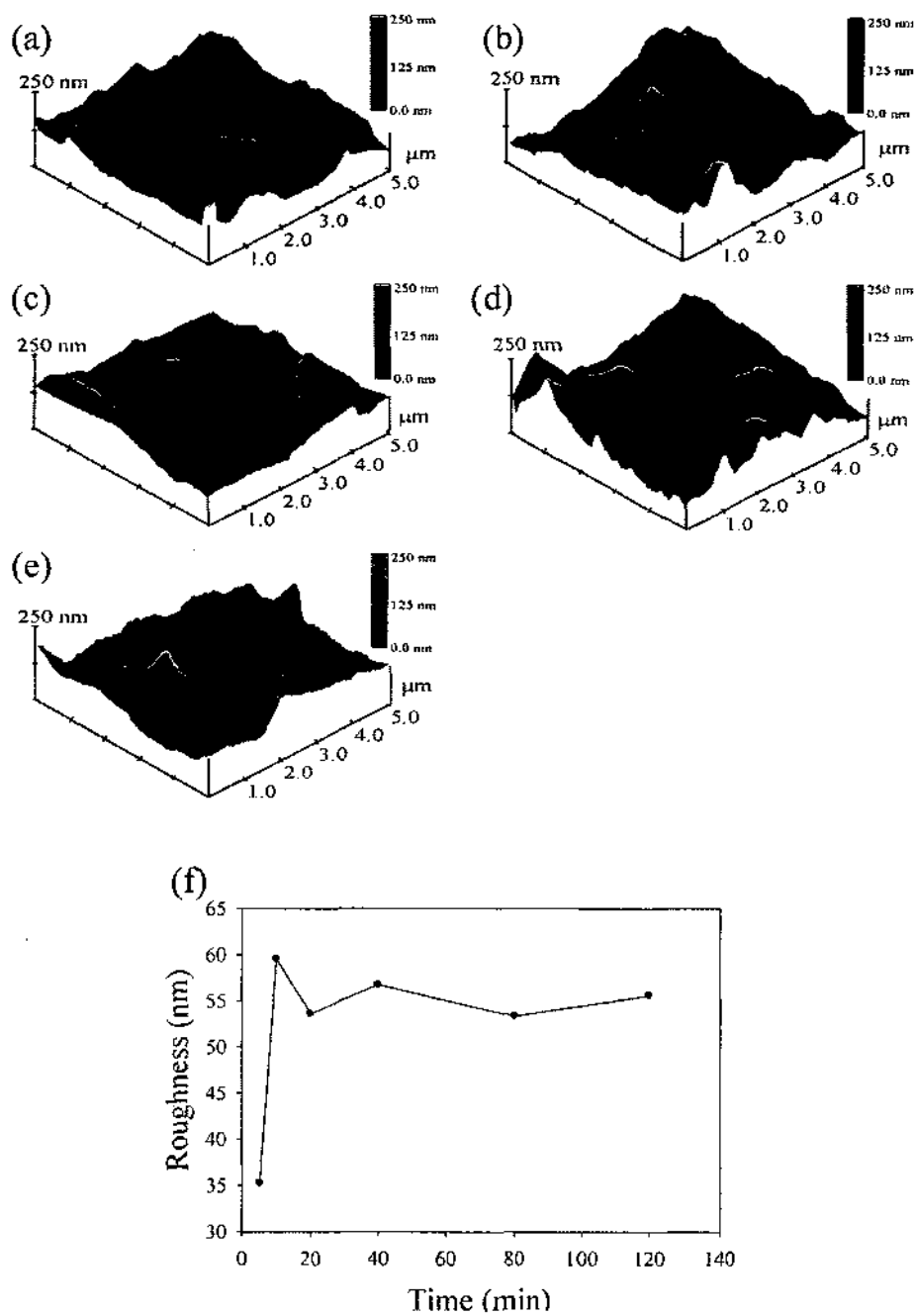
Fig. VI.5. Topographic AFM images (5μmx5μm) of the NbN$_x$ produced at different processing times. All were done in the same nitrogen pressure of 133 Pa (a) 5 min, (b) 10 min, (c) 20 min, (d) 40 min, (e) 80 min, and (f) the RMS surface roughness versus processing time.
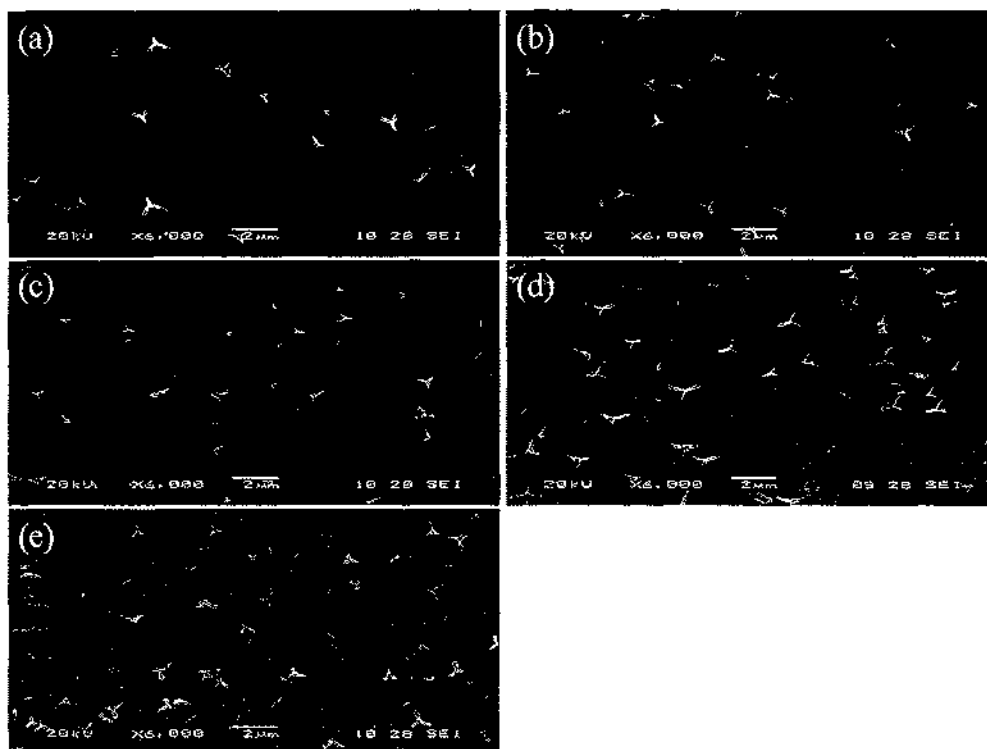
Fig. VI.6. SEM images (X6, 000) of the NbN$_x$ produced in different processing times (a) 5 min, (b) 10 min, (c) 20 min, (d) 40 min, and (e) 80 min. All were done in the same nitrogen pressure of 133 Pa nitrogen pressures and temperature of 900 °C.

The increase in the surface roughness is expected for samples processed for a long time since a longer heating time is more favorable for the formation of larger faceted islands due to atom migration by diffusion Fig. VI.6(e). It is clearly observed that heating of the Nb sample at 900 °C in 133 Pa nitrogen gas pressure causes an increase of surface roughness as NbN$_x$ develops on the surface. The SEM images confirm the same behavior as that observed in AFM images. The SEM analyses indicate that the grains are composed of small crystallites, as shown in Fig. VI.6.

VI.3.1.2. ELECTRONIC STRUCTURE

An X-ray photoelectron spectroscopy was conducted by Drs. Y. Ufuktepe and S. Kimura at the UVSOR facility, Institute for Molecular Science, Japan, for surface characterization of the NbN_x layer. Fig. VI.7 shows XPS spectra of Nb $3d$ core levels for NbN_x grown for various processing times at 900 °C in 133 Pa background nitrogen pressure. Binding energies are given with respect to the Fermi level. The corresponding peak positions are summarized in Table VI.1. Comparing the binding energy of NbN_x with that obtained from pure Nb spectra (205.5 and 202.3 eV), it appears that Nb $3d_{3/2}$ and $3d_{5/2}$ peaks are shifted to higher binding energies as a result of Nb-N bonding, indicating the transfer of electrons from niobium to nitrogen. Small binding energy differences for Nb $3d$ doublets are dependent on small variations in stoichiometry of NbN_x. Samples heated for 10, 20, and 80 min show the third peak at ~210 eV corresponding to Nb_2O_5 [187]. This suggests that these samples were contaminated by oxygen during or after deposition and exhibit a binding energy shift of $3d$ doublets toward higher energy more than the others due to oxygen bonding. The Nb $3d$ binding energies of NbN_x and NbN_xO_y agree with previous results [28, 187]. As soon as the NbN_x film is exposed to the ambient air, oxygen is quickly adsorbed by the surface. On the other hand, mechanical and chemical polishing of the Nb substrates can create roughness on the substrate surface and, thus, a rough surface provides a much larger adhesive contact area to the oxygen. Different roughness of the Nb substrates might be the possible reason of different oxygen contributions in the spectra.
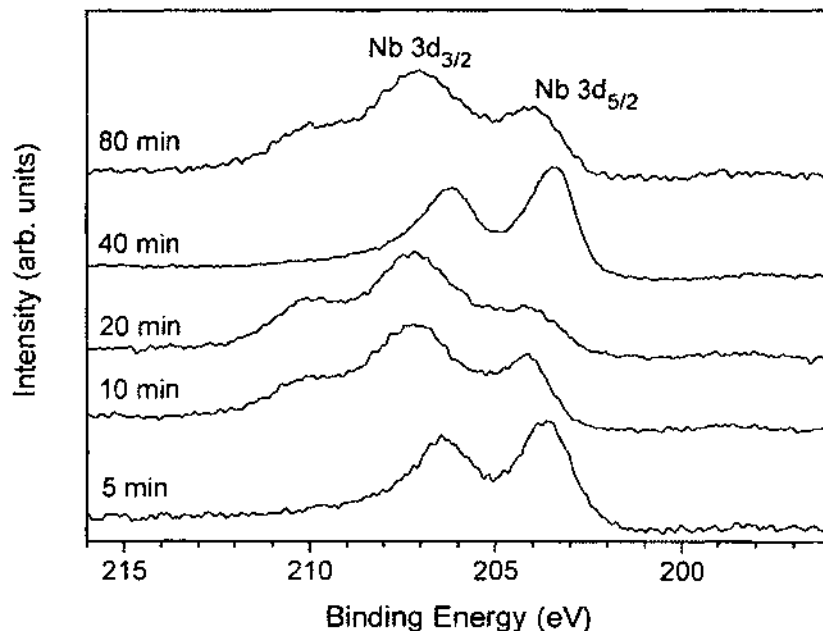
Fig. VI.7. Nb $3d$ XPS spectra of NbN_x surface layer produced for various processing times. All samples were heated in a nitrogen pressure of 133 Pa and temperature of 900 °C. Data were obtained and analyses were conducted by Drs. Y. Ufuktepe and S. Kimura at UVSOR facility, Institute for Molecular Science, Japan.

Fig. VI.8(a) and (b) show the best peak fit to spectra for samples processed for 5 and 80 min. Formation of an oxide layer on the surface of the NbN_x samples due to ex-situ XPS measurements. Studies on surface oxidation of NbN_x showed that a native oxide layer Nb_2O_5 grows on NbN_x when exposed to air [65, 144]. However, the Nb_2O_5 phase has higher binding energy than the NbN_x phases giving XPS peaks that are outside the range of Fig. V.8(a) [58, 144]. The two doublets in Fig. VI.8(a) could be attributed to the mix of the NbN_x and Nb oxynitride phase.
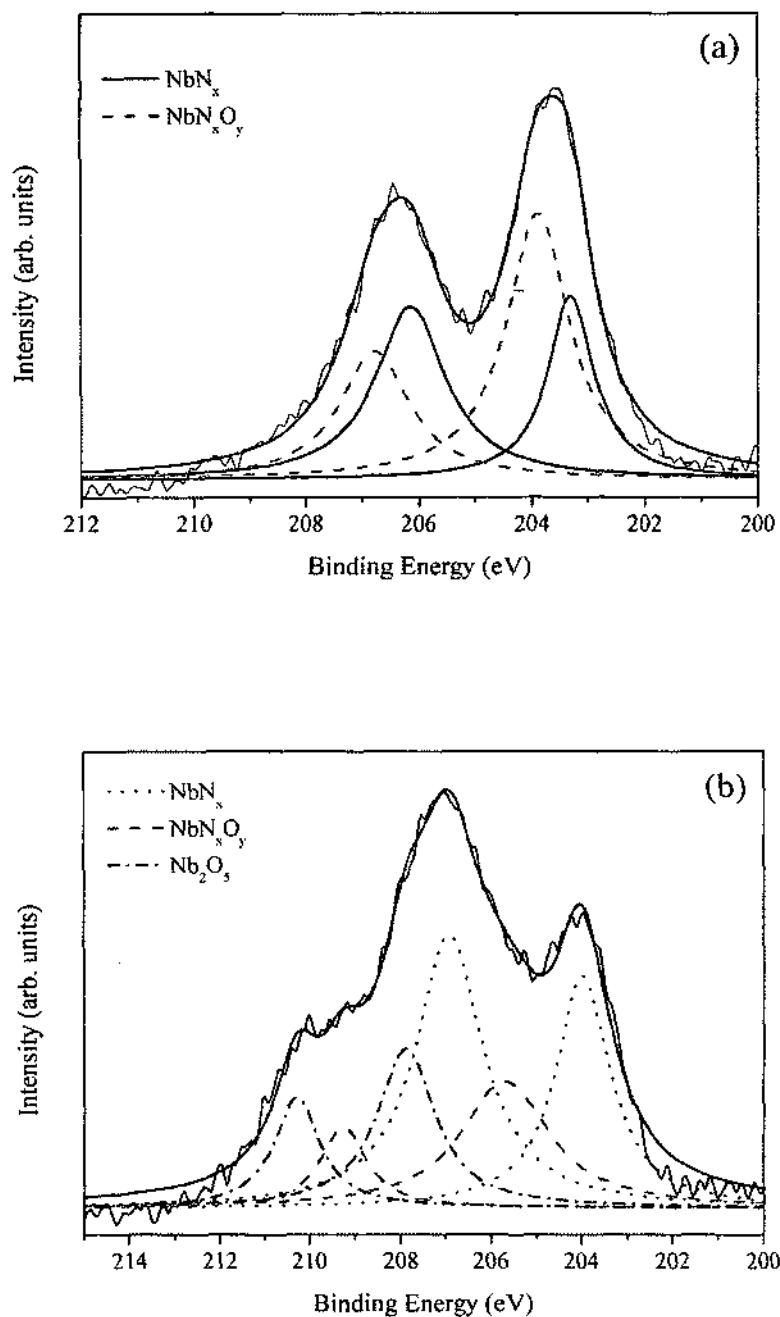
Fig. VI.8. Two representative spectra recorded from samples processed for 5 min (a) and 80 min (b). The various components used for peak fit to the spectra, the sum of which is shown by solid line. Data were obtained and analyses were conducted by Drs. Y. Ufuktepe and S. Kimura at the UVSOR facility, Institute for Molecular Science, Japan.

Table VI.1. Binding energies of Nb 3d doublets in NbN_x. Data were obtained and analyses were conducted by Drs. Y. Ufuktepe and S. Kimura at the UVSOR facility, Institute for Molecular Science, Japan.

Times (min)	Nb $3d_{5/2}$ ($\pm$ 0.05) (eV)	Nb $3d_{3/2}$ ($\pm$ 0.05) (eV)
5	203.6	206.4
10	204.1	207.1
20	204.1	207.2
40	203.4	206.1
80	203.9	207.0

The multiple peak fitting enabled us to distinguish two different contributions with different binding energies (BE); [NbN_x (BE $_{Nb\ 3d5/2}$) = 203.3 eV, full width at half maximum (FWHM) = 1.0 eV] and [NbN_xO_y ($BE_{Nb\ 3d5/2}$) = 203.9 eV, FWHM = 1.3 eV]. The binding energies and FWHM values obtained from the fitting procedure agree with literature values of a mixture of NbN_x, NbN_xO_y, and N_2O_5 [28, 58, 144]. The multiple peaks fit of Nb $3d_{5/2}$ binding energies in Fig. VI.8(b) can be resolved as a sum of three different doublets. Fig. VI.8(b) shows an additional weak shoulder is observed at ~210 eV which is due to Nb_2O_5. The best peaks fit to the measured data indicate the presence of Nb_2O_5, Nb oxynitride and NbN_x that are consistent with the previous work [28, 187]. From the peak fitting process, the higher Nb $3d_{5/2}$ binding energy doublet at 207.9 eV can be identified as Nb_2O_5, while the lowest binding energy doublet at 203.9 eV belongs to NbN_x. Finally, the third component at 205.7 eV is associated with the oxynitride NbN_xO_y [58, 187].

Fig. VI.9 shows UPS spectra of the Nb valence band (VB) obtained from the NbN_x. The UPS measurements and analyses were obtained by Drs. Y. Ufuktepe and S.

Kimura at UVSOR facility, Institute for Molecular Science, Japan. All spectra were normalized with respect to the intensity of the peak at ~6 eV below E_F. The broad region of UPS spectra from 3 to 9.5 eV is mainly due to strong hybridization between N $2p$-Nb $4d$ states. The difference spectrum was obtained by subtracting the spectrum for the sample processed for 5 min from that for the sample processed for 80 min and plotted in Fig. VI.9.
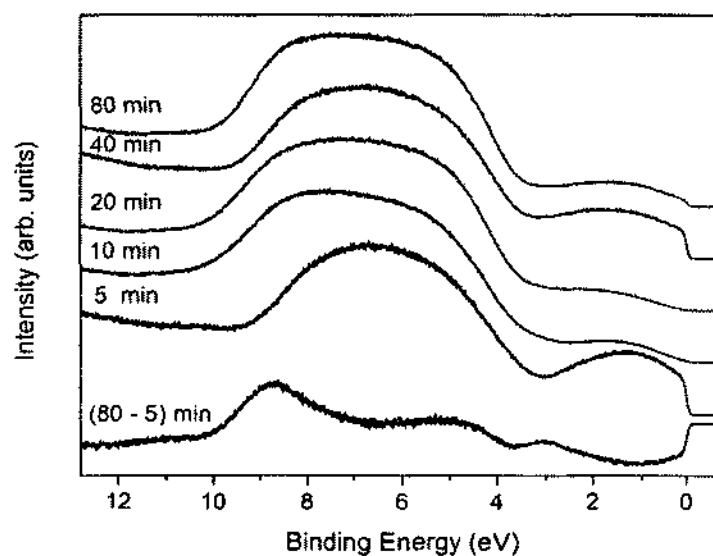
Fig. VI.9. UPS valence band spectra of NbN$_x$ deposited at 900 °C and 133 Pa nitrogen pressure for various processing times. Data were obtained and analyses were conducted by Drs. Y. Ufuktepe and S. Kimura at the UVSOR facility, Institute for Molecular Science, Japan.

The positive peak in different spectra at about 8.5 eV reflects the difference in nitrogen content. The higher nitrogen ratio in the NbN$_x$ sample heated for 80 min leads to increase in the peak intensity. At the same time, there is a negative peak centered at about

1.5 eV. It appears that the $4d$ and $5s$ states of Nb near the E_F lose intensity with the increase of nitrogen content in the film, which is consistent with the previous result [176]. Another reason for the negative peak is the presence of Nb_2O_5 and the associated d electrons from Nb $4d$ transferring to the $O-2p$ band. The valence band is dominated by two peaks centered at 6 and 1.5 eV.

In order to understand the higher intensity and broadening of the ~6 eV peak, the density of states (DOS) was calculated. DOS calculations for $\beta-Nb_2N$ and Nb_2O_5 were obtained using the density functional theory (DFT) and many-body perturbation theory, which is derived from the Abinit code [188]. The partial and total DOS of Nb_2O_5 oxide are shown in Fig. VI.10(b). The DOS calculations of hexagonal $\beta-Nb_2N$ are shown in Fig. VI.10(a) and are in agreement with previous experimental results [176, 189]. The VB spectrum of the hexagonal $\beta-Nb_2N$ is very sensitive to nitrogen content in the film. Measured and calculated DOS results in Fig. VI.9 and 10 allow the identification of these two peaks, which are arise from strong and weak hybridization of N $2p$–Nb $4d$ states (~6 eV peak) and N $2p$ and Nb $4d$ states (~1.5 eV peak), respectively. Nevertheless, the peak ~1.5 eV is mainly due to $4d$ and also $5s$ type electrons. This peak loses intensity with increasing processing time and increasing of N/Nb ratio in the film as a result of N-Nb bonding with weak nitrogen $2p$-Nb $4d$ hybridization.

VI.3.1.3. NANOMECHANICAL PROPERTIES

Hardness and measurements were acquired by Md. Mamun and explanations of the results were conducted by Md. Mamun and Dr A. Elmustafa. The hardness as a function of contact depth of indentation is shown in Fig. VI.11. The data presented are the average of ten indentation test results with error bar on each of the heated samples.

The hardness at deep indents converged for all of the samples to ~3 GPa, which agrees well with reported hardness values of Nb from the literature [33].
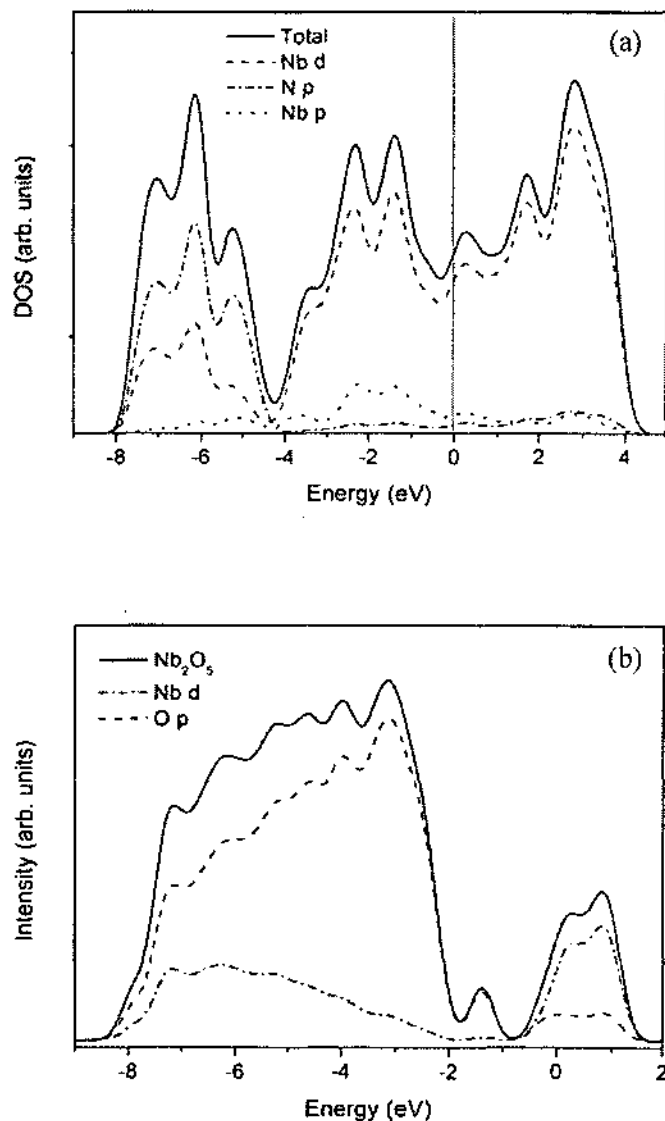
Fig. VI.10. (a) Calculated partial and total density of states (DOS) of (a) hexagonal β-Nb₂N. (b) Nb₂O₅ oxide. Data were obtained and analyses were conducted by Drs. Y. Ufuktepe and S. Kimura at the UVSOR facility, Institute for Molecular Science, Japan.

The composite film/substrate hardness at shallower depths depicted a gradual growth in film thickness as the processing time increases, which is shown in Fig. VI.12. Square of the thickness versus the processing time is shown in inset of Fig. VI.12. The straight line is a linear curve fit to experimental data which follows a parabolic rate law [3]. In the nitridation process, parabolic kinetics occur when the mass gain, due to NbN_x film formation on a substrate, is proportional to the square of the film thickness. The straight line relation is an indication that growth of the nitride in the samples is diffusion controlled [3]. For the shortest processing times (5 and 10 min), the zero crossing point of the straight line is observed, while for the longer processing times (≥ 20 min), the slope of the straight line decreases and, also, there are large deviations of the fitted line from the origin due to lower rate of nitrogen diffusion or the effect of nitrogen saturation.
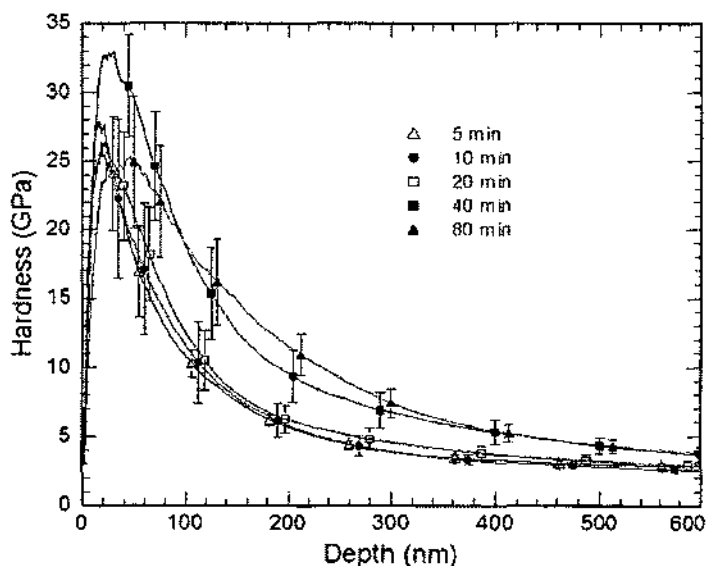
Fig. VI.11. Hardness as a function of contact depth for NbN_x deposited at 900 °C and 133 Pa nitrogen pressure for various heating times. Data were acquired by Md. Mamun and explanations of their results were conducted by Md. Mamun and Dr A. Elmustafa.

The hardness of NbN_x films increases with increasing processing time, with an average value in the range of ~26 ± 3 GPa. The modulus versus depth of indentation is shown in Fig. VI.13. The average modulus of the films is in the range of ~300 ± 20 GPa. The modulus at deep indents converges for all of the samples to the average substrate modulus of Nb (~100 GPa). The reported values of the bulk Nb Young's modulus vary between 100 and 110 GPa [190]. The measured bulk Nb modulus of 100 GPa correlates well with the literature data.
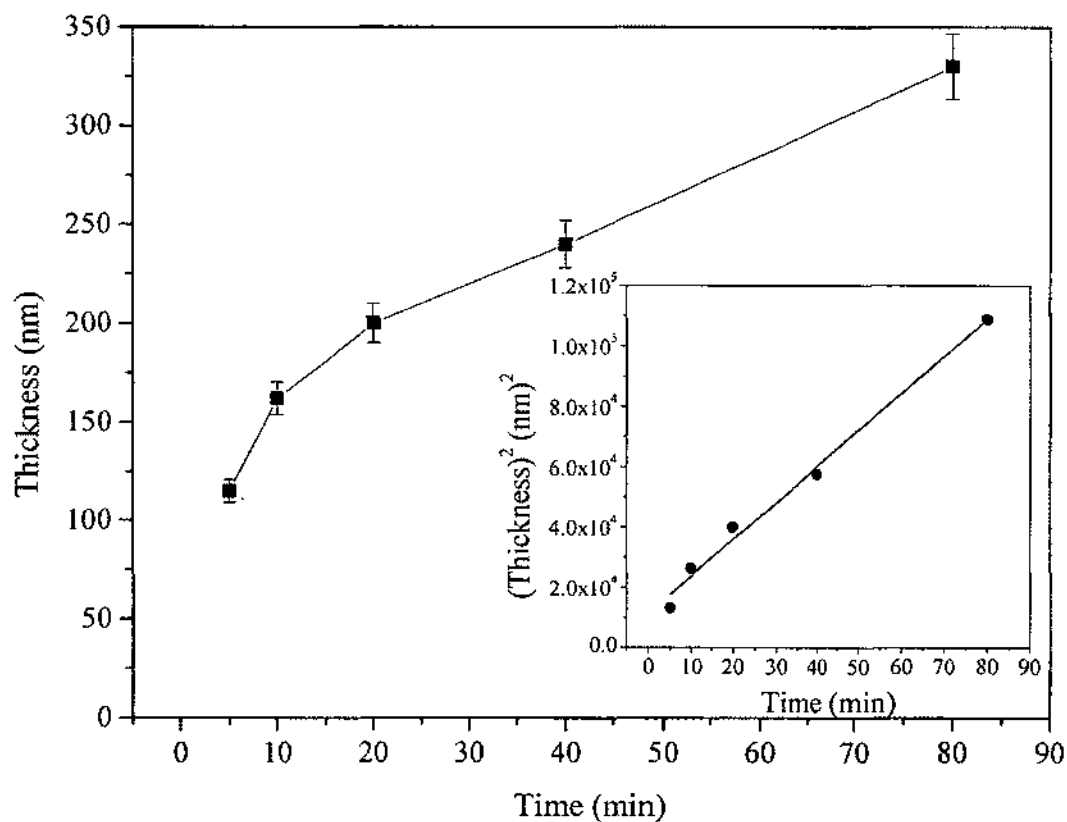
Fig. VI.12. Estimated thickness from nanoindentation measurements for NbN_x at various processing times. The inset shows the plot of the square of the NbN_x thickness as a function of processing time. The straight line is a linear curve fit. The error bars represent 5% of the thickness. Data were acquired by Md. Mamun.
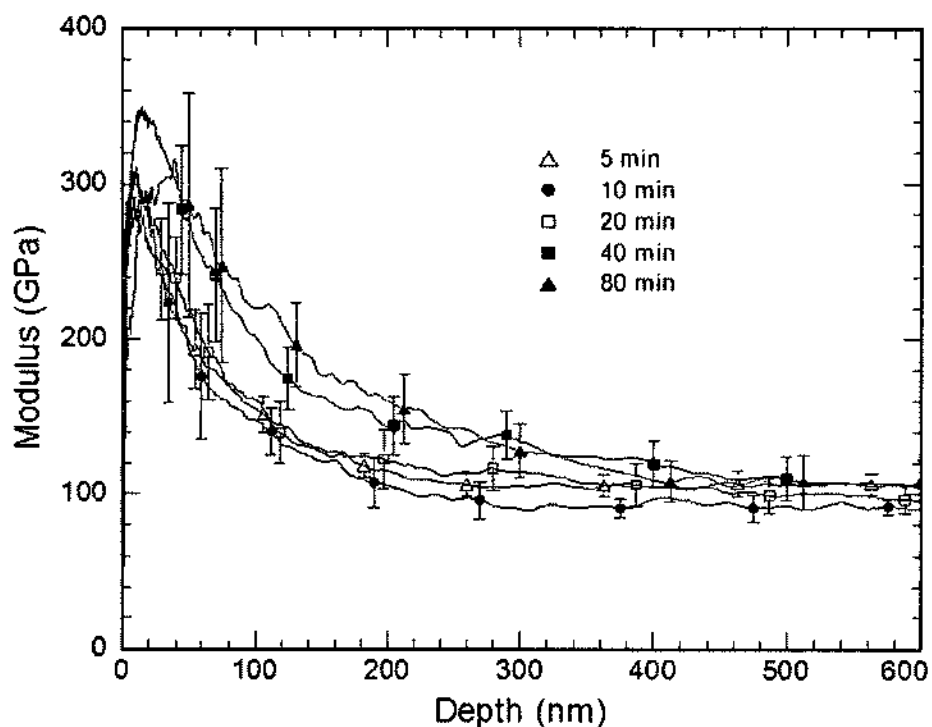
Fig. VI.13. Elastic modulus as a function of contact depth for NbN$_x$ deposited at 900 °C and 133 Pa nitrogen pressure for various heating times. Data were acquired by Md. Mamun and explanations of their results were conducted by Md. Mamun and Dr A. Elmustafa.

VI.3.2. HIGH TEMPERATURE THERMAL NIOBIUM NITRIDE FORMATION

VI.3.2.1.THIN SAMPLES

VI.3.2.1.1. STRUCTURE AND PHASE COMPOSITION

Fig. VI.14 shows the XRD of Nb and Nb substrates heated for 180 min at ~ 1.3x10^{-3} Pa of nitrogen pressure and different temperatures. XRD patterns for samples in this figure show that no nitridation occurs for samples processed at temperature ranging from 1200-1500 °C.

Two-dimensional (2D) XRD images of these samples heated at 1.3×10^{-3} Pa and different temperatures in the range 1250 to 1500 °C are shown in Fig. VI.15. The advantages of using 2D-XRD make XRD a good tool for phase identification of the crystal orientation of the samples.
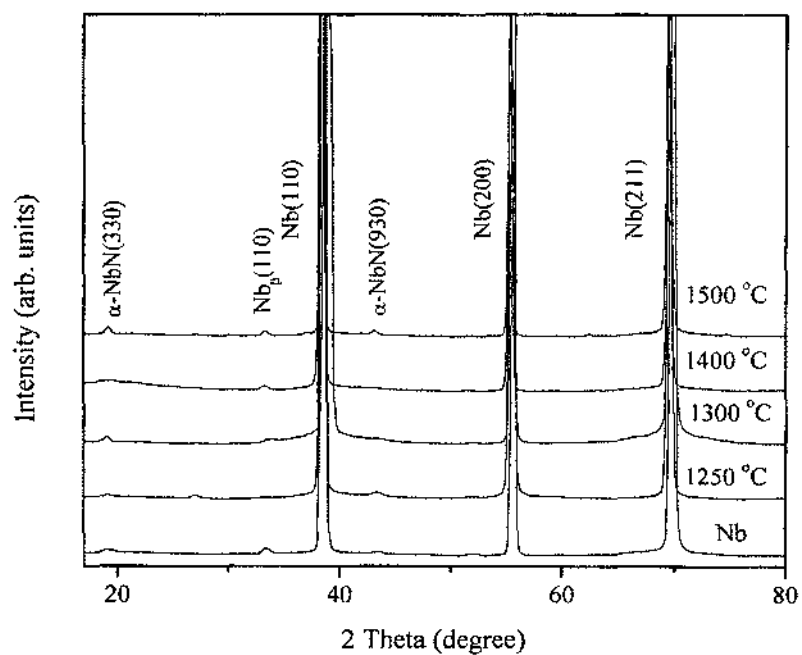
Fig. VI.14. XRD patterns of Nb and Nb substrates heated for 180 min at 1.3×10^{-3} Pa of nitrogen pressure and different temperatures.
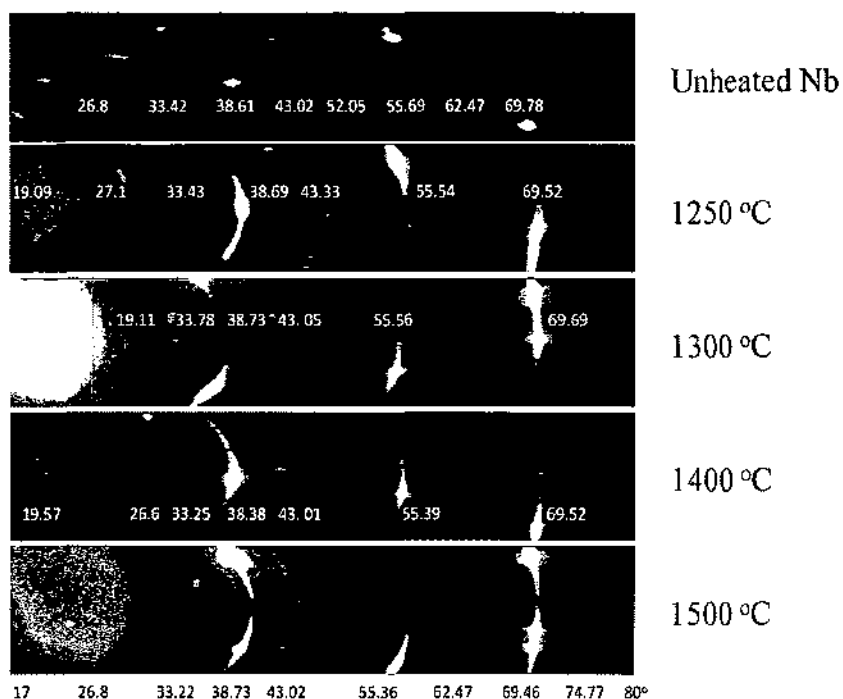
Fig. VI.15. 2D-XRD patterns of Nb heated for 180 min in1.3x10^{-3} Pa of nitrogen pressure and different temperatures.

Table VI.2. The 2θ values and lattice constants for highest three peaks for samples heated in1.3x10^{-3} Pa of nitrogen pressure.

	Peak positions, 2θ (°)			Lattice constant, a (Å)		
Nb	38.61	55.69	69.78	3.307	3.303	3.317
1250 °C	38.69	55.54	69.52	3.299	3.295	3.304
1300 °C	38.73	55.56	69.69	3.317	3.318	3.313
1400 °C	38.38	55.39	69.52	3.312	3.315	3.314
1500 °C	38.73	55.36	69.46	3.312	3.318	3.316

Table VI.2 shows the 2θ values and lattice constants for highest three peaks for samples heated in1.3x10^{-3} Pa of nitrogen pressure at different temperatures. The lattice constant of heated samples is higher than that of unheated Nb substrate. Increases of

lattice constant as nitrogen content increases in the samples was reported [90, 191]. The results of lattice constants increasing for samples heated here are in agreement with the previous report on the formation α-NbN phase. This confirms formation of α-NbN phase in our samples.

XRD patterns of Nb and Nb substrates heated at 1300 °C in different nitrogen pressures for 180 min are shown in Fig. VI.16. Also, XRD showed no interaction until nitrogen pressure reaches about 0.53 Pa. After that pressure, the β-Nb$_2$N phase starts to appear as mixed phase with α-NbN phase. Fig. VI.17 shows 2D-XRD images of Nb with Nb samples that were heated at 1300 °C in different nitrogen pressure in the range of $2.6 \times 10^{-4} - 3.3$ Pa.
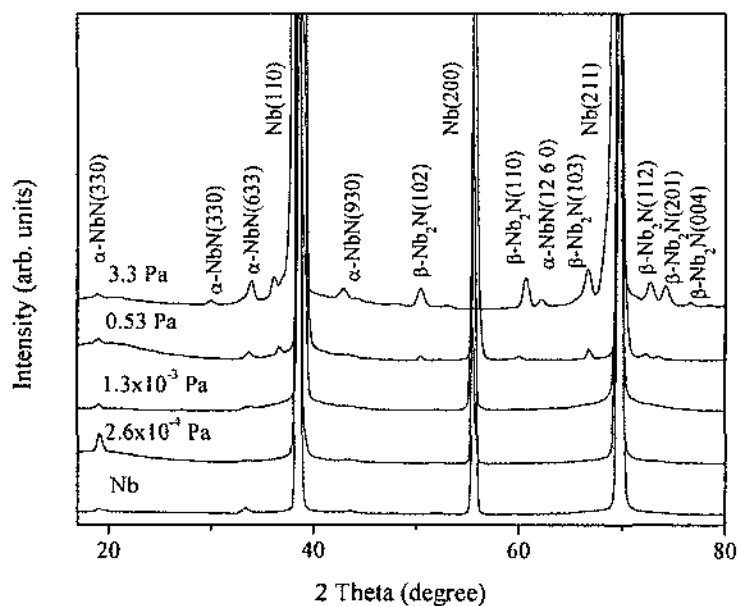
Fig. VI.16. XRD patterns of unheated Nb substrate and Nb heated for 180 min at 1300 °C in different nitrogen pressures.
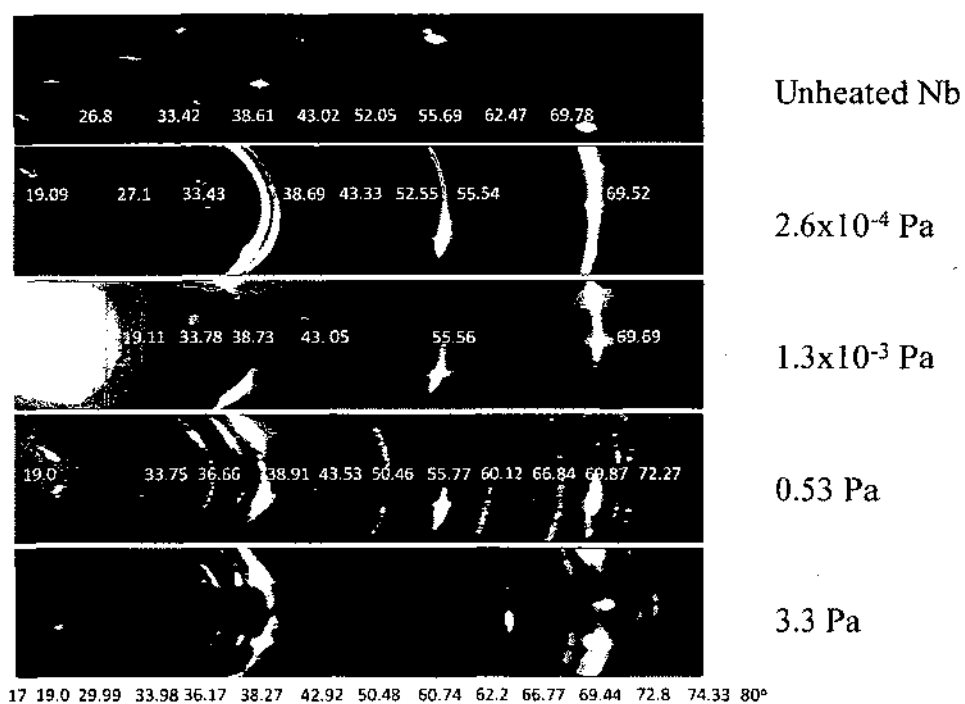
Fig. VI.17. XRD patterns of unheated Nb substrate and Nb heated for 180 min at 1300 °C in different nitrogen pressures.

Table VI.3. The 2θ values and lattice constants for highest three peaks for samples heated at 1300 °C.

	Peak positions, 2θ (°)			Lattice constant, a (Å)		
Nb	38.61	55.69	69.78	3.307	3.303	3.317
2.6×10^{-4} Pa	38.69	55.54	69.52	3.299	3.299	3.298
1.3×10^{-3} Pa	38.73	55.56	69.69	3.317	3.318	3.313
0.53 Pa	38.91	55.77	69.87	3.297	3.31	3.308
3.3 Pa	38.27	55.29	69.44	3.304	3.32	3.317

As pressure of nitrogen is set to 1.3×10^{-4} Pa, the shape of some spots on Nb substrate is changed into a continuous ring and this indicates growth of small grains with random orientations of crystallites, as indicated by a ring with uniform intensity. Further increase of the nitrogen pressure causes formation of larger grains, as can be seen by spots in 2D-XRD. As pressure is increased full spotty rings were obtained for alpha and other phase (β), which indicated formation of large grains on the surface with weak texture. The average values of crystallite size showed decreases from about 24 to 14 nm as pressure of nitrogen is increased from 2.6×10^{-4} to 3.3 Pa. Fig. V.18 shows average crystallite size and lattice constants calculated for peaks at three positions corresponding to Nb (211), (110) and (200) orientations. As shown in Fig. VI.18(a), the crystallites size is decreasing as pressure is increasing, which agrees with that seen in 2D-XRD images. The lattice constant is shown in Fig. VI.18(b). The error bars in this Fig. VI.18 represent standard deviations from the three positions. The trend of the lattice constant shows change from decreasing to increasing at 0.53 Pa as a result of the formation of β phase in the samples. Table VI.3 shows the 2θ values and lattice constants for highest three peaks for samples heated at 1300 °C in different nitrogen pressures. The lattice constant increases for heated samples compared to that on Nb is in agreement with the formation α-NbN phase in the samples.

XRD peaks for samples prepared at 3.3 Pa showed β-Nb$_2$N mixed with other peaks attributed to α-NbN. β-Nb$_2$N phases are attributed to (100), (002), (102), (110), (103), (112) , (201) and (004) orientations, while those of α-NbN phase are attributed (400), (620), (930) and (12 6 0) orientations. The formation of α-NbN and β-Nb$_2$N

phases agrees with equilibrium phase diagram of NbN_x and predicted β-Nb_2N phase should appear in this temperature range [192].

According to results by Zhitomirsky and coworkers the formation of α-NbN then β-Nb_2N phase was first obtained when the surface of Nb was heated at high temperature [192]. This is also in agreement with what was previously reported on the reactivity of Nb in nitrogen atmosphere in the same range of temperature as we have here[3]. The intensity of the peaks is enhanced as the nitrogen pressure is increased from 0.53 Pa to 3.3 Pa, as clearly observed from Fig. VI.17. The improvement of the peaks is due to increases of the samples' thickness; more reactions with nitrogen gas occur as the pressure increases. The lattice parameter of Nb solid solutions was reported as decreases as atomic percent of nitrogen increased [193].

Fig. VI.19 shows XRD patterns of the Nb substrate and the Nb after heating at 1400 °C in different nitrogen pressures for 180 min. The XRD patterns show no nitride formation until the nitrogen pressure reaches about 0.13 Pa. In Fig. VI.20, 2D-XRD images of Nb samples heated at 1400 °C in different nitrogen pressure in the range of 1.1×10^{-3} – 0.53 Pa are shown. Similar behavior is noticed as in Fig. VI.17.
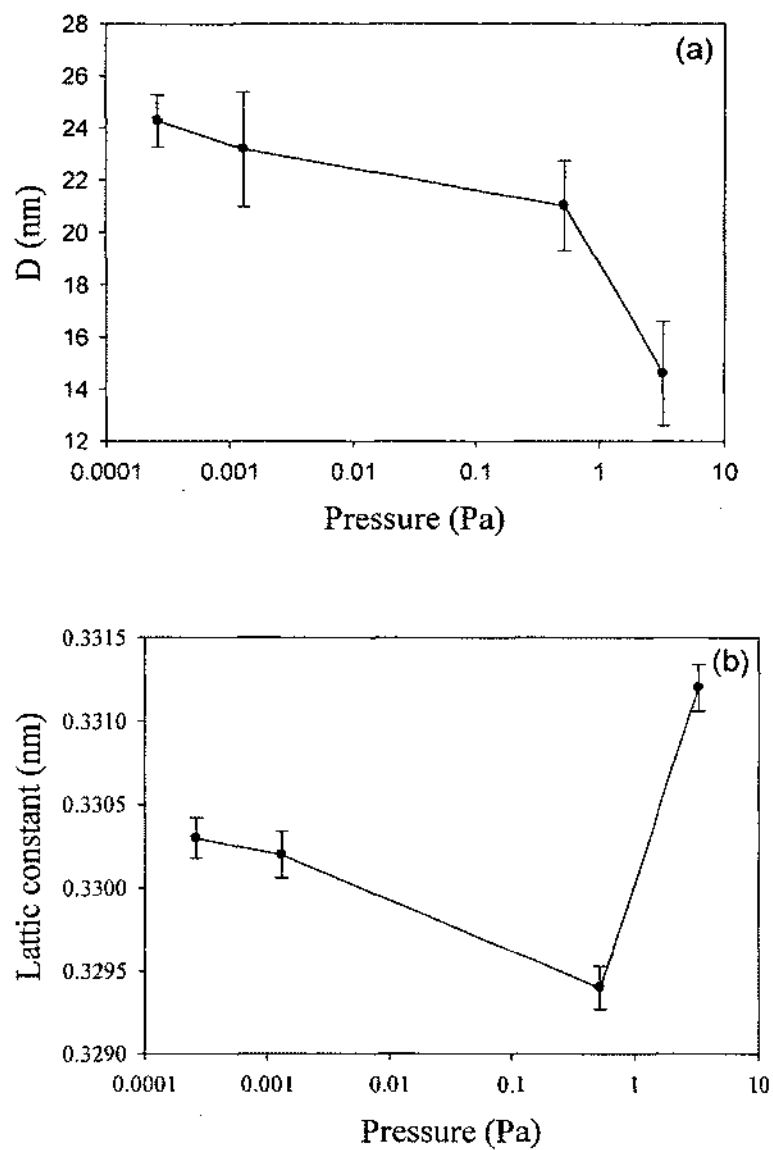
Fig. VI.18. (a) The mean hexagonal crystallite size and (b) lattice parameter of samples heated at 1300 °C in different nitrogen pressures.

The size of grown α-NbN grains is getting bigger as the nitrogen pressure is increased while the texture changes to weak textured as indicated by spotty rings for samples done at 0.53 Pa. The grown grains for samples heated at 1400 °C are with higher

textured coefficient compared to samples done at 1300 °C. The lattice constant calculated from three peaks corresponding to Nb (211), (110) and (200) for samples heated at 1400 °C shows the same style as shown for samples done at 1300 °C. The change in the trend of lattice constants from decreasing to increasing at 0.13 Pa for samples heated at 1400 °C is shown in Fig. VI.21. This change at 0.13 Pa is due to formation of mixed phases of NbN_x.
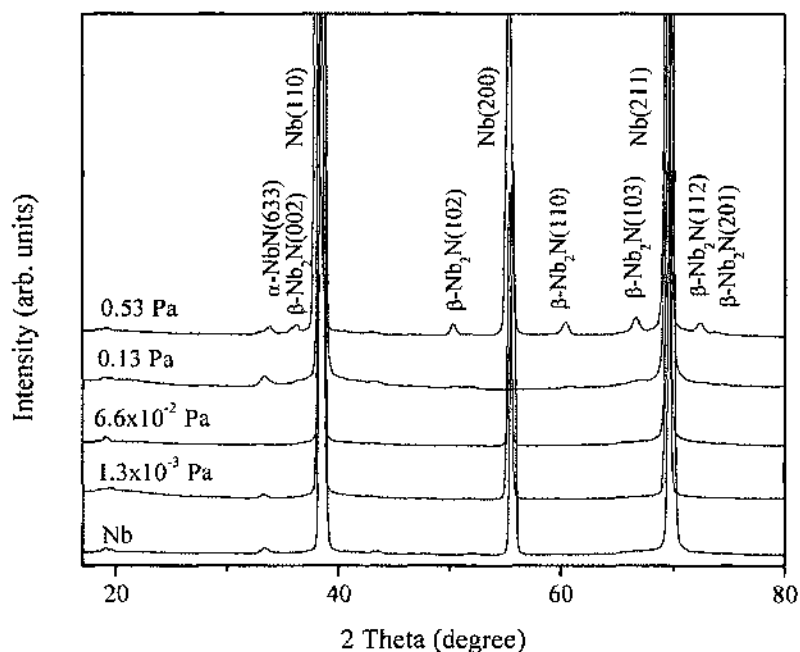
Fig. VI.19. XRD patterns of unheated Nb substrate and Nb heated for 180 min at 1400 °C in different nitrogen pressures.
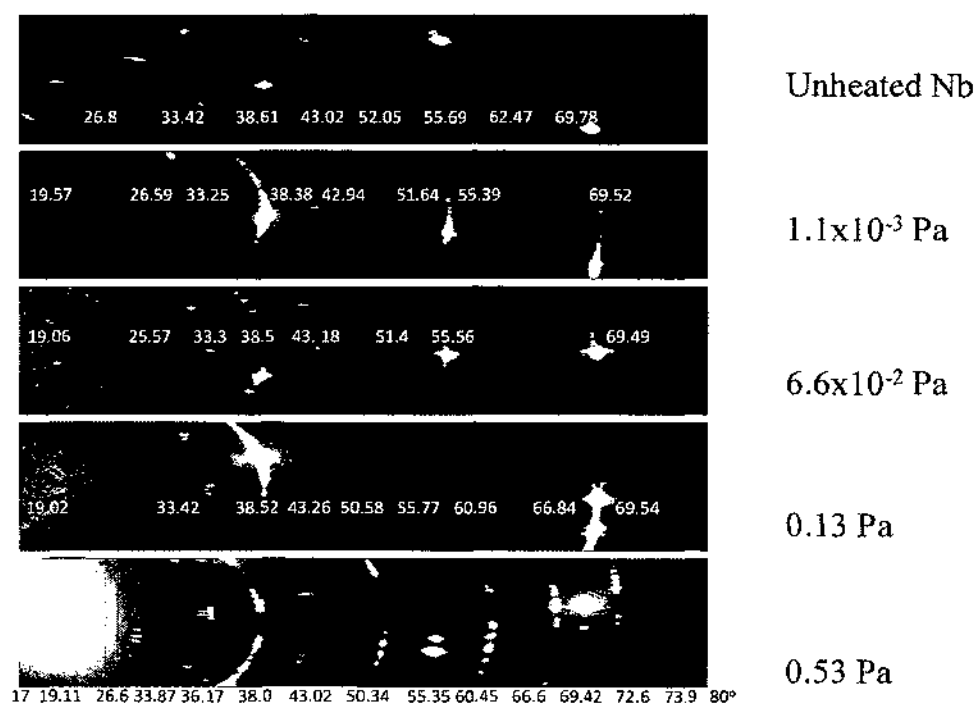
Fig. VI.20. XRD patterns unheated Nb substrate and Nb heated for 180 min at 1400 °C in different nitrogen pressures.
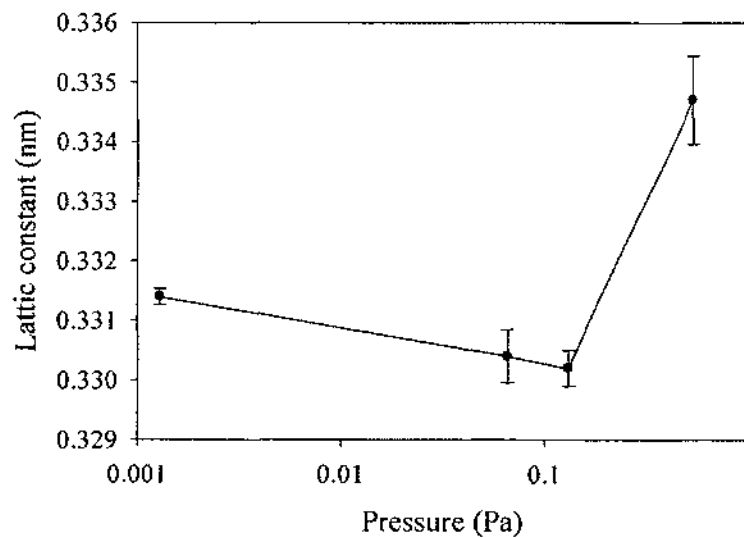
Fig. VI.21. The mean lattice parameter of samples heated at 1400 °C in different nitrogen pressures.

Table VI.4. The 2θ values and lattice constants for highest three peaks for samples heated at 1400 °C.

|	Peak positions,2θ (°)			Lattice constant, a (Å)		
Nb	38.56	55.69	69.73	3.307	3.303	3.317
1.3x10⁻³ Pa	38.	55.39	69.52	3.312	3.315	3.314
6.6x10⁻² Pa	38.5	55.56	69.49	3.314	3.311	3.311
0.13 Pa	38.52	55.77	69.54	3.303		3.307
0.53 Pa	38.0	55.35	69.42	3.307	3.313	3.308

Table VI.4 shows the 2θ values and lattice constants for highest three peaks for samples heated at 1400 °C in different nitrogen pressures. The lattice constant of heated samples is higher than that of unheated Nb substrate. The formation of solid solution alpha phase does not cause change in strain of Nb lattice, since nitrogen easily fits in the niobium lattice [27]. According to Taylor and Doyle [191], at about 10 at. %, N can be interstitially accommodated by Nb lattice at 2200 °C and 40.0 Pa, while only 1.0 at % is retained when it cools down. They also reported change in the lattice constant of Nb from a = 3.298 Å to 3.304 Å and to a = 3.306 Å when 0.77 at. % and 1.05 at. % of the nitrogen retained in solid solution samples, respectively [90, 191]. In this work, this increase in lattice parameters of heated samples can be noticed compared to that of bare Nb. The average lattice constant calculated here for Nb substrate is a = 3.298 Å, while for samples heated at 1.3 Pa and 1300 °C it increases to 3.316 Å. Similar behaviors of lattice constant increases can be seen for other set of samples (done at 1400 °C) heated at different nitrogen pressures. Also, it seems that the amount of retained nitrogen in samples after cooling down is complex and depends on samples preparation history as well as their dimensions [191]. Cost and Wert [27] in their XRD study for Nb samples could not

determine any other NbN_x phases except β-Nb_2N even at temperature as low as 840 °C with 0.8 at. % of nitrogen reported [191]. EPMA measurements of samples heated at 0.53 Pa and 1400 °C showed only about 5% at of nitrogen given both beta and alpha phases were detected in this sample.

VI.3.2.1.2. SURFACE MORPHOLOGY

Fig. VI.22 (a-d) shows the 3D-AFM images (2000 ×2000 nm^2) of samples done at different temperatures. The root mean square (RMS) surface roughness was obtained from the AFM images using Nanoscope V5.31r1 software. The dependence of RMS value on the temperature over and line scans at different temperature are shown in Fig. VI.22 (e). The roughness of the samples increases from about 0.7 nm at to 2.3 nm as temperature increases from 1250 to 1500 °C. Fig. VI.23 shows the SEM images of NbN_x samples heated at constant nitrogen pressure of 1.3×10^{-3} Pa.

The SEM images are clearly shown little differences between the treated surfaces with different temperatures. Increasing the temperature increases the surface roughness as recognized. The AFM confirms the same behavior observed in SEM images that shown in Fig. VI.23. Fig. VI.24(a-d) show 3D-AFM images of NbN_x prepared at different nitrogen pressures and 1300 °C. The RMS surface roughness versus nitrogen pressure is schemed in Fig. VI.24(e). The RMS was obtained by performing line scans taken diagonally of the AFM images (2000 × 2000 nm^2).
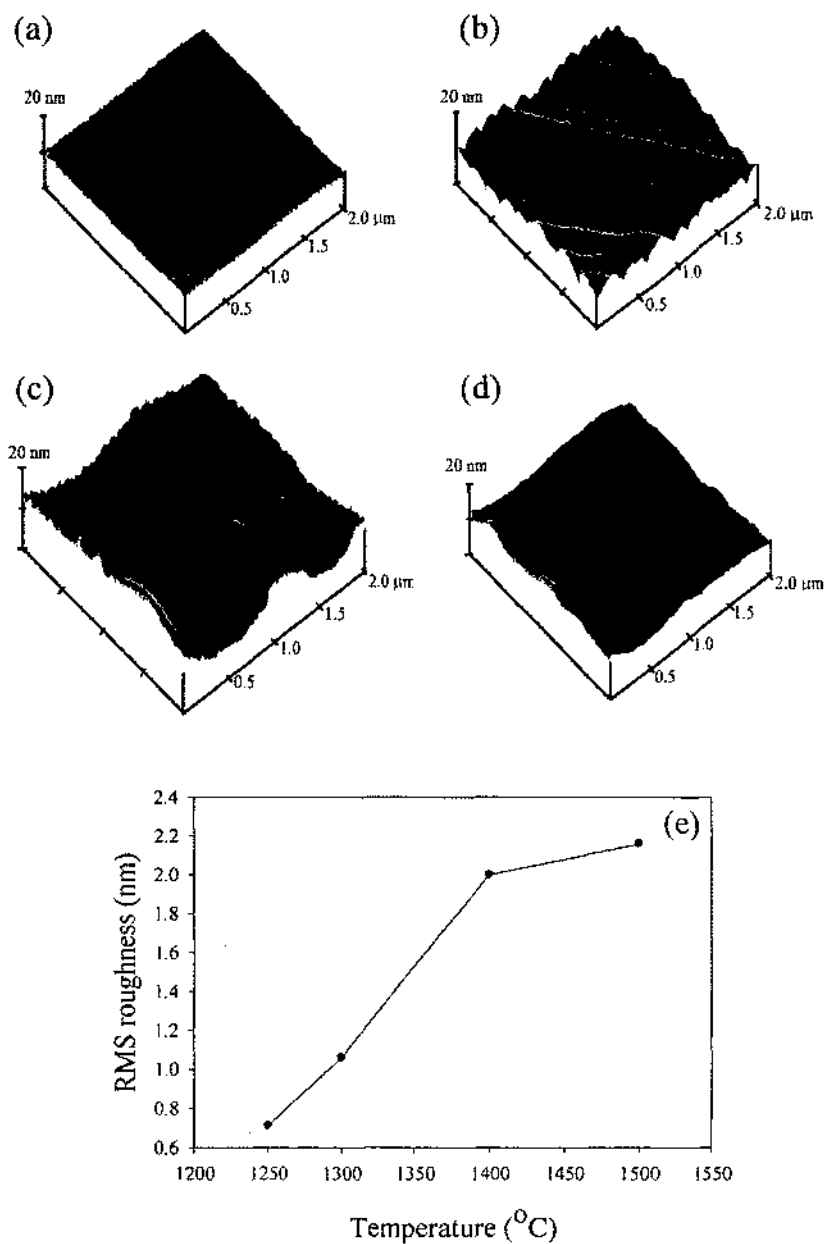
Fig. VI.22. 3D-AFM images of NbN$_x$ samples heated at (a) 1250 °C, (b) 1300 °C, (c) 1400 °C, and (d) 1500 °C. (e) Dependence of surface roughness RMS values on temperatures.

(a)

(b)

(c)

(d)
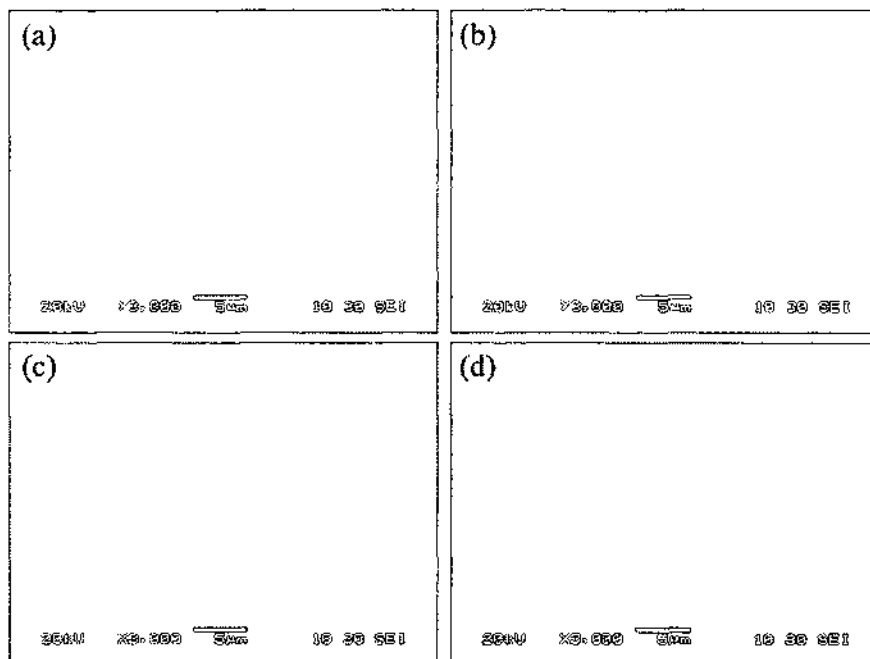
Fig. VI. 23. SEM images of NbN$_x$ samples (a) 1250 °C, (b) 1300 °C, (c) 1400 °C, and (d) 1500 °C heated at 1.3×10^{-3} Pa of nitrogen pressure.

The samples show slightly decrease in surface roughness as pressure increases and the surface became very smooth as shown in Fig. VI.24 (d). These observations are confirmed by SEM images of theses samples shown in Fig. VI.25. As the pressure increases to 3.3 Pa some regularly shaped islands started formed with appearance of β-Nb$_2$N phase in the samples. Fig. VI.26 and Fig. VI.27 show AFM and SEM images of NbN$_x$ grown at different nitrogen pressures and 1400 °C. As shown from these images, triangular submicron-sized islands are present. The shapes and sizes of these islands did not show much change with the increasing times of processing. It should be noted here that AFM images show the grain size while XRD gives the crystallite size, and these can be different. A comparison of the root-mean square surface roughness (RMS) as a function of processing time is shown in Fig. VI.26(e).
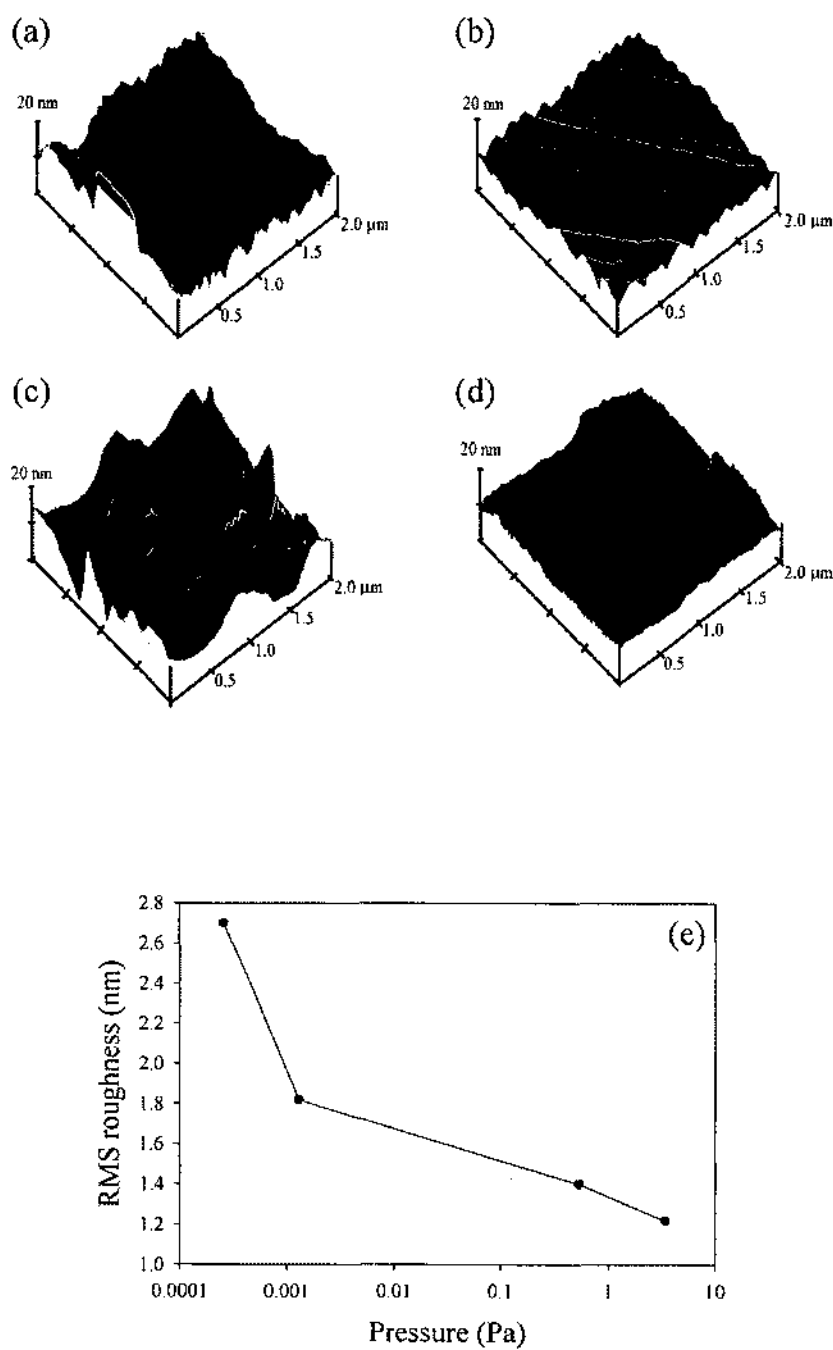
Fig. VI.24. 3D-AFM images of NbN$_x$ samples done at 1300 °C (a) 2.6×10^{-4} Pa, (b) 1.3×10^{-3} Pa, (c) 0.53 Pa, and (d) 3.3 Pa and. (e) Dependence of surface roughness RMS values on nitrogen pressure.
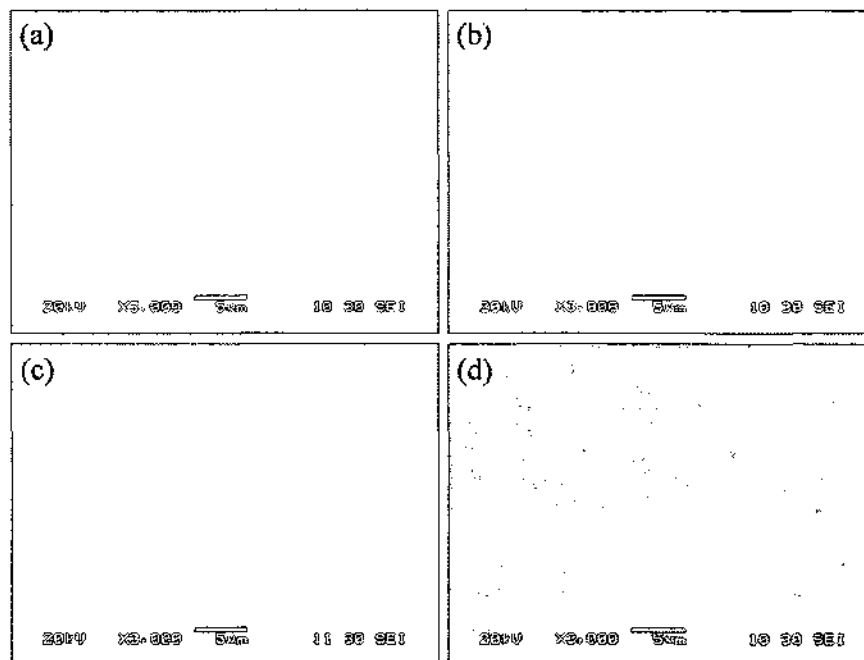
Fig. VI.25. SEM images of NbN_x samples done at 1300 °C (a) 2.6×10^{-4} Pa, (b) 1.3×10^{-3} Pa, (c) 0.53 Pa, and (d) 3.3 Pa.

The RMS surface roughness value sharply decreases with pressure and increase as Nb_2N phase start to show up in samples as confirmed by XRD. The increases of roughness in samples done at 0.53 Pa is due to formation of small grains as seen in Fig. VI.20 of 2D-XRD of these samples.
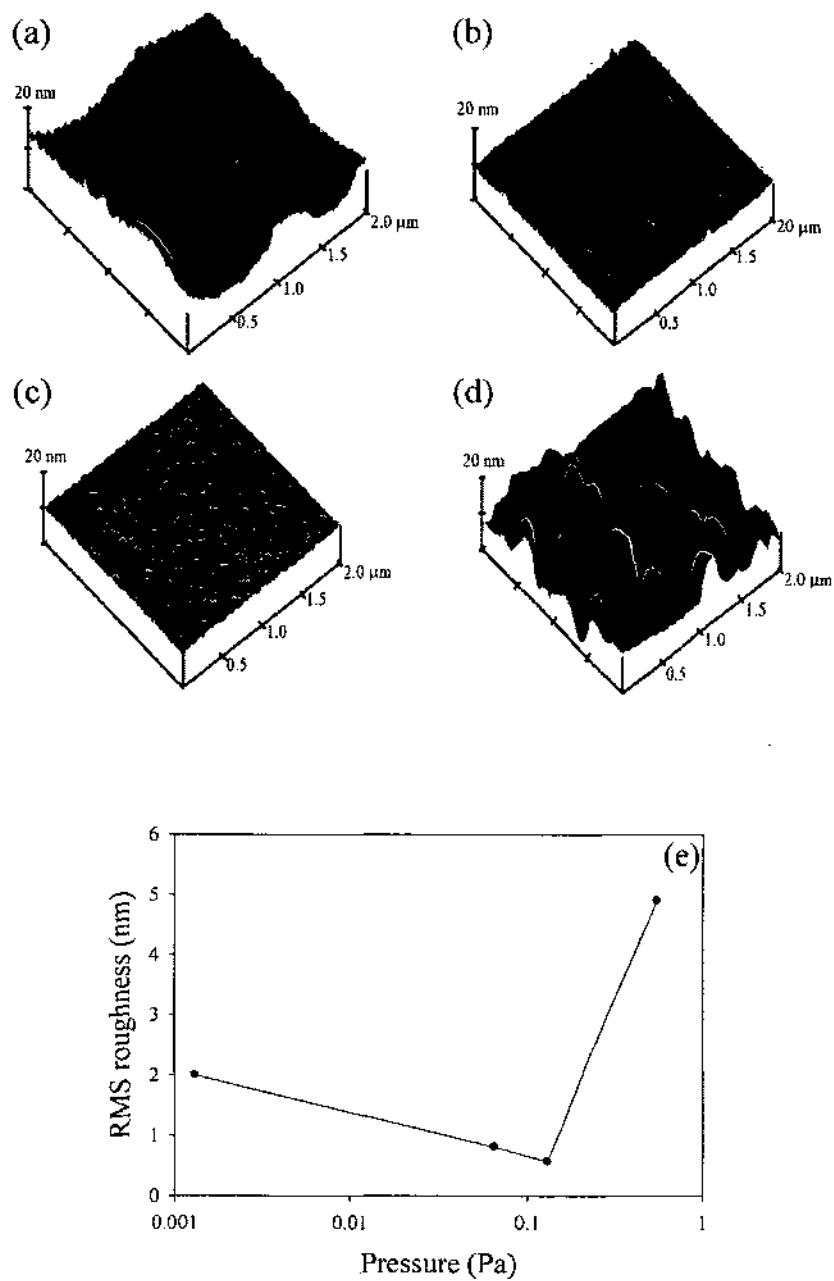
Fig. VI.26. 3D-AFM images of NbN$_x$ samples done at 1400 °C: (a) 1.3×10^{-3} Pa, (b) 6.6×10^{-2} Pa, (c) 0.13 Pa, and (d) 0.53 Pa. (e) Dependence of surface roughness RMS values on nitrogen pressure.
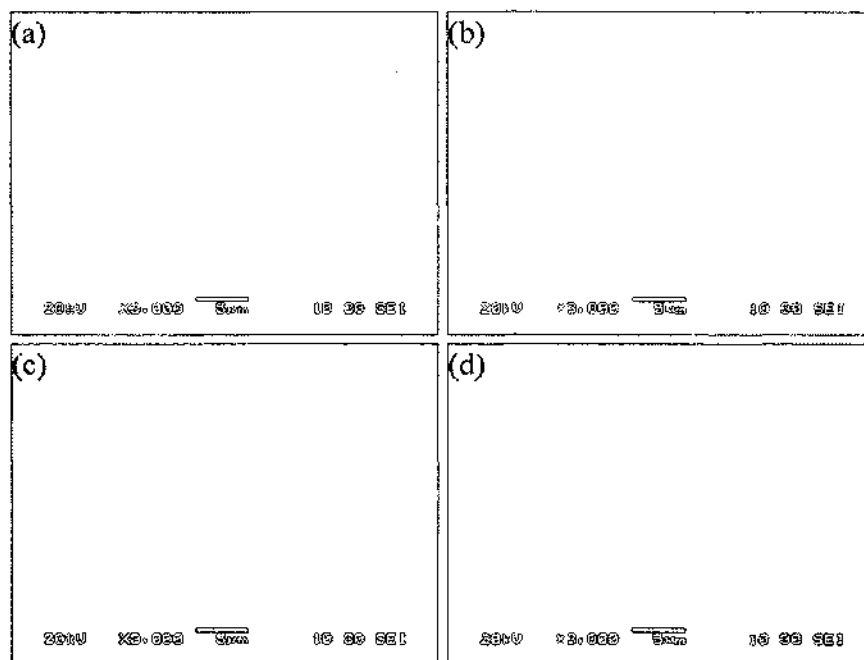
Fig. VI.27. SEM images of NbN$_x$ samples done at 1400 °C: (a) 1.3×10^{-3} Pa, (b) 6.6×10^{-2} Pa, (c) 0.13 Pa, and (d) 0.53 Pa.

VI.3.2.1.3. X-RAY ABSORPTION NEAR EDGE STRUCTURE (XANES) SPECTROSCOPY

XANES is considered a powerful tool to investigate the electronic and atomic structures of materials [72]. The sample does not need to be crystalline to be measured as this technique measures transitions from core levels. In the atom, each core shell has a distinct binding energy. When X-ray is absorbed, the binding energy of a core shell gives rise to the so-called absorption edge. The spectrum of the X-ray absorption as a function of energy is shown in Fig. VI.28.
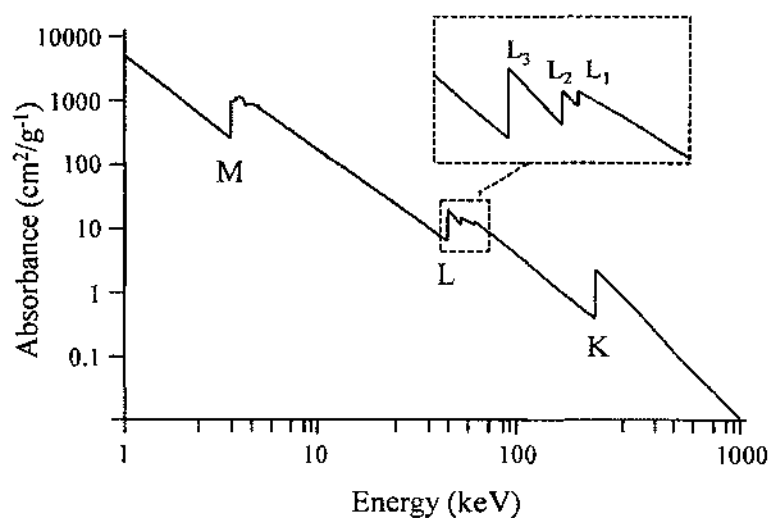
Fig. VI.28. X-ray absorption spectrum shows the three major transitions at K, L, and M edges. Inset shows higher resolution of the L edge splitting. Redrawn from [194].
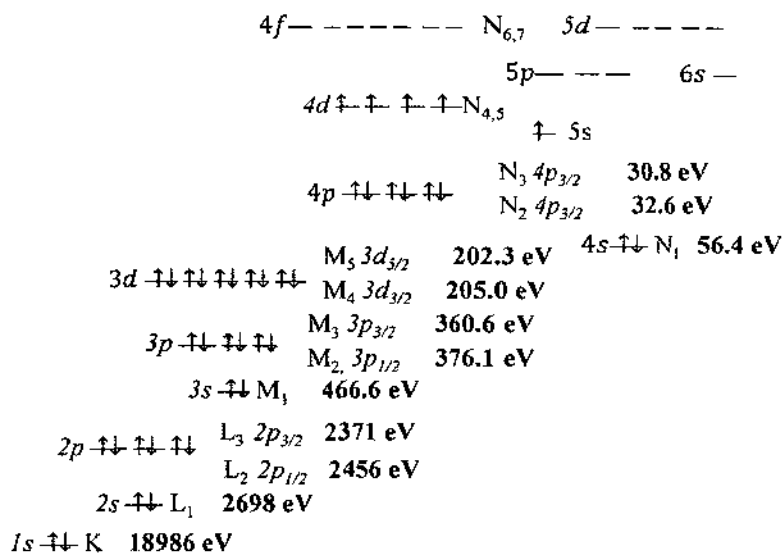
Fig. VI.29. Schematic representation of electronic configuration with standard spectroscopic nomenclature of Nb and spin-splitting state with electron binding energies for Nb element, taken from [195].

The name of the edges is according to the principle quantum number of the electron that is excited from this shell: K for n = 1, L for n = 2, and M for n = 3. The inset in Fig. VI.28 shows the three edges, L_1, L_2, and L_3 of L edge. L_1 corresponds to excitation of a 2s electron. The L_2 and L_3, edges correspond to spin-split of the 2p excitation due to spin–orbit coupling: L_2 corresponds to $2P_{1/2}$ excited state and L_3 corresponds to the $2P_{3/2}$ excited state at lower energy [194].

Fig. VI.29 shows a schematic of the electronic configuration of Nb elements with standard spectroscopic nomenclature of Nb and spin-splitting state with electron binding energies for Nb element. Spin–orbit coupling energies are relatively small for valence shells compared to core shells which can be quite large. For Nb as seen in Fig. VI.29, the L_2–L_3 splitting is about 85 eV compared to 2.7 and 1.8 eV splitting for M_2–M_3 and N_2–N_3, respectively. The absorption measurements done at 1000 eV or more are referred to as extended X-ray absorption fine structure (EXAFS). X-ray absorption near-edge structure (XANES) refers to studying the structure in the vicinity of the edge (30 eV)[194]. Therefore, the distinction between XANES and EXAFS is arbitrary. In X-ray photoemission spectroscopy (XPS), the photon energy is fixed and the photoelectron intensity is measured as a function of electron kinetic energy, In XANES the x-ray energy is scanned and the effect of the absorbed X-ray is measured. When X-ray is absorbed, it causes excitations of core electrons to empty states, lifting holes that are filled by Auger decay. In the case of XPS, the intensity of the emitted primary Auger electrons is a direct measure of the X- ray absorption process. For XANES, the primary Auger electrons create scattered secondary electrons, which dominate the total electron yield (TEY). The total electron yield (TEY) detection is commonly used to record spectra

of XANES. The sampling depth in XANES measurements is typically a few nanometers, while in XPS it is less than 1 nm [194].

Fig. VI.30 shows XANES of NbN_x samples heated at different temperatures (1250–1500 °C) and $1.3x10^{-3}$ Pa after background subtraction and normalization. Fig. VI.30(a) shows XANES results for Nb $M_{2,3}$ and N 1s peaks, while Fig. VI.30(b) is at O K edge, both as a function of heating temperature. Fig. VI.31 and Fig. VI.32 show XANES at Nb $M_{2,3}$ and O K edges for samples in Fig. VI.16 and Fig. VI.19, respectively. The Nb $M_{2,3}$ edges are attributed to the transition of Nb 3p electrons to unoccupied 4d and 5s states while that of the Nb $M_{2,3}$ edge the general shape of the Nb $M_{2,3}$ edges and is quite the same for the samples in Fig. VI.30. The two Nb 3p peaks at 365.5 and 380.5 eV can be assigned to the Nb $3P_{1/2}$ and $3p_{3/2}$, respectively. The peak at 365.5 eV is stronger than that at 380.5 eV. The intensity of N 1s peak at 406.5 eV did not show any alteration with changing in heating temperature of the samples. The same was observed from XPS results done on sputtered NbN_x films as they do Ar^+ ion etching [196]. The N 1s peak, at about 407 eV, is clearly seen at all temperatures in Fig. VI.30(a). The shift in peak position (N 1s at 409.9 eV) for this edge may be due to the formation of an oxide layer in the samples. The detection of this N 1s peak by XANES confirms the observations made before on the formation of alpha phase in these samples; even its peaks are hard to be distinguishing from Nb peaks in XRD patterns. The reason was attributed to formation of an oxide layer on the films with thickness 0.7-1.4 nm. There were no observed shifts in binding energies at both Nb 3P and N 1s as heating temperatures of samples was increasing. There should be more shifts by 1.4 eV or more in position of peak at 365.5 eV if niobium oxidation state other than Nb_2O_5 is found in the samples [66].
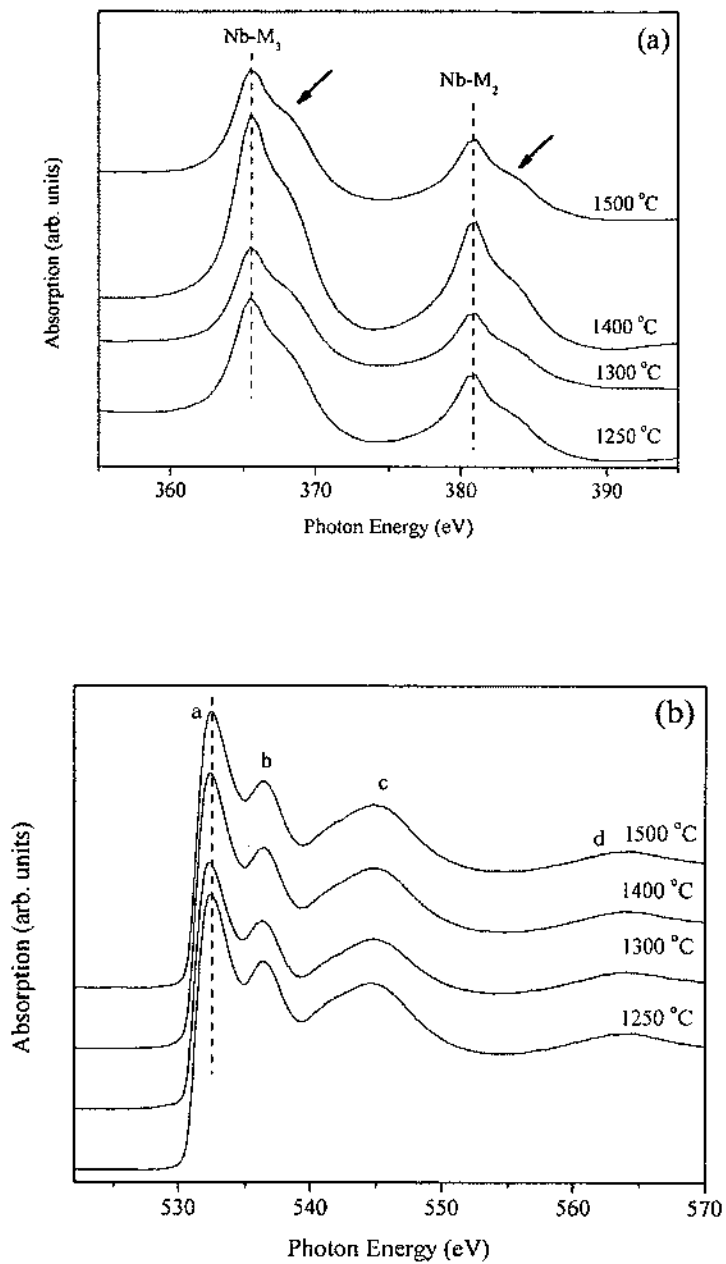
Fig. VI.30. XANES data samples at 1.3×10^{-3} Pa. (a) at Nb $M_{2,3}$ edge and (b) at O K-edge. Measurements performed on beamline 8.2 at the Stanford Synchrotron Radiation Lightsource in the SLAC National Accelerator Laboratory.

O K edge is attributed to a transition of O 1s electrons to the unoccupied 2p states. The O K edge is characterized by a double-peak structure, as shown by the first two peaks (labeled a and b) of XANES results in Fig. VI.30 (bottom) [66, 197]. The relative height and energy splitting between two peaks at a and b positions are characteristics for the kind of oxidation state in the samples. The splitting found here is around 3.9 eV and this very close to that reported for Nb_2O_5 oxidation [66].

Also, it is reported that the relative intensities between peaks a and b are very close in NbO_2, while in Nb_2O_5 they showed similar relative intensities [66]. The shapes of the peaks at 365.5 and 380.5 eV have some shoulders, as shown by small arrows in Fig. VI.30(a). This shape indicates the presence of double peaks for these two positions. These double-peaks were reported for $Nb-M_3$ and $Nb-M_2$ lines when Nb_2O_5 is formed in the samples but could not be detected for other oxide states [66, 198].

This confirms observations on O K edge measurements in Fig. VI.30(b) that Nb_2O_5 oxide state is found in the samples. The source of this oxide layer could be as a native layer on the Nb substrate or on surface of NbN_x samples that forms when handling samples in air. Fig. VI.31 shows the XANES results for samples heated at 1300 °C and different nitrogen pressures. There is not much difference between results in Fig. VI.31 and in Fig. VI.30 except for the sample that was done at 0.53 Pa and 1300 °C. Also the peak labeled "a" in Fig. VI.31(b) is slightly shifted to higher photon energy than other samples. This may be due to its higher concentrations of oxygen than other samples. It is reported for Nb oxide samples that the intensity ratio of Nb peaks decreases with increasing oxygen concentration in the material [197]. The change of the concentration of oxygen may result from differences in surface roughness of the Nb substrates.
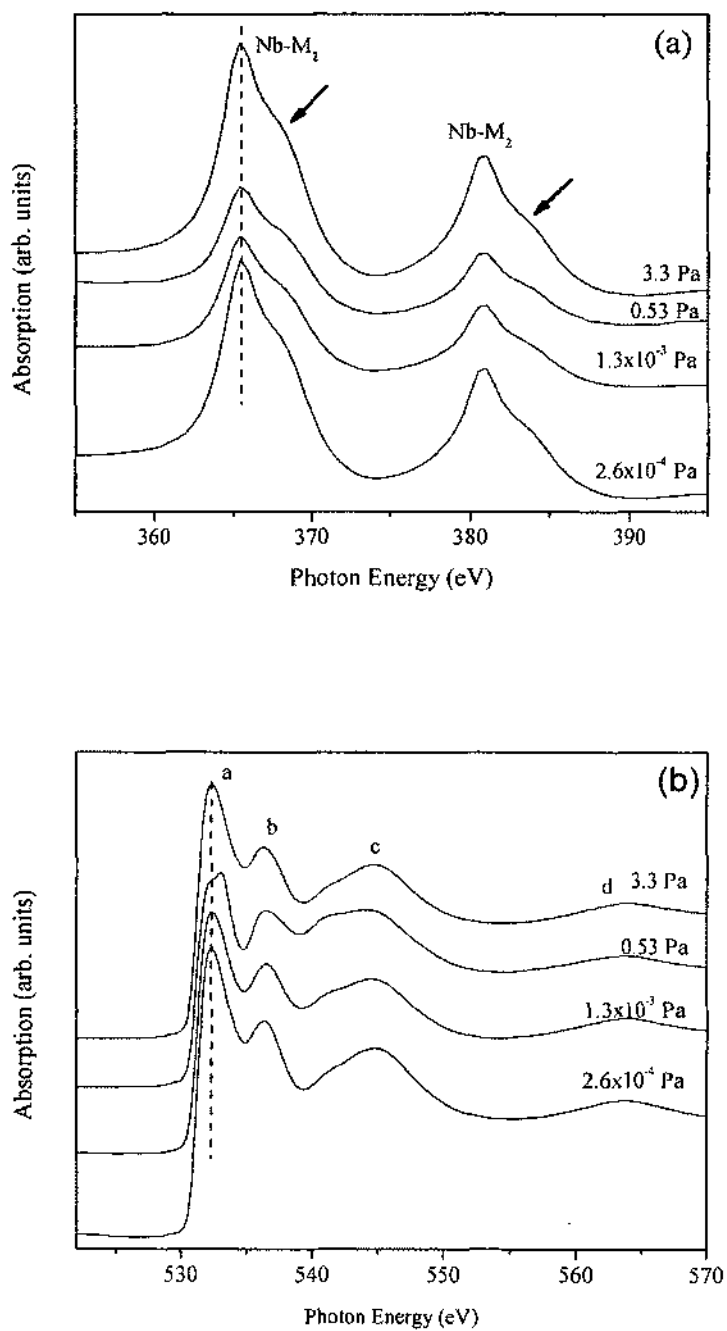
Fig. VI.31. XANES data for substrates heated for 180 min at 1300 °C temperature and different nitrogen pressures, (a) At Nb $M_{2,3}$ edge and (b) At O K-edge. Measurements performed on beamline 8.2 at the Stanford Synchrotron Radiation Lightsource in the SLAC National Accelerator Laboratory.

Fig. VI.32 shows the XANES spectra for samples done at 1400 °C in different nitrogen pressures. Fig. VI.32(a) is for spectra taken for Nb and nitrogen at Nb $M_{2,3}$ and 1s edges, respectively. The Nb $M_{2,3}$ edges show no changes in peak positions or intensities as pressure changes for this set of samples. This is the same for the N 1s peaks, except for the sample done at 0.13 Pa. The N 1s peak shows splitting and increases in the intensity. The peak centered on 402.3 eV in state of 407 eV is like other samples. Observation of this peak (402.3 eV) was reported for GaN thin films [199]. The authors found this peak is corresponding to the presence of interstitial molecular nitrogen in the films [199]. The reason for the formation of the molecular nitrogen could be due to high roughness as noticed on the surface of this sample. Other samples show much smoother surfaces than samples processed at 0.13 Pa. Fig. VI.32(b) shows XANES spectra of samples heated at 1400 °C measured at O K edge. There are no changes in peak positions or intensities as pressure changes.
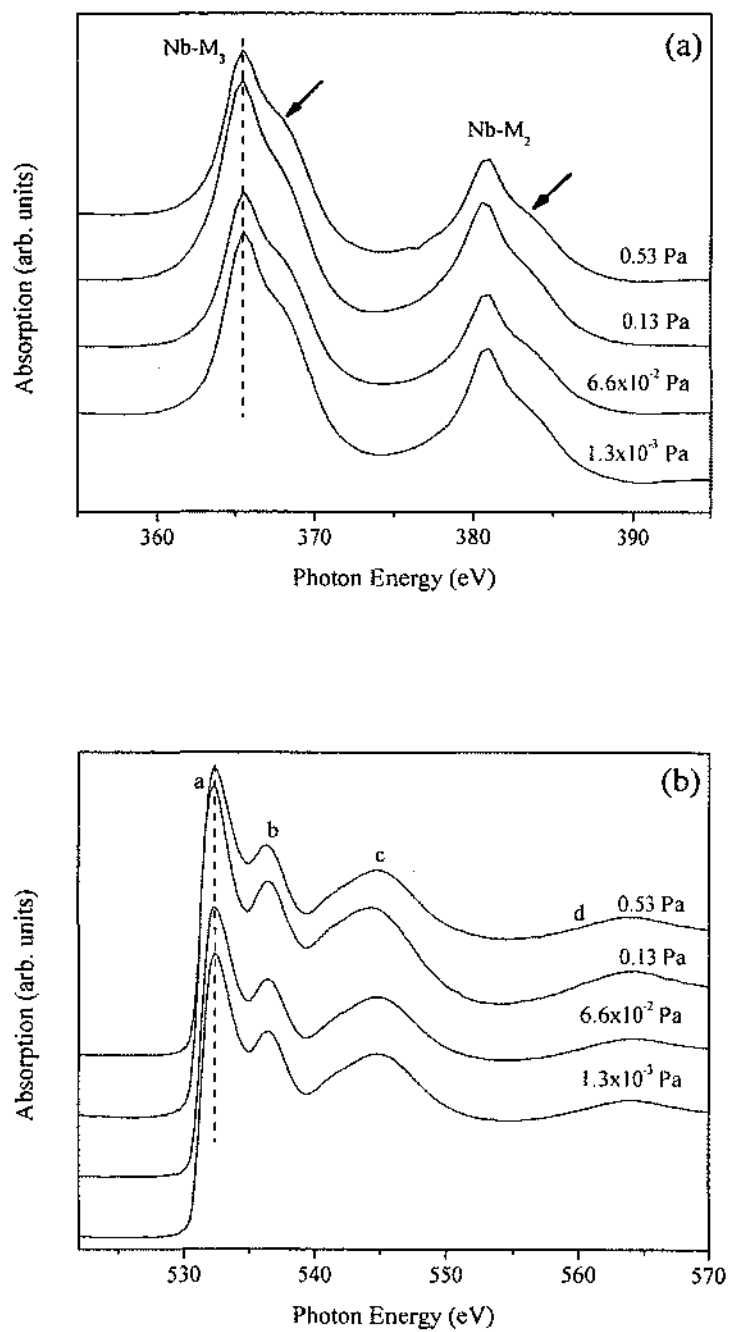
Fig. VI.32. XANES data for substrates heated for 180 min at 1400 °C temperature and different nitrogen pressures, (a) at Nb $M_{2,3}$ edge and (b) at O K-edge.

VI.3.2.2. THICK SAMPLES

XRD patterns of Nb with Nb substrates heated at about 0.13 Pa of nitrogen pressure in temperature range of 800-1150 °C for 60 min is shown in Fig. VI.33. No nitriding can be seen from XRD patterns for these samples until temperature of 1150 °C is reached. The same was noticed for the samples as shown by their 2D-XRD images in Fig. VI.34. The lattice constants of Nb three peaks with (110), (200) and (211) are shown in Fig. VI.33. There are slightly decreases in lattice constants with increasing temperature under constant pressure is about 0.9% of the values of lattice constant which can be considered within experimental errors of XRD measurements. The heating of these samples using spiral heater filament was not well controlled due large thickness (0.7 mm) of Nb substrates. That caused large temperature gradients over the samples since part of the sample was outside the heater.

Fig. VI.35 shows the XRD patterns of Nb substrate and samples heated at 900 °C in different nitrogen pressures 1.3×10^{-3}, 0.13 and 1.3 Pa for 60 min. The XRD patterns show the start of Nb nitrogen reaction as pressure is reaching 1.3 Pa, where sample shows peaks for mixed alpha and beta phases. The diffraction images of these samples are shown in Fig. VI.36. The 2D-XRD image of samples done at 1.3 Pa shows the formation of spotty rings for beta phase which is an indication of the formation of large size crystallites. The temperature at that pressure was not enough to cause more diffusion into material if it is compared to thin samples, and this is why large crystallites were formed.
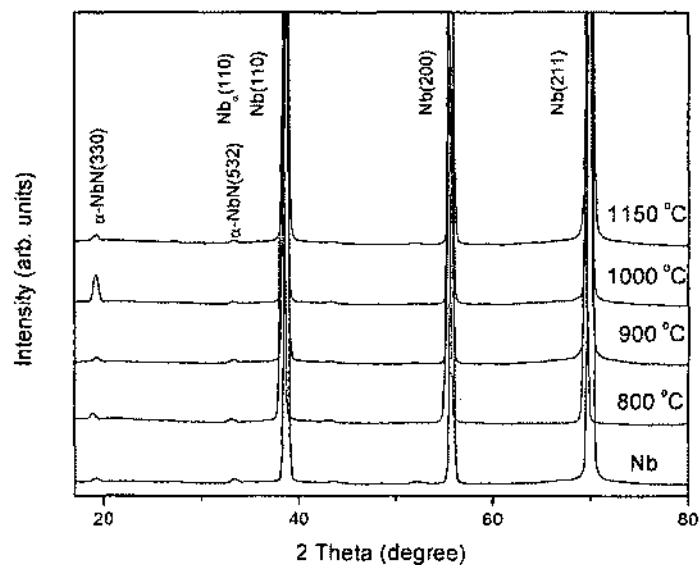
Fig. VI.33. XRD patterns of unheated Nb substrate and Nb heated for 60 min at 0.13 Pa of nitrogen pressure at different temperatures.
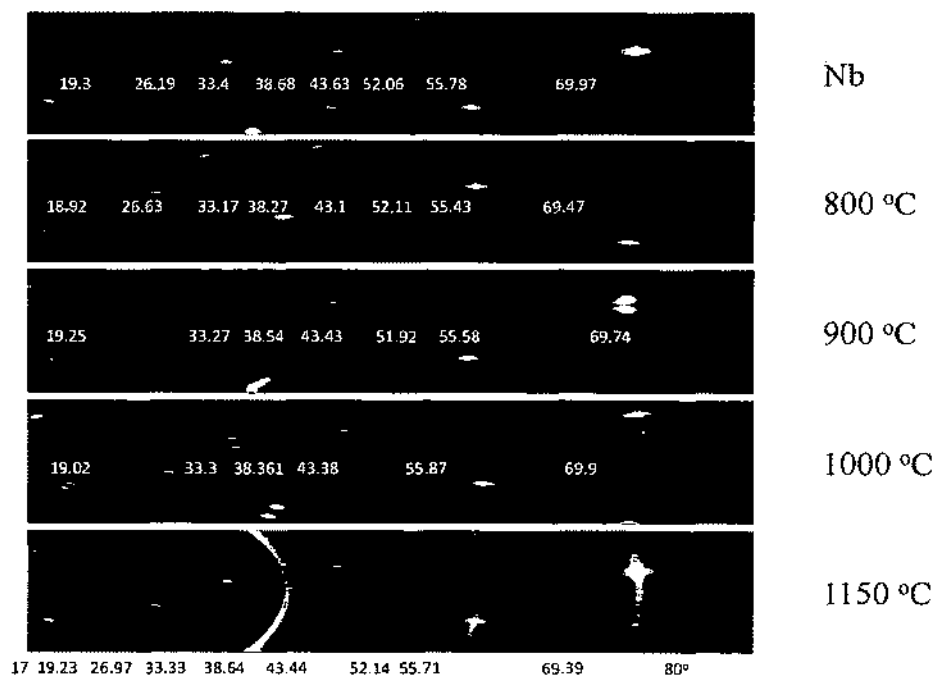
Fig. VI.34. 2D-XRD patterns of Nb heated for 60 min at 0.13 Pa of nitrogen pressure at different temperatures.
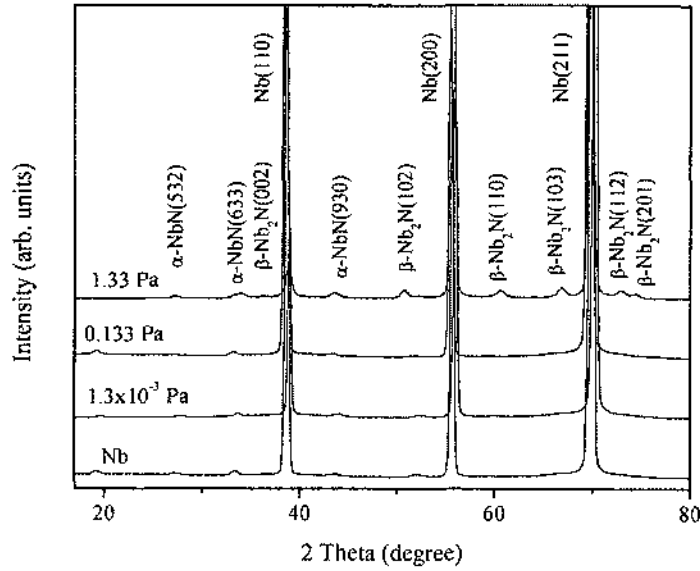
Fig. VI.35. XRD patterns of unheated Nb substrate and Nb heated for 60 min at 900 °C in different nitrogen pressures.
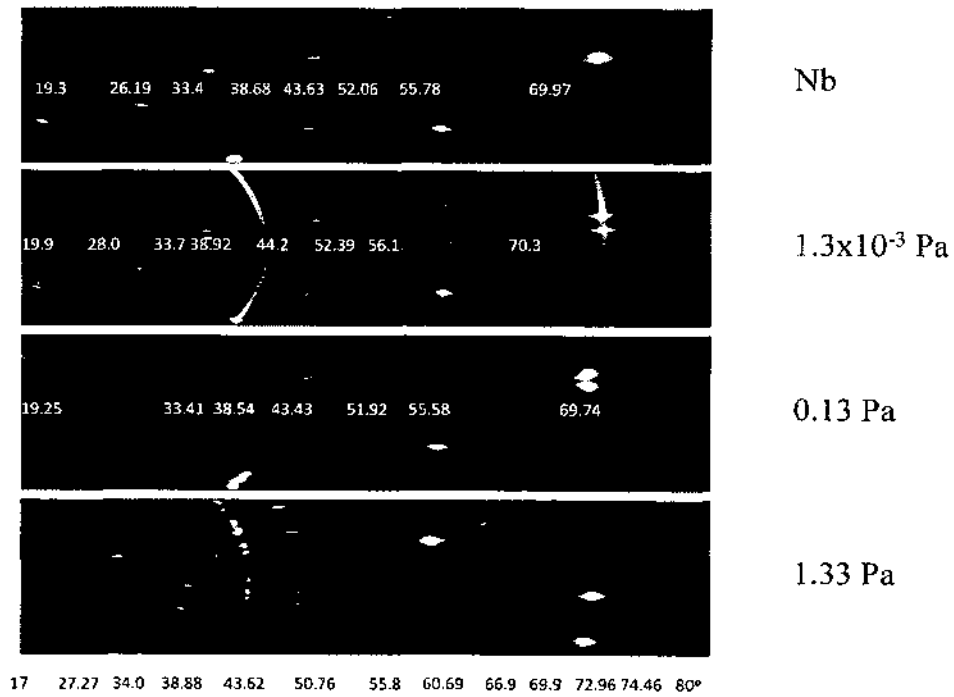
Fig. VI.36. XRD patterns of unheated Nb substrate and Nb heated for 60 min at 900 °C in different nitrogen pressures.

Fig. VI.37 shows XRD pattern of samples heated at 1000 °C, in pressure of 2.6x10^{-5} Pa at different heating times: 1, 3, and 6 hrs. Fig. VI.38 shows 2D-XRD images of unheated Nb substrate and Nb heated at 1000 °C, in pressure of 2.6x10^{-5} Pa. These samples were heated using 1″ diameter heater manufactured by HeatWave Labs Inc. As shown from the XRD pattern and 2D-XRD images, no change can be noticed for these samples with increased time of heating. Not much change is seen between unheated Nb substrate and those heated in a vacuum for several hours. No changes are noticed in peak positions of Nb (110), (200) and (211) or in the intensities of the peaks at 2Theta of about 19.3, 33.4 and 43.5°, even though they were seen in unheated Nb substrate, as shown in Fig. VI.38. These peaks may be attributed to multiple diffractions of main peaks of Nb. The peak at about 19.2° is at 2-theta value half that of Nb (110) or may be due to the monochromatic of X-ray source, as reported for peak at about 33.4°, is considered N(110) Kβ [200].

Fig. VI.39 shows samples heated using a 1 inch HetatWave Inc. heater. The temperature was raised to 1000 °C, then nitrogen gas was allowed to fill the chamber to pressure of 0.66 Pa. Samples were heated at different heating times: 10, 20, 30, 40, and 60 min as shown from XRD pattern of these samples; α-NbN and β-Nb$_2$N phases appear at lower heating times (10 and 20 min). As heating time is increased to 30 min, the samples developed another phase (δ-NbN) beside the other two phases. Increasing the heating time causes enchantments in the peak intensities for all phases. The δ-NbN peaks at (200) is starting to be seen in 2D-XRD as time of heating increases to 30 min.
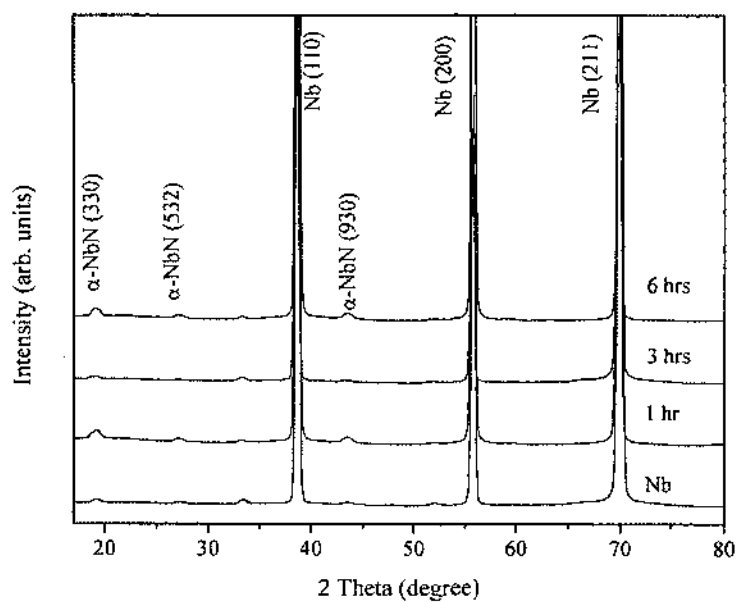
Fig. VI.37 XRD patterns of unheated Nb substrate and Nb samples that were heated at 1000 °C, in a pressure of 2.6×10^{-5} Pa.
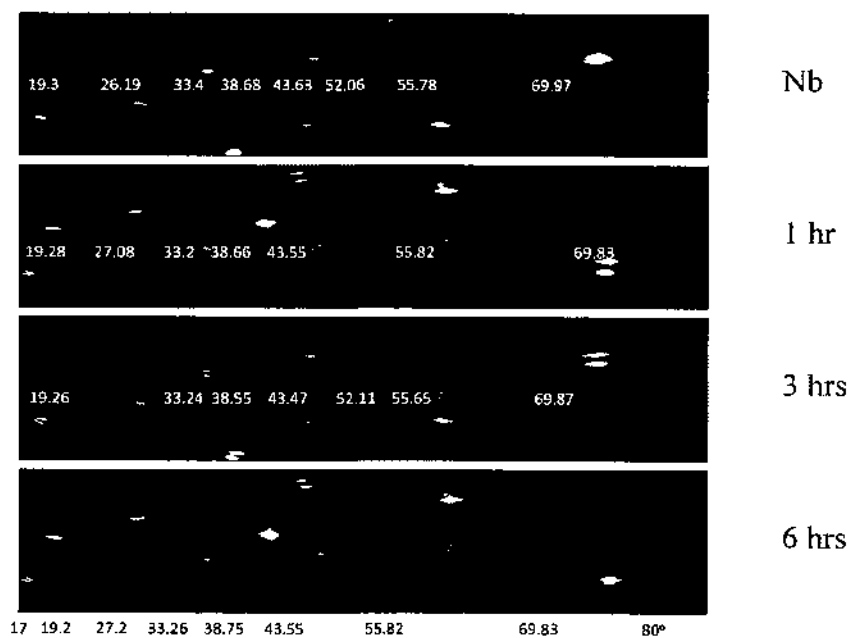
Fig. VI.38. 2D-XRD images of unheated Nb substrate and Nb that were heated at 1000 °C, in a pressure of 2.6×10^{-5} Pa.
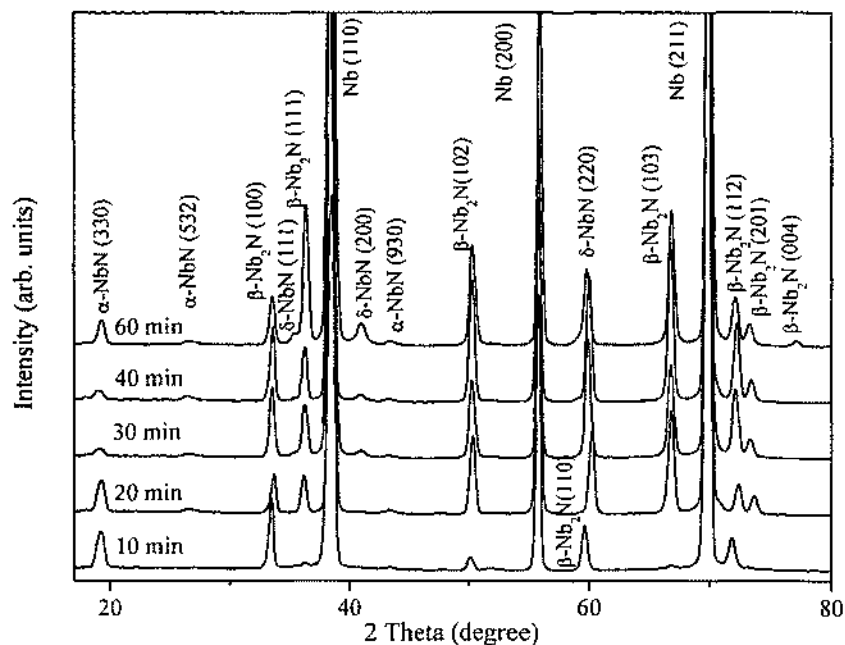
Fig. VI.39. XRD patterns of NbNx samples that were heated at 1000 °C, for different heating times in nitrogen pressure of 0.66 Pa.

The preferred orientation for the beta phase is showing change with time. The samples show phase transformation from XRD peak at β-Nb₂N (110) for samples heated at 10 and 20 min to δ-NbN (220) as the peak shifted to lower 2-Theta values with time of heating is increasing. 2D-XRD images for these samples are shown in Fig. VI.40. From the image of the sample heated for 10 min, one recognizes spotty features in the images, which are indications of growth of the β-Nb₂N phase with larger grain size. As time increases, the spots change to non-continuous rings, which indicated decease in the grain size of grown coating. The shape of the rings became more continuous with heating time increasing, which indicated formation of polycrystalline samples with smaller grain size than those obtained at lower heating times. The non-uniformity in the intensities of the diffraction rings is indication of texture of the formed crystallites. Diffraction spots

corresponding to alpha phase show spotty rings which are clearly seen in 2D-XRD in Fig. VI.40. This is an indication of the formation of large crystallites for alpha phase at short times of heating; then, crystallites' size decreases as heating time increases.
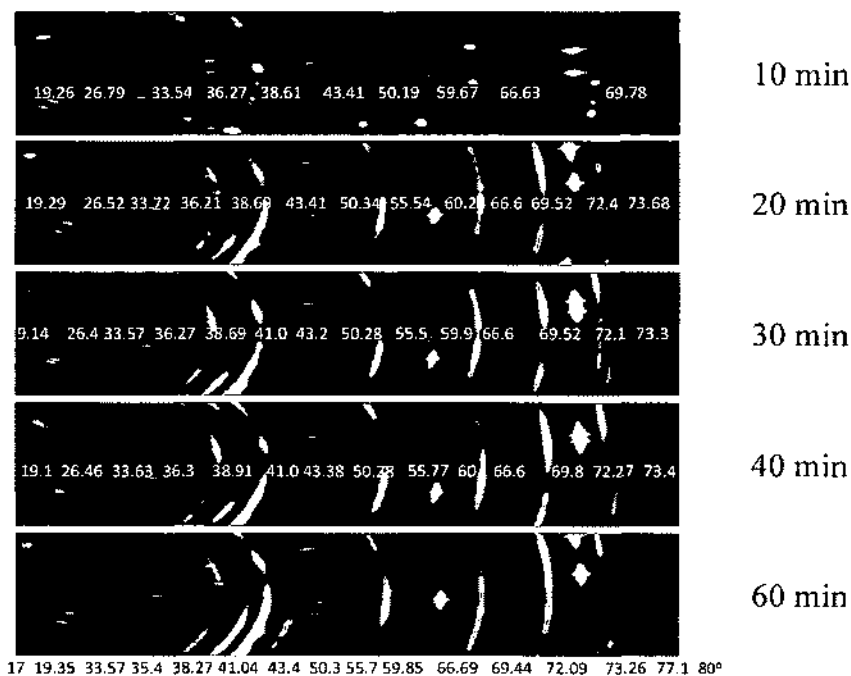
Fig. VI.40. 2D-XRD images of NbNx samples heated at 1000 °C for different heating times in nitrogen pressure of 0.66 Pa.

The c/a ratio of the hexagonal (β-Nb$_2$N) phase is shown in Fig. VI.41. As heating time increases, the c/a ratio of the hexagonal phase shows a small change until the δ-NbN phase becomes more pronounced in the samples. The decrease in c/a ratio may be because of the transformation of some XRD peaks of the β-Nb$_2$N phase into δ-NbN phase. Fig. VI.42 shows the mean crystallite sizes of hexagonal phase (β-Nb$_2$N) for

samples heated at 0.66 Pa, calculated from the Scherrer equation. At a very short time (10 min), the mean size of the crystallite is about 4 nm; as time of the heating increases to 20 min, the size of crystallites increases to between 12- 14 nm. There is not much change in crystallite size as heating time is increased to 60 min. The error bars shown in these figures represent standard deviations calculated from different peaks for same β-Nb_2N on each sample. NbN_x synthesis by reactive diffusion produced at higher pressure than that used here showed phase transformations as processing time increased [22]. Increasing processing time causes increase in the nitrogen content in the samples. XRD results confirm phase transformation of β-Nb_2N to δ-NbN as heating time is increasing. Such phase transformations are in agreement with phase diagrams of the Nb-N system and reported work on reaction of niobium with nitrogen [11, 91, 183].
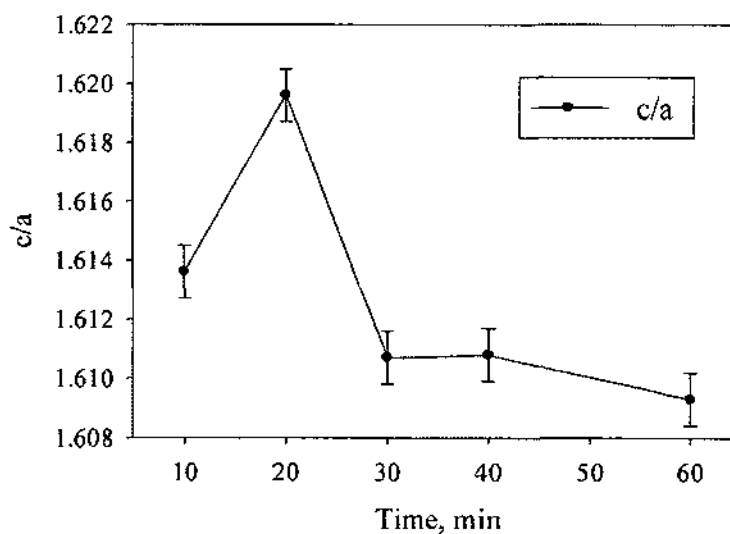
Fig. VI.41. The c/a ratio of hexagonal phase (β-Nb_2N) for samples heated at 0.66 Pa.
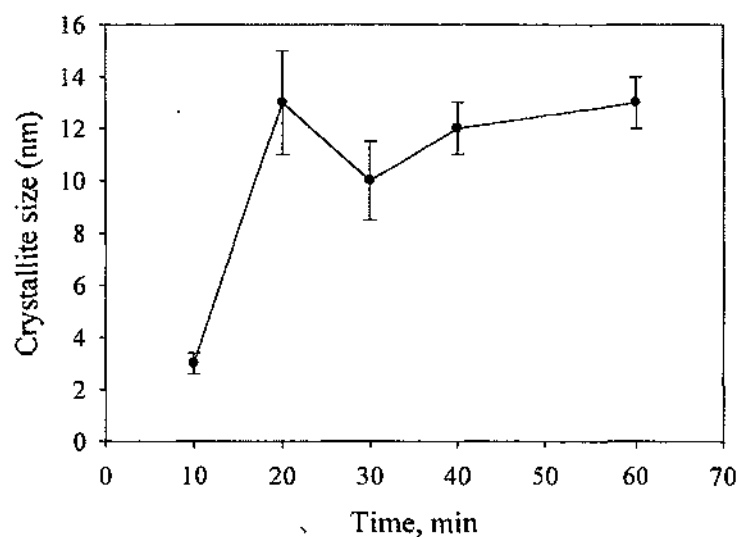
Fig. VI.42. Average crystallite size of hexagonal phase (β-Nb$_2$N) for samples heated at 0.66 Pa.

VI.4. CONCLUSION

VI.4.1. DIFFERENT PROCESSING TIMES

NbN$_x$ have grown using thermal diffusion of nitrogen. Nitriding was carried out at a temperature of 900 °C and occurred even for processing time as short as 5 min. Longer heating times resulted in larger grain size and higher N/Nb ratio in NbN$_x$. Analyses based on XRD, EPMA, AFM and XPS indicate that the surface layers are hexagonal β-Nb$_2$N. The NbN$_x$ surface layer thickness was observed to grow according to parabolic growth kinetics. XPS analyses confirm that the NbN$_x$ surface layer is reactive to oxygen contamination; especially when samples are exposed to air, a layer of Nb$_2$O$_5$ is formed. UPS measurements and DOS calculations of VB spectrum show a clear picture of two distinctive separations near E$_F$. In addition, strong and weak p-d hybridization is observed. Different heating times resulted in a thicker nitride layer with the increase of

nitrogen content in the NbN_x. However, longer processing times did not change the phase of the formed NbN_x. The present results indicate that a single hexagonal phase β-Nb_2N could be obtained by thermal diffusion at 900 °C in 133 Pa nitrogen atmospheres. Surface hardness was measured by nanoindentation. The hardness values ranged from 12 to 26 GPa, increasing with the nitride thickness. The idea of strengthening the surface hardness of Nb by growing NbN_x coating is applicable beyond superconducting cavities and can be useful in superconducting wires and in non-superconducting applications needing surfaces that are relatively chemically inert and have high hardness.

VI.4.2. LOW PRESSURE

VI.4.2.1. THIN SAMPLES

Four sets of thermal diffusion experiments were done on an Nb (0.2 mm thick) sheet. All samples were heated for same heating time (180 min). From XRD for samples heated at different temperatures (1250 – 1500 °C) and 1.3×10^{-3} Pa, formation of some grains can be recognized as α-NbN phase. Then, they get smaller as indicated by full rings obtained at 1500 °C. These values are also consistent with crystallite size calculations using the Scherrer relation. Crystallite size decreases from 23 nm at 1250 °C to about 17 nm at 1500 °C. No other phase is recognized in this set at all temperatures.

The XRD of Nb and the samples those heat-treated were presented. 2D-XRD images of samples processed at temperature range from 1250-1500 °C at low pressure of 1.3×10^{-3} Pa showed the formation of grains on Nb; this is due to alpha phase formation. The same thing was observed for samples processed at 1300 and 1400 °C. No changes were observed until nitrogen pressure reached 0.13 Pa, when β-Nb_2N phase starts to appear as mixed with existing phase. As pressure increases to 0.13 Pa and higher, the

samples have α-NbN phase mixed with β-Nb$_2$N phase. Lattice constants calculated from the three peaks with highest intensity showed transformation from decreasing to increasing manners as mixed phases appeared in samples

X-ray absorption near edge structure (XANES) measurements done at Nb M$_{2,3}$ edge showed Nb 3p peaks at 365.5 and 380.5 eV. The peak at 365.5 eV is stronger than that at 380.5 eV. These two peaks have double peaks for these two positions due to the formation of an oxide layer. From XANES done at Nb M$_{2,3}$ and O K edges, an oxide layer is confirmed to be an Nb$_2$O$_5$ layer on the surface of the samples. XRD and XANES measurements on thin samples confirm the formation of α-NbN phases for thin samples heated at high temperatures and low pressures. Increasing nitrogen pressure results in more alpha phase concentration, accompanied with an increase of other phase (β-Nb$_2$N).

VI.4.2.1. THICK SAMPLES

Some of the thick Nb substrates (0.7 mm) were heated in vacuum of 2.6×10^{-5} Pa at 1000 °C for different times. XRD showed not much change between unheated Nb substrate and the samples that were heated in vacuum at different times (1, 3, and 6 hrs). XRD of samples heated at 0.66 Pa nitrogen pressure and 1000 °C have mixed phases of (α-NbN) and (β-Nb$_2$N) at lower heating time (10 - 20 min) and (α-NbN), (β-Nb$_2$N) and (δ-NbN) as heating time was increased to 60 min. A transformation from (β-Nb$_2$N) to (δ-NbN) observed. The δ-NbN phases became more visible when heating time was increased to 60 min. Thick samples that were heated using a spiral filament heater were not well controlled. In the case of thin samples done at that pressure, a clear reaction is seen in XRD images. Thin samples were treated at higher temperatures than these done for thick samples.

CHAPTER VII

SUPERCONDUCTING NIOBIUM NITRIDE THIN FILMS ON Si (100) BY REACTIVE PULSED LASER DEPOSITION

VII.1. INTRODUCTION

The superconducting nature of niobium nitride (NbN_x) thin films makes them potential candidates for use in superconducting electronics, such as tunnel junctions [146, 167], coatings for superconductive cables [201], and single photon detectors [202-204]. Moreover, good mechanical properties, such as their high hardness [160, 205] and corrosion resistance [8, 177], make NbN_x suitable as a protective layer in active environments, such as in turbine engines and spaceships [11, 206]. The superconducting and mechanical properties of NbN_x are strongly affected by the composition and the crystal structure of the film. As the nitrogen content is changed in the Nb-N system, several types of crystallographic structures and phases are formed. NbN_x usually is found in mixed phases.

The growth of NbN_x on Si(100) is of much interest for optoelectronic applications because it can allow for integration with devices. Superconducting NbN_x films deposited on Si substrate can be used in hot electron bolometer (HEB) mixers [207, 208]. The preference for using Si substrate for these HEB mixers is because it shows low loss at operation frequencies of HEB mixers (few terahertz) [209]. Most studies on NbN_x are dealing with its superconducting properties [137-141] because of the highest transition temperature (17.3 K) [210]. Because of these extreme properties of NbN_x, considerable efforts have been devoted to the characterization and description of the physical, chemical, and mechanical properties of NbN_x.

In this chapter, NbN$_x$ films were deposited on Si(100) substrate at 800° C in different nitrogen gas pressures using reactive PLD. The morphology, electronic, and mechanical properties of the NbN$_x$ films were studied. The NbN$_x$ films showed different phase compositions and different T$_c$ as the pressures of nitrogen were changing. NbN nanoparticles were grown on Cu-grids and tested using a high resolution TEM.

VII.2. EXPERIMENTAL PROCEDURE

NbN$_x$ films were grown on a Si(100) single-crystal substrate by ablating an 1-inch diameter Nb target (99.995% pure). The chamber was equipped with a turbo-molecular and ion pump, operated at a base pressure of ~1.3×10^{-7} Pa. A pulsed Nd: YAG laser beam (wavelength λ = 1064 nm, repetition rate 10 Hz, pulse duration 40 ns) was focused with a 50 cm focal length lens at 45° onto a rotating (25 rpm) Nb target. The distance between the target and the substrate was fixed at 6 cm. The operating pressure of the nitrogen gas pressure is achieved by filling the chamber with the correct amount of gas and keeping it at the same pressure during deposition.

The Si(100) substrate was 3.0×12×0.5 mm^3, p-type boron doped with resistivity ranging between 0.060 and 0.075 Ωcm, and had a miscut angle 0.38°. The Si substrate was chemically etched using a modified Shiraki method [211] before being loaded into the chamber. In order to deposit cubic structure NbN$_x$ films, optimizations of the PLD parameters, such as the laser energy density, pulse repetition rate, and target-to-substrate distance, was done. The highly oriented crystalline structure of NbN$_x$ films was obtained with 15 J/cm^2 laser fluence and 800 °C substrate deposition temperature. The thickness of the deposited films is 25±5 nm, as measured by performing cross-sectional transmission electron microscopy measurements. The deposition rate was about 2-3 nm/min. The

thickness of the films was ~20 nm, as indicated by a high-resolution transmission electron microscopy (HRTEM) cross-sectional image.

Nb and NbN were grown on carbon-coated Cu grids using PLD. Laser fluence of 8 J/cm^2 and deposition temperature 300 °C were used. For growth of Nb pressure of ~3.6×10^{-5} Pa was used. NbN nanoparticles were grown at 40 Pa.

X-ray diffraction (XRD) was done using graphite-monochromated CuK_α radiation on a Bruker-AXS three-circle diffractometer, equipped with a SMART Apex II CCD detector. X-ray photoelectron spectroscopy (XPS) was performed by Drs. Y. Ufuktepe and S. Kimura at the UVSOR facility, Institute for Molecular Science, Japan, on 100-mm radius hemispherical photoelectron analyzer (VG Scienta SES-100) with Mg Kα X-ray radiation ($h\upsilon$= 1253.6 eV). The base pressure of the photoemission chamber was <2.0×10^{-8} Pa. Surface cleaning of the samples was performed at room temperature by using Ar$^+$ sputtering. The sputtering was carried out at 3 kV and 10 mA cm^{-2} beam current density, with an argon partial pressure of 1.5×10^{-5} Pa. The energy scale of the X-ray photoemission spectrum was calibrated by the binding energy of Au 4f level.

The morphology of the films examined using a Digital Instruments Dimension 3100 atomic force microscope (AFM). AFM images were taken in air using tapping mode. In addition, conventional four-point probe method measurements of thin films with a temperature accuracy of 0.01 K were used to obtain the superconducting transition temperature. The nanoindentation experiments probe the hardness and elastic modulus of the films, which is correlated to the structural, electronic, and superconducting properties of the thin films. Nanoindentation is an effective technique to investigate the mechanical properties of thin films and nanomaterial. This technique is capable of measuring the

moduli and hardness of thin films as a function of depth [190, 212, 213]. Nanoindentation experiments were conducted by Md. Mamun and Dr A. Elmsutafa at the ODU Applied Research Center, using a Nano Indenter® XP in conjunction with a continuous stiffness measurement (CSM) equipped with a three-sided diamond Berkovich indenter tip. During the CSM indentation testing, a small and well-controlled oscillation is introduced into the normal loading sequence of the nanoindenter, which enables the CSM to monitor the contact depth and the contact stiffness throughout the indentation loading. Hence, the CSM maintains the measurement of material properties as a continuous function of depth for a single indentation, as detailed elsewhere [184, 214]. A G-Series CSM Standard Hardness, Modulus, and Tip Cal method was adopted for the indentation experiments in this study. The indenter penetrated the sample surface with a harmonic displacement oscillation target of one nm at a frequency of 45 Hz to a depth of 500 nm with a strain rate of 0.05 per second. Surface detection criterion was set at 160 N/m for these tests. Ten indents were performed on each sample at different locations.

VII.3. RESULTS AND DISCUSSION

VII.3.1. TEM RESULTS

Fig. VII.1(a) shows the high-resolution TEM image for one of the NbN_x films grown at nitrogen background pressure of 13.4 Pa and substrate temperature of 800 °C. The TEM image of Fig. VII.1(a) depicts grains of columnar shape with random orientation. The film is continuous with no evidence of voids forming during the deposition. The TEM image in Fig. VII.1 (b) is for single grain enlarged from the image of Fig. VII.1 (a). It is evident that the grain size is ~ 25 nm.
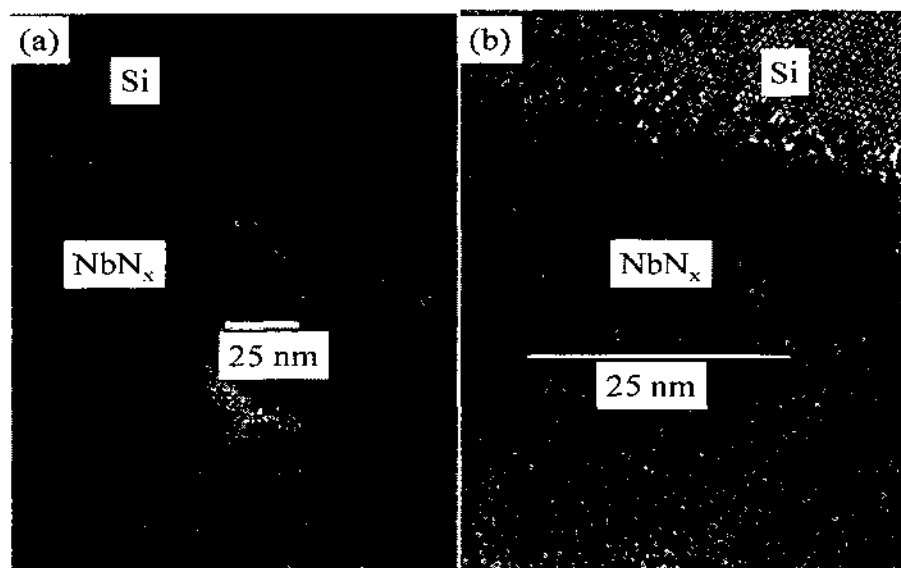
Fig. VII.1. TEM micrographs (a) TEM cross-section of NbNx thin film on Si(100) substrate. The film is deposited at 800 °C. (b) TEM images of NbN_x films. The grains are columnar and randomly oriented with an average grain size of 25 nm.

Nb and NbN nanoparticles were grown on Cu grids at laser fluence of 8.0 J/cm^2 and substrate temperature of 300 °C. Fig. VII.2 shows low magnification of high-resolution TEM (HRTEM) images and the diffraction patterns for (a) Nb sample prepared in vacuum and (b) NbN nanoparticles done at nitrogen pressure of 40 Pa. The formation of Nb is confirmed by the diffraction pattern of Fig. VII.2(a). NbN nanoparticles with varying sizes are formed as shown in Fig. VII.2(b). Diffraction patterns were obtained on one of these nanoclusters. High-resolution transmission electron microscopy images of samples deposited at 40 Pa is shown in Fig. VII.2. The sample shows show nanoparticles with multi-grains in these nanoclusters, as shown in HRTEM images Fig. VII.3.
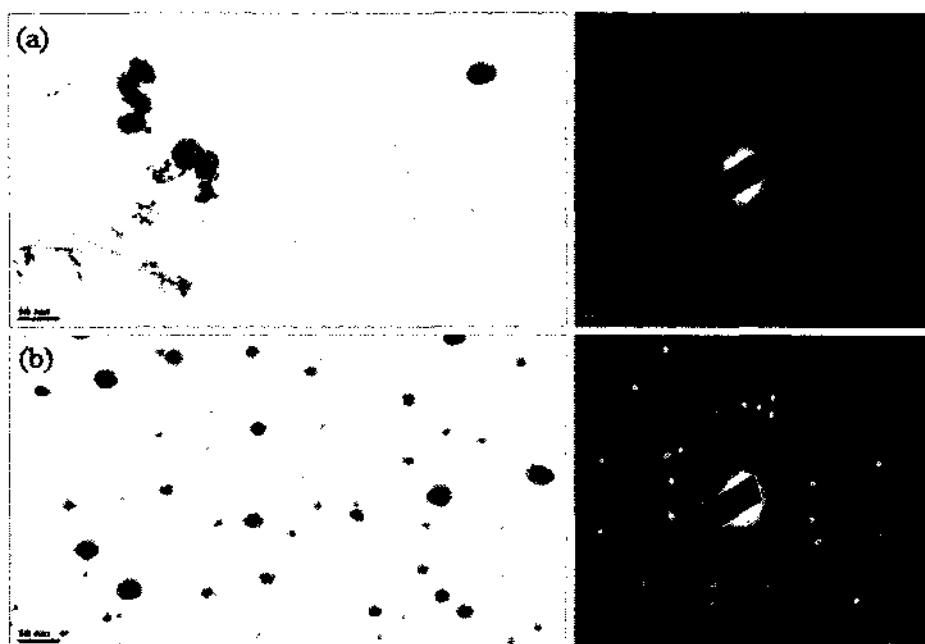
Fig. VII.2. HRTEM images and the corresponding diffraction pattern of (a) Nb samples deposited at 2.3×10^{-5} Pa and (b) NbN deposited at 40 Pa, with laser fluence of 8 J/cm^2.
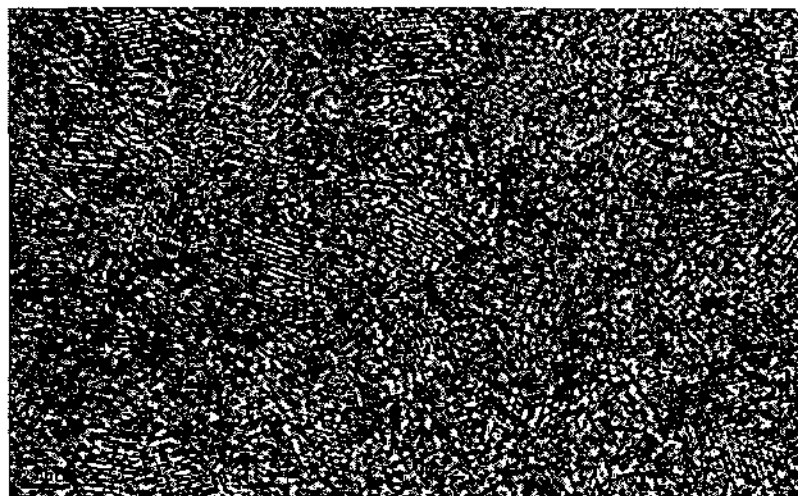
Fig. VII.3. HRTEM image of NbN sample deposited at nitrogen pressure of 40 Pa.

VII.3.2. STRUCTURE AND SURFACE MORPHOLOGY

The effect of nitrogen background pressure on the crystallinity of NbN_x thin films was examined by XRD measurements. Fig. VII.4 shows the XRD patterns of NbN_x films prepared at different nitrogen background pressures. The substrate temperature and laser energy density remained constant and only the nitrogen pressure was varied from 13.4-66.7 Pa. The influence of nitrogen pressure can be seen in Fig. VII.4. Two different crystalline structures were observed; the films were highly textured and were indexed with mainly the cubic phase of the δ-NbN and the tetragonal γ-Nb_4N_3. Variations of N/Nb ratio in the films may have contributed to the changes in the crystal structure with the increase of nitrogen pressure. Variations of the N/Nb ratio in the films may have contributed to the changes in the crystal structure for different nitrogen pressures.

Fig. VII.5 shows the variation of the lattice parameter and the crystallite size of the cubic phase calculated based on the (111) peak as a function of nitrogen background pressure. The mean crystallite size of δ-NbN was determined by the Sherrer formula [127]. The calculated values are in the range of 8.46 to 9.31 nm. The cubic δ-NbN phase can form over a specific stoichiometric range of $0.85< x <1.06$ with the change of lattice parameter a from 4.37 to 4.39 Å. The calculated values are in the range of $4.365 \leq a \leq 4.395$ and are consistent with the previous result [215]. Different lattice parameters were observed because crystal imperfections affect the lattice parameter; the higher the vacancies in NbN_x films, the lower a values [215].
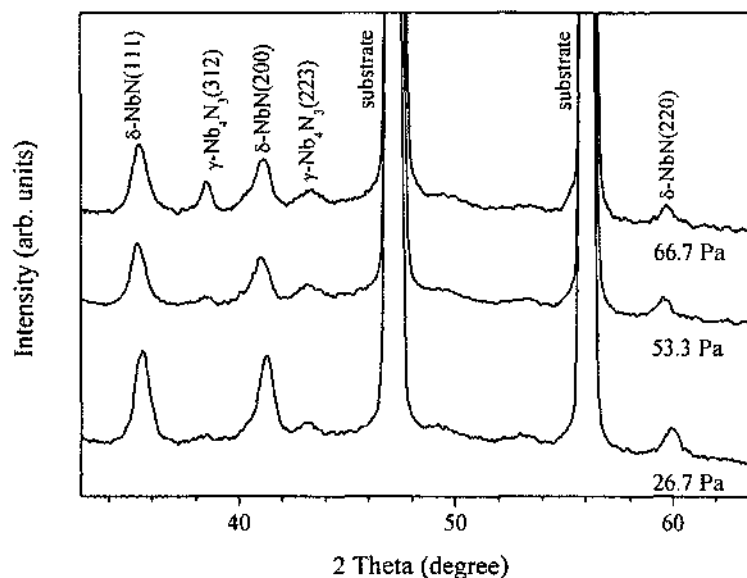
Fig. VII.4. XRD patterns of NbN$_x$ thin films deposited onto Si(100) substrate at different nitrogen background pressures.

The size of the (111) crystallite size in the film decreases with increasing background nitrogen pressure. The nitrogen background pressure reduces the kinetic energy and flux of the ablated materials. Therefore, for the lower deposition pressure, the surface mobility of adatoms is enhanced due to the high kinetic energy of atoms in the PLD flux. These enhancements in surface mobility result in larger crystallite size. In Fig. VII.4, the integrated area of the (111) peak for the sample grown at 26.7 Pa is higher than that for the other samples. Deposition at the lower pressures gives denser and highly (111)-oriented NbN$_x$ film consisting of larger crystallites. Higher background gas pressure not only lowers the kinetic energy of the ablated Nb but also the confinement of the plasma plume. This results in an increase in the probability of multiple collisions between ablated materials that yield formation of small crystallite size [216]. Therefore,

higher molecular nitrogen pressure is causing lower deposition rate and resulting in less

nitrogen ratio in the NbN_x film.
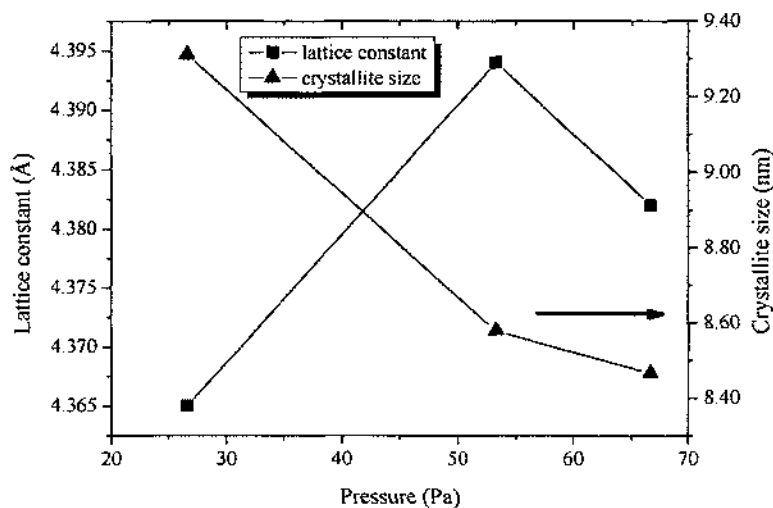
Fig. VII.5. Variation of lattice parameter and crystallite size of (111) plane with nitrogen background pressure. The solid lines are drawn as a guide for the eye.

AFM images of films prepared at different nitrogen background pressures are

shown in Fig. VII.6. The scanning area was 2 x 2 μm^2. The AFM image of the film

grown at 26.7 Pa consists of triangular islands of 100-200 nm sizes and heights of 15 nm,

as shown in Fig. VII.6(a). As the nitrogen pressure was increased to 53.3 Pa, the island

size and morphologies became more irregular in shape and with an average height of ~20

nm. For growth at a nitrogen pressure of 66.7 Pa, the size of the islands increases to

submicron as shown in Fig. VII.6(c). However, the average height of grains is ~21 nm,

which about the same as for film deposited at 53.3 Pa. When 66.7 Pa nitrogen pressure

was used, the island size increased significantly compared to lower pressures. At lower

nitrogen pressures, the niobium and molecular nitrogen flux incident on the substrate

surface are increased. The higher nucleation rate can cause smaller islands to grow. The reduced nitrogen content in the thin film with increased molecular nitrogen background could be due to reduced atomic nitrogen flux reaching the surface with pressure. As the nitrogen pressure is increased to 66.7 Pa, the diffusion length of the atomic nitrogen, generated from electron collision in the plasma plume with the background molecular nitrogen, is reduced and the recombination rate is increased.
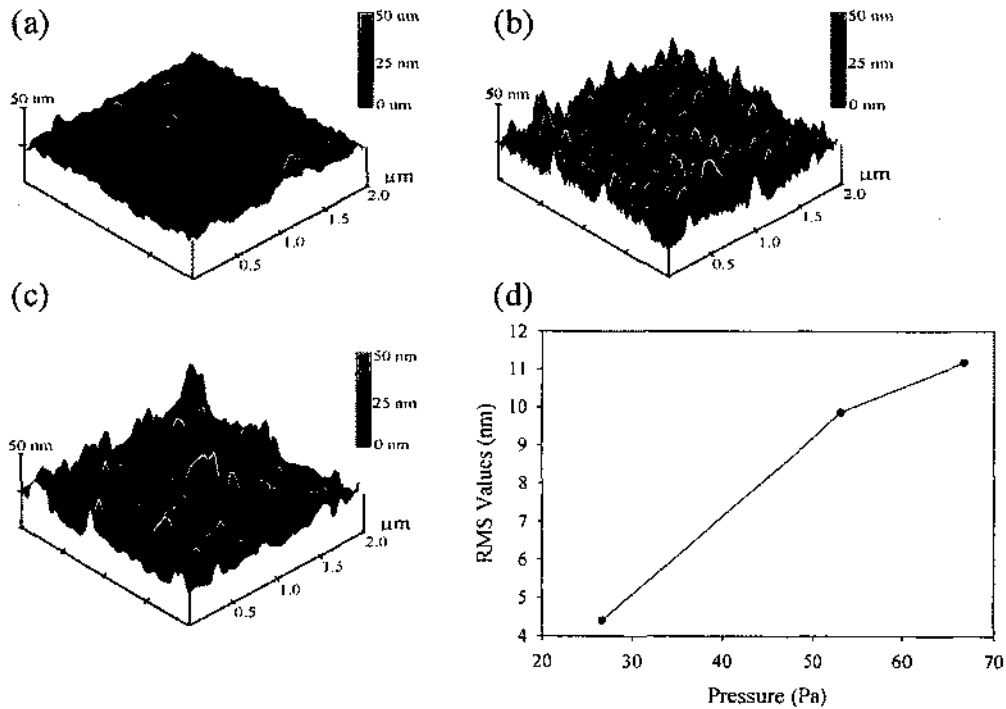
Fig. VII.6. The 3D-AFM images of films grown at (a) 26.7 Pa, (b) 53.3 Pa, and (c) 66.7 Pa and (d) Surface roughness RMS at different nitrogen pressures.

To check surface roughness, diagonal line scans on the AFM images were obtained. The root mean square surface roughness (RMS) was obtained from line scans

of AFM images. The surface roughness as a function of nitrogen background pressure is shown in Fig. VII.6(d). The surface roughness increases with increasing the nitrogen background pressure. The film grown at 26.7 Pa showed an RMS value of 4.4 nm. Roughness increased to 9.8 and 11.2 nm as the nitrogen gas pressure increased to 53.3 and 66.7 Pa, respectively. The increase in surface roughness is expected with increasing the background pressure. In PLD, the background pressure plays a crucial role in controlling the kinetic energy of adatoms and their diffusion into the surface. Low ambient gas pressure contributes to higher adatoms kinetic energy and this provides low surface roughness for the NbN_x films. The surface roughness results are consistent with that reported for β-Nb_2N films grown by PLD on Nb substrates for a similar range of nitrogen gas pressure [29].

VII.3.3. ELECTRONIC STRUCTURE

X-ray photoemission spectroscopy was used for electronic structure analyses. Fig. VII.7 shows XPS spectra of Nb $3d$ core levels for NbN_x films deposited at various nitrogen background pressures. The spectra are normalized so that maximum peak intensities are equal in each spectrum. Binding energies are given with respect to the Fermi level. The XPS spectra of the NbN_x films show a strong pair of peaks due to Nb $3d_{3/2}$ and $3d_{5/2}$ doublets. The corresponding peak positions are summarized in Table VII.1. Comparing NbN_x film spectra with that from pure Nb (205.5 and 202.3 eV), it appears that Nb $3d_{3/2}$ and $3d_{5/2}$ peaks are shifted to higher binding energies as a result of Nb-N bonding, indicating the transfer of electrons from niobium to nitrogen. The peak at ~210 eV corresponds to a niobium oxide, which suggests that the samples were contaminated by oxygen after deposition as they were exposed to air. The binding energy

values of Nb $3d_{3/2}$ and $3d_{5/2}$ doublets were previously determined for NbN_x, $NbN_{(1-y)}O_y$ and NbO [144, 217]. The results indicate that the $3d$ level of all the deposited films is not supporting the structure of a niobium oxide or oxynitride and the spectra are consistent with that of NbN_x [218-221].

Table VII.1. XPS binding energies of Nb 3d in NbN_x films deposited at different N_2 background pressures.

N_2 pressure (Pa)	Nb $3d_{5/2}$ (±0.05) (eV)	Nb$3d_{3/2}$ (± 0.05) (eV)	Nb-N bond (±0.05) (eV)
26.7	204.00	206.81	209. 83
53.3	204.09	206.92	209.64
66.7	204.08	206.90	209.72
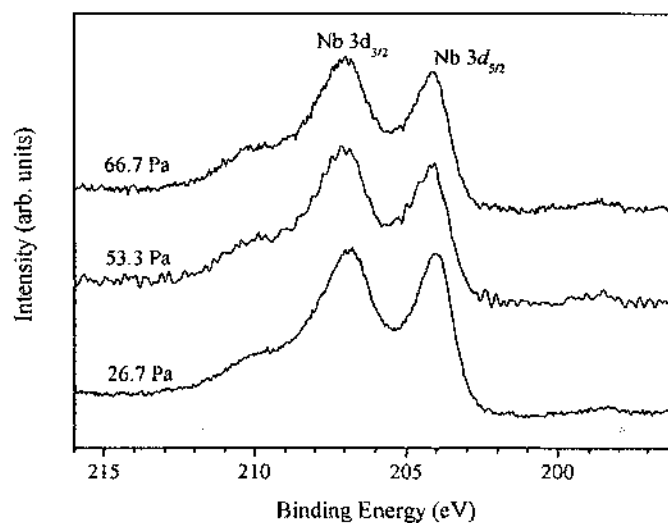
Fig. VII.7. Nb 3d XPS spectra of NbN_x films deposited at various N_2 background pressures. Data were obtained and analyses were conducted by Drs. Y. Ufuktepe and S. Kimura at the UVSOR facility, Institute for Molecular Science, Japan.
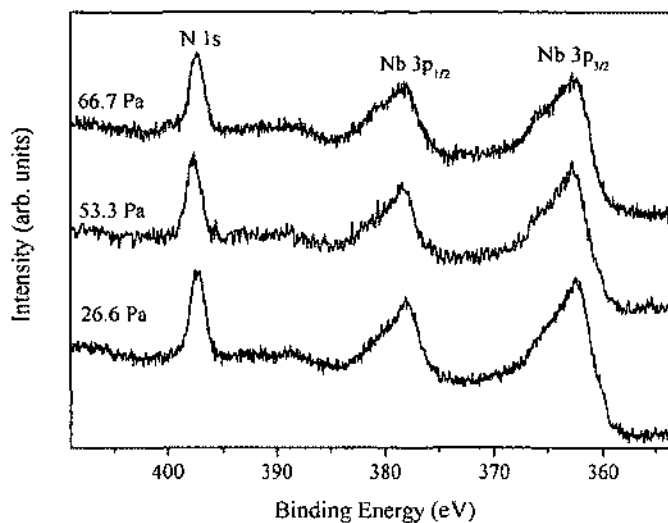
Fig. VII.8. XPS spectra of Nb 3p core level for NbN$_x$ films deposited at different background pressures. Data were obtained and analyses were conducted by Drs. Y. Ufuktepe and S. Kimura at the UVSOR facility, Institute for Molecular Science, Japan.

Nb 3p core level spectra of NbN$_x$ films are shown in Fig. VII.8. The spectra consist of two 3$p_{3/2}$ and 3$p_{1/2}$ doublets and strong N 1s peak. The corresponding binding energy values are given in Table VII.2, which are consistent with the previous NbN$_x$ studies [219, 220]. Note that the 3p binding energy doublets are shifted to the lower energy side as compared to the Nb 3p peak of pure Nb. This shift is in agreement with electron donation to the nitrogen atoms and a clear indication of the NbN$_x$ structure.

The intensity of photoelectron peaks is directly related to the content of Nb and N in the NbN$_x$ film and can be used for determination of the chemical composition of the surface. The relative concentration of nitrogen in NbN$_x$ as a function of background pressure was calculated by using the ratio of the background corrected integrated areas under the N 1s and NbN 3d peaks in the XPS spectra and normalizing with atomic cross-

section of each level at Mg $K\alpha$ radiation [222]. The calculated x (x = N/Nb) values are

0.90, 0.88, and 0.80 for 26.7, 53.3, and 66.7 Pa samples, respectively, which are in

agreement with previously reported on cubic and tetragonal phases of the Nb-N system

[3, 223]. The content of N in NbN_x films is slightly decreasing as the tetragonal phase

becomes visible with the increase of nitrogen background pressure during deposition. γ-

Nb_4N_3 has a distorted δ-NbN structure and the δ to γ phase transition was observed when

x in NbN_x changed [11, 148]. A N $1s$ spectrum showed that the peak position slightly

shifted to lower binding energy (0.2 eV) when the nitrogen background pressure changed

from 26.7 to 66.7 Pa. Broadening of the N $1s$ lines may be due to increasing the N/Nb

ratio and is related to the greater number of sites occupied by N atoms in NbN_x films

[37]. In Table VII.2, the energy separation between N $1s$ and Nb $3d_{5/2}$ peaks (Δ) shows

similar behavior. A decrease in (Δ) is due to an increase in charge transfer from Nb to N

when higher nitrogen background pressure is used. It is reported in the literature that the

binding energy value Δ associated with N $1s$ and NbN $3d$ indicates the covalence level of

the NbN_x film [206].

Table VII.2. The 3p doublet binding energies of NbN_x films deposited at different N_2 background pressures.

N_2 pressure (Pa)	NbN $3p_{5/2}$ (±0.05) (eV)	NbN $3p_{1/2}$ (±0.05) (eV)	N $1s$ (±0.05) (eV)	Δ=N $1s$ − NbN $3d_{5/2}$ (± 0.05) eV
26.6	362.47	378.00	397.50	193.29
53.3	362.63	378.10	397.29	193.21
66.7	362.85	378.20	397.30	193.17

Fig. VII.9(a) shows the UPS valence band (VB) spectra of the three different NbN$_x$ films. The valence band spectra were recorded using He II radiation (40.8 eV) from a discharge lamp. The VB spectra are mainly dominated by two peaks below the Fermi level. Strong and weak hybridization of Nb 4d and N 2p levels occur at about 1 and 6 eV, respectively. In the case of the sample grown at 26.7 Pa, the peak in the region of 6 eV is narrowed and shifted to lower binding energy in comparison with the other two films, while the emission just below the Fermi edge is characterized by broad emission. In order to compare two different phases of NbN$_x$ films, VB spectral subtraction of the samples grown at 26.7 and 66.7 Pa nitrogen is done as shown in Fig. VII.9(b). The difference between the spectra of films grown at 26.7 and 66.7 Pa is exhibited positive and negative peaks at 3.5 and 8 eV, respectively. This is due to the difference in nitrogen content and NbN$_x$ phases of these two films.

To better understand the valence band electronic structure of the NbN$_x$ system, the calculated density of states (DOS) of cubic and tetragonal NbN$_x$ is shown in Fig. VII.9. Density Functional Theory (DFT) calculations were carried out using the Abinit code [188], based on DFT and the Many-Body Perturbation Theory. It is clear from the figure that the electronic structures of these two phases are quite similar and two distinctive regions are visible by the peak centered at -6 eV and the second region between 0 and 4 eV. The first region is between -4 to -8 eV and mainly arises from the degeneracy between N 2p and NbN 4d states. The overlap of the nitrogen p and niobium d a level is associated with the covalent bonding between metal and non-metal elements. The second region, just below and above the Fermi level, originates mainly from the NbN 4d state.
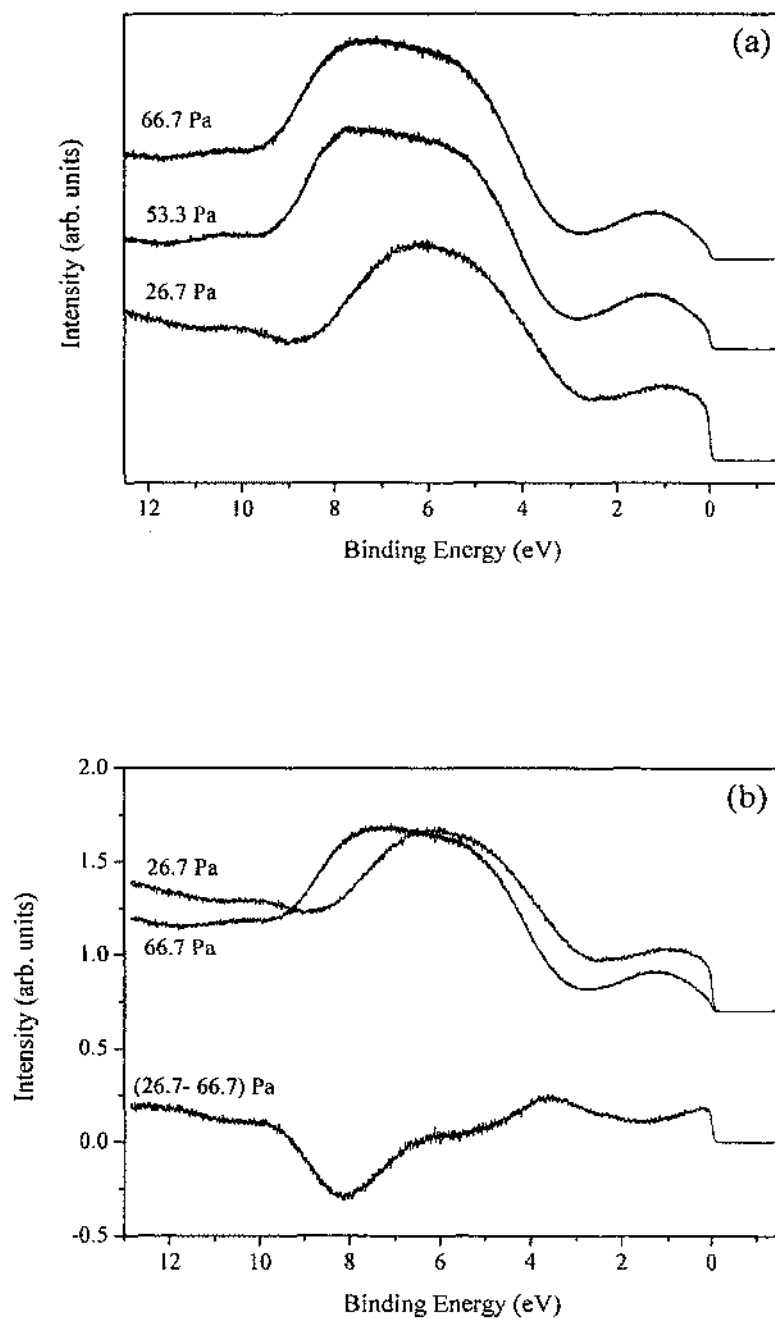
Fig. VII.9. UPS spectra (a) Valence band spectra of NbN_x thin films. (b) In each spectrum, the UPS signal of the Fermi edge was set to the same point. The difference in the VB spectrum was obtained by subtracting 26.7 and 66.7 Pa spectra shown at the bottom.

VII.3.4. SUPERCONDUCTOR PHASE TRANSITION TEMPERATURE

The superconductor measurements were performed to determine performances of the NbN_x films. The temperature dependence of the electrical resistivity for films at different nitrogen background pressures is shown in Fig. VII.10. All three samples had the transition to the superconducting state in the range of 7.66-15.07 K. Different transition temperatures related to the crystalline phases of the NbN_x films. The highest superconducting transition temperature (T_c) of 15.07 K is observed for NbN_x film deposited at 66.7 Pa nitrogen background pressure. XPS analyses showed that all films are nearly stoichiometric in composition, with a very small change of x in NbN_x observed with the increase of nitrogen background pressure. Lowest superconducting transition temperature observed for the film that deposited at 26.7 Pa could be understood based on the rich cubic phase of the film, which has a large amount of vacancies. Cubic δ-NbN phase has the highest superconducting transition temperature. It should be noted that one did not observe pure cubic phase at 26.7 Pa nitrogen pressure. The presence of mixed phases affects the critical temperature. As the nitrogen background pressure is increased, the number of vacancies in the film decreases, the lattice constant becomes larger, and the superconductor properties of the NbN_x film improve. The superconducting transition temperature (T_c) for each film increases from 7.66 to 15.07 K by varying the nitrogen background pressure from 26.7 to 66.7 Pa, as shown in Fig. VII.10, while the resistivity measured at 20 K increases from 60 x 10^{-3} to 120 x 10^{-3} Ohm.cm. The experimental results can be understood based on the crystal and electronic structure of the NbN_x films. The microstructure of the NbN_x films has great effect on the superconducting T_c, even when the stoichiometry is close. Changes in texture and granular structure of the NbN_x

films influence the T_c of the films [176]. The lowest T_c was observed for the sample deposited at a pressure of 26.7 Pa. This is mainly a consequence of the film structure being δ-NbN phase with a large number of vacancies. For deposition at 66.7 Pa nitrogen background pressure, the film had a mixed phase structure of δ-NbN and γ-Nb$_4$N$_3$ with reduced vacancies. This film exhibited a higher T_c value. Moreover, for deposition at 66.7 Pa, the lattice parameter becomes very close to the bulk (4.393 Å) of fcc δ-NbN, which favors higher T_c. It was reported that metal and nonmetal vacancies are effective in reducing T_c in NbN$_x$ [224]. When a sufficient number of vacancies are removed from NbN$_x$, electron transfers to the conduction band and increases the lattice size. Because of the effect on the electron concentration, T_c increases. The slope of the resistivity curve is an indication of film transport quality; a more negative slope indicates reduced electron scattering by grain boundaries and point defects such as vacancies. This slope is most negative for film deposited at 66.7 Pa, and this slope becomes less negative as the background nitrogen pressure is reduced.
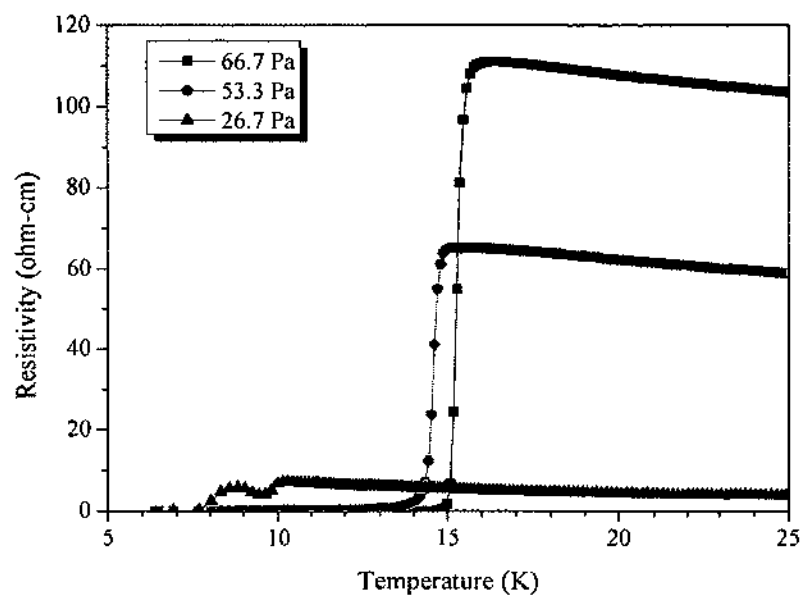
Fig. VII.10. Resistance versus temperature of NbN_x films deposited at different background pressures. Data were obtained by Dr. Y. Ufuktepe at the UVSOR facility, Institute for Molecular Science, Japan.
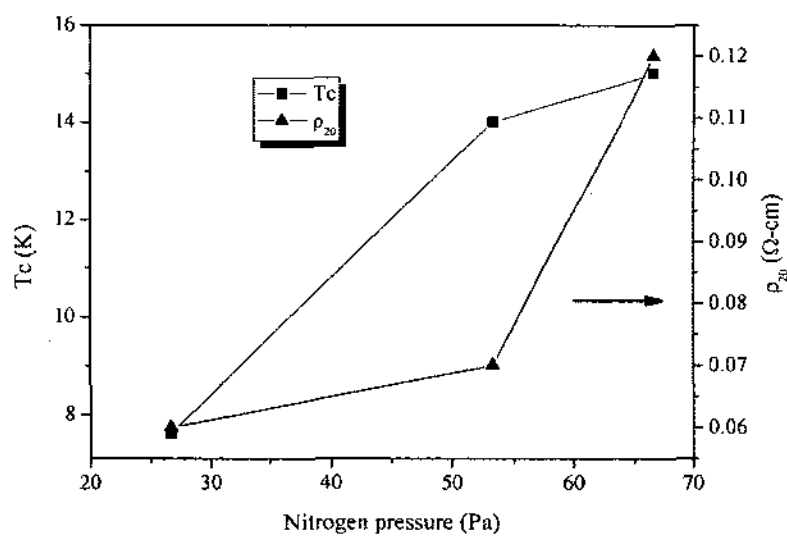
Fig. VII.11. Superconductor transition temperature (T_c) and the resistivity measured at 20 K (ρ_{20}) as a function of nitrogen background pressure.

VII.3.5. HARDNESS USING NANOINDENTATION

The nanohardness of NbN_x thin films on Si substrate deposited at different ambient nitrogen pressures was determined. The Meyer hardness is defined as the maximum load (from the load-depth curve) over the projected area. The measured hardness has an average of 12 GPa for deep indents, which represents the hardness of the Si substrate. At shallow depth of indentation; i.e., a depth of 20 nm, the hardness increases to an average value of 14, 16, and 18 *GPa* for the samples deposited with nitrogen pressures of 26.7, 53.3, and 66.7 Pa, respectively. The average hardness of the Si substrate agrees well with literature-reported values [225].

The superconducting and mechanical properties of NbN_x films are strongly affected by the Nb-N composition and the crystal structure. The hardness and elastic modulus correlate with the variation of the concentration of the hexagonal δ'-NbN phase [8, 146]. The films with high concentration of the hexagonal δ'-NbN phase exhibit high hardness and high elastic modulus [33]. Since FCC δ-NbN possesses superior superconducting properties, it is therefore essential to control the biaxial compressive stress in the film that might produce phase transformation [78]. The correlation between the nanomechanical properties and T_c of the NbN_x films was previously attributed to number of nonmetal vacancies found in the film. As the number of vacancies increases, the number of chemical bonds is reduced and this decreases the strength of the material [221]. Work done on group IVb nitrides (TiN_x, ZrN_x, and HfN_x) related the deceases in hardness and elastic module to the increases in the numbers of nonmetal vacancies in these films [48]. The film deposited at 66.7 Pa, which had highest T_c, showed the highest hardness values compared to the other two samples. The increase in hardness is related to

the reduced vacancy density and the increase in the γ -Nb$_4$N$_3$ phase mixed with δ-NbN for deposition at 66.7 Pa nitrogen. Fig. VII.11, of the resistivity curves for three films, shows a negative temperature coefficient of resistivity measured above ~16 K.

VII.4. CONCLUSION

Niobium nitride thin films grown on Si(100) at different nitrogen background pressures by PLD were studied. The reactive PLD process yields stoichiometric NbN$_x$ films, with high T$_c$ 15.07 K at 66.7 Pa, an ambient gas pressure, onto a silicon substrate held at 800 °C. Changing of the background gas pressure during deposition shows significant effects on the phase orientations, morphologies, and superconducting transition temperature. The lowest T$_c$ value of 7.66 K can be attributed to the existence of vacancies in cubic NbN$_x$. A systematic increase in lattice parameters with nitrogen background pressure and a decrease in the size of the crystallite are attributed to the second tetragonal NbN$_x$ phase. The shift in binding energy of Nb core level is directly related to the occupied number of electrons. Nevertheless, highly textured NbN$_x$ layers with good superconducting properties can be prepared on silicon using PLD. It is important to optimize all deposition parameters of PLD. The result reveals that controlling the nitrogen pressure in the deposition chamber at a suitable range could improve the crystalline quality to show better superconductivity. The formation of NbN nanoparticles is confirmed by HRTEM results done on sample prepared by PLD at laser fluence and nitrogen pressure of 8.0 J/cm^2 and 40 Pa, respectively.

CHPATER VIII

MICROSTRUCTURE AND ELECTRONIC PROPERTIES OF NbN_x

PREPARED BY LASER NITRIDATION

VIII.1. INTRODUCTION

The superconductivity and mechanical properties of niobium nitride compounds (NbN_x) are motivating the study of methods to grow and characterize their properties. These properties make them attractive in a wide range of applications such as in microelectronics, optoelectronics, and for hard and corrosion protective coatings. The superconducting microelectronic applications of NbN_x films include superconducting quantum interference devices (SQUIDs) [226], RF superconducting accelerator cavities [6] high resolution X-ray detectors, superconducting quantum mixers [209] and superconducting single-photon detectors (SSPDs) [227]. The properties of NbN_x films are affected by the film's crystal structures and composition. In addition, the attractive mechanical properties of NbN_x films such as, high hardness and wear resistance, make them promising in many surface coating applications. The NbN_x films have high values of bulk modulus and Vickers hardness which make them attractive as a coating for superconducting cavities for particle acceleration.

NbN_x has many different equilibrium phases such as: α-NbN solid solution of nitrogen in niobium, cubic δ-NbN, different hexagonal phases that include β-Nb_2N, δ'-NbN, ϵ-NbN, and η-NbN; and the tetragonal phase γ-Nb_4N_3. The δ-NbN phase is the phase of most interest for superconducting applications because of its relatively high critical temperature (17 K) [8]. The reactivity of Nb with nitrogen increases at high temperatures (>900 °C) [3]. One of the techniques to obtain thin films of NbN_x is by

heating of the Nb substrate at high temperature under nitrogen gas environment [6]. Here the study is on the nitridation of Nb by nanosecond and femtosecond laser heating in a nitrogen atmosphere.

The advantages of using pulsed laser heating to obtain nitrides over thermal nitriding include fast treatment, precise depth-profile control of the nitrogen content, adaptability to materials with different shapes, and applicability to materials that are sensitive to heat [7]. The basis of pulsed laser nitridation is the chemical-physical interaction of melted surface with plasma produced by laser in the background nitrogen [228]. The properties of the new compounds that result as an outcome of this reaction depend on the properties of the laser and also laser-substrate interactions. These reactions are complex since they depend on laser-plasma and substrate interactions. Conformal NbN_x coatings on Nb are important for radio frequency cavities with very high quality factors. A new generation of accelerators employs superconducting Nb radio frequency (RF) cavities to achieve the highest accelerating field. Hydrogen diffusion in Nb can adversely affect the performance of the superconducting RF cavity. A high-quality NbN_x coating on Nb increases hardness of the surface and also provides a barrier layer for hydrogen diffusion into Nb for potential application of RF cavities. Nitriding the surface of Nb improves the mechanical properties of the surface by increasing hardness and wear resistance [6, 64, 229, 230].

Pulsed laser nitriding was applied for many different materials including metals and their alloys [228, 231, 232]. A ruby laser (pulse duration of 25 ns) was used for nitriding of Nb in liquid nitrogen vessel [233]. Films in that work showed a mixture of δ-NbN and β-Nb$_2$N phases as shown in their XRD patterns. Nitridation by laser heating of

Nb using Nd: YAG (1064 nm) laser with pulse duration of 15 ns showed that the δ-NbN phase is not present up to a fluence of 3.9 J/cm^2 at nitrogen pressure of 7.3×10^4 Pa [15]. Although the simulation predicted that the Nb surface reaches its boiling point leading to a reaction with nitrogen.

In the present work, a series of experiments was performed to investigate formation of NbN$_x$ on Nb using femtosecond and nanosecond laser heating. The goal is to study the nitride growth parameters, especially optimized laser fluence required to obtain high quality NbN$_x$ films. The formation of different NbN$_x$ phases at various laser fluences and the resulting surface morphology were investigated.

VIII.2. EXPERIMENTAL SETUP

Nb substrates were cut by wire electro-discharge machining from niobium slice (CBMM Company, Brazil) to the dimensions of 8.6 × 6.6 × 0.7 mm^3. The surface preparation of the Nb was done in several steps. Before cutting the substrates, the surface of the Nb slice was mechanically polished with Al$_2$O$_3$ abrasive disks. The grain size of the Nb slice is of several cm^2; and therefore, the samples were either single crystals or had a single grain boundary. Then, a buffered chemical polishing (BCP) method was used for etching the samples [156]. The BCP solutions (1:1:1 and 2:1:1 HPO$_3$:HNO$_3$: HF) were used at a temperature of 10 °C during the cleaning process. Approximately a 50 micron layer of material was removed by BCP. The etched samples were rinsed in deionized water then dried under nitrogen flow. After uploading the Nb substrate into the vacuum chamber, the chamber was pumped down to a vacuum to ~8×10^{-6} Pa. The laser heating of the Nb substrates was done under nitrogen atmosphere. All samples were processed at room temperature. Two separate sets of experiments were done at different

laser fluences and nitrogen pressures. The laser fluence was measured just before entering to the camber and corrected for losses in the glass viewport on the chamber.

One laser used for nitridation was a Q-switched Nd: YAG laser operating at 1064 nm wavelength with a pulse width of 40 ns and repetition rate of 10 Hz. The laser beam size on the Nb surface was 350 ± 50 μm, as measured by the knife-edge method at target equivalent plane. The laser threshold fluence for nitride formation was about 1.9 ± 0.1 J/cm^2. During nitridation, the sample was moved in the x-direction with a speed of 0.43 ± 0.02 mm/s allowing the laser beam to raster the sample surface in the x-direction from one end to another followed by a step of 0.05 mm in the y-direction until all the surface of the sample was scanned by the laser. The samples were prepared at different laser fluences in the range 1.8 to 6.0 ± 0.1 J/cm^2 at room temperature and the same nitrogen pressure of 2.7×10^4 Pa.

Another laser used for nitridation was a femtosecond (fs) Ti: sapphire laser operation at a wavelength of 800 nm, pulse width of 100 fs, and repetition rate of 1.0 kHz. All samples processed by the fs laser were done at room temperature under constant nitrogen pressure of 4.0×10^4 Pa. The laser energy density is in the range was 0.11– 1.31 mJ/cm^2. Similar sample scanning was used as for the Nd: YAG laser.

Bruker-AXS three-circle diffractometer with graphite-monochromatic CuK_α radiation and a SMART Apex II CCD detector were used for the X-ray diffraction (XRD) measurements. An XRD of cleaned Nb substrate indicates that the Nb substrate exhibit crystallographic Nb with (110), (200), (211), and (310) orientations. The morphology of the samples was studied using a JEOL JSM-6060 LV scanning electron microscope (SEM). The SEM images were taken at an accelerating voltage of 20 kV. The chemical

composition (N/Nb = x) of the NbN$_x$ samples was determined by electron probe micro analyzer (EPMA) point scan using a Cameca SX100.

X-ray absorption near edge structure (XANES) measurements were performed on beamline 8.2 at the Stanford Synchrotron Radiation Lightsource (SSRL) in SLAC National Accelerator Laboratory. The base pressure during the experiment was of 2.0×10^{-7} Pa. The total electron yield (TEY) mode was used by measuring the sample current. The current measurements were done using a low noise preamplifier Stanford Research System Model SR570. The incoming synchrotron beam flux (I_o) signal from a gold grid was used to normalize the spectra.

VIII.3. RESULTS AND DISCUSSION

VIII.3.1. STRUCTURE AND PHASE FORMATION

Fig. VIII.1 shows the XRD patterns for samples prepared at different laser fluences from 1.8 to 6.0 ± 0.1 J/cm^2 at the same nitrogen background pressure of 2.7×10^4 Pa. Samples processed at laser fluences of 1.8 J/cm^2 or lower do not show any peak corresponding to NbN$_x$ and no laser effect is observed in XRD patterns. Samples processed at laser fluences above 1.8 J/cm^2 show XRD peaks of cubic δ-NbN with (111), (200) and (220) orientations. The other two peaks at 33.43° and 43.68° may be attributed to α-NbN with (633) and (930) orientations [234]. The cubic peaks showed slight increase in their intensities as the laser fluence was increased to 5.0 J/cm^2. The appearance of δ-NbN in the samples is consistent with previous work on laser nitridation of Nb by Nd: YAG laser [51]. Table VIII.1 shows the texture coefficient calculated for the cubic δ-NbN phase in samples prepared at different laser fluences. The texture

coefficient shows the change from predominantly (200) texture to (220) as the laser fluence is increased. XRD patterns in Fig. VIII.1 show slight changes in the crystal structure of samples prepared at different laser fluences. Small shifts in the peaks at (200) from 41.55° at 3.6 J/cm^2 to 41.16° at 4.0 J/cm^2 and also in the peak at (220) as it shifts from 60.33° to 59.73° with the increase in laser fluence. The mean crystallite size and lattice parameters for cubic phase of the samples prepared at different laser fluences are shown in Fig. VIII.2. The error bars in Fig. VIII.2 represent the standard deviations calculated from the data of three cubic δ-NbN with (111), (200) and (220) orientations.
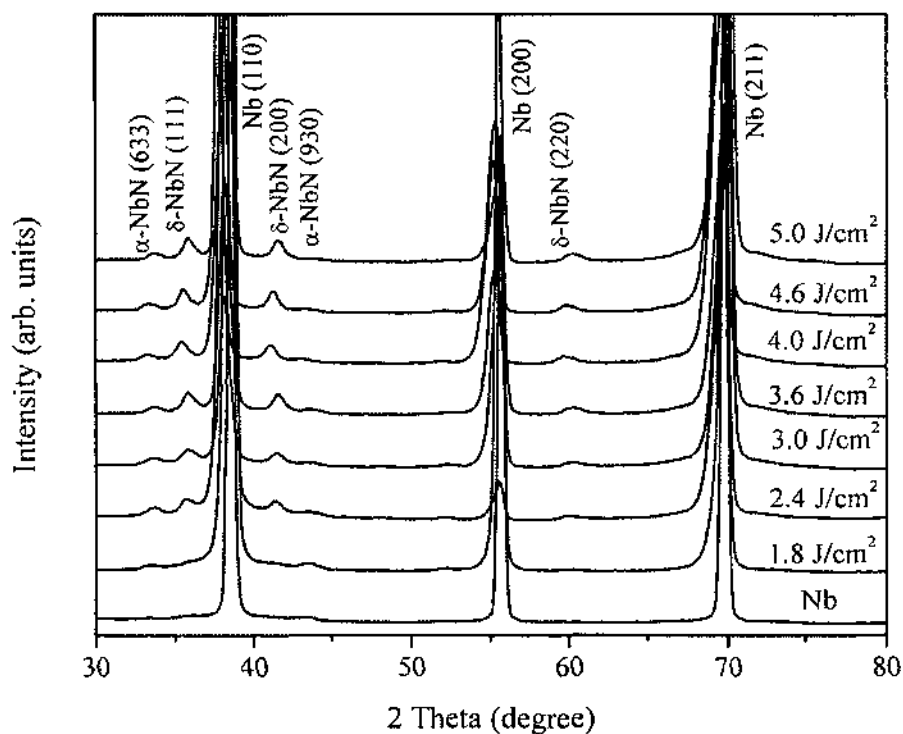
Fig. VIII.1. XRD for samples prepared at different laser fluences and all at same nitrogen pressure of 2.7x10^4 Pa.

Table VIII.1. Textured coefficients of the cubic δ-NbN phase in ns laser heated NbN_x samples at different laser fluences.

Laser Fluence, (J/cm^2)	TC(111)	TC(200)	TC(220)
5.0	0.93	1.01	1.06
4.6	0.92	1.01	1.07
4.0	1.12	0.55	1.33
3.6	0.79	1.00	1.21
3.0	0.99	1.00	1.00
2.4	1.05	1.44	0.51
1.8	0.89	1.38	0.73

The crystallite size was calculated form XRD peaks (Fig. VIII.1) by using the Scherrer equation and is 4.5 – 7.5 nm. The overall behavior of crystallite size is that it increases with increasing laser fluence, as shown in Fig. VIII.2. Increasing the laser fluence also results in higher XRD peaks which are an indication of larger crystallites. The lattice parameter showed little dependence on the laser fluence except for the sample prepared at 3.6 J/cm^2 which showed some decrease in lattice constant. This change in the lattice constant may be due to higher surface roughness of the Nb substrate. Changes in the lattice parameter of NbN_x was previously attributed to the formation of nitrogen and/or niobium vacancies, which cause distortion of the crystal lattice [22]. The lattice parameter of cubic phase was reported to decrease upon N/Nb ratio deviated from unity [22]. Fig. VIII.3 shows N/Nb ratio obtained from EPMA measurements of samples prepared at different laser fluences. The nitrogen contents in the samples increase as laser fluence increases from 1.8 to 4.6 J/cm^2. Then, the N/Nb ratio decreases as the laser fluence increases to 5.0 J/cm^2, as shown in Fig. VIII.3. The decrease in the N/Nb ratio at higher laser fluences could be due ablation of the nitride with subsequent laser pulses.

The error bars in Fig. VIII.3 represent the standard deviations calculated for measurements done at five different points on each sample.
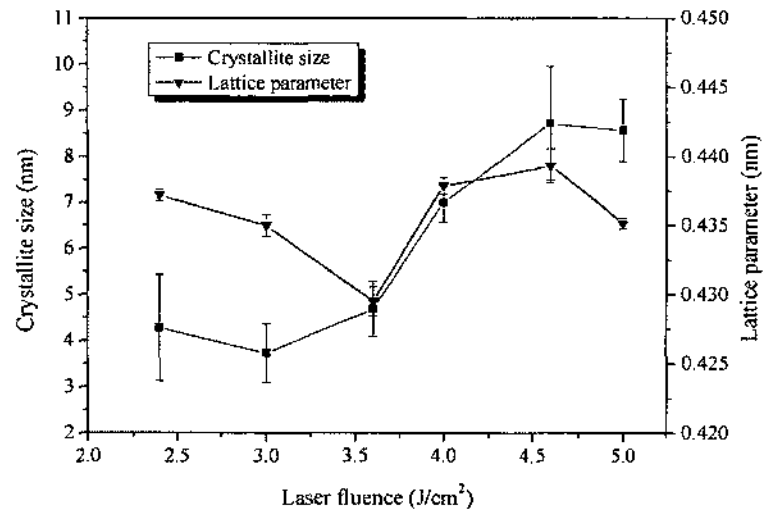
Fig. VIII.2. Variation of crystallite size and lattice parameter of cubic phase with laser fluences. The solid lines are drawn as a guide for the eye.
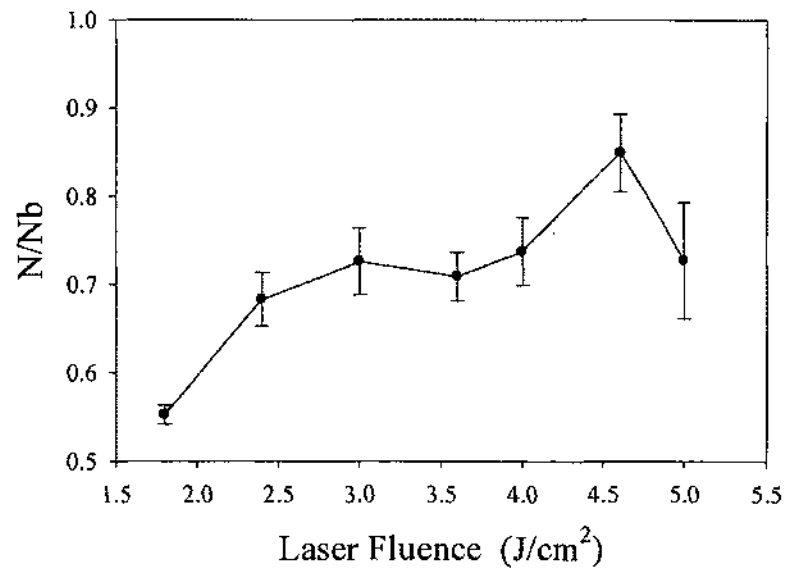
Fig. VIII.3. EPMA measurement of shows N/Nb ratio samples done at different laser fluences.

The X-ray diffraction patterns corresponding to the NbN_x films grown by femtosecond laser nitridation by different laser fluences at a constant nitrogen pressure (4.0×10^4 Pa) are shown in Fig. VIII.4. XRD peaks corresponding to Nb substrate are identified with (110), (200), and (211) orientations shown at the bottom. The NbN_x films have mixed phases of δ, β, and α. The cubic δ-NbN structure starts to appear at an energy density of 0.25 mJ/cm^2 with the corresponding reflections of (111), (200), and (220) planes. The intensities of these three peaks increase as laser density is increasing. The peaks of δ-NbN are dominated over peaks of other two phases. No nitriding occurs for sample done at 0.11 mJ/cm^2. As laser fluence is increasing to 0.25 mJ/cm^2 nitriding and the formation of NbN_x film appear. XRD diffraction peaks corresponding to α, β, and δ phases are visible when the fs laser fluence higher than 0.14 mJ/cm^2. There are no shifts observed in the position of the XRD peaks. However, there is a systematic increase in the intensity of the XRD peaks as the laser fluence is increased. The texture coefficient of δ phases for fs laser annealed samples given in Table VIII.2. The cubic phases showed predominate in (111) direction over the range of the laser fluences from 0.25 to 1.31 mJ/cm^2.

Fig. VIII.5 shows the EPMA results for the nitrogen-to-niobium ration (N/Nb) in the samples prepared by femtosecond laser nitridation at different laser fluences. The N/Nb increases as laser fluence is increased. The corresponding XRD patterns of these samples show increased in the peaks of NbN_x with the increased laser fluence, which is consistent with the increased nitrogen content observed in the EPMA measurement. The error bars in the EPMA measure represent the standard deviation calculated from measurements at five different points on each sample.
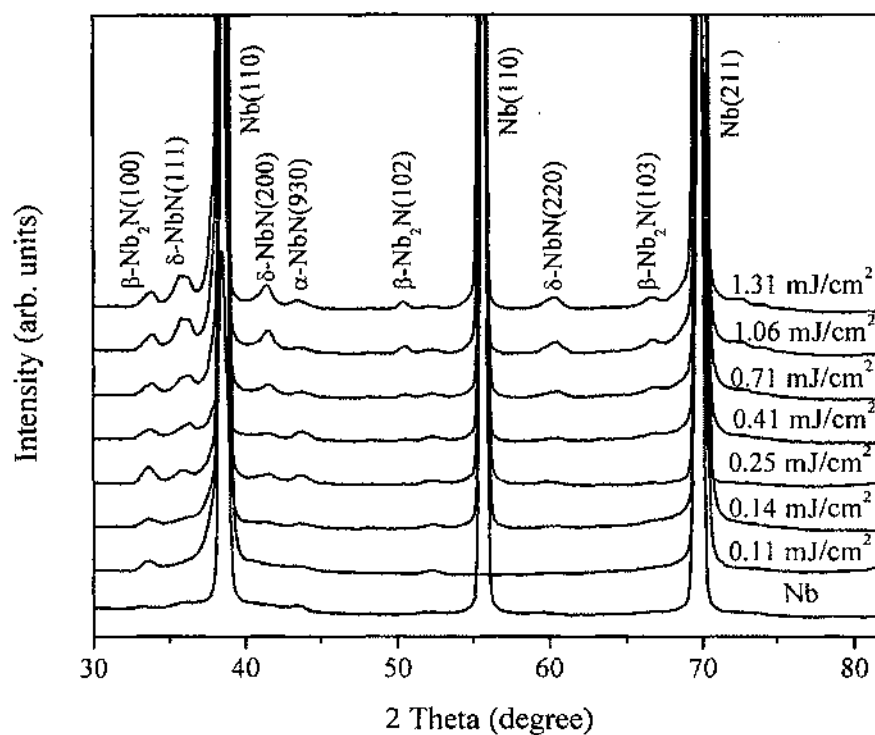
Fig. VIII.4. XRD of samples done by fs laser heating at different laser fluences.

Table VIII.2. Textured coefficients of the cubic δ-NbN phase in fs laser heated NbN_x samples at different laser fluences.

Laser Fluence, mJ/cm^2	TC(111)	TC(200)	TC(220)
1.31	1.11	0.80	1.08
1.06	1.15	0.81	1.04
0.71	1.07	0.93	0.99
0.41	1.21	0.92	0.87
0.25	1.17	1.09	0.74
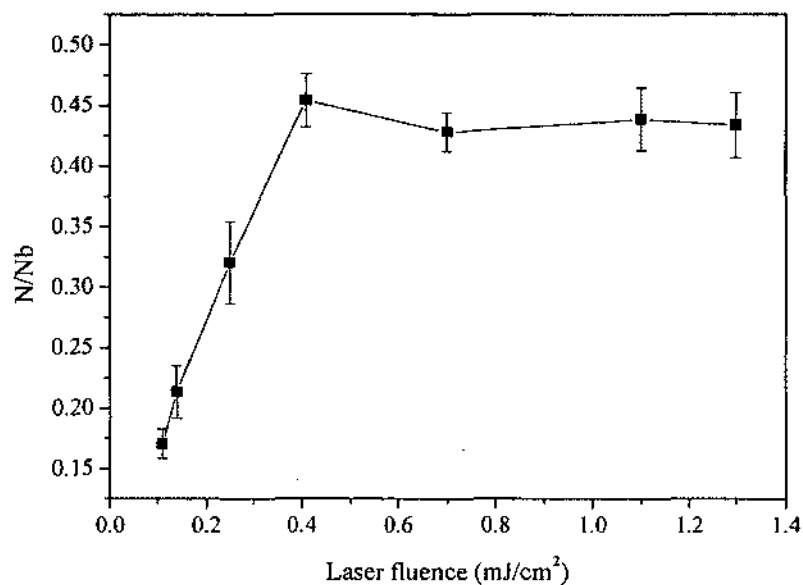
Fig. VIII.5. EPMA measurement of shows N/Nb ratio samples done at different fs laser fluences.
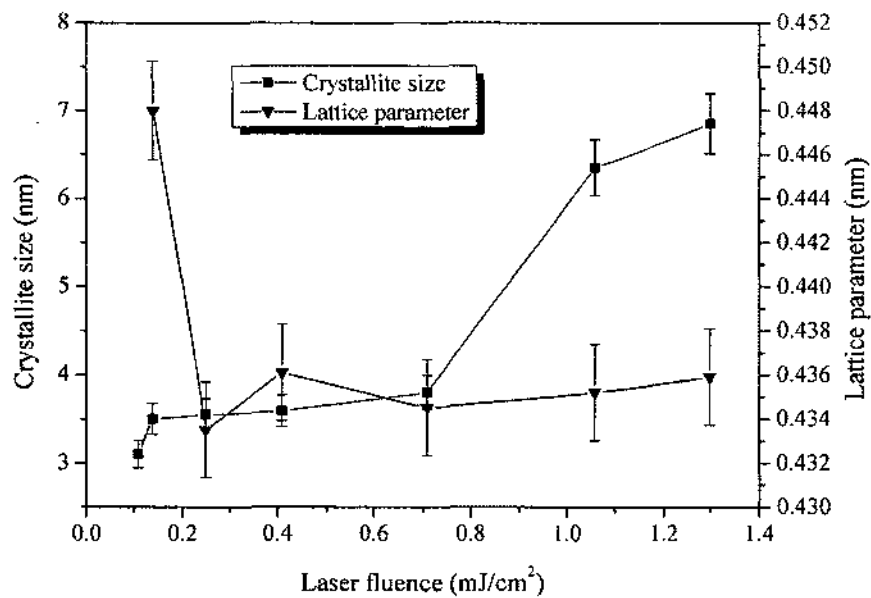
Fig. VIII.6. Variation with laser fluence of (a) crystallite size of and (b) lattice parameter of (200) peaks δ-cubic phase. The solid lines are drawn as a guide for the eye.

In femtosecond laser nitridation the lattice is heated on a picosecond time scale as a result a direct solid to vapor transition resulting in plasma formation [101]. While in the case of nanosecond laser nitridation, the heating time is long enough to cause melting of the surface followed by evaporation from the liquid melt [101]. For the femtosecond laser, the ablation depth is strongly dependent on the laser fluence [101]. As the laser fluence is increased the ablation depth increases with an increase in plasma density which leads to the formation of more phases than that observed in nanosecond laser nitridation. This could be the reason for the formation of the β-Nb$_2$N phase, as seen in their XRD patterns.

For pulsed laser surface heating and considering a two-dimensional heat diffusion model, the heat diffusion length $l = \sqrt{D\tau}$, where D is the diffusion coefficient of the material and τ is the laser pulse width. For equal fluence and for strongly absorbing materials such metals, when the laser pulse is reduced the diffusion length is also reduced, resulting in increased surface temperature. The maximum surface temperature exceedingly increases for pulses below 1 ps [103]. As pulse duration decreases the energy is absorbed to form vapor or superheating of the liquid rather than the formation of the liquid. For femtosecond laser ($\leq$100 fs), the pulse is short enough not to be absorbed by vapor. For longer pulses (>100 ps), more time is available for the heating to diffuse into the bulk before the vapor stage is achieved [103]. That makes significance effects on the type of nitride phases and their orientations on the surface.

Fig. VIII.6 shows that the mean crystallite size of the cubic phase increases from 3 to 7 nm as the laser fluence is increased from 0.11 to 1.31 mJ/cm^2. The error bars in both the crystallite size and lattice constant represent the standard deviations calculated

from the XRD data of the three cubic δ-NbN peaks from the (111), (200) and (220) plans. The increase in the crystallite size is expected due to narrowing of the XRD peaks with laser fluence increase. The lattice parameter of cubic phase did not show much change with laser fluence except for the sample done at 0.41 mJ/cm^2. The c/a ratio of the hexagonal β-Nb$_2$N phase increases with the laser fluence. The c/a ratios were calculated from the (100) and (102) and (103) peaks of β-Nb$_2$N. A similar trend was reported for NbN$_x$ films prepared at different laser fluences [31].

VIII.3.2. SURFACE MORPHOLOGY

Fig. VIII.7 shows SEM images of untreated Nb sample with these grown NbN$_x$ surfaces in which the laser energy density was varied while the nitrogen background pressure was kept at 2.7×10^4 Pa. For laser fluence ≤ 1.8 J/cm^2 no surface melting is observed. Further increase of the laser fluence results in an increase in surface roughness. At a laser fluence ≥ 1.8, the formation of melt splash is observed as the laser expels the melt resulting in increased surface roughness. Cracks are also observed on the surface of samples processed at 3.6 J/cm^2 (Fig. VIII.7(d)). This may be due to the greater quench rate and development of thermal stress [235].

Fig. VIII.8 shows SEM images of fs laser annealed samples done at different laser fluences. The SEM images of the samples show that the surface is uniformly covered with ripple periodic structure. The formation of laser induced periodic surface structures have been wildly studied on different types of materials including metals, semiconductors and dielectrics using femtosecond laser [236].

These ripples result from the interference between the incident beam and a surface wave that are scattered by the surface roughness [237]. The period of the ripples Λ

depends on the laser wavelength λ and beam polarization [238]. A spacing related to λ and angle of incidence θ by $\lambda/(1\pm\sin\theta)$ results when the ripples are oriented perpendicular to the incident beam polarization. Another type pattern mainly occurs by p-polarized beam, as in this case, when patterns oriented parallel to the beam polarization with the spacing of $\lambda/\cos\theta$ [237, 238]. From SEM images, the ripples are orientated vertically and parallel to the beam polarization. The spacing value calculated from last equation using λ = 800 nm and θ = 45° gives 1.13 μm which is very close to values measured from SEM images. Fig. VIII.9 shows increases in the periodicity as laser fluences increases. Increasing of the ripple periodicity is predicted form decreases of the refractive index n due to increases of the electron density as the laser fluence is increased [239].The morphology of the surface depends significantly on laser fluence. As the laser fluence is increased the density of grains and surface roughness increase, as observed from Fig. VIII.8. The decrease in periodicity as the laser fluences increase to 5.0 J/cm^2 can be attributed to increase in the surface roughness. It was previously reported that as the surface roughness of the samples gets larger the small or less change occurs in the ripple periodicity [239]. Laser heating of the Nb substrates causes an increase in surface roughness for both samples prepared by ns and fs lasers. The error bars in Fig. VIII.9 represent the standard deviations calculated from spacing measurements done at different locations on each SEM image.
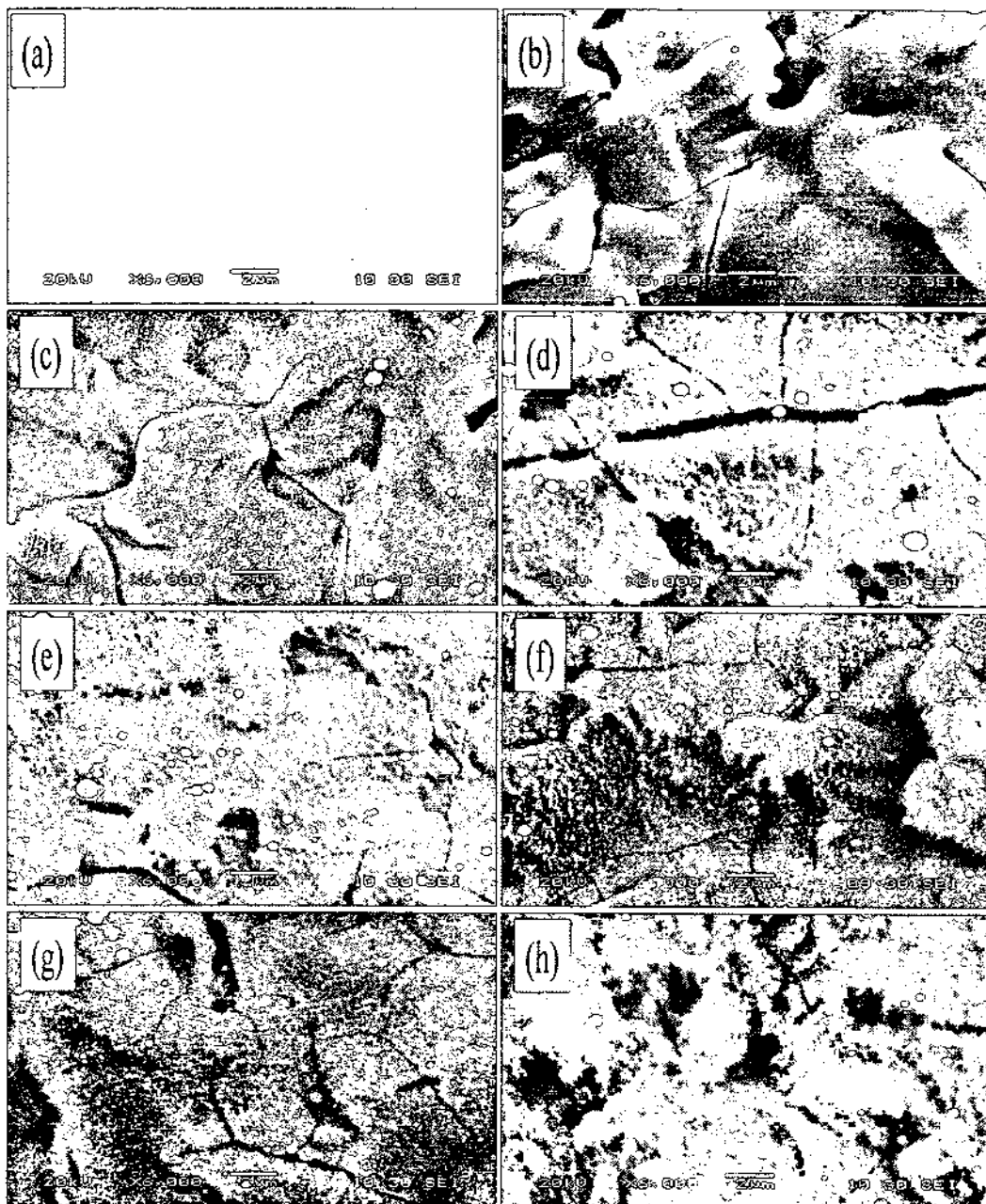
Fig. VIII.7. SEM images (X6,000) of the NbN$_x$ films produced at ns laser fluences (a) untreated Nb, (b) 1.8 J/cm^2, (c) 2.4 J/cm^2, (d) 3.0 J/cm^2, (e) 3.6 J/cm^2, (f) 4.0 J/cm^2, (g) 4.6 J/cm^2, and (h) 5.0 J/cm^2.
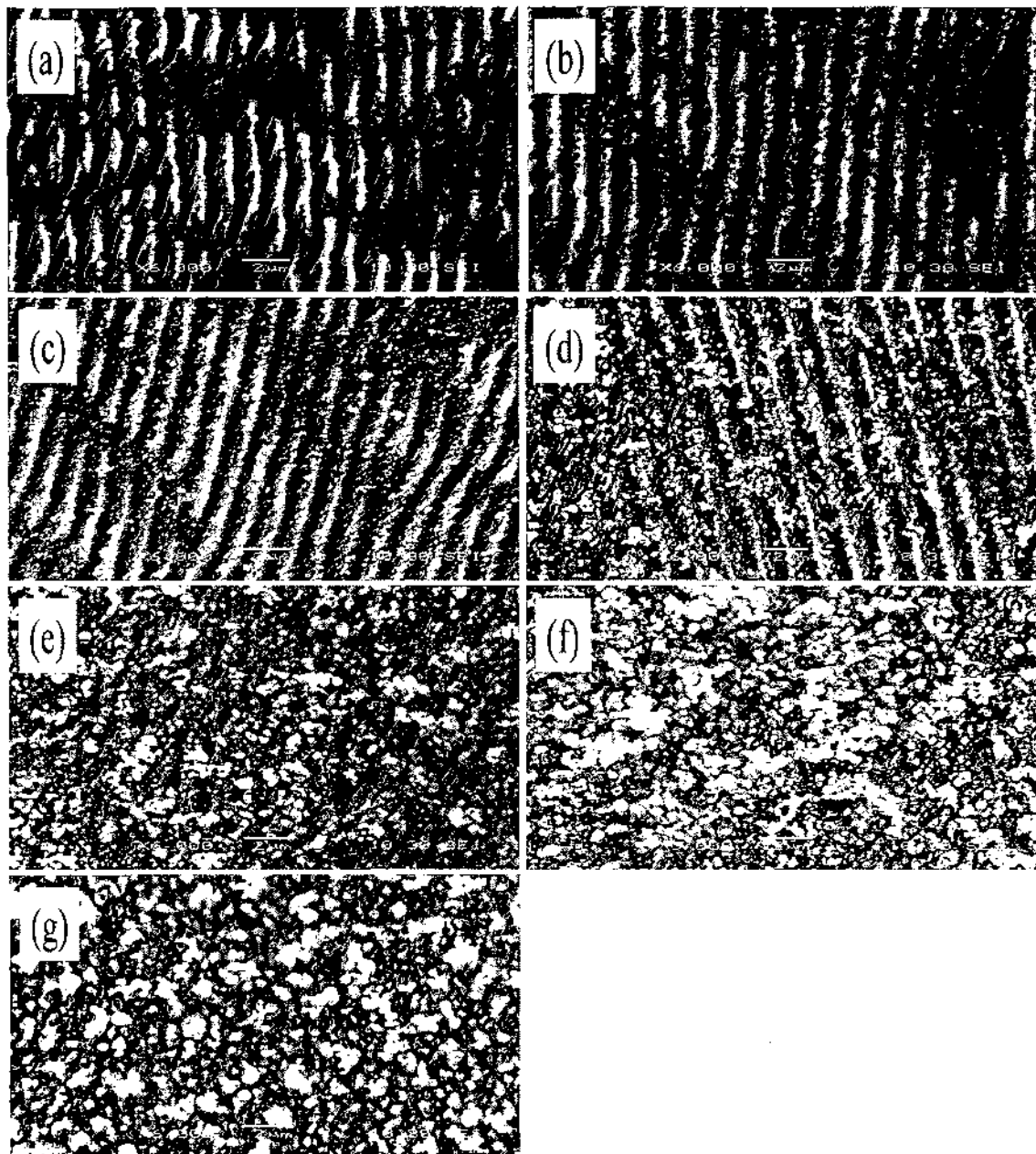
Fig. VIII.8. SEM images (X6,000) of the NbN$_x$ films produced at fs laser fluences (a) 0.11 mJ/cm^2, (b) 0.14 mJ/cm^2, (c) 0.25 mJ/cm^2, (d) 0.41 mJ/cm^2, (e) 0.71 mJ/cm^2, (f) 1.06 mJ/cm^2, and (g) 1.3 mJ/cm^2.
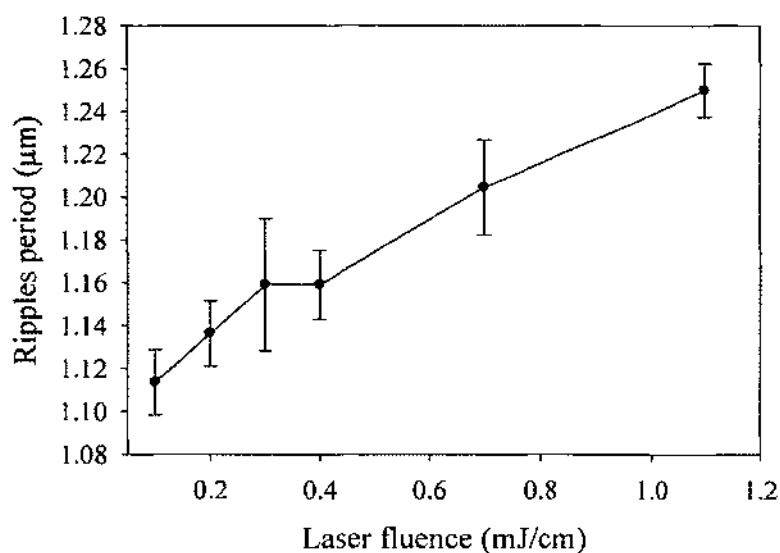
Fig. VIII.9. Dependence of the ripple periodicity on the laser fluence.

VIII.3.3. X-RAY ABSORPTION NEAR EDGE STRUCTURE (XANES) SPECTROSCOPY

XANES spectroscopy is one of the most powerful tools available for electronic structure determination. In this technique, the number of absorbed X-rays is monitored as a function of photon energy. Fig. VIII.10 shows normalized X-ray absorption spectra of NbN_x samples prepared at different laser fluences. The $Nb-M_3$ and M_2 edge spectra recorded at room temperature in total electron yield (TEY) mode by measuring the drain current of the sample as a function of the photon energy. All TEY signals are normalized to I_0 avoiding synchrotron dependent intensity variations. In addition, TEY spectra of NbN_x films normalized by subtracting a straight line fitted to the region before the M_3 edge (below 365 eV) and adjusting the intensity of the spectra to 1 at 395 eV.

The $M_{2,3}$ edge is mainly attributed to the transition of electrons from Nb $3p$ state to unoccupied $4d$ and $5s$ states. The shape of Nb $M_{2,3}$ edges is quite the same for all the samples in Fig. VIII.10 with two Nb $3p$ peaks split by about 15 eV due to the spin-orbit coupling of $4d$ electrons. The peaks at 365.5 and 380.8 eV are assigned to $3p_{3/2}$ and $3p_{1/2}$, respectively. Due to degeneracy, the peak at 365.5 eV always has a higher intensity than that at 380.8 eV [240]. Fig. VIII.11 shows measured $M_{2,3}$ intensity ratios as function laser fluence; was considered the integrated area under each M_3 and M_2 peak in Fig. VIII.10. The branching ratio (BR); $IM_3 / I (M_2 + M_3)$ represents a high-spin-state which is sensitive to the spin-states of $4d$ electrons. The area of the M_3 and M_2 lines would be the correct measure of their intensity, which is proportional to the oscillator strength of the $3p$–$4d$ spin–orbit interaction. The peak intensity ratio should hence give information on the valence band spin–orbit interaction and the electrostatic interaction in the final state [240]. The BR in Fig. VIII.11 changed significantly from 0.696 to 0.680. There must be the correlation between $4d$ occupancy and the BR in Fig. VIII.10. the branching ratio shows a small variation for all samples except that done at 3.6 J/cm^2. It suggests that $4d$ occupation is similar for most of the samples. However it appears to be a decrease in BR intensity for the sample processed by 3.6 J/cm^2 laser fluence. It has been shown that the high nitrogen ratio in the NbN$_x$ film results in weak N $2p$-Nb $4d$ hybridization which can explain the reduction of BR intensity [35].
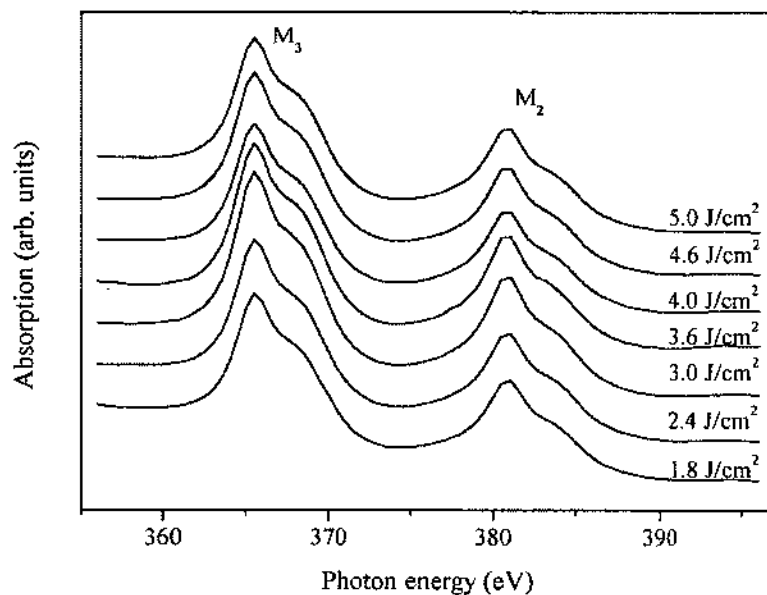
Fig. VIII.10. Measured XANES at the Nb-$M_{2,3}$ edges of NbN_x surface of different laser fluences samples.
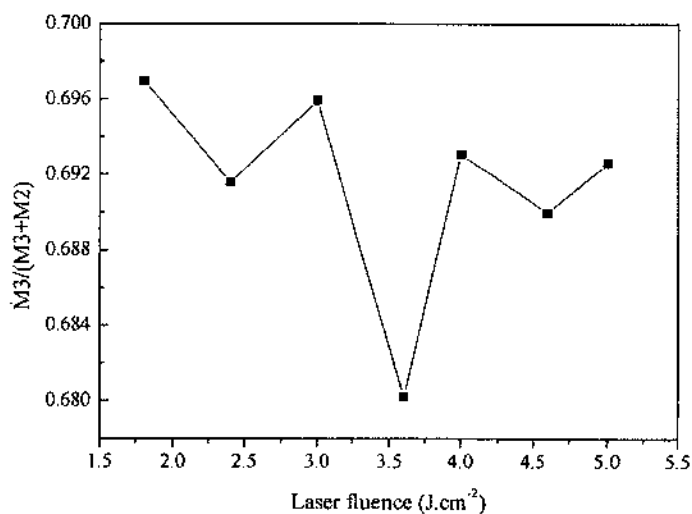
Fig. VIII.11. Normalized peak intensity ratio of M_3 to M_2. The intensity ratios calculated by considering the integrated area under each peak in Fig. VIII.10.

Fig. VIII.12 shows O K edge XANES spectra of samples done at different laser fluences. The spectra normalized by subtracting a straight line fitted to the region before the peaks (below 530 eV) and adjusting the intensity of the spectra to 1 at 555 eV. The O K edge is attributed to a transition of O $1s$ electrons to the unoccupied $2p$ states. The O K edge is characterized by a double-peak structure (peaks labeled a and b in Fig. VIII.12) [66, 197]. The relative height and energy splitting between these two peaks are determining the type of oxidation in the sample. The measured splitting between peak a and b is about 4.4 eV which is very close to that reported for Nb_2O_5 oxidation state, this splitting is around 2.8 eV for NbO [198].

The $M_{2, 3}$ edges for samples prepared by fs laser are shown in Fig. VIII.13. The spectra were normalized to current yield from of a standard gold mesh. In addition, the TEY spectra of NbN_x films were normalized by subtracting a straight line fitted to the region before the M_3 edge (below 365 eV) and adjusting the intensity of the spectra to 1 at 395 eV. The Nb $M_{2,3}$ edges is quite the same with two Nb $3p$ peaks split by about 15.5 eV due to the spin-orbit coupling of $4d$ electrons. The Nb $3p$ peaks are observed at energies of 365.5 and ~ 381 eV corresponding to Nb $3p_{3/2}$ and $3p_{1/2}$, respectively. Nb $M_{2, 3}$ peaks at 365.5 and 380.8 eV having shoulders at ~368 and ~383 eV respectively. This shape indicates presence of double peaks at these positions. These kind of double-peaks were reported for Nb-M_3 and Nb-M_2 lines when Nb_2O_5 is formed in the samples not but for other oxide states [66, 198]. Also, no shifts are observed in both Nb $3p$ and N $1s$ peaks as the laser fluence is increased. If niobium oxidation state other than Nb_2O_5 is found in the samples there will be shifts by 1.4 eV or more in position of the peak at 365.5 eV [66]. This confirms observations on formation of Nb_2O_5 in the samples.
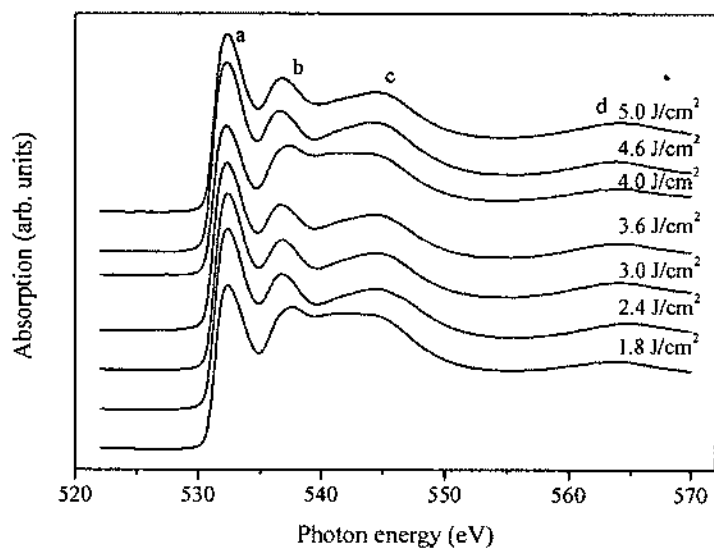
Fig. VIII.12. Oxygen 1s XANES spectra of NbN_x thin films prepared by an (ns) laser.
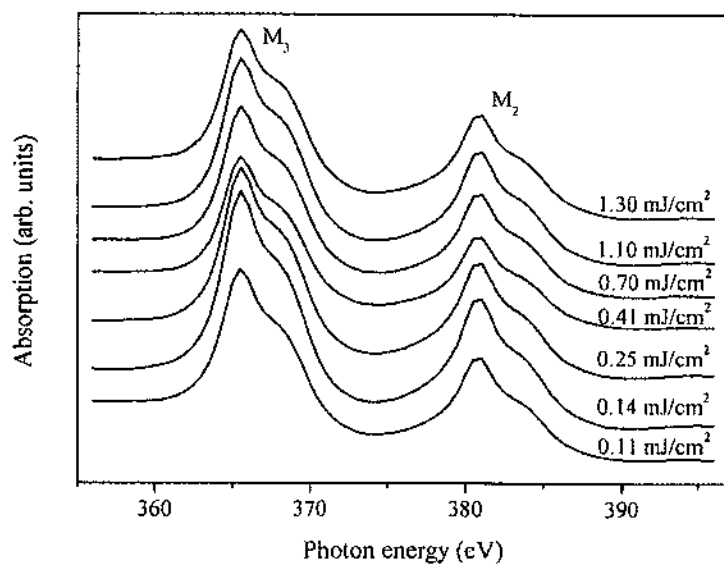
Fig. VIII.13. XANES at the Nb-$M_{2,3}$ edges of NbN_x surface of different (fs) laser fluences samples at different laser fluences.
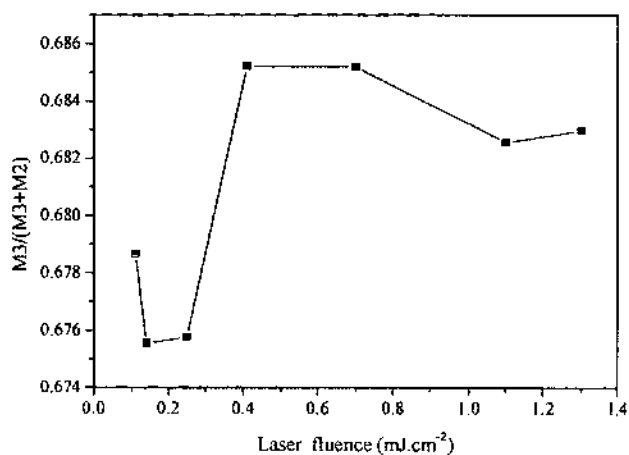
Fig. VIII. 14. Normalized peak intensity ratio of M_3 to M_2. The intensity ratios calculated by considering the integrated area under each peak in Fig. VIII.13
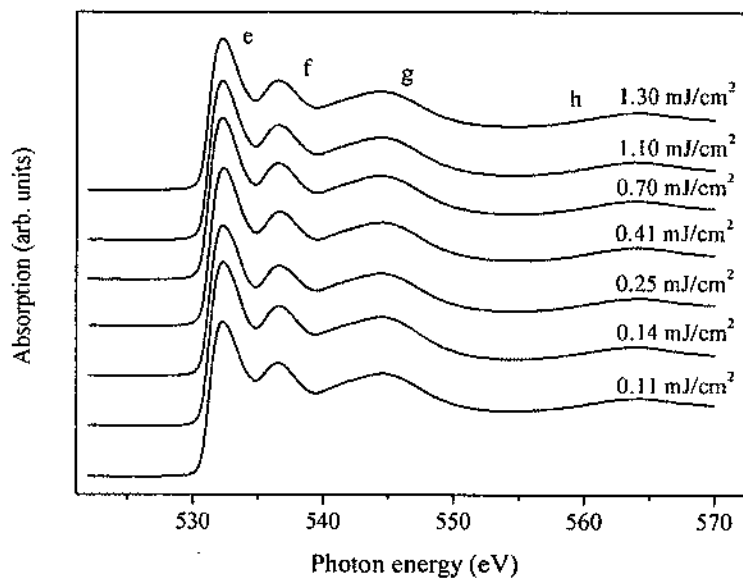
Fig. VIII.15. Oxygen 1s X-ray absorption spectra of NbN_x thin films prepared by (fs) laser at different Laser fluences.

Fig. VIII.14 shows intensity ratios of $M_{2,3}$ as function laser fluence. It is observed in v13 that the BR shows small variation after 0.25 mJ/cm^2 which is consistent with nitrogen-to-niobium ratio in the sample. No changes are seen in the intensities of the peaks, shape or positions for different laser fluences. This confirms the formation of stable nitrides. The shoulders of the Nb $3p_{1/2}$ and $3p_{3/2}$ peaks indicate the presence of double peaks. The double-peaks for Nb-M_3 and Nb-M_2 lines were reported if Nb_2O_5 formed in the samples [66, 198]. Also, no shifts in both Nb $3p$ ($M_{2,3}$) and N $1s$ peaks were observed as laser fluence increases.

The O K edge of the XANES spectra of NbN samples prepared by using a fs laser is shown in Fig. VIII.15. The O K edge is characterized by a double-peak structure (e and f in Fig. VIII.15) [66, 197]. The peaks labeled with e, f, g, and h located at energies of 532.3, 536.6, 544.4, and 564.0 eV, respectively. The relative height and energy splitting between these peaks are determining the type of oxidation in the sample. The splitting between peak e and f is about 4.2 eV which is close to that reported for Nb_2O_5 [66]. The source of this oxide layer could be as a native layer on the Nb substrate since niobium is highly reactive to oxygen, or on surface of NbN_x samples that forms when handling samples in air. Native oxide layer on Nb could be removed by thermal treatments of the substrate before processing.

VIII.4. CONCLUSION

In this work, NbN_x coatings were obtained by laser nitridation of niobium substrate in a nitrogen gas environment which was carried out with different laser fluencies. Detailed analyses of the texture electronic and surface morphology of polycrystalline films were presented. Nd: YAG ns and Ti: sapphire fs lasers were used

for laser nitriding of Nb. The samples were prepared at different laser fluences using ns laser were in the range 1.8 to 6.0 ± 0.1 J/cm^2 and constant nitrogen pressure of 2.7×10^4 Pa. The cubic peaks of δ-NbN with (111), (200) and (220) orientation showed slightly increases in their intensities as the laser fluence was increased up to 5.0 J/cm^2. The lattice constant shows changes in its trend as the other phases start to appear along with the cubic phase. The SEM images for samples done at different laser fluences showed increase in surface roughness as the laser fluence is increased.

No nitriding occurs for sample processed with laser fluences of at 0.11 mJ/cm^2 or below. XRD measurements confirm the formation of stable nitrides with mainly δ-NbN phase. As the laser fluence are increased, NbNx samples with three mixed phases including α,β, and δ phases were identified in XRD. The cubic δ-NbN structure is dominated over other two phases. The intensity of XRD peaks corresponding to the δ-NbN phase increases as with the laser fluence. The formation of β-Nb$_2$N phase in case of fs laser is due to the dependence of the ablation depth on the laser fluence of the poles, that leads to denser plasma than that formed by ns laser led to the formation of more phases. The samples processed by fs laser showed the common laser-induced periodic ripples surface structure with spacing that increases with the laser fluence.

X-ray absorption near edge structure (XANES) measurements done at Nb M$_{2,3}$ edges showed Nb 3p peaks with two doublet peaks due to the formation of the oxide layer. The formation of oxides is also confirmed by XANES measurements at the O K edge. The oxide layer is found to be Nb$_2$O$_5$ layer on the surface of the samples. Laser nitriding of niobium offers an alternative to the conventional techniques and particularly stands out by controlling the phase and morphology of NbN$_x$.

CHAPTER IX

SUMMARY AND CONCLUSIONS

Niobium nitride samples grown by different preparation techniques were investigated. NbN_x films were grown by pulsed laser deposition (PLD) on two types of substrates, namely, niobium (Nb) and Si(100). The thermal diffusion of nitrogen on Nb was used to prepare NbN_x samples at low and high pressures of nitrogen. Other samples were prepared by laser heating of Nb substrate under nitrogen gas.

A focused laser beam Nd: YAG nanosecond pulsed laser was used to ablate Nb target in nitrogen gas pressure. The effects of changing PLD parameters on the structural, phase formations and compositions of the films NbN_x on Nb were studied. The importance of growing NbN_x films on Nb substrate is to increase the efficiency of superconducting radio frequency (RF) cavities for particle accelerators. The enhancement in the hardness of NbN_x films compared to that of Nb metal is considered very attractive in parts of the superconducting RF cavity applications.

The effects of changing laser fluence, nitrogen gas pressure, and substrate temperature were studied for NbN_x films grown on Nb by PLD. For studying the effect of changing the laser fluence, the nitrogen background pressure and substrate temperature were maintained constant at 20 Pa and 600 °C, respectively, while NbN_x films were prepared at laser fluence in the range of 8–40 J/cm. The surface roughness, deposition rate, nitrogen content, and grain size increased as laser fluence was increased. These films show highly textured structure with a preferential orientation of (110) parallel to the

substrate. The NbN_x layers were formed in mixed phase (cubic and hexagonal). The ratio of hexagonal phase to cubic phase is strongly dependent on the laser fluence.

For the effect of nitrogen background pressures on the properties of NbN_x films nitrogen pressure in the range of 10.7 to 66.7 Pa with constant laser fluence of 15 J/cm^2 and substrate temperature 600 °C were used. It was found that the nitrogen pressure affected the ratio of the cubic-to-hexagonal phase of the NbN_x film. At low nitrogen background pressures both hexagonal (β-Nb_2N) and cubic (δ-NbN) phases were formed. As the nitrogen pressure increased, NbN_x films grew in single hexagonal (β-Nb_2N) phase.

NbN_x films were grown at different substrate temperatures from RT to 950 °C to investigate the effect of changing the temperatures on the phase, morphologies, and crystal structures of the films. The films were under constant values of nitrogen pressure and laser energy density of 13.3 Pa and 15 J/cm^2, respectively. Increasing the substrate temperature to 650 °C enhanced the crystalline quality of the film and as substrate temperature increased to 650 – 850 °C, NbN_x films with mixed phases, cubic (δ-NbN), hexagonal (β-Nb_2N), and δ'-NbN phases were obtained as revealed by X-ray diffraction. Film with a mainly hexagonal (β-Nb_2N) phase was obtained, as the temperature was increased to 850 °C. A systematic increase in lattice parameters and size of the grains was observed as the substrate temperature increased.

The NbN_x films grown on Si(100) substrates were investigated for their structure, electronic structure, and superconductivity nanomechanical properties. The films were deposited on Si(100) under different background nitrogen gas pressures (26.7-66.7 Pa) at constant substrate temperature of 800 °C and 15 J/cm^2 laser fluence. XRD revealed that highly textured NbN_x films with cubic (δ-NbN) were oriented in the (111) direction.

Increasing the nitrogen gas pressure during deposition affected the phase orientations, morphologies, and superconducting transition temperature. Residual resistance ratio (RRR) and superconducting transition temperature (T_c) increased as the nitrogen pressure of the films was increased. The highest T_c value of 15.07 K was achieved for NbN_x film deposited at 66.7 Pa nitrogen background pressure and the lowest T_c value of 7.66 K was achieved at 26.7 Pa. Different transition temperatures are related to the crystalline phases that appear in NbN_x films. NbN_x films grown on Si substrate showed mixed phase structures of cubic δ-NbN and tetragonal γ-Nb_4N_3 phases. Increasing the nitrogen pressure causes decreases in the number of vacancies in the film. The hardness increases with average values of 14, 16, and 18 GPa for nitrogen pressures of 26.7, 53.3, and 66.7 Pa, respectively. A correlation between increases in hardness and T_c of the NbN_x films is attributed to the number of nonmetal vacancies found in the film. As nitrogen pressure increases, the number of vacancies decreases and this increases the strength of the material. X-ray photoemission spectroscopy XPS spectra of NbNx films show shifts in Nb $3d_{3/2}$ and $3d_{5/2}$ peaks to higher binding energies. These shifts indicate the transfer of electrons from niobium to nitrogen for Nb-N bonding. The calculated x = N/Nb in the NbN_x film from intensity of photoelectron peaks shows deceases in x from 0.90, 0.88, to 0.80 for 26.7, 53.3, and 66.7 Pa. HRTEM results done on sample prepared by PLD on Cu grids at laser fluence of 8.0 J/cm^2 and nitrogen pressure of 40 Pa, showed NbN nanoparticles.

The other method that was employed to prepare NbN_x was a reactive thermal diffusion method. The formation of NbN_x on Nb causes strengthening of the surface

hardness of Nb that can be useful in many applications that are needed for relatively chemically inert and high hardness coatings.

One part of this work was done by heating Nb substrates in a nitrogen gas environment at high temperatures (900 °C and higher). The work was done on two folds of nitrogen gas pressure, high and low pressures. Samples prepared at high nitrogen pressure (133 Pa) and different heating times (5, 10, 20, 40, and 80 min) and heating temperatures of 900 °C were 0.7 mm thick. The effect of change in the heating time was investigated on structural, electronic, nanomechanical and surface properties of the NbN_x layers. The niobium nitride obtained by thermal diffusion crystallized in single phase of hexagonal (β-Nb_2N) that is predominantly oriented in the (110) direction. N/Nb ratio in the NbN_x increases as processing time increases. XPS of samples shows the third peak at ~210 eV, corresponding to Nb_2O_5 beside the peaks appear at 205.5 and 202.3 eV for Nb $3d_{3/2}$ and $3d_{5/2}$ levels. An oxide layer of Nb_2O_5 was formed as the sample was exposed to the ambient air. Both Nb $3p$ and $3d$ levels show a strong interaction with nitrogen along with binding energy shift. Nitrogen diffusion in samples is governed by parabolic kinetics that occur when the mass gain, due to NbN_x formation, is proportional to the square of the film thickness. Longer heating times resulted in layers with higher nitrogen-to-niobium ratios, with improvements in hardness and modulus of the film. The hardness values ranged from 12 to 26 GPa.

Nb substrates that were processed at low nitrogen pressures (1.3×10^{-3} – 2.6 Pa), including samples heated in a high vacuum (1.3×10^{-5} Pa), have two thicknesses (0.2 and 0.7 mm). First, for samples of 0.2 mm thickness, four sets of thermal diffusion experiments were done for the same heating time (180 min). The set of samples were

heated at 1.3×10^{-3} Pa of nitrogen pressure and different temperatures (1250–1500 °C). XRD and two-dimensional X-ray images (2D-XRD) confirmed that the formation of some grains can be ascribed to α-NbN phase. Then, they get smaller in size, as indicated by full spotty rings obtained at 1500 °C. These values are also consistent with crystallite size calculations using the Scherrer relation. Crystallite size decreased from 23 nm at 1250 °C to about 17 nm at 1500 °C.

The other three sets were for samples heated at temperatures 1300, 1400, and 1500 °C and each were done at different nitrogen pressures. For samples done at 1300 and 1400 °C, XRD patterns showed clear interaction of Nb with nitrogen at pressure of 0.53 Pa, as the hexagonal β-Nb$_2$N phase appeared as mixed phase with bcc α-NbN phase. 2D-XRD images of these two sets show changes in the diffraction spots of the Nb substrate to continuous rings at early pressures of 2.6×10^{-4}, 1.3×10^{-3}, and 1.3×10^{-5} Pa for 1300, 1400, and 1500 °C, respectively. The average lattice constant calculated for samples heated at 1.3 Pa and 1300 °C is 3.316 Å (Nb a = 3.298 Å). Similar behaviors of increases in lattice constant were seen for samples done with isothermal conditions at 1400 and 1500 °C with different nitrogen pressure.

NbN$_x$ samples done on 0.7 mm thick Nb substrates were heated in a vacuum of 2.6×10^{-5} Pa at 1000 °C for different times (1hr, 3 and 6 hrs). XRD did not show much change between unheated Nb substrate and the samples that were heated in a vacuum for several hours. The other set of thick samples heated at 1000 °C and 0.66 Pa show formations of both (α-NbN) and (β-Nb$_2$N) phases at lower heating time (up to 20 min). With increased heating time, transformation in XRD peak of (β-Nb$_2$N) at (110) to δ-NbN at (220) was observed. As heating time reached 60 min δ-NbN became more observable.

NbN_x samples were obtained by laser nitridation of niobium substrate under a nitrogen gas at different laser fluencies using Nd: YAG ns and Ti: sapphire fs lasers. The samples prepared by ns laser were at laser fluences in the range 1.8 to 6.0 ± 0.1 J/cm^2 and nitrogen pressure of 2.7×10^4 Pa. The samples showed cubic δ-NbN phase slightly increased in XRD intensities as the laser fluence was increased up to 5.0 J/cm^2. The lattice constant shows changes in its trend as the other phases start to appear along with the cubic phase.

For samples prepared with the fs laser, no nitriding occurs for laser fluences of 0.11 mJ/cm^2 or below. As the laser fluence is an increased, NbN_x with three mixed phases includingα, β, and δ phases were identified. The cubic δ-NbN structure is dominated over other two phases. The formation of β-Nb_2N phase in case of fs laser is due to the dependence of the ablation depth on the laser fluence of the poles, that leads to denser plasma than that formed by ns laser led to the formation of more phases. The samples processed by fs laser showed the common laser-induced periodic ripples surface structure with spacing that increases with the laser fluence. X-ray absorption near edge structure (XANES) measurements done at Nb $M_{2,3}$ edges showed Nb $3p$ peaks with two doublet peaks due to the formation of the oxide layer. The formation of oxides is also confirmed by XANES measurements at the O K edge. The oxide layer is found to be Nb_2O_5 layer on the surface of the samples.

BIBLIOGRAPHY

[1] S.L. Thomasson, A.W. Moopenn, R. Elmadjian, J.M. Murduck, J.W. Spargo, L.A. Abelson, H.W. Chan, IEEE Transactions on Applied Superconductivity, 3 (1993) 2058–2061.

[2] L. Zhang, N. Yoshikawa, M. Sugahara, IEEE Transactions on Applied Superconductivity, 3 (1993) 1987–1990.

[3] R. Musenich, P. Fabbricatore, G. Gemme, R. Parodi, M. Viviani, B. Zhang, V. Buscaglia, C. Bottino, Journal of Alloys and Compounds, 209 (1994) 319–328.

[4] P. Fabbricatore, G. Gemme, R. Musenich, R. Parodi, M. Viviani, B. Zhang, V. Buscaglia, Applied Superconductivity, IEEE Transactions on, 3 (1993) 1761–1764.

[5] M. Pham Tu, K. Mbaye, L. Wartski, J. Halbritter, Journal of Applied Physics, 63 (1988) 4586–4590.

[6] C. Benvenuti, P. Chiggiato, L. Parrini, R. Russo, Nuclear Instruments and Methods in Physics Research Section A: Accelerators, Spectrometers, Detectors and Associated Equipment, 336 (1993) 16–22.

[7] G. Gemme, P. Fabbricatore, R. Musenich, R. Parodi, T. Rossi, M. Viviani, B. Zhang, Journal of Applied Physics, 77 (1995) 257–264.

[8] N. Cansever, M. Danışman, K. Kazmanlı, Surface and Coatings Technology, 202 (2008) 5919–5923.

[9] V.N. Zhitomirsky, I. Grimberg, L. Rapoport, N.A. Travitzky, R.L. Boxman, S. Goldsmith, A. Raihel, I. Lapsker, B.Z. Weiss, Thin Solid Films, 326 (1998) 134–142.

[10] M. Radparvar, Cryogenics, 35 (1995) 535–540.

[11] W. Lengauer, M. Bohn, B. Wollein, K. Lisak, Acta Materialia, 48 (2000) 2633–2638.

[12] W. Zhen, H. Terai, A. Kawakami, Y. Uzawa, Applied Physics Letters, 75 (1999) 701–703.

[13] G. Brauer, Journal of the Less Common Metals, 2 (1960) 131–137.

[14] A.C. Jones, M.L. Hitchman, Chemical Vapour Deposition: Precursors, Processes and Applications, RSC Publishing, Cambridge, UK, 2009.

[15] P.R. Willmott, J.R. Huber, Reviews of Modern Physics, 72 (2000) 315–328.

[16] W.M. Steen, Laser Material Processing Springer, New York, 2001.

[17] D. Bauerle, J.D. Pedarnig, I. Vrejoiu, M. Peruzzi, D.G. Matei, G. Brodoceanu, M. Dinescu, Romanian Reports in Physics, 57 (2005) 935–952.

[18] D. Dijkkamp, T. Venkatesan, X.D. Wu, S.A. Shaheen, N. Jisrawi, Y.H. Min-Lee, W.L. McLean, M. Croft, Applied Physics Letters, 51 (1987) 619–621.

[19] J.J. Olaya, L. Huerta, S.E. Rodil, R. Escamilla, Thin Solid Films, 516 (2008) 8768–8773.

[20] P.R. Willmott, Progress in Surface Science, 76 (2004) 163–217.

[21] K. Sturm, S. Fähler, H.-U. Krebs, Applied Surface Science, 154–155 (2000) 462–466.

[22] A.V. Linde, R.M. Marin-Ayral, D. Granier, F. Bosc-Rouessac, V.V. Grachev, Materials Research Bulletin, 44 (2009) 1025–1030.

[23] A. Berendes, O. Brunkahl, C. Angelkort, W. Bock, F. Hofer, P. Warbichler, B.O. Kolbesen, Analytical and Bioanalytical Chemistry, 379 (2004) 554–567.

[24] S.J. Kim, H.F. Franzen, Journal of the Less Common Metals, 143 (1988) 339–343.

[25] G. Heger, O. Baumgartner, Journal of Physics C: Solid State Physics, 13 (1980) 58333–58341.

[26] A. Taylor, N.J. Doyle, Journal of the Less Common Metals, 13 (1967) 399–412.

[27] J.R. Cost, C.A. Wert, Acta Metallurgica, 11 (1963) 231–242.

[28] A. Darlinski, J. Halbritter, Surface and Interface Analysis, 10 (1987) 223–237.

[29] A.H. Farha, A.O. Er, Y. Ufuktepe, G. Myneni, H.E. Elsayed-Ali, Surface & Coatings Technology, 206 (2011) 1168–1174.

[30] A.H. Farha, A.O. Er, Y. Ufuktepe, G. Myneni, H.E. Elsayed-Ali, Applied Surface Science, 258 (2011) 1613–1618.

[31] A.H. Farha, A.O. Er, Y. Ufuktepe, H.E. Elsayed-Ali, Materials Chemistry and Physics, 132 (2012) 667–672.

[32] M.A. Mamun, A.H. Farha, A.O. Er, Y. Ufuktepe, D. Gu, H.E. Elsayed-Ali, A.A. Elmustafa, Applied Surface Science, 258 (2012) 4308–4313.

[33] M.A. Al Mamun, A.H. Farha, Y. Ufuktepe, H.E. Elsayed-Ali, A.A. Elmustafa, Journal of Materials Research, 27 (2012) 1725–1731.

[34] M.A. Mamun, A.H. Farha, Y. Ufuktepe, S.I. Kimura, T. Hajiri, K. Imura, F. Karadag, H.E. Elsayed-Ali, A.A. Elmustafa, Nanoindentation investigation of the reactive pulsed laser deposited superconducting niobium nitride thin films, in: TMS2013 Supplemental Proceedings, John Wiley & Sons, Inc., 2013, pp. 563–570.

[35] Y. Ufuktepe, A.H. Farha, S.-i. Kimura, T. Hajiri, F. Karadağ, M.A. Al Mamun, A.A. Elmustafa, G. Myneni, H.E. Elsayed-Ali, Materials Chemistry and Physics, 141 (2013) 393–400.

[36] S. Blundell, Superconductivity: A Very Short Introduction, 6th ed., Oxford University Press Inc., New York, 2009.

[37] G.-i. Oya, Y. Onodera, Journal of Applied Physics, 45 (1974) 1389–1397.

[38] Z. Wang, A. Kawakami, Y. Uzawa, B. Komiyama, Journal of Applied Physics, 79 (1996) 7837–7842.

[39] J.G. Chen, Chemical Reviews, 96 (1996) 1477–1498.

[40] P. Alén, M. Ritala, K. Arstila, J. Keinonen, M. Leskelä, Thin Solid Films, 491 (2005) 235–241.

[41] M. Fenker, M. Balzer, R.V. Büchi, H.A. Jehn, H. Kappl, J.J. Lee, Surface and Coatings Technology, 163–164 (2003) 169–175.

[42] M. Wittmer, Journal of Vacuum Science & Technology A: Vacuum, Surfaces, and Films, 3 (1985) 1797–1803.

[43] C. Tarantini, A. Gurevich, J. Jaroszynski, F. Balakirev, E. Bellingeri, I. Pallecchi, C. Ferdeghini, B. Shen, H.H. Wen, D.C. Larbalestier, Physical Review B, 84 (2011) 184522 (6 pp.).

[44] A. Berenov, J.L. MacManus-Driscoll, D. MacPhail, S. Foltyn, Ca Doping of YBCO Thin Films, in: Processing of High Temperature Superconductors, John Wiley & Sons, Inc., 2006, pp. 243–248.

[45] R. Jha, J. Jyoti, V.P.S. Awana, Journal of Superconductivity and Novel Magnetism, (2013) 1–6.

[46] B. Seeber, Handbook of Applied Superconductivity, 6th ed., Institute of Physics Publishing Ltd, Philadelphia, 1998.

[47] M. Larsson, P. Hollman, P. Hedenqvist, S. Hogmark, U. Wahlström, L. Hultman, Surface and Coatings Technology, 86–87, Part 1 (1996) 351–356.

[48] I.A. Rudnev, B.P. Mikhailov, P.V. Bobin, Technical Physics Letters, 31 (2005) 176–178.

[49] H. Holleck, Journal of Vacuum Science & Technology A: Vacuum, Surfaces, and Films, 4 (1986) 2661–2669.

[50] G.N. Gol'tsman, O. Okunev, G. Chulkova, A. Lipatov, A. Semenov, K. Smirnov, B. Voronov, A. Dzardanov, C. Williams, R. Sobolewski, Applied Physics Letters, 79 (2001) 705–707.

[51] S. Singaravelu, J.M. Klopf, G. Krafft, M.J. Kelley, Journal of Vacuum Science & Technology B: Microelectronics and Nanometer Structures, 29 (2011) 061803 (6 pp.).

[52] I. Nowak, M. Ziolek, Chemical Reviews, 99 (1999) 3603–3624.

[53] M. Peiniger, H. Piel, IEEE Transactions on Nuclear Science, 32 (1985) 3610–3612.

[54] B. Aune, R. Bandelmann, D. Bloess, B. Bonin, A. Bosotti, M. Champion, C. Crawford, G. Deppe, B. Dwersteg, D.A. Edwards, H.T. Edwards, M. Ferrario, M. Fouaidy, P.D. Gall, A. Gamp, A. Gössel, J. Graber, D. Hubert, M. Hüning, M. Juillard, T. Junquera, H. Kaiser, G. Kreps, M. Kuchnir, R. Lange, M. Leenen, M. Liepe, L. Lilje, A. Matheisen, W.D. Möller, A. Mosnier, H. Padamsee, C. Pagani, M. Pekeler, H.B. Peters, O. Peters, D. Proch, K. Rehlich, D. Reschke, H. Safa, T. Schilcher, P. Schmüser, J. Sekutowicz, S. Simrock, W. Singer, M. Tigner, D. Trines, K. Twarowski, G. Weichert, J. Weisend, J. Wojtkiewicz, S. Wolff, K. Zapfe, Physical Review Special Topics - Accelerators and Beams, 3 (2000) 092001 (25 pp.).

[55] T. Proslier, M. Kharitonov, M. Pellin, J. Zasadzinski, G. Ciovati, Applied Superconductivity, IEEE Transactions on, 21 (2011) 2619–2622.

[56] P. Kostić, B. Veal, A.P. Paulikas, U. Welp, V.R. Todt, C. Gu, U. Geiser, J.M. Williams, K.D. Carlson, R.A. Klemm, Physical Review B, 53 (1996) 791–801.

[57] F. Jeglitsch, in: Proceedings of the International Symposium Niobium, 2001, pp. 1001–1039.

[58] J. Halbritter, Applied Physics A, 43 (1987) 1–28.

[59] K.Y. Xie, T. Zheng, J.M. Cairney, H. Kaul, J.G. Williams, F.J. Barbaro, C.R. Killmore, S.P. Ringer, Scripta Materialia, 66 (2012) 710–713.

[60] D.A. Keszler, Current Opinion in Solid State and Materials Science, 1 (1996) 204–211.

[61] J.T. Sebastian, D.N. Seidman, K.E. Yoon, P. Bauer, T. Reid, C. Boffo, J. Norem, Physica C: Superconductivity, 441 (2006) 70–74.

[62] G. Ciovati, Applied Physics Letters, 89 (2006) 022507 (3 pp).

[63] M. Delheusy, A. Stierle, N. Kasper, R.P. Kurta, A. Vlad, H. Dosch, C. Antoine, A. Resta, E. Lundgren, J. Andersen, Applied Physics Letters, 92 (2008) 101911–101913.

[64] J. Halbritter, Journal of Applied Physics, 97 (2005) 083904 (12 pp).

[65] M. Grundner, J. Halbritter, Journal of Applied Physics, 51 (1980) 397–405.

[66] D. Bach, R. Schneider, D. Gerthsen, J. Verbeeck, W. Sigle, Microsc Microanal, 15 (2009) 505–523.

[67] E. Il'ichev, H.E. Hoenig, H.G. Meyer, A.B. Zorin, V.V. Khanin, M. Götz, A.B. Pavolotsky, J. Niemeyer, Physica C: Superconductivity, 352 (2001) 141–143.

[68] A. Pearlman, A. Cross, W. Slysz, J. Zhang, A. Verevkin, M. Currie, A. Korneev, P. Kouminov, K. Smirnov, B. Voronov, G. Gol'tsman, R. Sobolewski, Applied Superconductivity, IEEE Transactions on, 15 (2005) 579–582.

[69] F. Marsili, D. Bitauld, A. Fiore, A. Gaggero, F. Mattioli, R. Leoni, M. Benkahoul, F. Lévy, Opt. Express, 16 (2008) 3191–3196.

[70] Y.M. Yaman, M.C. Kuşhan, Journal of Materials Science Letters, 17 (1998) 1231–1234.

[71] ASM, ASM Handbook: Volume 3: Alloy Phase Diagrams, ASM International, Materials Park, OH 1992.

[72] N. Schonberg, Acta Chemica Scandinavica, 8 (1954) 208–212.

[73] M. Torche, G. Schmerber, M. Guemmaz, A. Mosser, J.C. Parlebas, Thin Solid Films, 436 (2003) 208–212.

[74] J. Brčka, I. Hotový, Vacuum, 46 (1995) 1407–1412.

[75] W. Zhen, A. Kawakami, Y. Uzawa, B. Komiyama, Journal of Applied Physics, 79 (1996) 7837–7842.

[76] D. Scheschkewitz, Angewandte Chemie International Edition, 45 (2006) 5912–5914.

[77] A.N. Christensen, C. Rusche, Journal of Crystal Growth, 44 (1978) 383–386.

[78] M. Wen, C.Q. Hu, C. Wang, T. An, Y.D. Su, Q.N. Meng, W.T. Zheng, Journal of Applied Physics, 104 (2008) 023527 (7 pp.).

[79] R. Eason, Pulsed Laser Deposition of Thin Films: Applications-Led Growth of Functional Materials, Wiley-Interscience, Hoboken, USA, 2006.

[80] A. Bhat, X. Meng, A. Wong, T.V. Duzer, Superconductor Science and Technology, 12 (1999) 1030–1032.

[81] V. Boffa, U. Gambardella, V. Marotta, A. Morone, F. Murtas, S. Orlando, G.P. Parisi, Applied Surface Science, 106 (1996) 361–364.

[82] R.E. Treece, J.S. Horwitz, J.H. Claassen, D.B. Chrisey, Applied Physics Letters, 65 (1994) 2860–2862.

[83] R.E. Treece, J.S. Horwitz, D.B. Chrisey, E.P. Donovan, S.B. Qadri, Chemistry of Materials, 6 (1994) 2205–2207.

[84] R.E. Treece, J.S. Horwitz, S.B. Qadri, E.F. Skelton, E.P. Donovan, D.B. Chrisey, Journal of Solid State Chemistry, 117 (1995) 294–299.

[85] R.E. Treece, M.S. Osofsky, E.F. Skelton, S.B. Qadri, J.S. Horwitz, D.B. Chrisey, Physical Review B, 51 (1995) 9356–9359.

[86] G. Cappuccio, U. Gambardella, A. Morone, S. Orlando, G.P. Parisi, Applied Surface Science, 109–110 (1997) 399–402.

[87] H. Bauer, Journal of Low Temperature Physics, 24 (1976) 219–227.

[88] Lide D. R. (Ed.), CRC Handbook of Chemistry and Physics, CRC Press LLC, Gaithersburg, Maryland, USA, 2001–2002.

[89] C. Angelkort, H. Lewalter, P. Warbichler, F. Hofer, W. Bock, B.O. Kolbesen, Spectrochimica Acta Part A: Molecular and Biomolecular Spectroscopy, 57 (2001) 2077–2089.

[90] A. Taylor, N.J. Doyle, Journal of the Less Common Metals, 13 (1967) 413–430.

[91] M. Joguet, W. Lengauer, M. Bohn, J. Bauer, Journal of Alloys and Compounds, 269 (1998) 233–237.

[92] H.M. Smith, A.F. Turner, Appl. Opt., 4 (1965) 147–148.

[93] Chrisey D. B., H.G. K., Pulsed Laser Deposition of Thin Films, John Wiley & Sons, Inc., New York, 1994.

[94] M.K. Wu, J.R. Ashburn, C.J. Torng, P.H. Hor, R.L. Meng, L. Gao, Z.J. Huang, Y.Q. Wang, C.W. Chu, Physical Review Letters, 58 (1987) 908–910.

[95] J. Perriere, E. Millon, W. Seiler, C. Boulmer-Leborgne, V. Craciun, O. Albert, J.C. Loulergue, J. Etchepare, Journal of Applied Physics, 91 (2002) 690–696.

[96] Z. Zhang, P.A. VanRompay, J.A. Nees, P.P. Pronko, Journal of Applied Physics, 92 (2002) 2867–2874.

[97] X.L. Tong, D.S. Jiang, L. Liu, H. Dai, Journal of Vacuum Science & Technology B: Microelectronics and Nanometer Structures, 26 (2008) 1398–1403.

[98] Z. Zhang, P.A. VanRompay, J.A. Nees, R. Clarke, X. Pan, P.P. Pronko, Applied Surface Science, 154–155 (2000) 165–171.

[99] H.E. Elsayed-Ali, T.B. Norris, M.A. Pessot, G.A. Mourou, Phys. Rev. Lett., 58 (1987) 1212–1215.

[100] R.K. Singh, J. Narayan, Physical Review B, 41 (1990) 8843–8859.

[101] B.N. Chichkov, C. Momma, S. Nolte, F. Alvensleben, A. Tünnermann, Appl. Phys. A, 63 (1996) 109–115.

[102] X. Liu, G. Mourou, Laser Focus World, 33 (1997) 6.

[103] P.P. Pronko, S.K. Dutta, D. Du, R.K. Singh, J. Appl. Phys., 78 (1995) 6233–6240.

[104] J. Meeker, A.E. Segall, V.V. Semak, Journal of Laser Applications, 22 (2010) 6.

[105] J. Shen, P. Ohresser, C.V. Mohan, M. Klaua, J. Barthel, J. Kirschner, Physical Review Letters, 80 (1998) 1980–1983.

[106] M.N.R. Ashfold, F. Claeyssens, G.M. Fuge, S.J. Henley, Chem. Soc. Rev., 33 (2004) 23–31.

[107] A.G. Zhidkov, L.V. Zhigilei, A. Sasaki, T. Tajima, Appl. Phys. A, 73 (2001) 741–747.

[108] C. Belouet, Applied Surface Science, 96–98 (1996) 630–642.

[109] T. Venkatesan, X.D. Wu, A. Inam, J.B. Wachtman, Applied Physics Letters, 52 (1988) 1193–1195.

[110] A. Ikeda, M. Matsumoto, S. Ogura, T. Okano, K. Fukutani, The Journal of Chemical Physics, 138 (2013) 124705 (6 pp.).

[111] T. Takiya, M. Han, M. Yaga, Thermodynamics of Nanoparticle Formation in Laser Ablation, 2011.

[112] S.I. Anisimov, D. Bäuerle, B.S. Luk'yanchuk, Physical Review B, 48 (1993) 12076–12081.

[113] D.L. Smith, Thin-Film Deposition: Principles & Practice, 6th ed., McGraw-Hill, , New York, 1995.

[114] L.W. Martin, Y.H. Chu, R. Ramesh, Materials Science and Engineering: R: Reports, 68 (2010) 89–133.

[115] S. Metev, K. Meteva, Appl. Surf. Sci., 43 (1989) 402–408.

[116] H. Spillmann, C. Clerc, M. Döbeli, P.R. Willmott, Applied Surface Science, 197–198 (2002) 304–311.

[117] S. Amoruso, B. Toftmann, J. Schou, Applied Physics A, 79 (2004) 1311–1314.

[118] S.S. Harilal, C.V. Bindhu, M.S. Tillack, F. Najmabadi, A.C. Gaeris, J. Phys. D: Appl. Phys., 35 (2002) 2935–2938.

[119] M.C. Foote, B.B. Jones, B.D. Hunt, J.B. Barner, R.P. Vasquez, L.J. Bajuk, Physica C: Superconductivity, 201 (1992) 176–182.

[120] H.-U. Krebs, M. Weisheit, J. Faupel, E. Süske, T. Scharf, C. Fuhse, M. Störmer, K. Sturm, M. Seibt, H. Kijewski, D. Nelke, E. Panchenko, M. Buback, Pulsed Laser Deposition (PLD) - A Versatile Thin Film Technique, in: B. Kramer (Ed.) Advances in Solid State Physics, Springer Berlin Heidelberg, 2003, pp. 505–518.

[121] J.A. Venables, Introduction to Surface and Thin Film Processes, 6th ed., Cambridge University Press, Cambridge, 2000.

[122] D. Kashchiev, Journal of Crystal Growth, 40 (1977) 29–46.

[123] P. Krehl, F. Schwirzke, A.W. Cooper, Journal of Applied Physics, 46 (1975) 4400–4406.

[124] J.A. Venables, G.D.T. Spiller, M. Hanbucken, Reports on Progress in Physics, 47 (1984) 399–459.

[125] V.M. Kaganer, B. Jenichen, R. Shayduk, W. Braun, H. Riechert, Physical Review Letters, 102 (2009) 016103.

[126] E. Bauer, J.H. van der Merwe, Physical Review B, 33 (1986) 3657–3671.

[127] B.D. Cullity, Elements of X-ray Diffraction, Addison-Wesley, New York, 1956.

[128] J.I. Langford, A.J.C. Wilson, J. Appl. Crystallogr., 11 (1978) 102–113.

[129] P. Scardi, M. Leoni, R. Delhez, J. Appl. Crystallogr., 37 (2004) 381–390.

[130] A. Monshi, M.R. Foroughi, M.R. Monshi, World Journal of Nano Science and Engineering, 37 (2012) 154–160.

[131] B.B. He, Two-dimensional X-Ray Diffraction, Wiley-Interscience, Hoboken, USA, 2009.

[132] A. Semenov, B. Günther, U. Böttger, H.W. Hübers, H. Bartolf, A. Engel, A. Schilling, K. Ilin, M. Siegel, R. Schneider, D. Gerthsen, N.A. Gippius, Physical Review B, 80 (2009) 054510 (10 pp.).

[133] P.R. Chalker, A.M. Jones, C. Johnston, I.M. Buckley-Golder, Surface and Coatings Technology, 47 (1991) 365–374.

[134] B.B. He, Powder Diffraction, 18 (2003) 71–85.

[135] I. Savin de Larclause, T. Paulmier, I. Enache, H. Caquineau, P. Raynaud, F. Massines, N. Gherardi, Plasma Science, IEEE Transactions on, 37 (2009) 970–978.

[136] G. Binnig, C.F. Quate, C. Gerber, Physical Review Letters, 56 (1986) 930–933.

[137] Y.M. Shy, L.E. Toth, R. Somasundaram, Journal of Applied Physics, 44 (1973) 5539–5545.

[138] A.B. Kaul, T.D. Sands, T. Van Duzer, Journal of Materials Research, 16 (2001) 1223–1226.

[139] C.Z. Antoine, S. Berry, M. Aurino, J.F. Jacquot, J.C. Villegier, G. Lamura, A. Andreone, IEEE Transactions on Applied Superconductivity, 21 (2011) 2601–2604.

[140] A. Lascialfari, A. Rigamonti, E. Bernardi, M. Corti, A. Gauzzi, J.C. Villegier, Physical Review B (Condensed Matter and Materials Physics), 80 (2009) 104505 (10 pp.).

[141] K.S. Il'in, M. Lindgren, M. Currie, A.D. Semenov, G.N. Gol'tsman, R. Sobolewski, S.I. Cherednichenko, E.M. Gershenzon, Applied Physics Letters, 76 (2000) 2752–2752.

[142] G.N. Gol'tsman, K. Smirnov, P. Kouminov, B. Voronov, N. Kaurova, V. Drakinsky, J. Zhang, A. Verevkin, R. Sobolewski, Applied Superconductivity, IEEE Transactions on, 13 (2003) 192–195.

[143] B. Delaet, J.C. Villegier, W. Escoffier, J.L. Thomassin, P. Feautrier, I. Wang, P. Renaud-Goud, J.P. Poizat, in: 10th International Workshop on Low Temperature Detectors (LTD-10), 7–11 July 2003, Elsevier, Netherlands, 2004, pp. 541–543.

[144] K.S. Havey, J.S. Zabinski, S.D. Walck, Thin Solid Films, 303 (1997) 238–245.

[145] F. Levy, P. Hones, P.E. Schmid, R. Sanjines, M. Diserens, C. Wiemer, in: 26th International Conference on Metallurgical Coatings and Thin Films, 12–15 April 1999, Elsevier, Switzerland, 1999, pp. 284–290.

[146] M. Benkahoul, E. Martinez, A. Karimi, R. Sanjinés, F. Lévy, Surface and Coatings Technology, 180–181 (2004) 178–183.

[147] K. Senapati, N.K. Pandey, R. Nagar, R.C. Budhani, Physical Review B, 74 (2006) 104514 (8 pp.).

[148] V.I. Ivashchenko, P.E.A. Turchi, E.I. Olifan, Physical Review B (Condensed Matter and Materials Physics), 82 (2010) 054109 (9 pp.).

[149] R. Schneider, B. Freitag, D. Gerthsen, K.S. Ilin, M. Siegel, Crystal Research and Technology, 44 (2009) 1115–1121.

[150] S. Chaudhuri, M.R. Nevala, T. Hakkarainen, T. Niemi, I.J. Maasilta, in, Institute of Electrical and Electronics Engineers Inc., NJ, 2011, pp. 143–146.

[151] A.B. Kaul, T. Van Duzer, in: 2000 Applied Superconductivity Conference, 17–22 Sept. 2000, IEEE, USA, 2001, pp. 88–91.

[152] T. Ishiguro, K. Matsushima, K. Hamasaki, Journal of Applied Physics, 73 (1993) 1151–1153.

[153] X.-J. Chen, V.V. Struzhkin, Z. Wu, M. Somayazulu, J. Qian, S. Kung, A.N. Christensen, Y. Zhao, R.E. Cohen, H.-K. Mao, R.J. Hemley, Proceedings of the National Academy of Sciences of the United States of America, 102 (2005) 3198–3201.

[154] W.M. Roach, J.R. Skuza, D.B. Beringer, Z. Li, C. Clavero, R.A. Lukaszew, Superconductor Science and Technology, 25 (2012) 125016 (6 pp.).

[155] A. Gurevich, Applied Physics Letters, 88 (2006) 012511 (3 pp.).

[156] H. Padamsee, J.a. Knobloch, T. Hays, RF Superconductivity for Accelerators, John Wiley & Sons, Inc., New York, 1998.

[157] Powder Diffraction File 00-034-0370, International Center for Diffraction Data, 2000.

[158] C.S. Sandu, M. Benkahoul, M. Parlinska-Wojtan, R. Sanjinés, F. Lévy, Surface and Coatings Technology, 200 (2006) 6544–6548.

[159] Powder Diffraction File 00-040-1274, International Center for Diffraction Data, 2000.

[160] S.A. Barnett, M. Shinn, Annual Review of Materials Science, 24 (1994) 481–511.

[161] Powder Diffraction File 00-038-1155, International Center for Diffraction Data, 2000.

[162] Powder Diffraction File 01-089-5126, International Center for Diffraction Data, 2001

[163] P. Scardi, M. Leoni, Acta Crystallographica Section A, 58 (2002) 190–200.

[164] P. Haier, B.A. Hermann, N. Esser, U. Pietsch, K. Lüders, W. Richter, Thin Solid Films, 318 (1998) 223–226.

[165] M.S. Hegazy, H.E. Elsayed-Ali, Journal of Applied Physics, 99 (2006) 054308 (5 pp.).

[166] Powder Diffraction File 00-020-0801, International Center for Diffraction Data, 2004.

[167] L.E. Toth, Transition Metal Carbides and Nitrides., Academic Press, New York, 1971.

[168] H.O. Pierson, Handbook of Refractory Carbides and Nitrides: Properties, Characteristics, Processing and Applications, Noyes Publications, Westwood, New Jersey, 1996.

[169] A.V. Gusarov, A.G. Gnedovets, I. Smurov, Journal of Applied Physics, 88 (2000) 4352–4364.

[170] S. Weissmantel, G. Reisse, Diamond and Related Materials, 10 (2001) 1973–1982.

[171] E.F. Skelton, M.R. Skokan, E. Dukauskas, Journal of Applied Crystallography, 14 (1981) 51–57.

[172] H.P. Klug, L.E. Alexander, X-ray Diffraction Procedures: For Polycrystalline and Amorphous Materials, Wiley-Interscience, New York, 1974.

[173] M. Wen, C.Q. Hu, Q.N. Meng, Z.D. Zhao, T. An, Y.D. Su, W.X. Yu, W.T. Zheng, Journal of Physics D: Applied Physics, 42 (2009) 035304 (8 pp.).

[174] Y. Lifshitz, S.R. Kasi, J.W. Rabalais, Physical Review Letters, 62 (1989) 1290–1293.

[175] D.R. McKenzie, D. Muller, B.A. Pailthorpe, Physical Review Letters, 67 (1991) 773–776.

[176] J.J. Olaya, S.E. Rodil, S. Muhl, Thin Solid Films, 516 (2008) 8319–8326.

[177] G.-i. Oya, Y. Onodera, Journal of Applied Physics, 47 (1976) 2833–2840.

[178] I. Hotový, J. Huran, D. Búc, R. Srnánek, Vacuum, 50 (1998) 45–48.

[179] P. Heitjans, S. Indris, Journal of Physics: Condensed Matter, 15 (2003) R1257–R1289.

[180] V. Buscaglia, F. Caracciolo, M. Ferretti, M. Minguzzi, R. Musenich, Journal of Alloys and Compounds, 266 (1998) 201–206.

[181] S.T. Oyama, The Chemistry of Transition Metal Carbides and Nitrides, Springer, Blackie, London, 1996.

[182] K.S. Keskar, T. Yamashita, Y. Onodera, Japanese Journal of Applied Physics, 10 (1971) 370–374.

[183] R. Berger, W. Lengauer, P. Ettmayer, Journal of Alloys and Compounds, 259 (1997) L9–L13.

[184] W.C. Oliver, G.M. G. M. Pharr, Journal of Materials Research, 7 (1992) 1564–1583.

[185] W.C. Oliver, G.M. Pharr, Journal of Materials Research, 19 (2004) 3–20.

[186] M. Kidszun, R. Hühne, B. Holzapfel, L. Schultz, Superconductor Science and Technology, 23 (2010) 025010 (6 pp.).

[187] G. Jouve, C. Séverac, S. Cantacuzène, Thin Solid Films, 287 (1996) 146–153.

[188] X. Gonze, B. Amadon, P.M. Anglade, J.M. Beuken, F. Bottin, P. Boulanger, F. Bruneval, D. Caliste, R. Caracas, M. Côté, T. Deutsch, L. Genovese, P. Ghosez, M. Giantomassi, S. Goedecker, D.R. Hamann, P. Hermet, F. Jollet, G. Jomard, S. Leroux, M. Mancini, S. Mazevet, M.J.T. Oliveira, G. Onida, Y. Pouillon, T. Rangel, G.M. Rignanese, D. Sangalli, R. Shaltaf, M. Torrent, M.J. Verstraete, G. Zerah, J.W. Zwanziger, Computer Physics Communications, 180 (2009) 2582–2615.

[189] G. Aeppli, H.J. Stolz, R.A. Pollak, Physical Review B, 24 (1981) 4128–4135.

[190] M.F. Tambwe, D.S. Stone, A.J. Griffin, H.H. Kung, Y. Cheng, M. Nastasi, Journal of Materials Research, 14 (1999) 407–417.
[191] A. Taylor, N.J. Doyle, Journal of the Less Common Metals, 13 (1967) 399–412.
[192] C.C. Koch, J.O. Scarbrough, D.M. Kroeger, Physical Review B, 9 (1974) 888–897.
[193] W. DeSorbo, Physical Review, 132 (1963) 107–121.
[194] J.E. Penner-Hahn, X-ray Absorption Spectroscopy, in, John Wiley & Sons, Ltd, 2001.
[195] J. Kirz, D. Vaughan, X-ray Data Booklet, Lawrence Berkeley Laboratory, University of California, 1985.
[196] M. Azuma, Y. Nakato, H. Tsubomura, Journal of Electroanalytical Chemistry and Interfacial Electrochemistry, 255 (1988) 179–198.
[197] D. Bach, R. Schneider, D. Gerthsen, Microsc Microanal, 15 (2009) 524–538.
[198] D. Bach, H. Stormer, R. Schneider, D. Gerthsen, J. Verbeeck, Microsc Microanal, 12 (2006) 416–423.
[199] J.B. Metson, H.J. Trodahl, B.J. Ruck, U.D. Lanke, A. Bittar, Surf. Interface Anal., 35 (2003) 719–722.
[200] R. Banerjee, E.A. Sperling, G.B. Thompson, H.L. Fraser, S. Bose, P. Ayyub, Appl. Phys. Lett., 82 (2003) 4250–4252.
[201] V.E. Shaternik, S.Y. Larkin, T.A. Khachaturova, Physica C: Superconductivity, 435 (2006) 96–98.
[202] K.L. Rutherford, P.W. Hatto, C. Davies, I.M. Hutchings, Surface and Coatings Technology, 86–87, Part 2 (1996) 472–479.
[203] S.P. Chockalingam, M. Chand, J. Jesudasan, V. Tripathi, P. Raychaudhuri, Physical Review B, 77 (2008) 214503 (8 pp.).
[204] G.N. Gol'tsman, A.D. Semenov, Y.P. Gousev, M.A. Zorin, I.G. Godidze, E.M. Gershenzon, P.T. Lang, W.J. Knott, K.F. Renk, Superconductor Science and Technology, 4 (1991) 453–456.
[205] M.A. Mamun, A.H. Farha, A.O. Er, Y. Ufuktepe, D. Gu, H.E. Elsayed-Ali, A.A. Elmustafa, Applied Surface Science, 258 (2012) 4308–4313.
[206] R. Sanjinés, M. Benkahoul, C.S. Sandu, P.E. Schmid, F. Lévy, Thin Solid Films, 494 (2006) 190–195.
[207] A.D. Semenov, H.-W. Hubers, J. Schubert, G.N. Gol'tsman, A.I. Elantiev, B.M. Voronov, E.M. Gershenzon, Journal of Applied Physics, 88 (2000) 6758–6767.
[208] S. Cherednichenko, P. Khosropanah, E. Kollberg, M. Kroug, H. Merkel, Physica C: Superconductivity, 372–376, Part 1 (2002) 407–415.
[209] J.R. Gao, M. Hajenius, F.D. Tichelaar, T.M. Klapwijk, B. Voronov, E. Grishin, G. Gol'tsman, C.A. Zorman, M. Mehregany, Applied Physics Letters, 91 (2007) 062504 (3 pp.).
[210] K.S. Keskar, T. Yamashita, Y. Onodera, Japanese Journal of Applied Physics, 10 (1971) 370–374.
[211] A. Ishizaka, Y. Shiraki, Journal of the Electrochemical Society, 133 (1986) 666–671.
[212] X. Li, B. Bhushan, Thin Solid Films, 340 (1999) 210–217.
[213] W.C. Oliver, C.J. McHargue, Thin Solid Films, 161 (1988) 117–122.
[214] W.C. Oliver, G.M. G. M. Pharr, Journal of Materials Research, 19 (2004) 3–20.
[215] W. Lengauer, Surface and Interface Analysis, 15 (1990) 377–382.

[216] D. Riabinina, E. Irissou, B.L. Drogoff, M. Chaker, D. Guay, Journal of Applied Physics, 108 (2010) 034322 (6 pp.).

[217] N. Özer, D.-G. Chen, C.M. Lampert, Thin Solid Films, 277 (1996) 162–168.

[218] G. Jouve, C. Séverac, S. Cantacuzène, Thin Solid Films, 287 (1996) 146–153.

[219] M. Lucci, S. Sanna, G. Contini, N. Zema, V. Merlo, M. Salvato, H.N. Thanh, I. Davoli, Surface Science, 601 (2007) 2647–2650.

[220] R. Krishnan, C. David, P.K. Ajikumar, S. Dash, A.K. Tyagi, V. Jayaram, B. Raj, Surface and Coatings Technology, 206 (2011) 1196–1202.

[221] V. Yeh, S.Y. Wu, W.H. Li, Colloids and Surfaces A: Physicochemical and Engineering Aspects, 313–314 (2008) 246–249.

[222] J.J. Yeh, I. Lindau, Atomic Data and Nuclear Data Tables, 32 (1985) 1–155.

[223] G. Brauer, Journal of the Less Common Metals, 2 (1960) 131–137.

[224] C.D. Gelatt, Jr., A.R. Williams, V.L. Moruzzi, Physical Review B, 27 (1983) 2005–2013.

[225] P. Mishra, S.R. Bhattacharyya, D. Ghose, Nuclear Instruments and Methods in Physics Research, Section B: Beam Interactions with Materials and Atoms, 266 (2008) 1629–1634.

[226] M. Faucher, T. Fournier, B. Pannetier, C. Thirion, W. Wernsdorfer, J.C. Villegier, V. Bouchiat, Physica C: Superconductivity, 368 (2002) 211–217.

[227] A. Gaggero, S.J. Nejad, F. Marsili, F. Mattioli, R. Leoni, D. Bitauld, D. Sahin, G.J. Hamhuis, R. Notzel, R. Sanjines, A. Fiore, Applied Physics Letters, 97 (2010) 15110 (3 pp.).

[228] E. Carpene, P. Schaaf, M. Han, K.P. Lieb, M. Shinn, Applied Surface Science, 186 (2002) 195–199.

[229] S. Singaravelu, J.M. Klopf, C. Xu, G. Krafft, M.J. Kelley, Journal of Vacuum Science & Technology B: Microelectronics and Nanometer Structures, 30 (2012) 051806 (7 pp.).

[230] P. Kneisel, G. Ciovati, J. Sekutowicz, L. Turlington, IEEE Transactions on Applied Superconductivity, 19 (2009) 1416–1418.

[231] S. Peter, Progress in Materials Science, 47 (2002) 1–161.

[232] D. Bäuerle, Laser Processing and Chemistry, Springer, Berlin 2000.

[233] K. Nakamura, M. Hikita, H. Asano, A. Terada, Japanese Journal of Applied Physics, 21 (1982) 672–673.

[234] Powder Diffraction File 00-043-1420, International Center for Diffraction Data, 2000.

[235] J.P. Ulerich, L.C. Ionescu, J. Chen, W.O. Soboyejo, C.B. Arnold, in: Photon Processing in Microelectronics and Photonics VI, (2007) 645819 (10 pp.).

[236] J. Reif, F. Costache, M. Henyk, S.V. Pandelov, Applied Surface Science, 197–198 (2002) 891–895.

[237] F. Costache, M. Henyk, J. Reif, Applied Surface Science, 208–209 (2003) 486–491.

[238] J.E. Sipe, J.F. Young, J.S. Preston, H.M. van Driel, Physical Review B, 27 (1983) 1141–1154.

[239] Y. Yang, J. Yang, L. Xue, Y. Guo, Applied Physics Letters, 97 (2010) 141101 (3 pp.).

[240] B.T. Thole, G. van der Laan, Physical Review B, 38 (1988) 3158–3171.

APPENDIX A

PULSED LASER DEPOSITION SYSTEM

A.1. SYSTEM DESIGN AND COMPONENTS

The main components of the system are shown in Fig. A.1. Images for the rest of the components appears later in the operation description.

A.2. OPENING THE PLD SYSTEM

Before opening the PLD chamber, check to been sure that the ion gauge is off, all wires all wires are disconnected, and the electron gun is off; then proceed very carefully to the steps below.

1. Turn ON the mechanical pump; then turn ON the turbo pump; and let them run for about 20 min.

2. Turn OFF the ion pump; then slowly open UHV.

3. Wait 30 minutes for the system to be pumped by the turbo and the mechanical pumps.

4. Turn off the turbo and then the mechanical pump.

5. Fill in the chamber with dry nitrogen gas to reach atmospheric pressure using Venting valve shown in Fig. A.1.

Venting valve to nitrogen source

Turbo pump

Hose to mechanical

Laser –In view port

Power electrodes

High precision leak valve

UHV valve

Convectron gauge

¼ inch SS tubing gas line

Ion pump
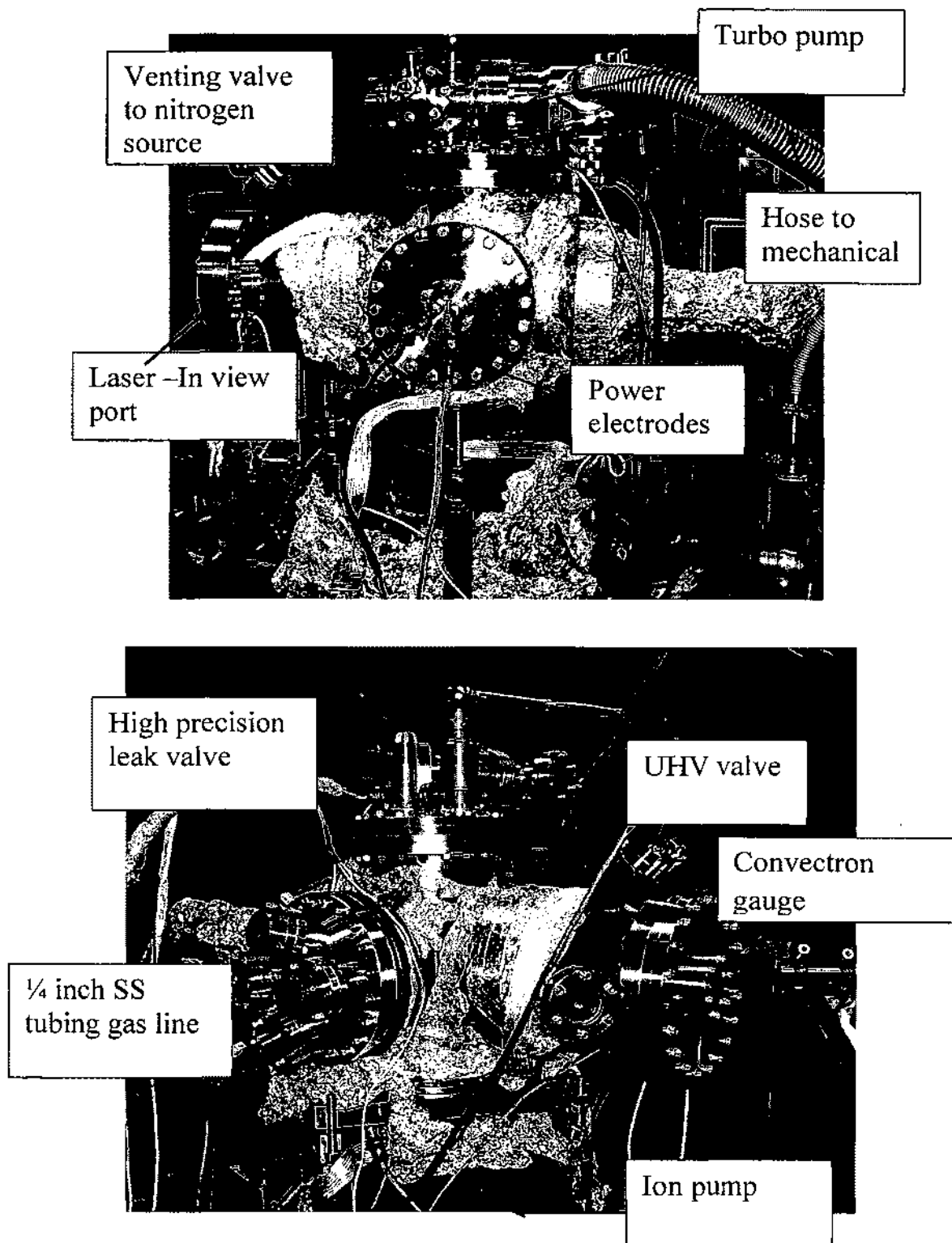
Fig. A.1. The main components of a PLD system.
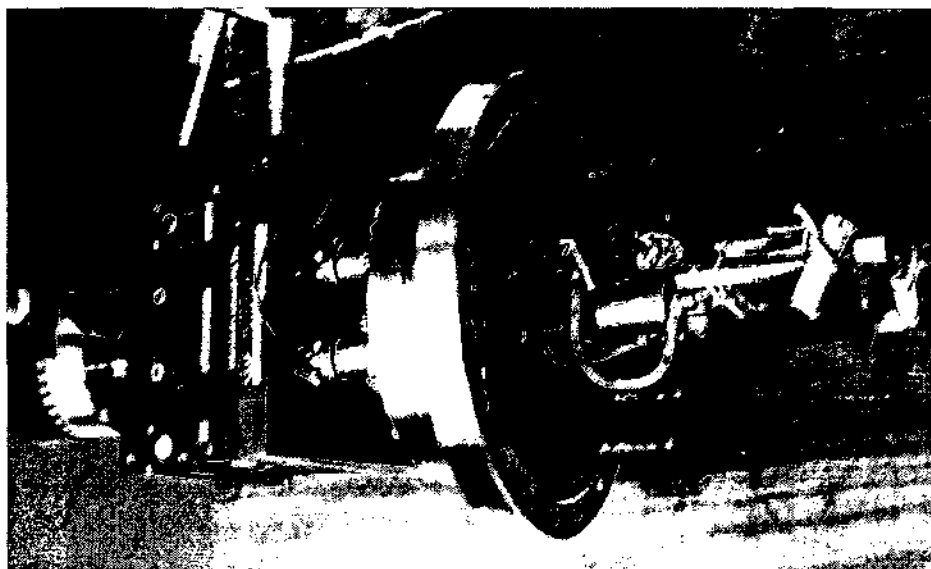
Fig. A. 2. Sample manipulator.

6. Unscrew the screws flange which holds the sample manipulator (Fig. A.2) or any other part you need to take out. The chamber should not be left open for a long time. You need to cover the open ports. When handling or removing old copper gaskets avoid scratching the knife-edge of the CF flange. Use a new copper gasket and clean the vacuum components with isopropyl alcohol (IPA).

A.3. CLEANING THE SUBSTRATE

You have to change the substrate after each run. It is recommended to have at least a few chemically cleaned samples. Sample cleaning is done by using a modified Shiraki method for Si sample and buffered chemical polishing (BCP) for Nb samples. Samples cleaning should be done under working fume hood. Be cautious when using HF to avoid direct exposure to the skin and do not inhale its fumes. Steps for cleaning are

given below. A homemade sample heater made of ceramic beads and tungsten wire is shown in Fig. A.3.
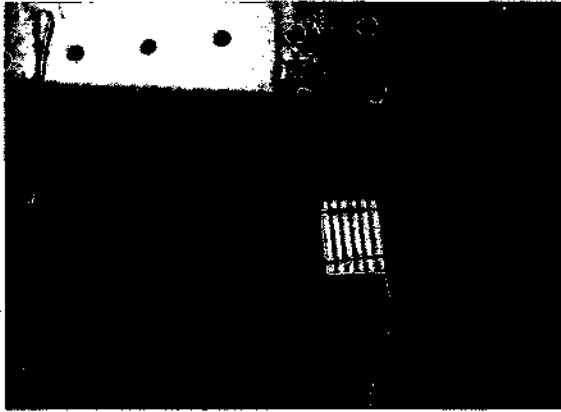
Fig. A. 3. Substrate heater.

1. Clean the Si substrates by the modified Shiraki method. The samples are dipped into a solution of H_2SO_4 (97 wt %): H_2O_2 (30 wt %) = 4:1 (by volume) for 10 min, rinsed with ultra-pure water for 10 min, then dipped into a solution of HF (50 wt %): H_2O = 1:10 (by volume) for 1 min. Unused clean samples are stored in ethanol.

2. Clean the Nb substrates, BCP: The BCP solutions (1:1:1 and 2:1:1 HPO_3:HNO_3:HF) are cooled down to 10 °C during the cleaning process. Approximately a 50 micron layer of material was removed by BCP that resulted in Nb substrates The etched samples were rinsed in deionized water, dried under nitrogen flow, and then degassed for several hours at ~800 °C in the UHV chamber under a base pressure of ~1.3×10^{-7} Pa before starting deposition.

3.   When installing a Si sample, put the thermocouple between the clips and the sample so that it firmly touches the sample's surface. In the case of Nb samples, W wire used to attach sample to the homemade heater.

4.   Install the sample manipulator back to the system by fastened all screws.

A.4. CHANGING THE TARGET

1.   Unscrew the 2 ¾ " flange holding the target holder.

2.   Hold by unscrewing the screw set that is holding the shaft.

3.   Place the target hold upside-down on a clean surface.

4.   Use the heat gun to heat the target-holder interface for a few minutes by directing the heat gun to different areas. Remove the target when the target is completely detached from the holder; then, use a razor to remove the Torr Seal residuals.

5.   Prepare the Torr Seal for 2:1 volume to stick the Nb sputtering target to the shaft.

6.   Install the target holder base to its location; fasten the set screw of the shaft.

7.   Install the 2 ¾'' CF flange back and tighten all the screws.

A.5. PUMPING THE SYSTEM DOWN AND BAKE OUT THE SYSTEM

After fishing installing the sample and target to chamber you need to you start to pump down. To do this, follow these steps:

1.   Turn on the mechanical pump and then turn on the turbo pump. You need to make sure the UHV valve to turbo pump is closed and fan is working to cool down the turbo pump. Watch the speed and temperature of the turbo pump during pumping down. Normally, the turbo pump should come to the maximum speed in a couple of minutes. If not, check to determine if there are any untightened screws.

2.   When the turbo reaches its maximum pumping speed, turn on the ion gauge.

3. In several hours, the base pressure should be low at 10^{-4} Pa. Then, you can start the bake-out procedure under turbo and mechanical pumps.

4. When pressure low 10^{-7} Pa, turn on ion pump.

5. Pressure should be low at 10^{-5} Pa. Then, start cooling down the chamber.

A.6. Nd: YAG LASER OPERATION

The Lumonics YAG Master 200 laser was used to ablate germanium and excite silicon substrate, as shown in Fig. 4. Make sure that you have enough cooling water inside the chiller located at the bottom of the power supply. Once every month, water level must be checked.
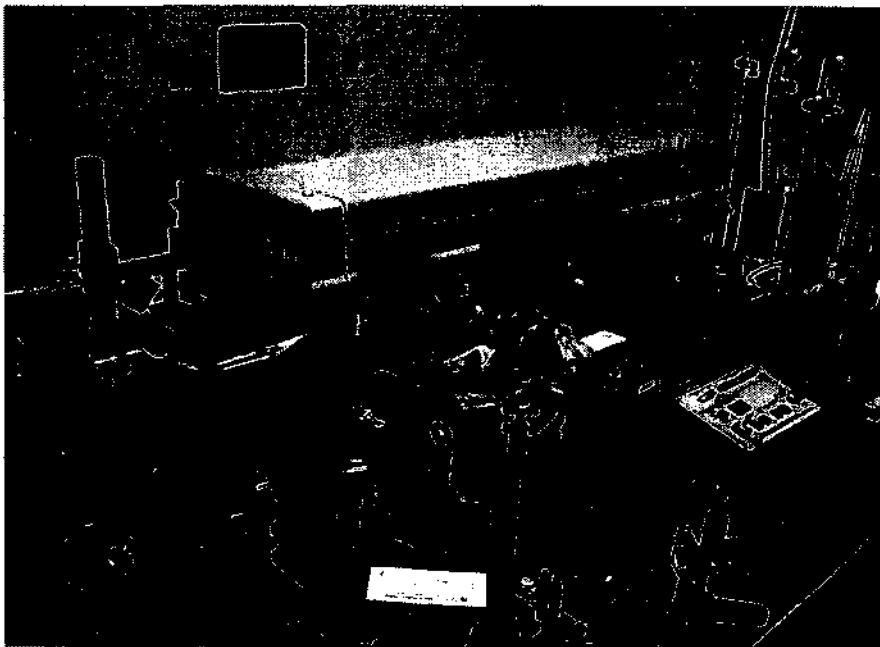

Fig. A. 4. Lumonics YAG Master (YM) 200 laser system.

A.6.1. TURN ON PROCEDURE

1. Wear laser eye protection goggles.

2. Turn on the external cooling water.

3. Rotate the "red" main switch to "on" position. That will start the cooler pump. Allow at least 30 minutes for the cooling to reach operating temperature.

4. To enable the power supply, turn 'enable" key switch clockwise to horizontal position on the control unit.

5. After a few seconds, you will hear a sound and the "on" LED, next to the key switch will light up indicating the start of the flashlamp.

6. From the pockels cell divider, push the button to provide the desired frequency. 10 Hz is obtained by pushing ÷ 5 dividing button to divide the default frequency 50 Hz by 5.

7. Use the flashlamp "oscillator selector" to change the laser power.

8. Press the oscillator "on" button, the flashlamp will begin to pulse.

9. Press the "open" button to open the shutter.

10. To temporarily stop the beam, without turning off the laser, press the "close" shutter button.

A.6.2. TURN OFF PROCEDURE

1. Press "close" button to close the shutter; then press the oscillator OFF button.

2. Turn the "enable" key to "off" vertical position.

3. Leave the cooler pump "on" for at least 30 minutes to cool down the system.

4. Switch "off" the cooler.

APPENDIX B

FEMTOSECOND LASER OPERATION AND MAINTENANCE

B.1. OPERATION OF THE LASER

The femtosecond laser system consists of an oscillator and a ReGen amplifier. The ReGen amplifier consists of stretcher, amplifier, and compressor. There are three chillers: one for the oscillator, one for the pump laser Darwin, and another big one to cool down the Darwin chiller. The Ti-light oscillator was modified by replacing the pump laser with Excel from Laser Quantum Company. One needs to follow the following procedure to turn on the oscillator and amplifier. The oscillator chiller, pumping controller and Ti-light laser are shown in Fig. B.1

- Make sure the chiller for the oscillator is "on" and the temperature is around 23 °C for oscillator stability and performance.

- Use PuTTY software that controls and displays the operation of pump laser.

- After turning on the laser system, wait around 20 min for Excel to warm-up. Normal operation is between 23-38 °C and is optimized at 26.9-27.1 °C.

- Excel power is set to 2200 mW. The Ti-light shutter is a push button located in the controller of air purging (APS-100); push this round button to get output laser.

- Push modelocking button at the back of the oscillator.

- You can check the pulse train; you should see something like that shown in Fig. B.2. The pulse train should have straight pulses if modelocking is obtained properly. Also, the spectrum from the oscillator when it is modelocking should look like that in Fig. B.3, with a FWHM of 40-45 nm.
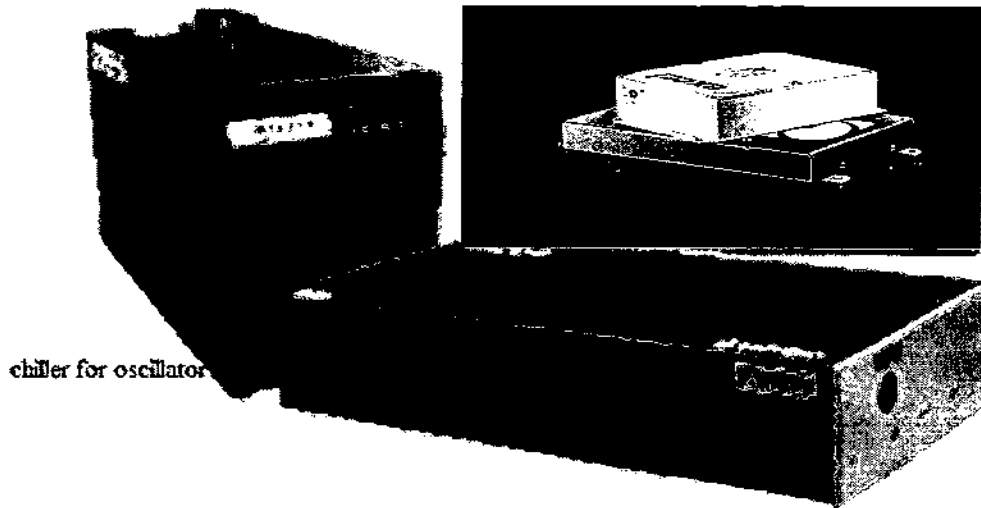
Fig. B. 1. Ti-light laser system after modification.

(a)   (b)
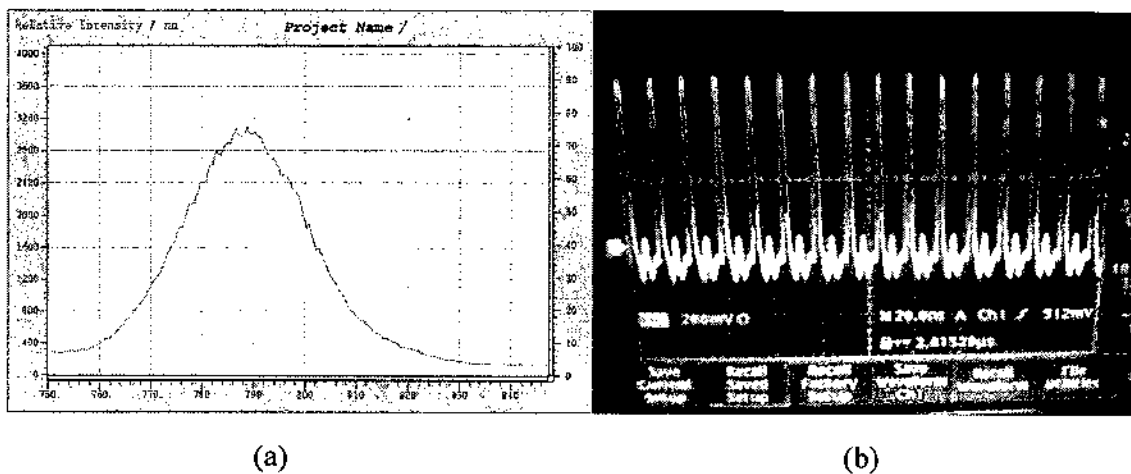
Fig. B. 2. (a) Spectra from oscillator shows modelocking. (b) Photodiode signal from oscillator shows modelocking.

- Once you check the spectrometer, pulse train and power from the oscillator before you start the amplifier, make sure you connect the BNC cable back to the oscillator, since it is used for the external trigging of the amplifier

- Turn "on" the big chiller, which is dedicated to the amplifier in LAB106.
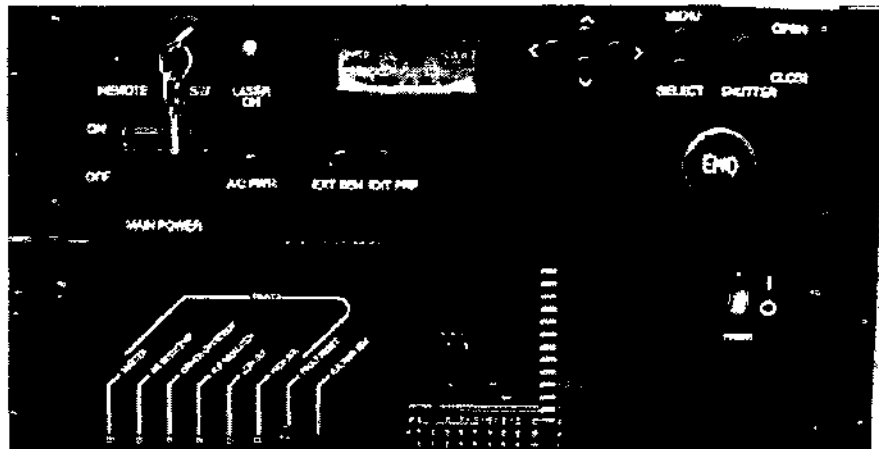
Fig. B. 3. Front panel of Darwin controller.

- Turn the key clockwise and a bit farther refer to Fig. B.4 for the front panel of Darwin controller. Wait ~10 minutes for the amplifier to warm up. You may see an error sign on the Darwin chiller display upon starting. That should go in a couple of minutes.

- Push "menu" button and set the temperature to 17.5 °C; then press "select".

- Go to "mode set" and select PRF source and change from "internal" to "external".

- Once temperature is around ~17.5.0±0.1, open the "shutter" and increase the current value slowly to ~28.0 A.

- Watch the pulse train from the amplifier. If necessary, touch two pump mirrors in the amplifier to have a better pulse train shape, as shown in Fig. B.5. To optimize power and shape, touch three mirrors in multipass while watching the power. Note that the most stable performance is obtained by adjusting the timing and V_B value, so that the pulse train includes the one pulse that is just past the maximum.

Fig. B. 4. Pulse train from cavity dumping amplifier with backup diode signal with yellow color.

B.2. TI-LIGHT OSCILLATOR

B.2.1. TI-LIGHT OSCILLATOR MAINTENANCE
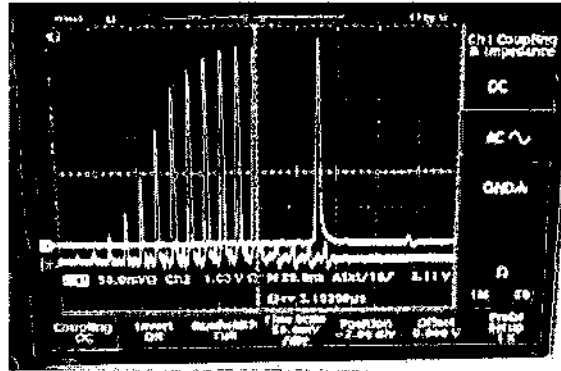
- Do not re-optimize the power with the mirror position in ML-range.

- Always, power optimization must be done at CW max position with at least 10 divisions away from modelocking position.

- If modelocking power drops in long-term operation, check to determine if the crystal needs to be cleaned. It is good to clean crystal only if necessary. You must exercise extreme caution when doing that. Block the pump laser and clean the crystal by folding a lens tissue carefully so that you can have a tip at the end. This should be smaller than the crystal surface size so that when you clean it, you don't touch the indium foil.

- . Normally, when you push prism, you should get modelocking again.

- When touching any mirror you only use X and Y, not one between X and Y.

- Keeps air purging running all the time so no dust sticks on the crystal.

B.2.2. TI-LIGHT PERFORMANCE & SETTINGS

Ti-Light output: ~ 340 mW at CW position and power before mode locked ~ 200 mW when out of ML, ~250 mW. Do not change position of pump lens: 6.36 mm prism

position: 2.55mm, slit fully open; only touch when spectrometer is used to see spectrum. C2 CW-max position 10.25 mm. ML position: 10.05mm - +/- 5 divisions (+/- 0.05mm) are possible and still in mode lock.

If modelocking gets worse and cleaning of the crystal and optics don't do that much, you have to optimize the power. Follow the steps below:

- Write down all micrometer settings for reference

- Move the second curved mirror to CW max position. This is generally around 20 divisions from the ML position or it is written in the report sent from the company.

- Optimize the CW-power by adjusting the output coupler (OC) mirror, then the high reflector (HR) mirror. Use the horizontal key first.

- Find the modelocking range by moving the second curved mirror closer to the crystal in small steps, from old ML position; and in each step, push the prism and watch to see if it gets modelocking. The modelocking range normally has ~ 10 divisions. ML power should always be higher than CW-power. If necessary to center the spectrum at 800 nm wavelength, move the prism accordingly. The spectrum is roughly at 770-780 nm. If this does not help, try the following:

- Check the overlap between the green and IR spots with the IR-viewer on the first curved mirror C1 (from the direction of the sapphire crystal). Both spots should have the same horizontal level and the IR has to be on the right side of the green. The green spot is weaker and smaller than the IR. To make it stand out, block and unblock the IR cavity as we talked about. It is not easy to judge how close together they should be, so try the following strategy.

- At CW max position, use the alignment keys for both HR and OC at the horizontal screw (lower one).

- Then pick a direction for the HR, e.g., clockwise, and go a small bit, like 5 min, turn on the clock.

- As a result, the power will drop slightly; now max it back up with the other mirror, the OC. This way you walk the cavity and the overlap will change.

- Repeat the above step, if necessary, by moving the key in the HR the next tiny step and check overlap between the two spots.

- Now, move the C2 to ML range.

B.3. REGEN MAINTENANCE

- After tune-up of the Ti-Light, the amplifier seed input mirrors may need to be tweaked (S1 and S1 to center the beam center on irises A1' and A2, as shown in Fig. B.6.)

- If the beam is not centered on the irises, then use mirror S1 to center beam on iris A1' (added by us) and mirror S2 to center beam on iris A2.

- Then, make sure the shape of the beam on each one of the stretcher components is as shown below in Fig. B.7 before you proceed to touch anything else.

- After that, if the beam is not going through the element FR#11, then you need to use mirror M#10 to move the beam into the center of it.

- To make sure the seed beam is centered on the first crystal Ti: s #21, close the iris A3 and check to determine if the beam is going through it or not. If not, you first need to touch mirror M#22, if it does not help, you also need to touch the other mirror, M# 18. You do all of this with pumping beam blocked.

Fig. B. 5. Lasers and ReGen amplifier beam path.
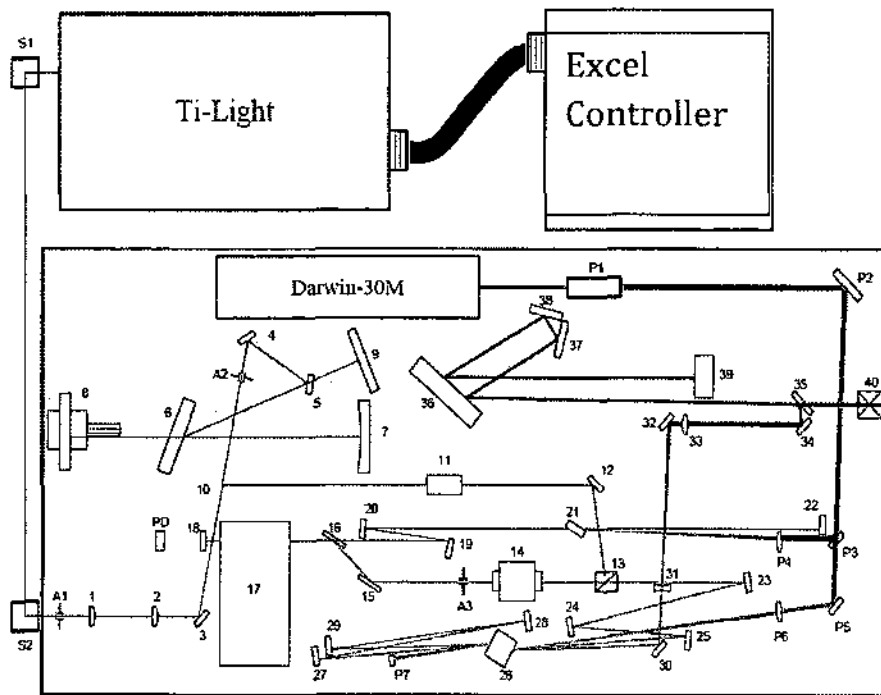

Grating #6
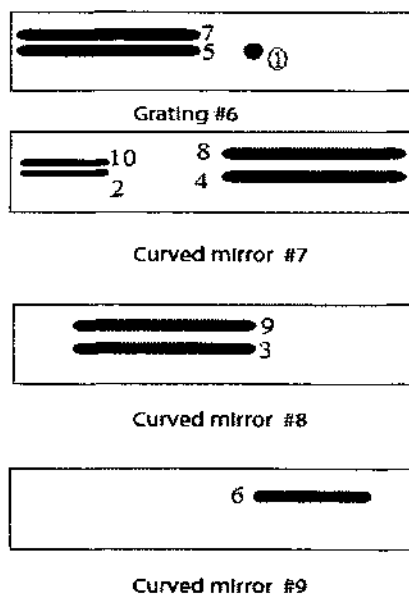
Curved mirror #7

Curved mirror #8

Curved mirror #9

Fig. B. 6. Beam shape and path on the stretcher components of ReGen. The numbers on the stretcher components represent the order in which the beam goes on them.

- Once you see the envelope of pulse train on the oscilloscope you need to change the timing and/or Pockels cell voltages to get cavity dumping; then, after that refinement, optimizations of the power can be done as in the following points.

- Block the pumping beam to the second crystal (put the blocker before PM#5) and check the power by putting the power meter in front of mirror M#27. The power should be around 0.5-0.6 W or if you put it outside it should read about 0.3 W. If not, you need to touch mirror M#29 first and then mirror M#25.

- To optimize the power coming from the pumping green on the 1st crystal (Ti: s#21), you need to touch pumping mirror PM#4 and on the 2nd crystal (Ti: s#26), you need to touch mirror PM#5 first and then, if possible, touch mirror PM#7. You do this one by one until the power is optimized (output power 1.7 W).

- You need to keep an eye on the power and pulse train shape.

APPENDIX C

LIST OF MANUFACTURER CONTACTS

Equipment	Name & Address	Phone	Fax & E-mail
Vacuum components	**MDC Vacuum Products, LLC** 23842 Cabot Boulevard Hayward, CA 94545.	800-443-8817 510-265-3500	510-887-0626 webtechsales@mdcvacuum.com
Vacuum components & pump rebuild	**DUNIWAY Stockroom Corp.** 1305 Space Park Way Mountain View, CA 94043.	800-446-8811 650-969-8811	650-965-0764 info@duniway.com
Vacuum components	**Kurt J. Lesker Company** 3983 1st Street Livermore, CA 94551.	800-245-1656 925-449-0104	925-449-5227 salesus@lesker.com
Surface science instruments (CCD camera, phosphor screens...)	**k-Space Associates, Inc.** 2182 Bishop Circle East Dexter, MI 48130.	734-426-7977	734-426-7955 requestinfo@k-space.com
Electron gun repair filaments supply	**Eurovac Sweden** SE11859 Stockholm, Sweden	+46-8-4299600	+46-8-4299604 sales@eurovac.se
Sputtering target	**Kurt J. Lesker Company** 1515 Worthington Avenue Clairton, PA 15025.	800-245-1656	412-233-9705 materials@lesker.com
Sputtering target	**ESPI metals** 1050 Benson Way Ashland, OR 97520	800-638-2581 541-488-8311	541-488-8313 sales@espimetals.com
Optical components & assemblies	**Newport Corporation** 1791 Deere Avenue Irvine, CA 92606.	800-775-5273	949-253-1680 sales@newport.com
Optics components	**Edmund Optics, Inc.** 101 East Gloucester Pike Barrington, NJ	800-363-1992	856-573-6295 sales@edmundoptics.com

	08007.		
Chemicals & Materials (Ethanol, HF, H_3Po_4 and HnO_3) –	**Alfa Aesar** 26 Parkridge Road Ward Hill, MA 01835.	800-343-0660 978-521-6300	800-322-4757 info@alfa.com
Safety supplies (acid apron, coats & masks)	Lab Safety Supply/Grainger PO Box 1368 **Janesville, WI 53547.**	800-356-0783	800-543-9910 LabSafety@cs.LabSafety.com
Thermocouples, electric heater, Ceramics & process control instruments	**OMEGA Engineering, Inc.** One Omega Drive P.O. Box 4047 Stamford, CT 06907.	800-848-4286 203-359-1660	203-359-7700 cservice@omega.com info@omega.com
Electron microscopy supplies, tungsten wire & instruments	**Ted Pella, Inc.** P.O. Box 492477 Redding, CA 96049.	800-237-3526 530-243-2200	530-243-3761 sales@tedpella.com
Gas cylinders	**Praxair GTS-WELCO** 1637 Commerce Rd Richmond, Va 23224.	800-932-0624 908-252-9300	908-252-0811 info@spectragases.com
AFM tips	**MikroMasch** 111 N. Market Street, 6th Floor San Jose, CA 95113.	866-776-8477 919-636-3463	919-869-2443 usa@mikromasch.com
Tubing, fitting & tools	**Small Parts, Inc.** 13980 N.W. 58TH Court P.O. Box 4650 Miami Lakes, FL 33014	800-220-4242	800-423-9009 smlparts@smallparts.com
Tubing, fitting & tools	**Dibert Valve & Fitting Co., Inc.** 1174 Lance Rd Norfolk, VA 23502	757-461-1441	757-461-0387 info@dibert.swagelok.com
Laboratory supplies	**Fisher Scientific** 2000 Park Lane Drive Pittsburgh, PA 15275.	800-766-7000	800-926-1166
Laboratory supplies	**LabSource** 1186 Arbor Dr Romeoville, IL 60446.	800-545-8823	630-343-1701 kathy@labsource.com

VITA

Ashraf Hassan Farha

PROFESSIONAL CHRONOLOGY

- **Ph.D. Student** (June 2007 – present), Department of Electrical and Computer Engineering, Old Dominion University, Norfolk, VA.

- **Teaching Assistant** (March 2004- June 2007), Department of Physics, Faculty of Science, Ain Shams University, Cairo, Egypt,

- **Research Assistant** (January 2000 – March 2004), Department of Physics, Faculty of Science, Ain Shams University, Cairo, Egypt.

AWARDS

- Outstanding Ph.D. Researcher Award 2013, Department of Electrical and Computer Engineering, Old Dominion University.

- Jefferson Science Associates, LLC, Thomas Jefferson National Accelerator Facility, Jefferson Lab fellowship, 2012 and 2013.

SELECTED PUBLICATIONS

1. **A. H. Farha**, Ali Oguz Er, Yüksel Ufuktepe, Ganapati Myneni, and Hani E. Elsayed-Ali, Applied Surface Science **258 (4), 1613-1618 (2011)**.
2. **A. H. Farha**, Ali O. Er, Yüksel Ufuktepe, Ganapati Myneni, and Hani E. Elsayed-Ali, Surface and Coatings Technology **206 (6), 1168-1174 (2011)**.
3. **A. H. Farha**, Ali Oguz Er, Yuksel Ufuktepe, and Hani Elsayed-Ali, *Materials Chemistry and Physics* **132, 667-672 (2012)**.
4. M. A. Mamun, **A. H. Farha**, Y. Ufuktepe, H. E. Elsayed-Ali, and A. A. Elmustafa, *Journal of Materials Research* **27(13), 1725-1731 (2012)**.
5. M. A. Mamun, **A. H. Farha**, A. O. Er, Y. Ufuktepe, D. Gu, H. E. Elsayed-Ali, and A. A. Elmustafa, *Applied Surface Science*, **258, 4308-4313 (2012)**.
6. Y.Ufuktepe, **A. H. Farha**, S.I. Kimura, T.Hajiri, K. Imura, M. A. Mamun, F. Karadag, A. A. Elmustafa, H. Elsayed-Ali, , *Thin Solid Films* **545, 601-607 (2013)**.
7. Y. Ufuktepe, **A. H. Farha**, S.-i. Kimura, T. Hajiri, F. Karadağ, M. A. Al Mamun, A. A. Elmustafa, G. Myneni, and H. E. Elsayed-Ali, *Materials Chemistry and Physics* **141, 393-400 (2013)**.
8. M. A. Mamun, **A. H. Farha**, Y. Ufuktepe, H. E. Elsayed-Ali, and A. A. Elmustafa, *Journal of Materials Research*, **27 (13) 1725-1731 (2012)**.